SISSA

PhD in Astrophysics

Academic Year 2008/2009

Thesis submitted for the degree of Doctor Philosophiæ

Optical versus X–ray afterglows of GRBs: towards understanding the emission processes.

Candidate:
Marco Nardini

Supervisors:
Annalisa Celotti
Gabriele Ghisellini
Giancarlo Ghirlanda

To Alessia

Contents

Preface

Gamma–Ray Bursts (GRBs) are the most distant objects ever detected after the recombination epoch. They consist of a short intense emission episode of gamma-rays (10 keV–2 MeV) with typical duration between 10^{-2} and 10^{3} seconds. This is called the "*prompt*" emission phase. GRBs are classified, according to their observed duration, into short GRBs (lasting less than 2s) and long GRBs (lasting more than 2 s). During the prompt phase GRBs are the brightest objects in the gamma–ray sky.

The gamma–ray prompt emission is accompanied by a long lasting emission, called "afterglow", covering the whole spectral range from the radio to the X–rays. The afterglow emission can be observed up to months after the prompt phase ceased.

After the discovery of the GRB afterglow made possible by the Dutch-Italian satellite *BeppoSAX*, and the confirmation of their cosmological origin, the GRB community reached a general consensus about the nature of these sources which led to the formulation of the so called "standard fireball model". This model was able, until recently, to account for most of the observational properties of the both the prompt and the afterglow emission.

In this scenario, long GRBs are thought to be produced by the core collapse of massive stars. The gamma–ray prompt emission is produced by the "internal shocks" developed by the collisions of different plasma shells ejected by the central engine with different Lorentz factors. The afterglow emission is due to the "external shock" produced by the deceleration of a relativistically expanding fireball by the external medium. The leading radiative mechanism responsible for the prompt and the afterglow emission is synchrotron radiation by electrons accelerated at the internal/external shocks. An important assumption of the standard model is that both the optical and the X–ray afterglows are produced by the same mechanism, taking place in the same region.

The launch of the *Swift* satellite (in November 2004), in synergy with the available network of automatic ground based optical telescopes, signed a remarkable improvement (a kind of "revolution") of our "view" of GRB afterglows. Thanks to the fast repointing capabilities of *Swift*, now X–ray and optical afterglows can be observed starting only few minutes after the prompt GRB

emission. Before the launch of *Swift*, instead, afterglow observations started typically several hours after the burst detection.

This new observational window, opened on the early times afterglow emission, unveiled a picture that is much more complex than what had been seen before *Swift* when the optical and X–ray light curves were usually well described by simple power law decays. The early time light curves observed in the X–rays (and sometimes in the optical), show different phases characterised by different decay indices, chromatic breaks and sudden rebrightenings. Another important finding of *Swift* is the fact that often the GRB optical light curve does not track the X–ray one. This cannot be explained in the framework of the standard model which assumes that both the X–ray and the optical emission have the same origin and, therefore, should behave similarly.

For this reason, in the last few years, several alternative models have been proposed in order to account for the new "afterglow picture" depicted by the *Swift* observations. Most of these models, however, try to reconcile the observed X–ray and optical light curve complexity through some modifications of the standard afterglow model. Usually, these alternative scenarios assume, as in the standard model, that the optical and X–ray emission are due to the same emission mechanism operating in the same emitting region and therefore suffer of the same main problem of the standard model i.e. they can hardly reproduce the diverse light curves of the optical and X–ray emission of individual GRBs.

My thesis is devoted to the study of this issue, i.e. the study of the GRB afterglows to understand the physical mechanisms that produce the observed optical and X–ray emission. The aim of my thesis is to study and to test with the available observations a possible alternative scenario to the standard model that fails to explain the complex behaviour of the X-ray and optical afterglow emission of GRBs.

To this aim I studied the intrinsic (i.e. rest frame) afterglow properties simultaneously taking into account the optical and X–ray light curves. This is possible exploiting the rich broad band follow up that is now available for a large number of events. I analysed the optical luminosities of long GRBs finding an unexpected clustering and bimodality of the optical luminosity distributions. I proved that these results are not due to observational selection effects and that the X–ray luminosity are not in agreement with what found in the optical. These results can hardly be explained in the framework of the standard afterglow model.

Together with the group I am working with, I analysed the light curve of the optical and X–rays rest frame luminosity of a sample of 33 long GRBs. We modelled the broad band light curve evolution as due to the sum of two separate components, contrary to the usual assumption of a common origin of the optical and X–ray emission. We obtain a good agreement with the observations, accounting for the light curves complexity and diversity.

This two component model makes predictions about the broad band spectral energy distribution (SEDs), that I tested analysing the observed SEDs. Through this analysis I confirm that our two component model is consistent with the observed data also form the spectral point of view.

This led us to propose a new view of the afterglow emission mechanism following the so called late prompt scenario proposed by Ghisellini et al. 2007. According to our view, the central engine activity lasts for long time (up to months after the trigger) keeping on producing slower shells that are responsible for the emission of optical and X–ray radiation that competes with the standard forward shock emission. This generates the complexity of the observed broad band light curves and explains the diversity between the optical and X–ray temporal evolution.

We suggest that the late time activity of the central engine is sustained by the accretion of the material that failed to reach the escape velocity from the exploding progenitor star, and falls back. The presence of this mechanism is strengthened by the similarity between the temporal evolution of the late prompt component, and the expected time profile of the accretion rate of the fall back material.

Collaborations

The work presented in this thesis has been published (or submitted for publication) in the following scientific papers:

- "*Clustering of the optical-afterglow luminosities of long gamma-ray bursts*"
  Nardini, M., Ghisellini, G., Ghirlanda, G., Tavecchio, F., Firmani, C., Lazzati, D., 2006, A&A, 451, 821

- "*The unexpected clustering of the optical afterglow luminosities*"
  Nardini, M., Ghisellini, G., Ghirlanda, G., Tavecchio, F., Firmani, C., Lazzati, D., 2006, Il Nuovo Cimento B, vol. 121, Issue 12, 1539

- "*Optical afterglows of gamma-ray bursts: a bimodal distribution?*"
  Nardini, M., Ghisellini, G., Ghirlanda, G., 2008, MNRAS, 243, 1049

- "*Optical afterglow luminosities in the Swift epoch: confirming clustering and bimodality*"
  Nardini, M., Ghisellini, G., Ghirlanda, G., 2008, MNRAS, 386, L87

- "*Precursors in Swift Gamma Ray Bursts with Redshift*"
  Burlon, D., Ghirlanda, G., Ghisellini, G., Lazzati, D., Nava, L., **Nardini, M.**, M., Celotti, A., 2008, ApJ, 685, L19

- "*A unifying view of gamma-ray burst afterglows*"
  Ghisellini, G., **Nardini, M.**, Ghirlanda, G., Celotti, A., 2009, MNRAS, 393, 253

- "*The puzzling clustering and bimodality of long GRBs optical afterglow luminosities*"
  Nardini M., Ghisellini G., & Ghirlanda G., 2009a, Proceeding of the 44th Rencontres de Moriond "Very High Energy Phenomena in the Universe", arXiv:0907.5426v1

- "*Testing an unifying view of Gamma Ray Burst afterglows*"
  Nardini M., Ghisellini G., Ghirlanda G., & Celotti A., 2009b, Proceeding of the 44th Rencontres de Moriond "Very High Energy Phenomena in the Universe", arXiv:0908.0338v1

- "*Testing an unifying view of GRB afterglows*"
  Nardini M., Ghisellini G., Ghirlanda G., & Celotti A., 2009c, Proceeding for the conference 'Frontiers of Space Astrophysics: Neutron Stars & Gamma Ray Bursts" Cairo and Alexandria, Egypt, March 30 - April 4 2009 arXiv:0908.0734v1

- "*Testing an unifying view of Gamma Ray Burst afterglows*"
  Nardini M., Ghisellini G., Ghirlanda G., & Celotti A., 2009d, MNRAS, submitted (pre-print arXiv:0907.4157v1)

- "Prolonged activity of the central engine of Gamma Ray Bursts"
  Ghisellini G., **Nardini M.**, & Ghirlanda G., Proceeding for the conference 'Frontiers of Space Astrophysics: Neutron Stars & Gamma Ray Bursts" Cairo and Alexandria, Egypt, March 30 - April 4 2009 arXiv:0908.0732v1

- "Low-Resolution Spectroscopy of Gamma-ray Burst Optical Afterglows: Biases in the Swift Sample and Characterization of the Absorbers"
  Fynbo, J. P. U., Jakobsson, P., Prochaska, J.X., Malesani, D., Ledoux, C., de Ugarte Postigo A., **Nardini, M.**, et al., 2009, ApJS submitted (pre-print arXiv:0907.3449v2)

Chapter 1

Introduction

1.1 General picture

Gamma–Ray Bursts (GRBs) are short intense flashes of gamma rays (10 keV–2MeV) coming from random directions in the sky. They have been first observed around the end of the 1960s and we now know that they are associated to broad band emission covering all the electromagnetic spectrum from the radio to the gamma ray wavelengths.

GRBs are characterised by an early phase of emission in gamma rays (i.e. the actual Gamma Ray burst event) of typical duration between 10^{-2} and 10^{3} seconds called "*prompt*" emission. They are usually observed at energies between a few keV and a few MeV[1]. When a GRB occurs, it is the brightest source of gamma rays in the sky. Typical GRB fluences in gamma rays are in the range between $\sim 10^{-7}$ and 10^{-5} erg cm^{-2}. During the prompt phase the light curve is characterised by very strong variability (up to millisecond scale) and depending on their observed duration it is possible to recognise two families of GRBs: i) short GRBs lasting less than 2 seconds and ii) long GRBs lasting more than 2 seconds (Kouveliotou et al. 1993).

The gamma ray prompt emission is accompanied by long lasting emission covering all the spectral range between the radio and the X–rays. This emission (called "*afterglow*" phase) is characterised by a much smoother decaying evolution and it is visible up to months after the gamma ray prompt event until the flux becomes too small for the available instrumental sensitivity.

GRBs are the most distant events ever observed in the universe after the recombination. At the date of writing the "record holder" object with the largest spectroscopic redshift ever measured is GRB 090423 ($z \cong 8.2$; Tanvir et al. 2009).

[1]The availability of new high energy gamma ray instruments like the *Fermi* satellite allowed the detection of photons associated to GRBs (e.g. GRB 080916c) at energies up to several GeV (Abdo et al. 2009). See §1.2 for a wider more detailed.

The mean redshift of long GRBs is around $\langle z \rangle \cong 2$ ($\langle z_{Swift} \rangle \cong 2.3$ if considering only *Swift* GRBs as shown by Fynbo et al. 2009). Knowing the GRB distance it is possible to give an estimate of the total energy emitted in gamma rays during the prompt phase. Assuming that GRBs emit isotropically, the estimated energies for long GRBs are of the order of 10^{52} – 10^{54} erg. This is a huge amount of energy that is emitted in a very short time. GRB 080916c, located at redshift 4.35, emitted in about 13 s (rest frame) an isotropic equivalent energy $E_{\gamma,\mathrm{iso}} = 6.5 \times 10^{54}$ erg (during the prompt phase) that corresponds to about $4 M_{\odot} c^2$ (Greiner et al. 2009). In at least some cases this energy estimate is probably overestimated since GRB emission is not isotropic, but is collimated inside a narrow jet with typical opening angles θ_{j} of a few degrees. Correcting the emitted energy estimate for this geometrical effect allows to reduce it to more "reasonable" values. The collimation corrected emitted energy is therefore written as $E_{\gamma} \approx E_{\gamma,\mathrm{iso}}(1 - \cos\theta_{\mathrm{j}})$ and is in the range between 10^{49} and 10^{52} erg (see e.g. Frail et al. 2001, Ghirlanda et al. 2004).

In this introduction, after a brief introduction about the GRB science history from the discovery to the present times, I will present a brief review of the observational properties of these events. I will then discuss the main ideas of the so called "GRB standard model" that describes the physical mechanisms that are at the basis of the observed emission. Since in my thesis I focused on the long GRBs afterglow emission, I will mainly concentrate on the afterglow emission theory but I also give a brief description of the prompt emission mechanisms in the framework of the standard model.

1.1.1 A brief history

After a decade of cold war, in the early '60s, a policy of non-proliferation of nuclear weapons policy started to be applied by the USA, United Kingdom and URSS. In particular the Nuclear Test Ban Treaty signed in 1963 and the Outer Space Treaty[2] in 1966 ban the States Parties to the Treaty from placing nuclear weapons or any other weapons of mass destruction in the Earth orbit, installing them on the Moon or any other celestial body, or to otherwise station them in outer space. In 1963 the United States started to launch some satellites in order to verify the compliance of the treaty. The name of these satellite was *VELA* (from the Spanish verb velar that means "to look"). On board on the *VELA* some large field gamma ray detectors.

On 1967 July 2nd the instruments on board of the *VELA* satellites detected an unidentified gamma ray event. In the following years these satellites detected a large number of similar gamma ray events. These gamma–ray detectors were unable to localise the direction of the detected high energy photons but

[2]The full text of these threats ca be found on the United Nation website at the address `http://www.unoosa.org/oosa/SpaceLaw/outerspt.html`

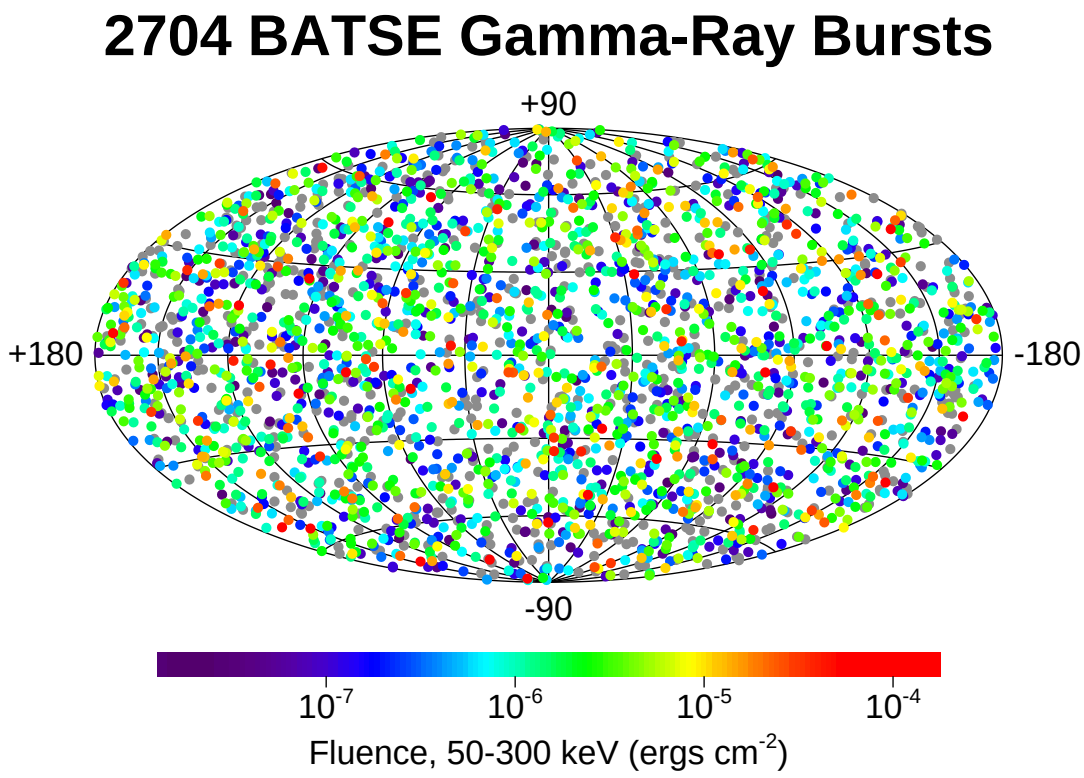

Figure 1.1: Map of the location of 2704 GRBs detected by BATSE in Galactic coordinates. The colour scale represents the different GRB fluences as labelled.

the triangulation method (made possible with the launch of the two additional satellites *VELA 5* and *VELA 6*) allowed to exclude that this unidentified emission was produced in the terrestrial atmosphere, on the Sun or Moon surface.

The information about the discovery of these gamma ray events was announced in 1973 June 1st when a paper appeared on ApJ. reporting this discovery (Klebesadel, Strong & Olson 1973).

For the following 2 decades the orbiting gamma ray detectors went on observing these unexplained events but the lack of remarkable instrumental improvements in the gamma ray instrumentation did not allow a better comprehension of the physical nature of these events. A fervent discussion took place in the literature. At the beginning of the 1990s more than 110 models had been proposed in order to explain the nature of the GRB emission (Nemiroff 1994) invoking very different sources (e.g. neutron stars, extragalactic supernovae, asteroids impacts...). In particular the discussion focused on the distance at which these events take place. Some models invoked nearby sources (inside our Galaxy or even inside the Solar system) while other models put the GRB progenitors at cosmological distances. Since the observed GRB flux is very large, the latter hypothesis implies

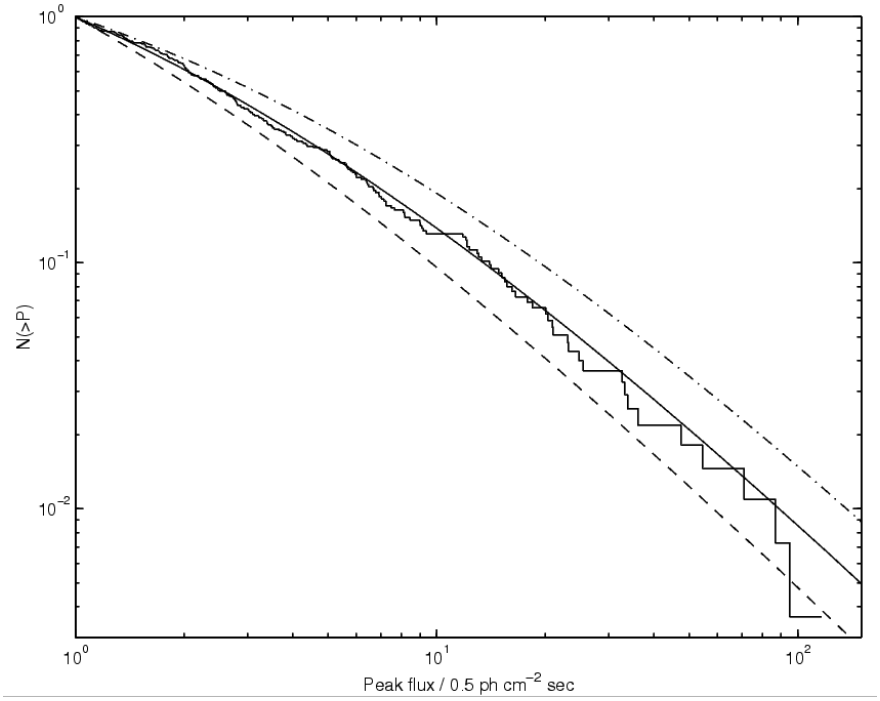

Figure 1.2: log N-log S distribution of the full sample of GRBs detected by BATSE. Different curves correspond to different cosmological model (Piran et al. 1999).

an enormous amount of energy to be released in a very short time making the GRBs the most powerful explosion known in the universe.

In 1991 the Compton Gamma-ray Observatory (CGRO) was launched. On board there was an instrument called *Burst And Transient Source Experiment* (BATSE) dedicated to the study of transient gamma ray sources. This instrument was sensitive to photons in an energy range between 20 keV and 2 MeV with a limiting flux of about 10^{-7} erg cm^{-2} s^{-1} and a large field of view ($\sim 2\pi$). These instrumental capabilities, together with a much improved spatial resolution ($\sim$ 1 degree), allowed a remarkable improvement in understanding of our the GRB nature. In about one decade of activity CGRO detected 8021 gamma ray events and among them about 2704 were GRBs. A first fundamental discovery was the fact that GRBs came from random directions in the sky as shown in fig. 1.1. This discovery proved that GRBs are not related to sources located in the Galactic plane or inside nearby galaxies. The possibilities that GRBs occur very close in the Solar system surroundings or in the Galactic halo were not excluded by this evidence but this can be considered the first step in proving the cosmological origin of GRBs.

Much more constraining is the combination of the observed isotropy with the information obtained from the study of the log N-log S distribution of a large GRB sample. As can be seen in fig. 1.2, due to the lack of weak burst, the log N-

$\log S$ distribution is incompatible with a local distribution and forced the GRBs cosmological interpretation (see e.g. Paczynski 1991, Fishman et al. 1994, Hakkila et al. 1994, Piran 2004). As shown by Meegan et al. (1992), the number versus intensity distribution does not follow the $-3/2$ power law expected for a spatially extended homogeneous distribution of sources, but at the same time the angular distribution is isotropic within statistical limits. Taken together, these results are inconsistent with the spatial distribution of any known population of galactic objects, but may be consistent with the bursts being at cosmological distances.

The "smoking gun" that finally proved the cosmological nature of GRBs arrived only in 1997 with the launch of the Italian–Dutch satellite *BeppoSAX* (Boella et al. 1997). *BeppoSAX* opened a new era on GRB science. The great instrumental improvement was the fact that gamma ray detector spatial resolution was greatly improved ($\sim$ 3 arcmin). This resolution allowed a good localisation of the source coordinates, the spacecraft was able to slew in a few hours and point the on board X–ray telescope (with a spatial resolution of about 60 arcsec) in the direction of the gamma ray detector error box. This allowed to detect the first GRB X–ray counterpart (afterglow) in GRB 970228 (Costa et al. 1997). The accurate localisation of the X–ray afterglow of GRB 970228 allowed to point the ground based optical telescopes in the direction of the source discovering the first GRB optical afterglow (Van Paradijs et al., 1997). In the same year Metzger et al. (1997) identified some absorption lines in the optical afterglow spectrum of GRB 970508 measuring the first GRB redshift (z=0.835). The afterglow of GRB 970508 was the first one observed also in the radio bands (Frail et al., 1997). The GRB redshift measurement finally proved the cosmological nature of these events.

The *BeppoSAX* satellite activity went on until 2002 allowing the detection of a large number of GRBs and the measure of the redshift for about 40 of them.

A new fundamental step in the GRB science is related to the launch of the American-English-Italian satellite *Swift* on 2004 November 24th (Gehrels et al. 2004). *Swift* is a multi-wavelength observatory specifically designed for GRB observations. On board on *Swift* there are three instruments:

- BAT (Burst Alert Telescope): a gamma ray telescope sensitive to photons in the energy range between 15 and 150 keV. A coded mask allows a quite precise angular resolution (of about 17 arcmin). The BAT field of view is about 14 sr.

- XRT (X–Ray Telescope): an X–ray telescope with Wolter configuration characterised by a good angular resolution (HEW=15 arcsec) and effective area ($A_{\rm eff}$ @ 1keV=150 cm^2) sensitive to an energy range between 0.3 and 10 keV.

- UVOT (Ultra Violet Optical Telescope): a small (30 cm) telescope with a field of view of 17'×17'. It has 3 optical filters (U, B, V) and 3 Ultra Violet

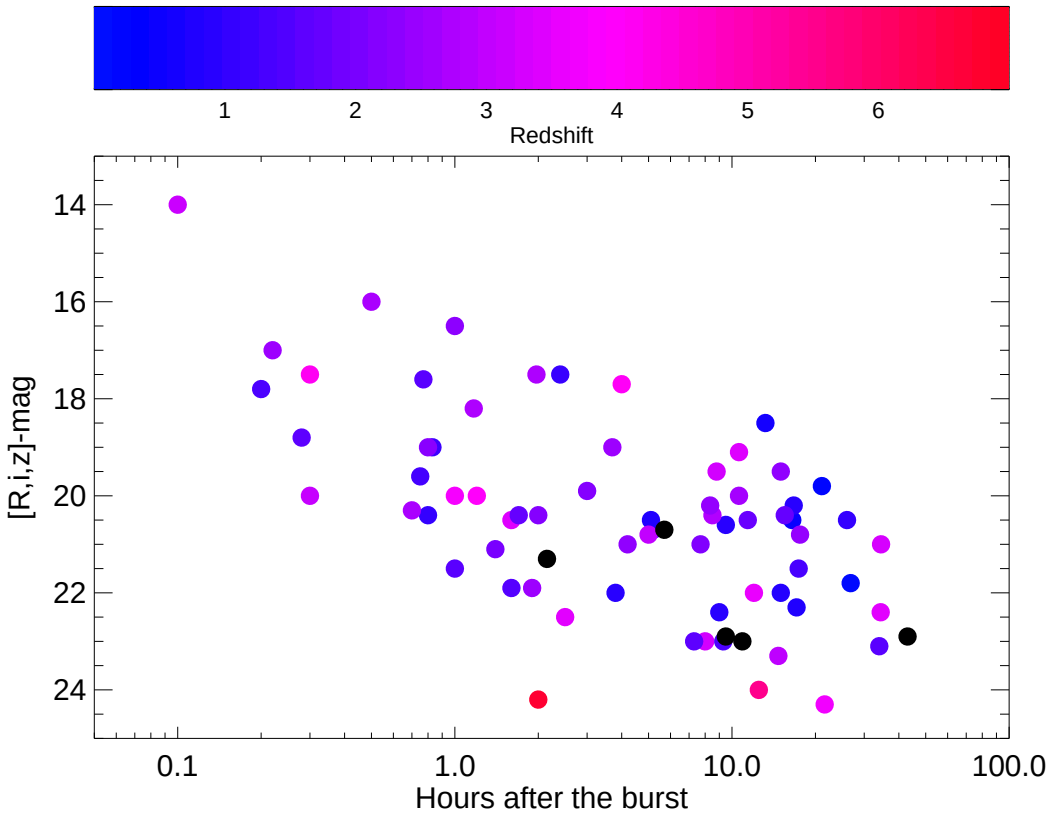

Figure 1.3: The R, i or z– band magnitudes of the *Swift* GRBs optical afterglows in the acquisition image for the spectroscopy as a function of the time when the spectroscopic observation started. The colour bar in the top indicates the colour code for the measured redshifts. Black points represent spectra for which a redshift determination was not possible (Fynbo et al. 2009).

filters (UVW1, UVW2 and UVM2). UVOT is co-aligned with XRT in order to have simultaneous observations.

The fundamental feature that allowed *Swift* to make an instrumental revolution in GRB observation is the possibility for the spacecraft to slew automatically in the direction of the BAT error box in a few tens of seconds allowing X–ray, optical and UV observations starting from about 100 s after the gamma ray trigger. The automatically derived GRB coordinates are promptly diffused to a network of ground robotic telescopes that start observing the BAT error box a few seconds (in some cases less than 20 s) after the trigger. The fast precise afterglow localisation allows also to point larger telescopes within 1 hour after the trigger and to measure the GRB redshift when the afterglow is still very bright (see fig. 1.3). These fast redshift measurements, together with the good BAT sensitivity, allowed to measure a large number of $z > 5$ redshifts. At the time of writing 3 $z > 6$ have

been measured with a record of $z = 8.2$.

Some of the most intriguing *Swift* discoveries are:

- short GRBs also have afterglows similar to the long GRBs ones;
- short GRBs are at cosmological distances;
- the early time X–ray light curve is much more complex than what expected before (see §2.1 for a detailed discussion);
- the X–ray light curve sometimes does not track the optical temporal behaviour (see §5 for a detailed discussion);
- a not negligible fraction of events do not show any detectable optical emission even if they have been observed at deep limiting magnitudes (see De Pasquale et al. 2003, Nardini et al. 2008b, Fynbo et al. 2009, and §3.2 for a more detailed discussion.)
- with the early times observations of GRB 060218/SN 2006aj (Kennea et al. 2006) we had the first case in which a supernova has been observed in the first seconds after the explosion. This represents a great step in the supernovae science studies

1.2 GRB observational properties

1.2.1 Prompt phase

Prompt emission temporal properties

The prompt phase of a GRB is operationally defined as the time interval when the gamma ray intrument detects a signal above background. This phase can approximately last from 10^{-2} to 10^3s. The usual measure for the duration is T_{90} (T_{50}) which corresponds to the time in which 90% (50%) of the counts are detected. Depending on their T_{90}, GRBs have been divided into two different families (i.e. short GRBs with $T_{90} < 2$s and long GRBs with $T_{90} > 2$s; Koveliotu et al. 1993). This choice is due to the fact that the T_{90} distribution of the GRBs observed by BATSE showed a clear bimodality (see fig. 1.4) with a gap around 2 s. The mean duration of the short and long GRBs are $\langle T_{90}^{\rm short}\rangle \approx 0.6$s and $\langle T_{90}^{\rm long}\rangle \approx 20$s respectively. Some groups (e.g. Horváth 1998, Mukherjee et al. 1998) claimed the presence of a third intermediate duration group but it is not clear if this division into three classes is statistically significant (Hakkila et al. 2000). The BATSE era long–short GRB divide was strengthened also from the spectral point of view (Dezalay et al. 1996, Kouveliotou et al. 1996) since short

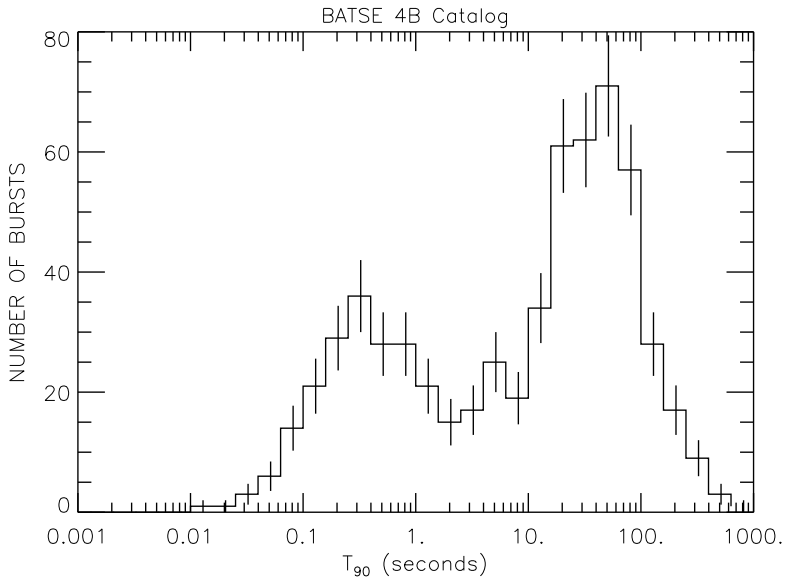

Figure 1.4: Distribution of the prompt emission observed duration (T_{90}) of all the GRBs detected by BATSE

GRBs were usually characterised by harder gamma ray spectra than long ones (see the following section for a discussion about GRB prompt spectra).

In the *Swift* era this subdivision has been questioned by several groups and I will discuss this issue in §1.2.5.

Most GRB gamma ray light curves are characterised by strong flux variations in time intervals δt much shorter than T_{90}. The variability time scale, δt, is determined by the width of the gamma ray light curves peaks and is usually of the order of fraction of seconds but sometimes $\delta t \sim 10^{-3}$ s have been observed (McBreen et al. 2001, Nakar & Piran 2002). Even if, usually, different GRBs show very different light curve morphology, most of GRB light curves are characterised by short pulses lasting from a fraction of seconds to dozen of seconds. Individual pulses display a hard to soft evolution with the peak energy (i.e. the peak energy of the $\nu F(\nu)$ spectrum described in 1.1) decreasing exponentially with the photon flux (Ford et al. 1995, Liang & Kargatis 1996, Norris et al. 1996). Other events, instead, show much smoother light curves that can be described with a typical FRED (Fast Rise Exponential Decay) shape.

When comparing the light curve of a single GRB at different energies, it had been noticed that the emission at lower energies (e.g. in the BATSE detector the energy channels had energy ranges: 20-50 keV, 50-100 keV, 100-300 keV) was delayed with respect to the high energy channel ($>$ 300 keV) one (Norris et al 1996). For the long GRBs Norris et al. (1996) have also found that these spectral lags are anti-correlated with the luminosity of the bursts: more luminous bursts have shorter lags. This anti correlation seems not to appear in the short duration

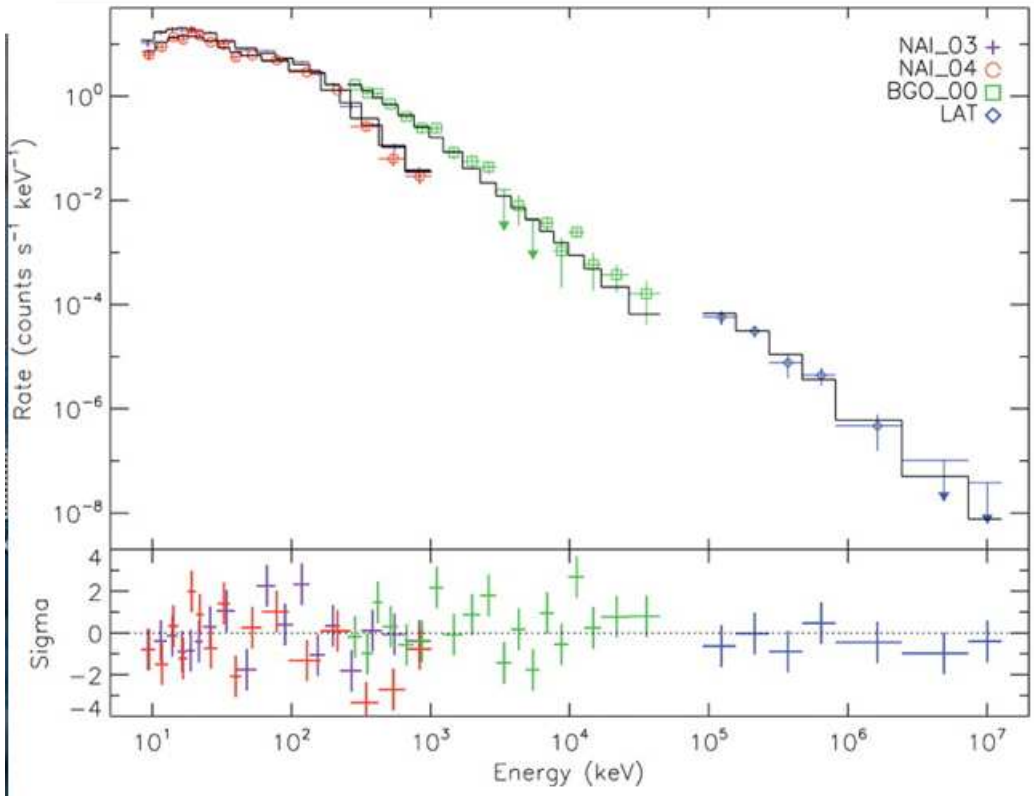

Figure 1.5: The gamma ray spectrum of GRB 080916c (from Abdo et al. 2009) as detected by the *Fermi* GBM (red and green dots) and LAT (blue dots) instruments.

GRB sample. Fenimore et al. (1995) proposed also that the pulses low energy light curves are wider compared to the high energy light curves. The width goes as $\sim E^{-0.4}$.

It is also possible to analyse the prompt light curve evolution through the standard Fourier analysis in order to obtain the light curve power spectrum. Beloborodov et al. (2000) found that the slope of such a power spectrum is $\sim -5/3$.

In some long GRBs the main prompt event is anticipated by a weaker, well separated precursor activity (Koshut et al. 1995, Lazzati 2005, Burlon et al. 2008). In some cases the quiescence time between the precursor and the beginning of the main prompt event can last for some hundreds of seconds. In Burlon et al. (2008) we found neither a correlation between the two spectral properties of the precursor and the main event nor a tendency for the precursors spectra to be systematically harder or softer than the prompt ones.

Prompt emission spectral properties

The observed prompt emission gamma ray spectrum appears non thermal. It usually peaks around some hundred keV. Even if GRB spectra differ strongly from

one burst to another, Band et al. (1993) proposed a phenomenological fit to the spectrum that is able to well represent the observed GRB spectra. It is a smoothly joining broken power law with a break energy at $(\tilde{\alpha}-\tilde{\beta})E_0$ that can be written as:

$$N(\nu) = N_0 \begin{cases} (h\nu)^{\tilde{\alpha}}\ e^{-\frac{h\nu}{E_0}} & h\nu < (\tilde{\alpha}-\tilde{\beta})E_0 \\ e^{\tilde{\beta}-\tilde{\alpha}}[(\tilde{\alpha}-\tilde{\beta})E_0]^{\tilde{\alpha}-\tilde{\beta}}(h\nu)^{\tilde{\beta}} & h\nu > (\tilde{\alpha}-\tilde{\beta})E_0 \end{cases} \quad (1.1)$$

where $\tilde{\alpha}$ and $\tilde{\beta}$ are the low and high energy spectral indices[3].

This empirical description of the GRB spectra has no particular theoretical motivation but it is able to well reproduce the observed spectra covering more than 6 decades. The *Fermi* Gamma-ray Space Telescope, launched on 11 June 2008, provides broad energy coverage and high sensitivity for GRBs detection through the Gamma-ray Burst Monitor (GBM) and the Large Area Telescope (LAT) covering an energy range between 8 keV and 300 GeV (Atwood et al. 2009). This very large energy range allows to well constrain the gamma ray spectral shape (for the few GRBs detected by LAT). Figure 1.5 shows the *Fermi* broad band gamma ray spectrum of the extremely powerful GRB 080916c. As can be seen the spectrum from 8 keV up to 10 GeV can be well represented by the Band model.

1.2.2 Afterglow phase

The GRB gamma ray prompt emission is accompanied by a long lasting (up to months) emission covering all the electromagnetic spectrum from the radio to the X–rays. The study of the nature of this so called afterglow is the main topic of this Ph.D. thesis and will be discussed in detail both from the observational and from a more theoretical point of view along the following sections.In this section I will only give some brief information that can be useful in order to better understand the following discussion. In particular I will define the nomenclature and the formalism that will be used in this thesis. Note that the parameter definitions can sometimes be different with respect to what can can be found in the literature since there is no standard agreement on the used formalism. Since I will focus on the optical and X–ray afterglow emission, in this introduction I will concentrate on these bands.

Temporal properties of the afterglow phase

The temporal evolution of the afterglow emission is characterised by light curves that are much smoother than the erratic, spiky and rapidly evolving gamma ray prompt emission. Despite the differences than can be seen in the afterglow light

[3]We used the notation $\tilde{\alpha}$ and $\tilde{\beta}$ in order to avoid confusion with the afterglow phase temporal and spectral indices usually written as α e β.

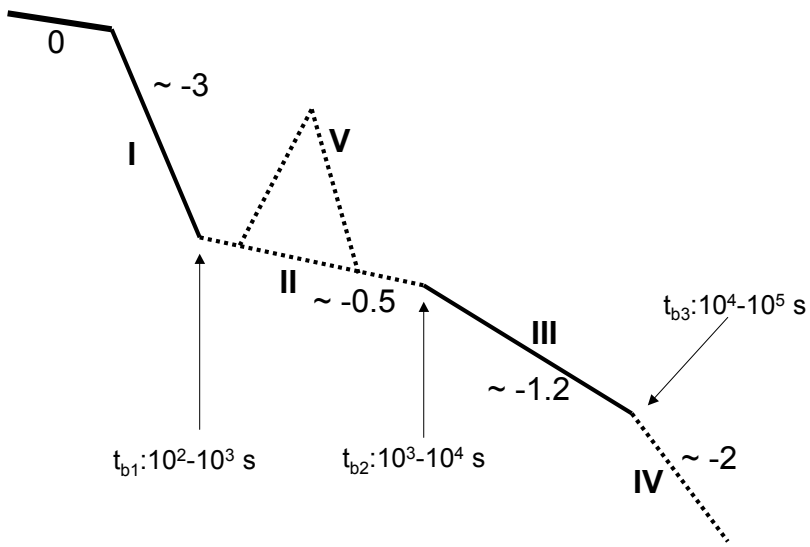

Figure 1.6: Sketch proposed by Zhang et al. (2006) showing the typical "canonical" behaviour observed in the X–ray light curves observed by XRT.

curves of different GRBs, these are in general much more similar one another than the prompt phase light curves.

For some GRBs the spacecraft slewed fast enough to observe the X–ray afterglow while BAT was still observing the prompt emission. In these cases the X–ray emission observed during the prompt phase is dominated by the low energy extrapolation of the gamma ray prompt emission. Immediately after the end of the prompt phase, the X–ray flux suddenly decreases of few orders of magnitude in some dozens of seconds. This fast decline is usually followed by a much shallower decay phase lasting 10^3– 10^5 seconds that ends with a break in the light curve at a time called $T_{\rm A}$ (Willingale et al. 2007). After $T_{\rm A}$ the X–ray flux smoothly declines as a power law $F(t) \propto t^{-\alpha}$ with $\alpha \sim 1.2$. In some cases at a few days after the trigger a further steepening of the light curve is observed and the temporal decay index becomes $\alpha \sim 2$. This is the so called "canonical" X–ray GRB light curve that is schematically presented in fig. 1.6 and will be discussed in detail in §2.1. In a recent study of the X–ray properties of a large number (162) GRBs detected by *Swift* , Evans et al. (2009) showed that this canonical light curve well describes about half of the observed GRBs, while about 30% show only one break, a few (∼

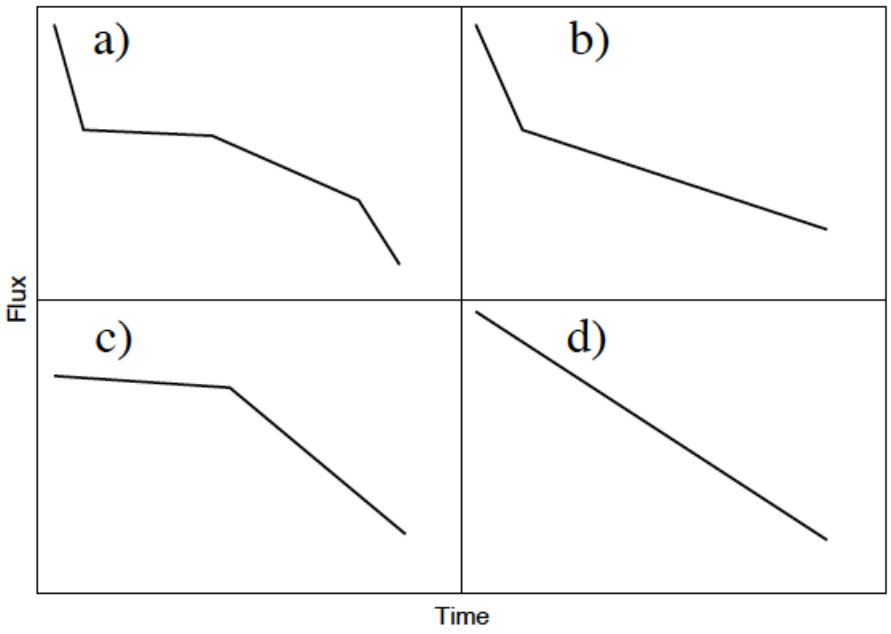

Figure 1.7: Schematic diagrams of the different observed X–ray light curve morphologies. Panel a) shows the so-called "canonical" light curves. Panels b)–c) are those with one break, either shallowing (b) or steepening (c). Panel d) are those with no breaks. (Evans et al. 2009)

4%) can be well described by a single power law decline with one forth of them having more complex light curves (defined oddballs in their paper). Figure 1.7 taken from Evans et al. (2009) schematically shows the different observed X–ray behaviours.

About half of the observed GRBs show some flaring activity in the X–rays (e.g. Chincarini et al. 2007). These flares are characterised by a sudden X–ray flux increase (sometimes of the order of 500%) followed by a very steep decline. If T is the time after the trigger at which the flare occurs and δt is the flare duration, in most cases $\delta t \ll T$. A more detailed description of the X–ray flare phenomenon and a discussion on its nature is given in §2.5.

Also the optical afterglow emission is characterised by a rather smoothly evolving temporal behaviour, but often does not track the X–ray light curve evolution. Thanks to the presence of a net of ground based robotic telescopes, we have the possibility to observe the GRB optical counterpart a few seconds after the gamma ray trigger. In some cases it was possible to detect the optical afterglow during the prompt phase and in a couple of cases also in the gamma ray quiescent period between the precursor and the main prompt event. Differently to what happens in the X–ray, the optical fluxes observed during the prompt phase is not usually dominated by the low energy extrapolation of the gamma ray

prompt emission and the prompt optical light curve is smoothly connected with the standard afterglow one (e.g. GRB 050820a, GRB 060729). In some cases (e.g. GRB 060418 and GRB 060607a; Molinari et al. 2007) the optical light curve shows an increase at early times that has been explained as the onset of the afterglow (Molinari et al. 2007). In other cases the optical fluxes track the same shallow decay phase observed in the X–rays (e.g. GRB 060729; Grupe et al. 2007). GRB 080319b instead, showed an extremely bright (it reached the 5th magnitude even if it was located at redshift ∼1) prompt optical emission that was claimed to be produced in the same region of the gamma ray prompt emission (Racusin et al. 2008, Kumar & Panaitescu 2008).

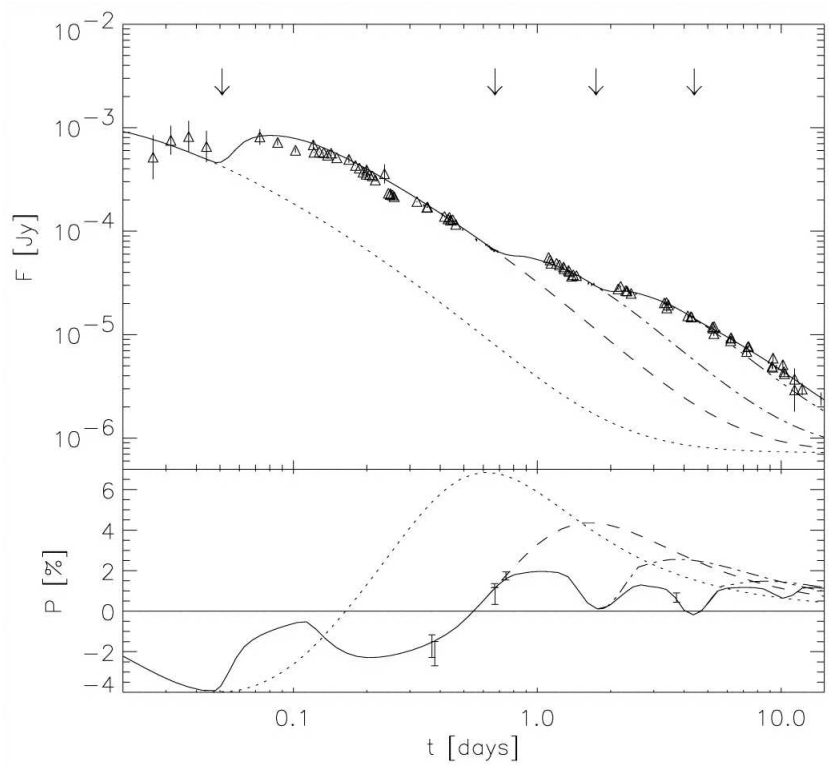

Figure 1.8: R band light curve of GRB 021004 (Björnsson et al. 2004)

At later times (a few $\times 10^3$ s), the optical light curves smoothly decline as a power law with with temporal indices $\alpha \sim 1$. In some cases, a few days after the trigger, the optical light curve steepens with a post break temporal decay index $\alpha \sim 2$.

In some GRBs the optical light curves follow a more complex behaviour with deviations from a power law decay also at later times. They sometimes show several bumps superposed to a power law decay as for example in GRB 021004 (see fig. 1.8) or rebrightenings like in the case of GRB 071003.

Spectral properties of the afterglow phase

The spectrum of GRB X–ray afterglows are usually well described by a single power law $f(\nu) \propto \nu^{-\beta}$ covering the observed energy range (i.e. 0.3 – 10 keV in case of XRT) with two intervening absorption systems, one located in our Galaxy (at redshift 0), and the second located at the source redshift. A possible alternative is discussed in §7. The distribution of the spectral indices $\beta_{\rm X}$ is centred around 1 and extends between $\beta_{\rm X} = 0$ and $\beta_{\rm X} = 2$ (Evans et al. 2009).

During the early steep decay phase and during the flaring activity, X–ray spectra show a strong temporal evolution and are sometimes better fitted with a broken power law model instead of a single power law. During the flat phase and the later steeper decay the X–ray spectra do not show any temporal evolution and no spectral change is observed around $T_{\rm A}$ (see §7).

In the pre *Swift* era X-ray lines were observed in 7 GRBs: GRB 970508 (Piro et al. 1999), GRB 970828 (Yoshida et al. 1999), GRB 990705 (Amati et al. 2000), GRB 991216 (Piro et al. 2000), GRB 001025a (Watson et al. 2002), GRB 000214 (Antonelli et al. 2000b) and GRB 011211 (Reeves et al. 2002). Most of these lines were interpreted as red-shifted Fe Kα iron emission lines. In one case (i.e. GRB 000214) the position of this line in the X–ray spectrum was used in order to estimate the GRB redshift.

The fact that after the launch of *Swift* no event has shown such lines has cast doubts about these results.

The optical afterglow spectra are usually described as single power laws as in the X–rays. The analysis of the spectral slope is complicated by the lack of information about the properties of the dust reddening occurring in the GRB host galaxy. The optical spectral index $\beta_{\rm o}$ is usually estimated analysing the Infra Red – optical – UV spectral energy distribution (sometimes combining also ground based optical spectroscopy), assuming that the host galaxy dust absorption can be well described by an extinction curve similar to the only ones that we directly measured (i.e. the ones describing the dust absorption in the Milky Way (MW), the Small Magellanic Cloud (SMC) and the Large Magellanic Cloud (LMC)). Figure 1.9 shows these extinction curves (Pei 1992). For an exhaustive description of the method used to estimate the optical spectral index from the optical spectral energy distributions see for example Kann et al. (2006). In fig. 1.10 we show a typical SED obtained superposing the optical spectrum with the photometric points.

The de-absorbed optical spectral indices are usually in the range between $\beta_{\rm o} = 0.5$ and $\beta_{\rm o} = 1.2$ but can be even harder with $\beta_{\rm o} = 0.2$ (e.g. Kann et al. 2006, 2009). The optical spectral index is usually not evolving in time but in some cases a colour evolution has been seen in correspondence with changes of the light curve behaviour (see §8 for some examples).

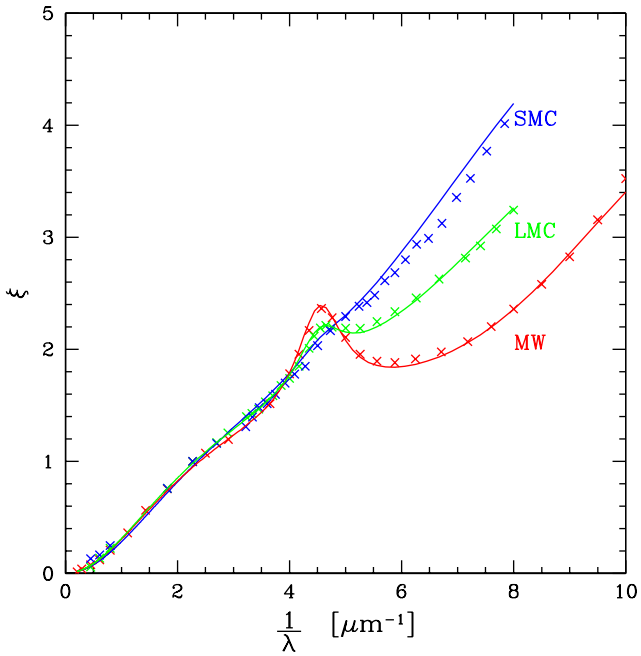

Figure 1.9: Dust extinction curves versus the inverse of the wave length measured in μm. Different colours represent the curves in different galaxies (i.e. Large Magellanic Cloud, Small Magellanic Cloud, and Milky way). The points are the observed values while the solid lines represent the analytical fit proposed by Pei (1992) that is often used to estimate the extinction occurred in extra galactic sources. The parameter $\xi(\lambda)$ is defined as the ratio between the absorption at a wavelength λ and the absorption in the B band.

1.2.3 GRBs/Supernovae connection

It is now widely accepted that long GRBs are related to the explosive death of massive stars[4]. Extensive studies of GRB afterglow revealed the connection of some long GRBs with core collapse type Ib,c supernovae. Already in 1998, about one year after the first optical afterglow discovery, the observations of GRB 980425 revealed an association with a type Ic supernova called SN98bw (Galama et al. 1998). GRB 980425 was a quite unusual GRB, it was associated with a low redshift galaxy ($z = 0.0085$) and its isotropic gamma ray energy release ($E_{\rm iso} = 8.5 \times 10^{47}$ erg) was about 3 orders of magnitudes smaller than the typical long GRBs (Frail et al. 2001; Bloom, Frail & Kulkarni 2003). The fact that GRB 980425 showed some differences with respect to the typical long GRBs properties, cast some doubt on

[4]Part of this discussion is inspired by the review on "*The Supernova–Gamma-Ray Burst Connection*" by Woosley & Bloom (2006)

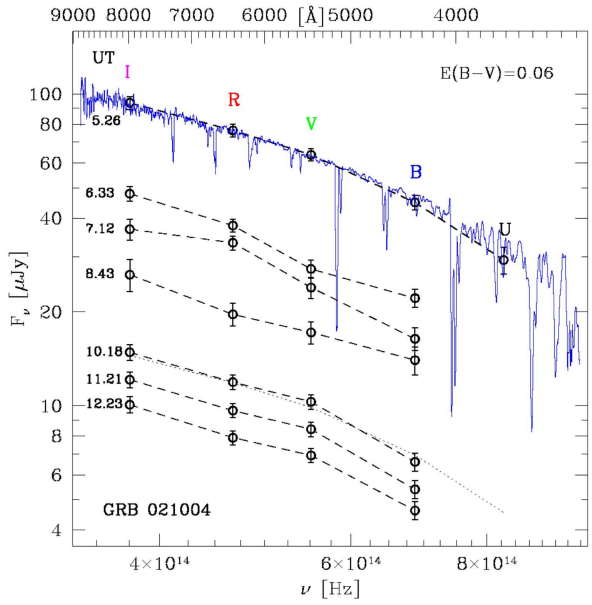

Figure 1.10: Optical spectrum of GRB 021004 superposed to the contemporaneous optical photometric data. Black symbols in the bottom part of the figure are later time (hours after trigger are written on the left) photometric data. From Bersier et al. (2003).

the possibility to use it as the proof of the GRB/SN connection.

A strong confirmation of this association has been given by the observation of the bright GRB 030329 located at low redshift ($z = 0.1685$; Greiner et al. 2003). After the first days in which the optical emission of GRB 030329 followed a typical GRB afterglow evolution, the afterglow flux faded enough to unveil the rise of the SN 2003dh emission. The optical spectral observations 6.6 and 7.7 days after the GRB (see fig. 1.11), started to show a deviation from a pure power law and the emergence of broad SN spectral features (Chornock et al. 2003; Garnavich et al. 2003a; Hjorth et al. 2003b; Kawabata et al. 2003; Matheson et al. 2003a,b; Stanek et al. 2003).

Another signature of the existence of an underlying supernova in the optical emission of GRBs is the observation of a late time ($\sim$ 15 days after the trigger) optical bump in the light curve. Without knowing the GRB redshift and without a spectral analysis of such an bump, the simple detection of a late time optical bump cannot be considered as a secure proof of the presence of a supernova associated to the GRB but concerted multi epoch ground-based and space-based observing campaigns following several GRBs strengthened the notion that late time bumps were supernovae signatures (Bloom et al. 2002; Garnavich et al. 2003b; Price et al. 2003; Stanek et al. 2005).

More recently, another low redshift (GRB 980425 at $z = 0.0085$ Tinney et al. 1998) GRB has been spectroscopically associated with a Type Ic supernova (SN

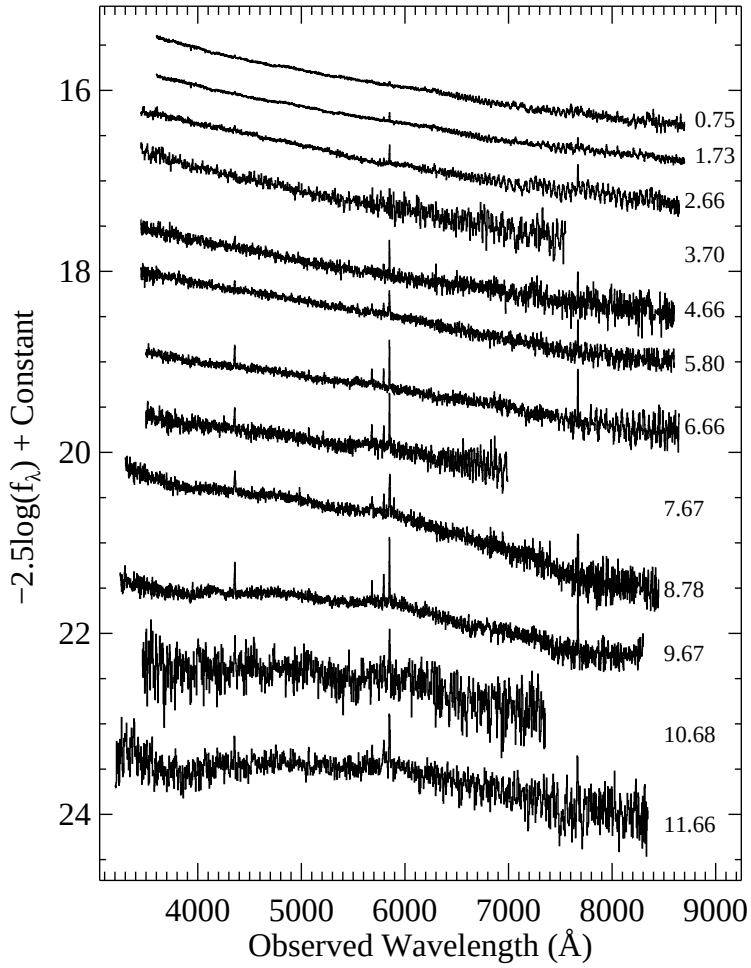

Figure 1.11: The discovery spectra of the emergence of SN 2003dh from the glare of the afterglow of GRB 030329. Shown is the observed spectra, a combination of afterglow (simple power law spectra on the top) and supernova (bottom spectra rich of features). Days since the GRB are noted at right. The narrow emission lines are from the host galaxy and do not change in intensity throughout. From Matheson (2004).

2006aj). This event is particularly intriguing because, thanks to the fast XRT re-pointing, a thermal X–ray component related to the supernova explosion was observed (Campana et al. 2006). Usually, a supernova is detected several days after the explosion with the rise of the optical bump. This is the first time that a signature of a supernova has been observed a few minutes after the explosion (but see Ghisellini, Ghirlanda & Tavecchio 2007 for an alternative interpretation).

Even if the association of long GRBs with the collapse of massive stars is

now widely accepted, there are some nearby long GRBs for which deep late times optical observations allowed to exclude the presence of an associated underling supernova with very constraining limits on the supernova luminosity. In particular several papers appeared in the literature in order to discuss the observation of GRB 060505 and GRB 060614. Both bursts are nearby long GRBs, but the association of these bursts with a supernova explosion can be excluded down to very strict limits (Fynbo et al. 2006; Della Valle et al. 2006; Gal–Yam et al. 2006). The nature of these events has been discussed in several papers (e.g. wrong redshift measurement, short nature of these events; Cobb et al. 2006) but no widely accepted interpretation has been found. Several papers proposed that a new GRB classification scheme is needed in order to explain the supernovae-less long GRBs (e.g. Gehrels et al. 2006).

1.2.4 The GRB redshift distribution

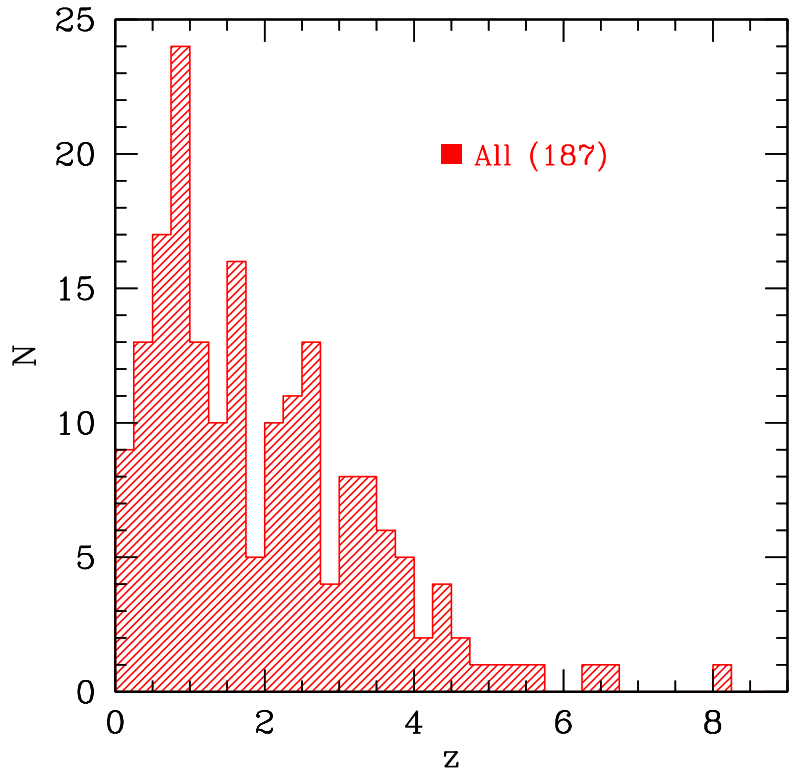

Figure 1.12: Redshift distribution of all the long GRBs observed before the end of July 2009.

GRBs are the most distant objects ever observed in the universe after the recombination. Their redshift distribution spans from $z = 0.0331$ of GRB 060218 (Mirabal & Halpern 2006) to $z = 8.2$ of GRB 090424 (Tanvir et al. 2009). The mean redshift has remarkably increased after the *Swift* satellite launch and it is now around $\langle z \rangle \sim 2$ ($\langle z \rangle \sim 2.3$ when only considering *Swift* GRBs; Fynbo et al. 2009). Figure 1.12 shows the redshift distribution of all the long GRBs observed before the end of July 2009.

1.2.5 Long/short GRBs divide

The distinction between long and short GRBs can be studied in more detail through the comparison of their spectral properties. Using the GRBs detected by BATSE, it has been shown that the time integrated spectrum of short GRBs is harder due to a harder low energy spectral component with respect to long GRBs. Instead the spectra of short GRBs are similar to the first 1–2 s of emission of long GRBs (Ghirlanda et al. 2008).

In the *Swift* era this separation looks much less clear . The bimodality in the observed *Swift* GRBs T_{90} distribution is much less evident than in the pre–Swift era (Zhang & Choi 2008) and the *Swift* short GRBs looks less hard than in the BATSE era ($\langle \log (HR)^{\rm short} \rangle = 0.03 \pm 0.25$ and $\langle \log (HR)^{\rm long} \rangle = 0.31 \pm 0.32$; Ghirlanda et al. in prep).

We are now able to measure the distance of a few short GRBs. Contrary to the expectations of a prevalence of short bursts originating at low z if due to the merger of two compact objects, some short bursts have been found at redshifts larger than 1. For example GRB 090426 with a duration T_{90} (15-350 keV) of 1.2± 0.3 s, (Sato et al. 2009) has a redshift $z = 2.609$ (Levesque et. al. 2009).

When the observed duration of a high redshift GRB is close to 2 s (i.e. the timescale usually adopted for distinguishing long from short GRBs) the simple duration analysis can not lead to a conclusive association to one of the two families. When assuming the nature of long and short GBRs progenitors, the most direct and strict method for testing the short or long nature of a GRB is testing the presence or absence of an underlying supernova in the optical- UV light curve. Unfortunately this is not possible for high redshift GRBs (z > 1) and in these cases other tests are required.

As an example of the long/short divide ambiguity I will briefly present the case of GRB 071020, a GRB with an observed $T_{90} \approx 3$s (Tueller et al. 2007) and located at redshift z=2.45 (Jakobsson et al. 2008). This discussion is taken from Nardini et al. 2009e (in preparation).

Neglecting spectral time evolutions, GRB 071020 has a rest frame duration $T_{90}^{\rm rf} = T_{90}^{\rm obs}/(z+1) = 1.1$ or 1.3 for the Konus-Wind and BAT duration respectively. This duration corresponds to an intermediate value in the rest frame duration distribution analysed by Zhang & Choi (2008) and also the observed (329 keV)

and rest frame (1034 keV) peak energies can not be used for discriminating the nature of the event, being intermediate in the hardness versus T_{90} plot.

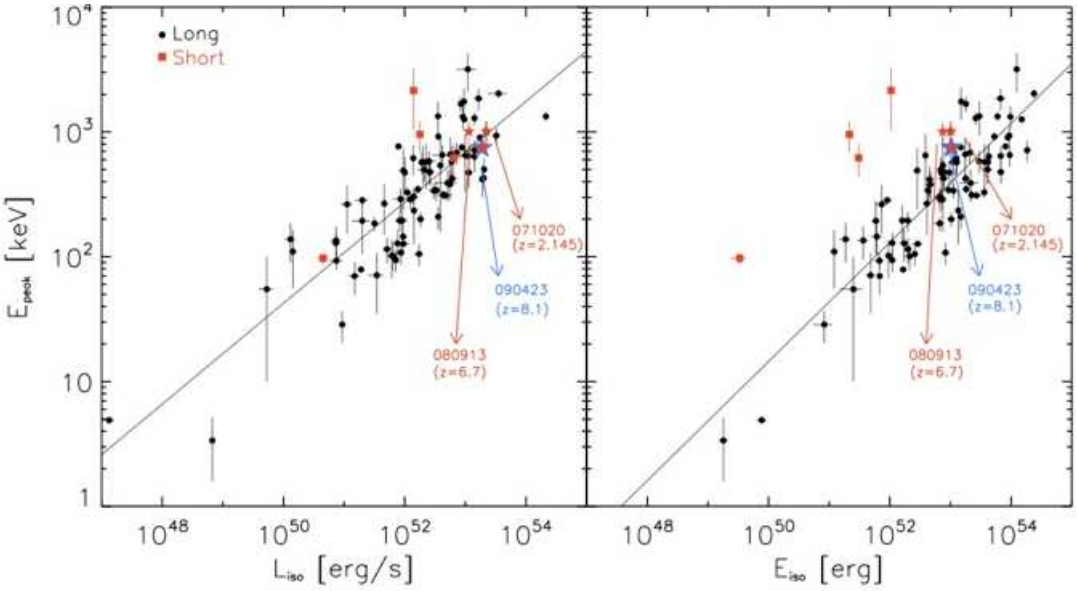

Figure 1.13: Left panel: $E_{\rm p} - L_{\rm iso}$ ("Yonetoku") correlation for the sample of 92 long GRBs (black symbols) with measured redshifts. The position of short GRBs (red squares) are consistent with this relation. GRBs shown with red stars are long events accordingly to their observed T_{90} but they have an intrinsic duration <2 seconds. Right panel: $E_{\rm p} - E_{\rm iso}$ ("Amati") correlation for the same sample of long GRBs (black symbols). Note the inconsistency of short GRBs with the $E_{\rm p} - E_{\rm iso}$ correlation defined by long events. Figure adapted from Ghirlanda et al. (2009) and taken from Nava et al. (2009).

In a recent paper Ghirlanda et al. (2008) studied the prompt emission spectral and energetic differences between a large sample of long and short GRBs. Considering all GRBs with known redshift and measured $E_{\rm p}$ they find that both long and short GRBs are consistent with the so-called Yonetoku (Yonetoku et al. 2004) correlation between $E_{\rm p}$ and the isotropic equivalent peak luminosity $L_{\rm iso}$. Short GRBs instead, seem to be outliers of the so called Amati (Amati et al. 2002) correlation between $E_{\rm p}$ and the isotropic equivalent energy $E_{\rm iso}$ since they lie on the left of this correlation (see fig. 1.13). GRB 071020 is consistent with their findings, it obeys the Yonetoku correlation (within 1 σ) and it is almost consistent with the (3 σ) Amati relation. (see fig. 1.13).
This burst seems therefore an "intermediate" event.

Another method that has been proposed for distinguishing long GRBs from short GRBs is related to the temporal lag between prompt gamma ray light curves observed in different bands (Norris 2002, 2006). Gehrels et al. (2006) moreover

studied the correlation between the peak luminosity $L_{\rm p}$ and the spectral lag $t_{\rm lag}$ between 50-100 keV and 15-25 keV channels corrected for k–correction and time dilation. They found an anti-correlation between $t_{\rm lag}$ and $L_{\rm p}$ for the long GRBs while short GRBs occupy a separate area of the parameter space with smaller $t_{\rm lag}$ and $L_{\rm p}$. The large $L_{\rm p}$ combined with the small $t_{\rm lag}$ found by Tueller et al. (2007) make GRB 071020 fully consistent with the long GRBs lag-luminosity anti correlation (less than 1σ from Gehrels et al. (2006) fit).

In two recent papers Kann et al. (2009) and Nysewander et al. (2008) compared the rest frame luminosities of the long and short GRBs optical and X–ray afterglows. They found short GRBs to be less luminous than long GRBs especially in the optical. The average R band luminosity at 12 h rest frame after trigger is even smaller than the typical values of the optically underluminous family events analysed by Nardini et al. (2008b).

They also found a correlation between the afterglow luminosities and $E_{\rm iso}$. Since the optical and X–ray luminosities of GRB 071020 are comparable with long GRBs, as well as the $E_{\rm iso} = 1.02 \times 10^{53}$erg, GRB 071020 lies in the long GRBs populated area of the $L_{\rm opt}$-$E_{\rm iso}$ and $L_{\rm X}$-$E_{\rm iso}$ plots.

GRB 071020 is not the only long GRB (observed $T_{90} > 2$ s) characterised by a rest frame duration smaller than 2 s for which a possible intrinsic short nature was claimed. We can for example compare the properties of this GRB with the ones of GRB 080913 (Schady et al. 2008) with $z = 6.7$ (Fynbo et al. 2008), and GRB 090423 the highest redshift ever measured GRB with z=8.2 (Tanvir et al. 2009).

GRB 080913 has an observed BAT duration $T_{90} = 8.1 \pm 1$ s (Stamatikos et al. 2008) that corresponds to a rest frame duration of about 1.1 s. This burst triggered also Konus-Wind and a combined Band model fit of both Konus-Wind and BAT data gives a peak energy value $E_{\rm p} = 121^{+232}_{-39}$ keV that corresponds to a rest frame $E_{\rm p}^{\rm rf} = 1009$ keV and an isotropic bolometric energy $E_{\rm iso} = (7.49 \pm 0.9) \times 10^{52}$ erg (Pal'shin et al. 2008). These values are very close to the ones obtained for GRB 071020 therefore also GRB 080913 is consistent with the 3σ Amati relation.

The similarity is reinforced when noting that GRB 080913 is perfectly consistent with the Yonetoku relation [having $L_{\rm iso} = (1.14 \pm 0.15) \times 10^{52}$erg s^{-1} (Ghirlanda et al. 2008)] and with the lag-luminosity relation [having a spectral lag between the 50-100 keV and 15-25 keV channels $t_{\rm lag} = 0.148^{+0.094}_{-0.084}$ s (Greiner et al. 2008)].

Apart from the presence of intense X–ray flaring activity in the early GRB 080913 light curve, the temporal behaviour of these two afterglows is very similar. They both show an almost contemporaneous rebrightning in optical and in X–rays around 5000 s (rest frame) even if in GRB 080913 is more intense. From an energetic point of view GRB 071020 is 2-3 times brighter before the rebrightning while at later times the rest frame light curves are almost overlapping.

Almost the same argument can be applied to GRB 090423. This GRB has an

observed duration $T_{90} = 10.3 \pm 1.1$ s that corresponds to a rest frame duration of about 1.2 s. As discussed by Nava et al. (2009), GRB 090423 has an isotropic equivalent energy $E_{\rm iso} = 1.0 \times 10^{53}$ erg, an isotropic equivalent peak luminosity $L_{\rm iso} = 1.88 \times 10^{53}$ and a rest frame peak energy $E_{\rm p} = 746$ keV (observed $E_{\rm p} = 48 \pm 6.2$ keV). As can be seen in fig 1.13, GRB090423 is remarkably similar to GRB 080913 and GRB 071020 with respect to the Amati and Yonetoku correlations. Krimm et al. (2009) analysed also the spectral lag in GRB 090423 finding a result similar to the one obtained for GRB 071020. They argue that: *The lag in each case (channel) is consistent with zero, but the 1 σ error bars are roughly as large as the median lag values for long bursts. Thus this burst is too dim for us to utilise lags as a discriminant for long vs. short.*

As a conclusion we can say that we do not have single parameter that is able to give a secure classification of these intermediate GRBs as long or short. In these three cases the combined analysis of all the available information seems to lead to a long GRB nature of these events. Some more information can be obtained from the analysis of the rest frame hardness ratio versus duration plot (Ghirlanda et al. in preparation) or by checking for the presence of underlaying supernova emission for the nearby events. The availability of next generation gravitational wave detectors that should be sensible enough to detect the signal from the merger of a compact object binary system will probably be a fundamental step in the understanding of this issue.

1.2.6 Dark GRBs

The launch of *Swift* , thanks to the presence of the XRT X–ray telescope, allowed to detect the X–ray afterglow of all the GRBs that have been observed by XRT at early time. This is not the case in the optical. Despite the effort that has been put in order to obtain early times follow up of all the well localised GRBs detected by *Swift*, a remarkable fraction of them ($\sim$ 30-40% depending on the sample selection) do not show any detectable IR–optical–UV counterpart. They are the so called "dark" GRBs (other definitions can be found in the literature i.e. FOAs Failed Optical Afterglows, or GHOSTs, Gamma ray burst Hiding an Optical Source Transient).

This problem was known also in the pre–*Swift* epoch and several possible reasons for the non detection in the optical of a large fraction of GRBs have been proposed:

1. High redshift GRBs: Because of the Lyman α absorption, all the bursts with redshifts larger than ~ 5 are not detectable in the optical. In order to detect their optical afterglow infrared observations are required.

2. Poor observational conditions: If the optical follow up is carried up with

too restrictive telescope limiting magnitudes or at too late times (when the afterglow emission has faded below the telescope sensitivity).

3. Highly obscured GRBs: The presence of a large amount of dust in the GRB host galaxy can make the optical afterglow undetectable even if it is intrinsically bright.

4. Intrinsically underluminous events: The emitted optical flux can be intrinsically faint.

The second solution (Poor observational conditions) can be excluded by the analysis of all the upper limits of the dark bursts that proves that the sensitivity of the telescopes that have been used to point most of the dark GRBs is similar to the sensitivity of the telescopes that observed the afterglow of the optically bright GRBs (see Nardini et al. 2008a, Nardini et al. 2008b, Lazzati, Covino & Ghisellini 2002).

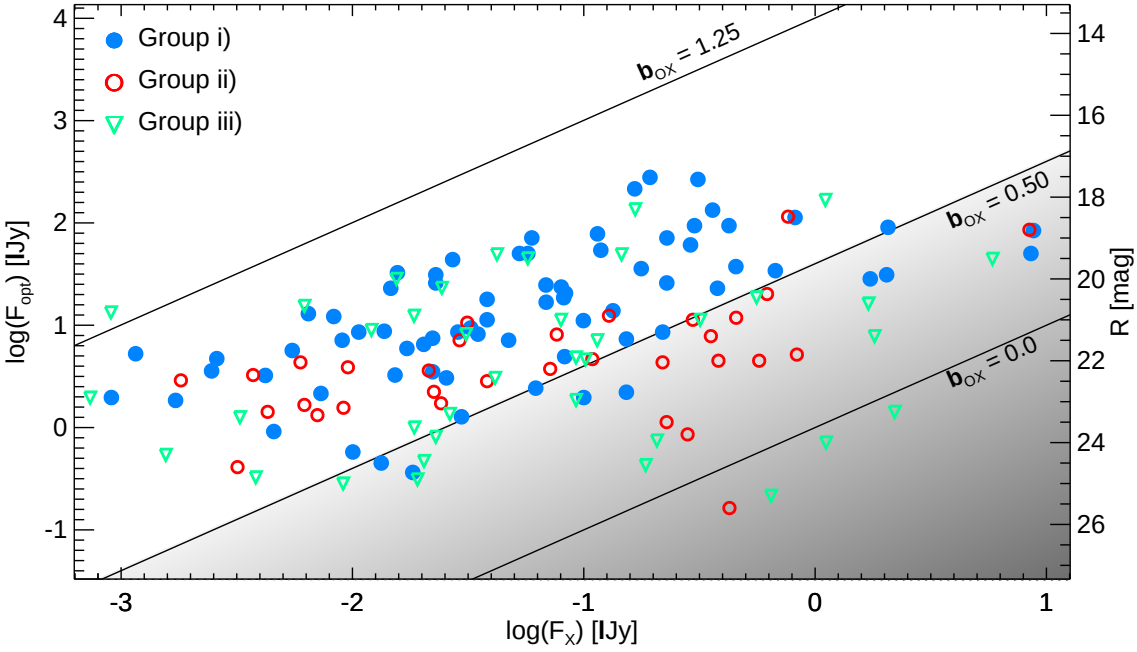

Figure 1.14: The dark burst diagram (F_{opt} vs. F_X), of all the *Swift* GRBs (Fynbo et al. 2009). A similar plot was first presented in Jakobsson et al. (2004). GRB with $\beta_{o,X} < 0.5$ are defined as dark bursts. The β_{OX} values were calculated in the same way as in Jakobsson et al. (2004). The only difference is that here 11 hr are not used as a reference time. Rather, when possible, measurements obtained a few hours after a burst have been selected to avoid the early stage of the X-ray canonical behaviour. For low-z bursts late-time measurements have been avoided to prevent any host contamination in the optical afterglow flux.

Property/group	*ii)*	*iii)*
0.3-10 keV flux 1000 s	0.17	1.1×10^{-2}
0.3-10 keV flux 5000 s	0.17	3.9×10^{-4}
0.3-10 keV flux 20000 s	6.1×10^{-2}	4.8×10^{-4}
$N_{\rm H}$ in excess to the Galactic value	2.1×10^{-3}	7.0×10^{-7}
15-350 keV fluence	0.21	3.5×10^{-2}
15-350 peak flux	0.20	0.29
T_{90}	0.76	0.71
$\theta_{\rm sun}$	0.78	5.3×10^{-3}

Table 1.1: KS test probabilities that the bursts in group *ii)* (optical afterglow detected, but no optical afterglow spectroscopy based redshift) and group *iii)* (no optical afterglow detection) are drawn from the same distribution as group *i)* (bursts with optical afterglow spectroscopy based redshift measurement).

Jackobsson et al. (2004, 2006) proposed an operational definition of dark bursts as those bursts that are optically subluminous with respect to what is predicted by the fireball model, i.e., that have an optical–to X-ray spectral index $\beta_{\rm o,X} < 0.5$ (see fig. 1.14 from Fynbo et al. 2009). This value corresponds to a situation in which the cooling frequency is very close to the low energy limit of the X–ray band energy range (see the following section for a definition of the cooling frequency). This definition assumes a theoretical shape of the optical to X–ray afterglow spectral energy distribution (SED). In order to avoid such an assumption, in Nardini et al. (2008a,b) and in Fynbo et al. (2009) we considered as dark all the GRBs that have been pointed with optical telescopes in good observing conditions but no optical afterglow has been detected.

In Fynbo et al. (2009) we compared some properties of three samples of long GRBs detected by *Swift*:

Group i) : GRBs for which it has been possible to measure the redshift from the afterglow spectrum.

Group ii) : GRBs for which a limit on the value of the redshift can be put since their afterglow has been detected in the optical bands

Group iii) : Dark GRBs without any optical detection.

We compared the distributions of several parameters of these three GRB groups using the standard two tailed Kolmogorov Smirnof test (KS). The KS test probabilities that the group ii) and group iii) distributions come from the same parent distribution of group i) are reported in tab. 1.1. In figs. 1.15 and 1.16 we report all the obtained distributions.

We found that

- Since the Sun angle $\theta_{\rm sun}$ is a good measure for how long a burst can be observed during night time from the ground, it is clear that bursts with no OA detections tends to be closer to the Sun and hence are more difficult to observe. This is one of the contributing reasons why these bursts do not have detected OAs.

- The gamma ray prompt phase parameters (i.e. T_{90} duration, 15–150 keV fluence, and peak flux) distributions are quite similar. Dark GRBs have slightly smaller fluences but the KS probability is only 3.5×10^{-2}.

- Dark GRBs are sensibly fainter also in the X–rays especially at late times. We compared the X–ray de–absorbed 0.3–10 keV fluxes at three different times (i.e. 1 ks, 5 ks, and 20 ks after the trigger) finding that the dark GRBs distribution is quite different from the known redshift sample one. Comparing the dark GRB distribution with the one of group *ii)* we find that the KS test gives a probability of about 10^{-3}. Both these results are in agreement with what found by De Pasquale et al. (2003).

- The $N_{\rm H}$ column densities in excess to the Galactic value calculated from the soft X–ray absorption assuming for all the GRBs that this additional absorber is located at $z = 0$, is much larger in the dark GRB sample. This could imply that dark GRBs are more affected by dust extinction in the optical bands. This interpretation assumes a direct connection between optical reddening and $N_{\rm H}$ X–ray absorption in the GRB host galaxy that is not observed. In the following chapters of this thesis I will discuss the details of this issue.

The fact that dark GRBs tend to be characterised by larger $N_{\rm H}$ column density in excess to the Galactic value can be seen also if we use the definition of dark burst based on the value of $\beta_{\rm o,X}$ by Jackobsson et al. (2004). In fig. 1.17 we plot $\beta_{\rm o,X}$ against the $N_{\rm H}$ column densities in excess to the Galactic value showing that GRBs with $\beta_{\rm o,X} < 0.5$ tend to have large $N_{\rm H}$ excess consistent with the interpretation that these bursts are obscured by dust.

In the right panel of figure 1.18 I show that there is no clear correlation between $\beta_{\rm X}$ and the X-ray excess absorption.

The left panel of fig. 1.18 shows the values of $\beta_{\rm o,X}$ against the X–ray spectral indices $\beta_{\rm X}$. If both the optical and X–ray bands are produced by the same synchrotron mechanism we expect that some of the GRBs (i.e. the ones in which the optical to X–ray SED can be fitted with a single power law) have $\beta_{\rm o,X} = \beta_{\rm X}$ and no event should have $\beta_{\rm o,X} < 0.5$. It is important to notice that these values of $\beta_{\rm o,X}$ are not corrected for the reddening in the host galaxy and, therefore, they are in most cases under-estimated. This argument shows the importance of the optical to X–ray SED analysis of each single GRB in order to verify whether the

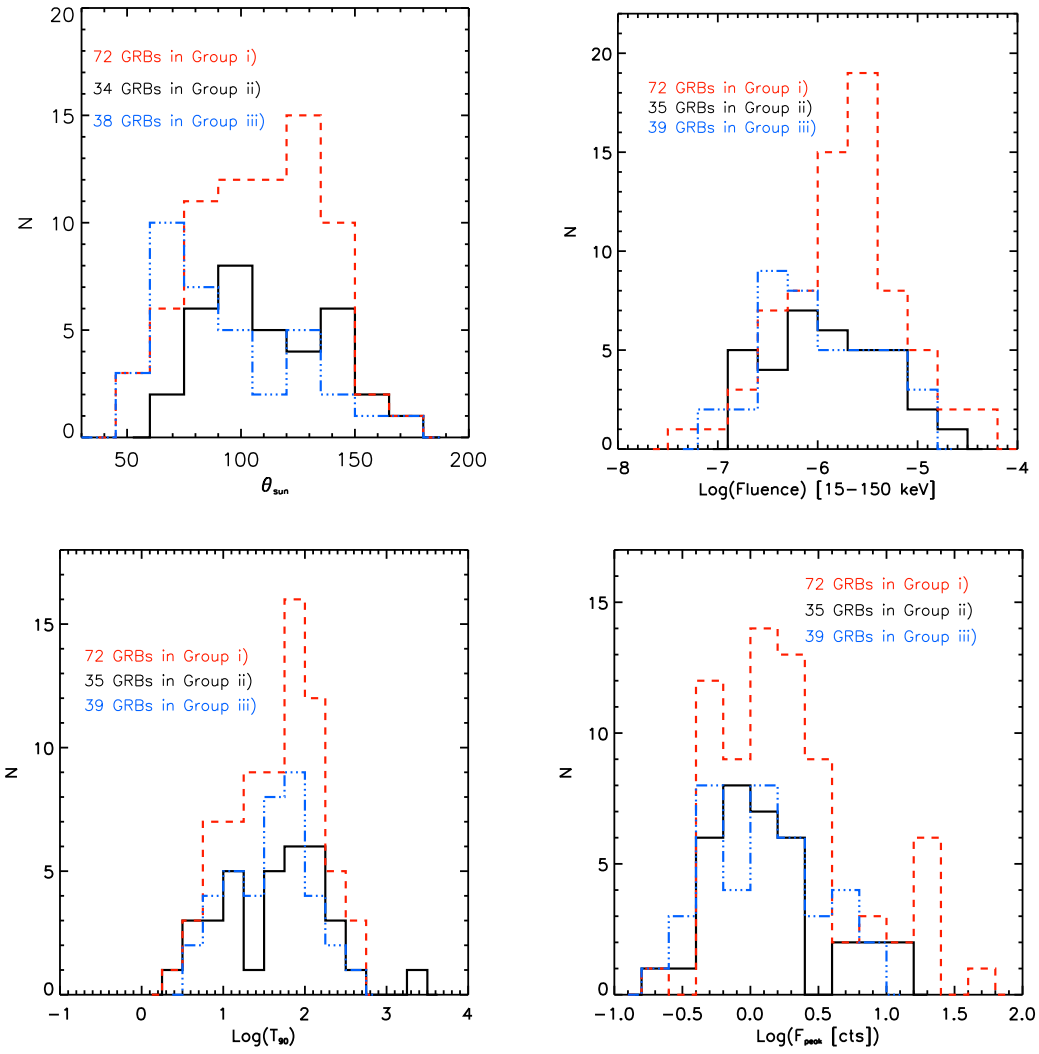

Figure 1.15: Distributions of the Sun angle (upper left panel) and of the gamma ray prompt emission parameters for the three GRB samples described in the text.

"darkness" of a burst can be explained with a large amount of optical extinction in the host. In the following section I will discuss the fact that in some GRBs this is not the case. The optical emission should be intrinsically faint in some events or alternatively, some unknown shape of the extinction curve should take place in the GRB host (Nardini et al. 2008a, Nardini et al. 2008b, Nardini et al. 2009a).

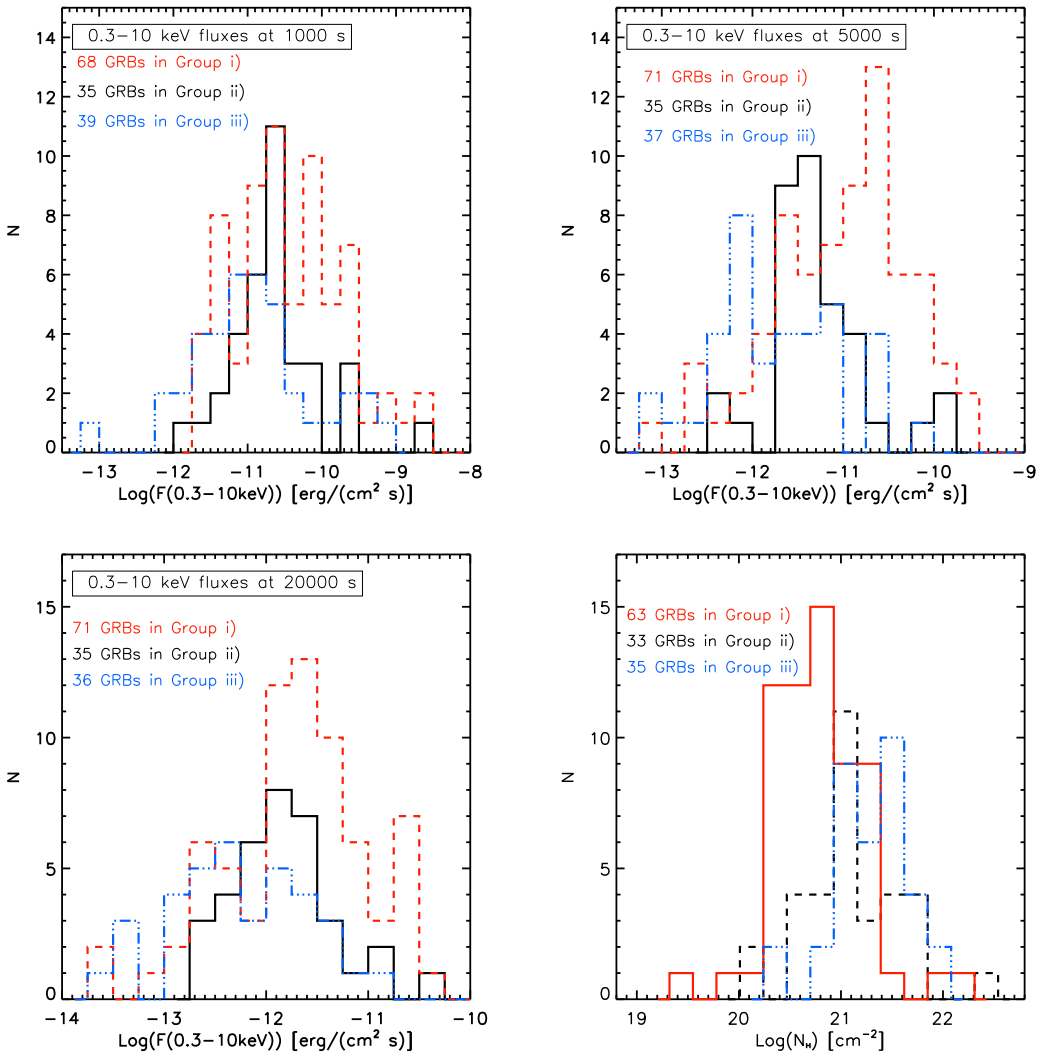

Figure 1.16: Distributions of the X–ray 0.3–10 keV deabsorbed fluxes and of the $N_{\rm H}$ column density in excess to the Galactic value (bottom right panel) for the three GRB samples described in the text.

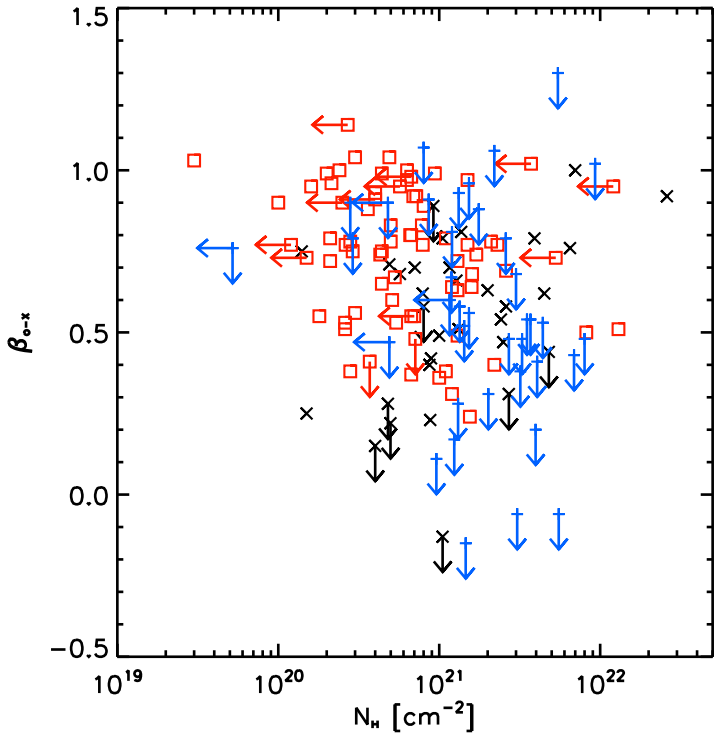

Figure 1.17: $\beta_{\mathrm{o,X}}$ plotted against N_{H} column density in excess to the Galactic value. These GRBs with $\beta_{\mathrm{o,X}} < 0.5$ tend to have large N_{H} column density excesses consistent with the interpretation that these bursts are obscured by dust. The different colours represent the three different GRB groups as in figs. 1.15 and 1.16.

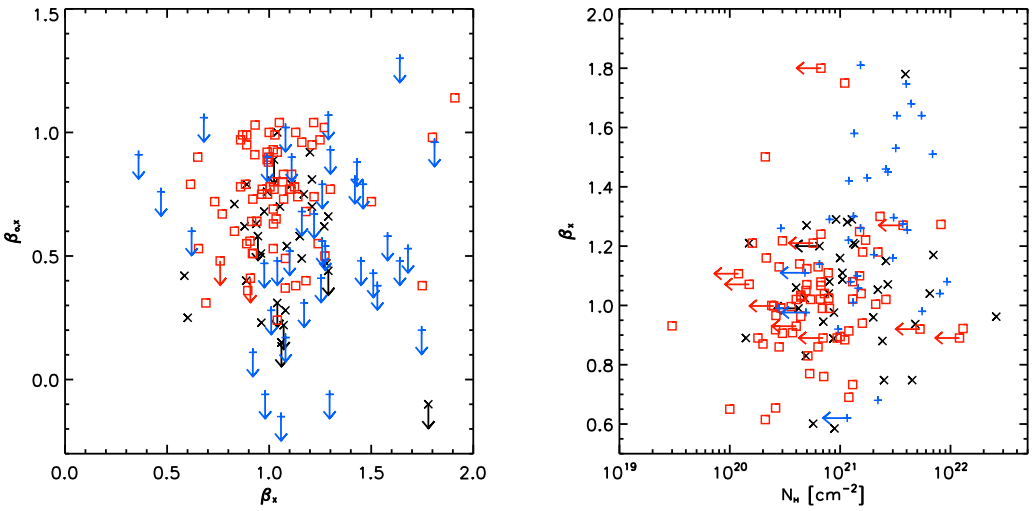

Figure 1.18: Left panel: $\beta_{o,X}$ as a function of the X–ray spectral index β_X. Right panel: the X–ray spectral index β_X versus the N_H column density in excess to the Galactic value. The different colours represent the three different GRB groups as in figs. 1.15 and 1.16.

1.3 The standard model

Since the discovery of the first GRB, several models have been proposed in order to explain these events. Around the end of the 1990s the BATSE and BeppoSAX observations allowed to construct a model that started to be considered as the most reliable by the majority of the GBR scientific community because of its consistency with the observations. This is the so called "standard GRB fireball model". Despite some problems this model has been widely used in order to explain all the observations about both the prompt and the afterglow phases of the GRBs. As it will be discussed in this thesis, the new observational window made available by the *Swift* satellite prompted a large number of scientists to call this model into question.

Since in this thesis I will focus on some of the standard GRB fireball model limitations arisen in the last years and on some possible theoretical alternative proposals, in this section I will briefly introduce some of the main points of the standard GRB fireball model. In particular I will focus on the standard description of the afterglow emission processes but for completeness I will also briefly discuss the proposed prompt emission scenario.

1.3.1 Compactness problem

The first theoretical clue on the nature of the GRB progenitor can be obtained by a simple reasoning based only on the gamma ray prompt temporal and spectral features.

GRBs show a non thermal spectrum. The gamma ray prompt emission is highly variable and in some extreme cases a variability time scale δt of the order of milliseconds has been observed. In order for two points placed at distance R inside the source to be causally connected, we have that the minimum variability time scale is $R \leq \frac{\delta t}{c}$ where c is the speed of light. A millisecond variability time scale implies a source dimension of the order of $R \lesssim 3 \times 10^7$cm.

If this size was true, a naive calculation implies that the source is optically thick. Suppose to observe a fluence $\mathcal{F}$ from a source at a distance D from the observer and to calculate from the variability time scale a source dimension R. For a typical photon energy $\tilde{E}_\gamma$ the photon density at the source is given by

$$\rho_\gamma \sim \frac{L}{R^2 c \tilde{E}_\gamma} \approx \frac{4\pi D^2 \mathcal{F}}{\tilde{E}_\gamma c^3 \delta t^2} \tag{1.2}$$

The high density at the source frame of photons with energies exceeding $m_e c^2 = 511$ keV makes the process $\gamma + \gamma \rightarrow e^+ + e^-$ very likely to happen for couple of photons γ_1 and γ_2 that satisfy the relation $\sqrt{E_{\gamma_1} E_{\gamma_2}} > m_e c^2$. If we define $f_{e\pm}$ as a numerical factor denoting the fraction of photons over this threshold, whose

energy is large enough for pair creation, the optical depth $\tau_{\gamma\gamma}$ for pair creation can be written as (Lithwick & Sari 2001)

$$\tau_{\gamma\gamma} = \frac{f_{e\pm}\sigma_T \mathcal{F} D^2}{R^2 m_{\rm e} c^2} \tag{1.3}$$

where $m_{\rm e}$ is the electron rest mass and σ_T is the Thomson cross section. Inserting typical values in equation 1.3 we can rewrite it as

$$\tau_{\gamma\gamma} = 10^{13} f_{e\pm} \left(\frac{\mathcal{F}}{10^{-7}\ \mathrm{erg\ cm^{-2}}}\right) \left(\frac{D}{3\ \mathrm{Gpc}}\right)^2 \left(\frac{\delta t}{10\ \mathrm{ms}}\right)^{-2} \tag{1.4}$$

This optical depth is extremely large. This is, of course, inconsistent with the observations of gamma–ray photon energies above $m_{\rm e}c^2$. This simple argument is known as "compactness problem".

The compactness problem can be solved if the emitting matter is moving relativistically towards the observer with a large Lorentz factor $\Gamma = 1/\sqrt{1 - v^2/c^2}$. In this case relativistic corrections must be applied to the observed parameters.

* The photons observed with an energy $h\nu_{\rm obs}$ have been blue shifted by the relativistic motion towards the observer. In the source rest frame their energy can be written as
$$h\nu' = \frac{h\nu_{obs}}{2\Gamma}$$

* For the same reason only a smal fraction of photons has a rest frame energy above threshold. If the spectrum is a power law $\mathcal{N}(E) \propto E^{-\alpha}$, the fraction of photons over threshold is
$$f_{e\pm} \propto \Gamma^{-2\alpha} \tag{1.5}$$

* Because of the relativistic Doppler contraction, the implied size of a source moving towards us with a Lorentz factor Γ estimated from the variability argument, is reduced by a factor Γ^2 with respect to the non relativistic case. The minimum source dimension is therefore given by
$$R \leq \Gamma^2 \frac{\delta t}{c} \tag{1.6}$$

* This effect increases the required source dimension and therefore it modifies the density estimate by a factor Γ^{-4} and it influences the optical depth as Γ^{-2}

Taking into account all these effects we can rewrite the equation 1.3 for the optical depth $\tau_{\gamma\gamma}$ as

$$\tau_{\gamma\gamma} = \frac{f_{e\pm}\sigma_T \mathcal{F} D^2}{\Gamma^{2\alpha} R^2 m_e c^2}. \tag{1.7}$$

Introducing fiducial numbers equation 1.4 can be written as

$$\tau_{\gamma\gamma} = 10^{13} \frac{f_{e\pm}}{\Gamma^{(4+2\alpha)}} \left(\frac{\mathcal{F}}{10^{-7} \text{ erg cm}^{-2}} \right) \left(\frac{D}{3 \text{ Gpc}} \right)^2 \left(\frac{\delta t}{10 \text{ ms}} \right)^{-2} \tag{1.8}$$

The compactness problem can be therefore solved reaching the condition

$$\tau_{\gamma\gamma} \approx 1 \tag{1.9}$$

This condition can be obtained when the Lorentz factor is of the order of

$$\Gamma \sim 10^{\frac{13}{4+2\alpha}} \approx 10^2 \tag{1.10}$$

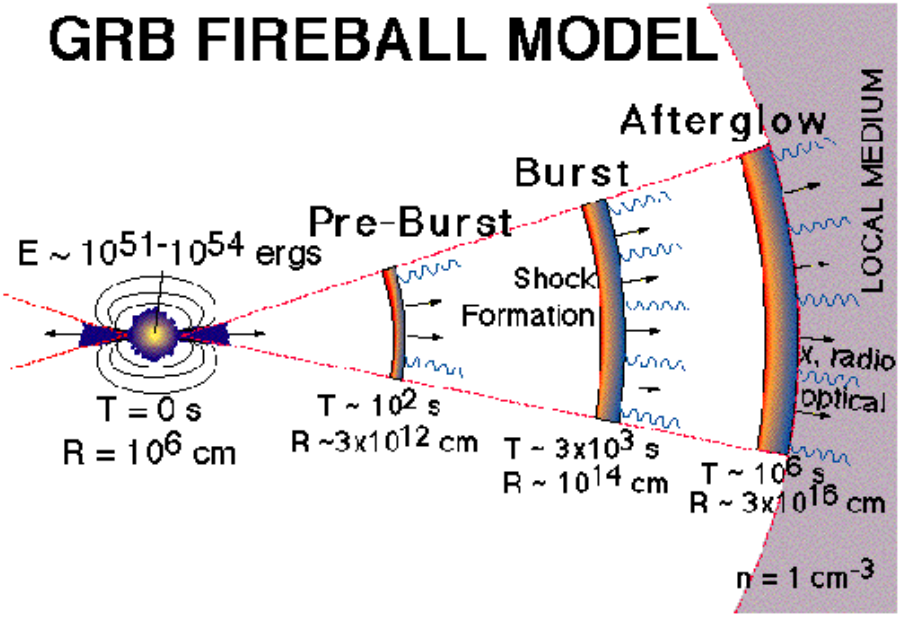

Figure 1.19: Artistic picture representing the expansion of a fireball in the interstellar medium in the standard fireball model scenario. The different emitting mechanisms that take place and the typical scales at which they occur are labelled.

Now that we have shown that the emitting region must be moving relativistically towards the observer, we need to understand the mechanisms that are able to convert in photons a very large amount of energy of the source.

The simplest scenario that satisfies all the conditions required above is that a central engine (in this first stage we do not focus on the nature of the central engine itself) produces a so called *fireball* that is expanding and reaching relativistic velocities in the direction of the observer. This fireball is composed by an hot and dense plasma of leptons and baryons. The baryons are immersed in an high

energy photons bath. The intense pressure accelerates the fireball. The internal energy is converted in kinetic energy of ordered motion while the co-moving system temperature decreases. After this acceleration phase, the fireball starts moving with an almost constant speed before it reaches the external medium surrounding the GRB progenitor.

1.3.2 Internal shocks

In this section I will briefly discuss the mechanism that has been proposed in the standard fireball model in order to explain the GRB prompt gamma ray emission. In this scenario the gamma ray prompt emission is due to dissipation of the kinetic energy of the relativistic flow through a process called "internal shocks".

Suppose that the central engine is producing more than one plasma shell relativistically moving towards the observer. Each shell has a different Γ Lorentz factor.

If for example that the central engine produces a plasma shell with mass m and Lorentz factor Γ_1. At later times the central engine produces a second shell with mass M and a different Lorentz factor Γ_2. Let the second shell be faster than the first one with $\Gamma_2 > \Gamma_1$.

At a given time, the faster second shell collides with the slower first one producing a relativistic shock. After that shock the two shells have merged forming a single shell of mass $M + m$ and a resulting Lorentz factor $\Gamma_{\rm F}$. In the collision some kinetic energy must be dissipated. We can define ε' the dissipated energy in the rest frame.

We can apply the energy and momentum conservation laws to the system. It is a two equations system with two unknowns and therefore we can solve it in order to obtain the values of $\Gamma_{\rm F}$ and ε' from the initial conditions.

We have that

$$\begin{cases} M\Gamma_2 + m\Gamma_1 = \Gamma_{\rm F}[M + m + \frac{\varepsilon'}{c^2}] \\ \\ M\sqrt{\Gamma_2^2 - 1} + m\sqrt{\Gamma_1^2 - 1} = [M + m + \frac{\varepsilon'}{c^2}]\sqrt{\Gamma_F^2 - 1}. \end{cases} \tag{1.11}$$

From the first equation in eq. 1.11 we can immediately obtain the relation that explicitly gives the value of the dissipated energy ε' as a function of $\Gamma_{\rm F}$

$$\frac{\varepsilon'}{c^2}\Gamma_{\rm F} = M\Gamma_2 + m\Gamma_1 - m\Gamma_{\rm F} - M\Gamma_{\rm F} \tag{1.12}$$

We can now define the dissipated energy in the observer frame

$$\varepsilon^p = \varepsilon'\Gamma_{\rm F} = Mc^2(\Gamma_2 - \Gamma_{\rm F}) + mc^2(\Gamma_1 - \Gamma_{\rm F}) \tag{1.13}$$

It is important to find an explicit equation that expresses $\Gamma_{\rm F}$ as a function of known quantities. To this aim we can divide the second equation of the system in eq. 1.11 for the first one obtaining

$$\frac{M\sqrt{\Gamma_2^2-1}+m\sqrt{\Gamma_1^2-1}}{M\Gamma_2+m\Gamma_1}=\frac{\sqrt{\Gamma_{\rm F}^2-1}}{\Gamma_{\rm F}} \tag{1.14}$$

If we calculate the square of eq. 1.14 we have

$$\begin{array}{c}\frac{M^2(\Gamma_2^2-1)+m^2(\Gamma_1^2-1)+2mM\sqrt{(\Gamma_2^2-1)(\Gamma_1^2-1)}}{(M\Gamma_2+m\Gamma_1)^2}=\frac{\Gamma_{\rm F}^2-1}{\Gamma_{\rm F}^2}\\ \frac{1}{\Gamma_{\rm F}^2}=\frac{M^2\Gamma_2^2+m^2\Gamma_1^2+2mM\Gamma_2\Gamma_1-M^2\Gamma_2^2+M^2-m^2\Gamma_1^2+m^2-2mM\sqrt{(\Gamma_1^2-1)(\Gamma_2^2-1)}}{(M\Gamma_2+m\Gamma_1)^2}\end{array} \tag{1.15}$$

that gives

$$\Gamma_{\rm F}=\frac{(M\Gamma_2+m\Gamma_1)}{\sqrt{m^2+M^2+2Mm\Gamma_2\Gamma_1-2mM\sqrt{(\Gamma_1^2-1)(\Gamma_2^2-1)}}} \tag{1.16}$$

If both the shells are ultra relativistic with $\Gamma_2>\Gamma_1\gg 1$ we can simplify the square root on the dividend of eq. 1.16. In this we obtain

$$\Gamma_{\rm F}\approx\frac{M\Gamma_2+m\Gamma_1}{\sqrt{M^2+m^2}} \tag{1.17}$$

that can be inserted in equation 1.13.

We can compare this result with different formulations of the same quantities appeared in literature. For example rewriting the equations in function of β instead of gamma with

$$\Gamma=\frac{1}{\sqrt{1-\beta^2}} \tag{1.18}$$

we have

$$\beta_{\rm f}\;=\;\frac{m\Gamma_1\beta_1+M\Gamma_2\beta_2}{m\Gamma_1+m\Gamma_2} \tag{1.19}$$

and defining the new parameters

$$\alpha_\Gamma\;\equiv\;\frac{\Gamma_2}{\Gamma_1};\qquad \alpha_m\;\equiv\;\frac{M}{m} \tag{1.20}$$

in equation 1.19, we obtain

$$\beta_f\;=\;\frac{\beta_1+\alpha_m\alpha_\Gamma\beta_2}{1+\alpha_m\alpha_\Gamma} \tag{1.21}$$

that is the formulation proposed by Lazzati, Ghisellini & Celotti (1999) in their equation 8.

The nature of the radiative mechanism that is responsible for the GRB prompt emission is still a matter of fervent discussion. The presence of a large number of charged particle in relativistic motion in a region probably characterised by the presence of magnetic fields seems to imply that synchrotron radiation plays a fundamental role in the GRB prompt emission. On the other end the synchrotron internal shock scenario has severe problems for what concerns the low efficiency of this mechanism and to explain the observed shape of the prompt gamma ray spectra (e.g. low energy spectral index, ratio between the prompt and the afterglow fluences ...)(see e.g. Preece et al. 1998, Ghirlanda, Celotti & Ghisellini 2002). A better comprehension of the prompt gamma-ray emission could benefit from the the broad band prompt observations (from the optical to hundreds of GeV) that are now available for some GRBs thanks to the contemporaneous presence in orbit of the *Swift* and *Fermi* observatories.

1.3.3 External shocks

The simplest way to explain the deceleration of a relativistic fireball is the interaction with an ambient medium that can be at rest as in the case of the interstellar medium (ISM) or moving with a much smaller velocity with respect to the fireball as in the case of a stellar wind. The interaction between this shell and the ambient medium produces a relativistic shock called "external shock" (Rees & Mészáros,1992).

Suppose that a plasma shell with mass $M_{\rm shell}$ in relativistic motion with a Lorentz factor $\Gamma_{\rm s}$ collides in an inelastic way with the ambient medium (for simplicity we assume an homogeneous ISM medium) at rest. In case of spherical expansion, the amount of ISM mass that the shell collects during the motion depends only on the radius r. At a given r the shell mass is therefore the sum of the initial mass $M_{\rm shell}$ plus a function $m(r)$ that gives the total ISM mass inside the sphere with radius r.

At the beginning, the amount of collected material is not large enough to decelerate the shell in a remarkable way. Increasing radius the deceleration effect starts to be important. For simplicity we can use as a reference the moment at which the shell has halved its Lorentz factor. The mass required to obtain this decrease is $m = M_{\rm shell}/\Gamma_{\rm s}$. The radius at which the deceleration starts to be important is therefore

$$R_{\rm ext} = \left(\frac{3E}{4\pi n m_p c^2 \Gamma_{\rm s}^2}\right)^{\frac{1}{3}} = 6 \times 10^{16} E_{52}^{\frac{1}{3}} \Gamma_{\rm s,2}^{-\frac{2}{3}} n_0^{-\frac{1}{3}} \ {\rm cm} \qquad (1.22)$$

where m_p is the proton rest mass, n is the number of particles, n_0 is the ISM density (in particles /cm^3), E is the equivalent isotropic fireball energy, and the standard notation $X_n = X$ in units of 10^n is used.

Since the shell is in relativistic motion, the time at which this transition occurs is nothing but $R_{\rm ext}$ divided by c. The observer measures a much shorter time because of the Doppler contraction:

$$t_{\rm ext,obs} \sim \frac{R_{\rm ext}}{2\Gamma_{\rm s}^2 c} = 100\ E_{52}^{\frac{1}{3}} \Gamma_2^{-\frac{8}{3}} n_0^{-\frac{1}{3}}\ {\rm s} \tag{1.23}$$

Assuming that the ambient medium is at rest with respect to the observer frame, we can apply the standard energy and momentum conservation laws, as done in the case of the internal shock case. We obtain a system of two equations with two unknowns. The known parameters are the initial shell mass $M_{\rm shell}$ and Lorentz factor $\Gamma_{\rm s}$. The unknowns are the Lorentz factor as a function of the radius $\Gamma(r)$ and the dissipated energy ε'.
We have

$$\begin{cases} M_{\rm shell}\Gamma_{\rm s} + m(r) = \Gamma(r)[M_{\rm shell} + m(r) + \frac{\varepsilon'}{c^2}] \\ M\sqrt{\Gamma_s^2 - 1} = \left[M_{\rm shell} + m(r) + \frac{\varepsilon'}{c^2}\right] \sqrt{\Gamma^2(r) - 1} \end{cases} \tag{1.24}$$

If we divide the second equation by the first one and calculating the square of the obtained relation we have

$$\begin{aligned} \frac{M^2(\Gamma_{\rm s}^2 - 1)}{[M_{\rm shell}\Gamma_{\rm s} + m(r)]^2} &= 1 - \frac{1}{\Gamma^2(r)} \\ \frac{1}{\Gamma^2(r)} &= \frac{[M_{\rm shell}\Gamma_{\rm s} + m(r)]^2 - M_{\rm shell}^2(\Gamma_{\rm s}^2 - 1)}{[M\Gamma_{\rm s} + m(r)]^2} \end{aligned} \tag{1.25}$$

Inverting eq. 1.25 we obtain

$$\Gamma^2(r) = \frac{[M_{\rm shell}\Gamma_{\rm s} + m(r)]^2}{M_{\rm shell}^2\Gamma_{\rm s}^2 + m(r)^2 + 2mM_{\rm shell}\Gamma_{\rm s} - M_{\rm shell}^2\Gamma_{\rm s}^2 + M_{\rm shell}^2}. \tag{1.26}$$

that becomes

$$\Gamma(r) = \frac{M_{\rm shell}\Gamma_{\rm s} + m(r)}{\sqrt{m(r)^2 + 2mM_{\rm shell}\Gamma_{\rm s} + M_{\rm shell}^2}}. \tag{1.27}$$

From the first equation in the system 1.24 we can directly obtain the relation

$$\frac{\varepsilon'}{c^2}\Gamma(r) = M_{\rm shell}\Gamma_{\rm s} + m(r) - \Gamma(r)(M_{\rm shell} + m(r)). \tag{1.28}$$

Inserting the relation for $\Gamma(r)$ obtained in equation 1.27, we can obtain for $\varepsilon'(R)$

$$\frac{\varepsilon'(r)}{c^2} = \sqrt{M_{\rm shell}^2 + m(r)^2 + 2\Gamma_{\rm s}mM_{\rm shell}} - [M_{\rm shell} + m(r)]. \tag{1.29}$$

In this phase the deceleration becomes very strong. An increasing fraction of the initial energy is dissipated and part of this dissipation is emitted as electromagnetic radiation. This is the afterglow.

In the last phase of this process the decelerated fireball moves with a Γ factor ~ 1 and at a certain time transits from a relativistic to a non relativistic regime. Almost all the initial kinetic energy has been therefore released in the process:

$$\varepsilon \approx \varepsilon' \approx M_{\rm shell}\Gamma_{\rm s}c^2 \tag{1.30}$$

The external shocks very likely happen in a scenario where a relativistic shell is expanding in a medium. Since the difference of Γ between the shell and the medium at rest is much larger than the $\Delta\Gamma$ between the two interacting shells, the external shock are expected to be a much more efficient mechanism than the internal shocks. Since the energy released during the prompt phase is larger than the one released in the afterglow (a factor $\sim$10 times larger as measured comparing the prompt gamma–ray energy $E_{\gamma,\rm iso}$ with the estimate of the afterglow energy release from the X–ray studies; Willingale et al. 2007) one could think that the external shocks could be responsible for the prompt emission but, as shown by Sari and Piran (1997), the external shock can not account for the fast variability observed in the prompt phase and for the fact that the spikes that are observed in the prompt gamma ray light curve have almost equal duration. For an alternative view see e.g. Dermer and Mitman who considered the interaction blast wave with clouds in a clumpy external medium.

1.3.4 Afterglow emission mechanism

During the fireball deceleration process, part of the kinetic energy is transferred as internal energy to the baryons, to the electrons and to the magnetic field that are present in the plasma. In the most common scenario, the accelerated electrons are assumed to be energised following a power law energy distribution

$$N(\gamma_e) \propto \gamma_e^{-p} \tag{1.31}$$

defined for electron Lorentz factors γ_e larger than a minimum value $\gamma_{\rm m}$. The fraction of energy transferred to the electrons is defined by the parameter $\epsilon_{\rm e}$ while the fraction of energy transferred to the magnetic field is defined by the parameter $\epsilon_{\rm B}$. We assume that the available energy given to the electrons and to the magnetic field is constant in time because we are in adiabatic case. The comoving electrons and the magnetic field energy densities are

$$U'_{\rm e} = n\langle\gamma_{\rm e}\rangle m_{\rm e}c^2 = \epsilon_{\rm e}U' \qquad U'_{\rm B} = \frac{B'^2}{8\pi} = \epsilon_{\rm B}U' \tag{1.32}$$

where

$$U' = n\Gamma^2 m_{\rm p}c^2 \tag{1.33}$$

and $n = n'/\Gamma$ cm^{-3} is the particle number density measured in the observer frame and n' is measured in the comoving frame.

We have

$$\gamma_{\rm m} = \frac{p-2}{p-1}\langle\gamma'_{\rm e}\rangle \tag{1.34}$$

The mean value of $\gamma'_{\rm e}$ is defined as

$$\langle\gamma'_{\rm e}\rangle = \frac{\int_{\gamma_{\rm m}}^{+\infty}\gamma\gamma^{-p}d\gamma}{\int_{\gamma_{\rm m}}^{+\infty}\gamma^{-p}d\gamma} \tag{1.35}$$

so

$$\gamma_{\rm m} = \epsilon_{\rm e}\frac{m_p(p-2)}{m_{\rm e}(p-1)}\Gamma \tag{1.36}$$

The brief discussion I will present here follows Hurley, Sari & Djorgovsky (2003).

If the dominating radiative emission process is synchrotron, the emitted spectrum can be described by only five parameters, i.e. the slope p of the energy distribution, and the synchrotron characteristic frequencies $\nu_{\rm m}$, $\nu_{\rm c}$. $\nu_{\rm a}$, and the normalisation of the spectrum. These parameters are:

- $\nu_{\rm m}$: is the typical synchrotron frequency emitted by electrons with random Lorentz factor $\gamma_{\rm m}$:

$$\nu_m \cong \frac{eB}{2\pi m_{\rm e}c}\gamma_{\rm m}^2 \tag{1.37}$$

where e is the electron charge, $B = 0.4\sqrt{\epsilon_{\rm B}n}\Gamma$ Gauss is the magnetic field. Transforming this to the observer frame (blue shifted by the Lorentz factor and redshifted by a factor of [1+z]) we have the relation in the observer frame

$$\nu_{\rm m} = 1.4\times10^{13}{\rm Hz}(1+{\rm z})^{-1}\left(\frac{\epsilon_{\rm e}}{0.1}\right)^2\left(\frac{\epsilon_{\rm B}}{0.1}\right)^{\frac{1}{2}}\left(\frac{\Gamma}{10}\right)^4 n^{\frac{1}{2}} \tag{1.38}$$

- $\nu_{\rm c}$: is the cooling frequency. The cooling time of an electron is inversely proportional to its Lorentz factor $\gamma_{\rm e}$. Therefore, electrons with a Lorentz factor higher than a critical Lorentz factor $\gamma_{\rm c}$ cool on the dynamical timescale of the system. In the observer frame this critical value is given by the relation

$$\frac{\sigma_T c\Gamma\gamma_{\rm c}B^2t}{6\pi(1+z)} = m_{\rm e}c^2 \tag{1.39}$$

The cooling frequency is therefore given by

$$\nu_c = 1.2\times10^{13}{\rm Hz}(1+z)\left(\frac{\varepsilon_B}{0.1}\right)^{-\frac{3}{2}}\left(\frac{\Gamma}{10}\right)^{-4} n^{-\frac{3}{2}}t_{\rm days}^{-2} \tag{1.40}$$

- $\nu_{\rm a}$: is the self absorption frequency. Below this critical frequency, the flux is self–absorbed When $\nu_{\rm a} < \min(\nu_{\rm m}, \nu_{\rm c})$, the self absorbed spectrum goes like ν^2 and $\nu_{\rm a}$ is given by

$$\nu_{\rm a} = 93{\rm GHz}(1+z)^{-\frac{13}{5}} \left(\frac{\epsilon_{\rm B}}{0.1}\right)^{\frac{6}{5}} \left(\frac{\Gamma}{10}\right)^{\frac{28}{5}} n^{\frac{9}{5}} t_{\rm days}^{\frac{8}{5}} \tag{1.41}$$

for $\nu_c < \nu_m$ and

$$\nu_{\rm a} = 87{\rm GHz}(1+z)^{-\frac{8}{5}} \left(\frac{\epsilon_{\rm e}}{0.1}\right)^{-1} \left(\frac{\epsilon_{\rm B}}{0.1}\right)^{\frac{1}{5}} \left(\frac{\Gamma}{10}\right)^{\frac{8}{5}} n^{\frac{4}{5}} t_{\rm days}^{\frac{3}{5}} \tag{1.42}$$

for $\nu_c > \nu_m$

- $F_{\rm m}$: is the spectrum normalisation given by the total number of radiating electrons $4\pi R^3 n/3$ times the peak flux from a single electron, resulting in

$$F_{\rm m} = 220{\rm mJy}(1+z)^{-2} d_{L,28}^{-2} \left(\frac{\epsilon_{\rm B}}{0.1}\right)^{\frac{1}{2}} \left(\frac{\Gamma}{10}\right)^{8} n^{\frac{3}{2}} t_{\rm days}^{3} \tag{1.43}$$

where $d_{L,28}$ is the luminosity distance in units of 10^{28} cm.

The spectral evolution depends on the characteristics of the surrounding medium. In case of a homogeneous medium at rest (ISM) the Lorentz factor decreases with the radius as

$$\Gamma \propto R^{-\frac{3}{2}} \tag{1.44}$$

while the time t in the observer frame goes like

$$t \propto \frac{R}{\Gamma^2}. \tag{1.45}$$

We therefore have

$$\Gamma \propto t^{-\frac{3}{8}}. \tag{1.46}$$

The synchrotron characteristic frequencies are

$$\begin{aligned} \nu_{\rm m} &= 6\times 10^{15}{\rm Hz}(1+z)^{\frac{1}{2}} E_{52}^{\frac{1}{2}} \epsilon_{\rm e}^2 \epsilon_{\rm b}^{\frac{1}{2}} t_{\rm days}^{-\frac{3}{2}} & (1.47)\\ \nu_{\rm c} &= 9\times 10^{12}{\rm Hz}(1+z)^{-\frac{1}{2}} E_{52}^{-\frac{1}{2}} \epsilon_{\rm b}^{-\frac{3}{2}} t_{\rm days}^{-\frac{1}{2}} n^{-1} & (1.48)\\ \nu_{\rm a} &= 2\times 10^{9}{\rm Hz}(1+z)^{-1} \varepsilon_{\rm e}^{-1} \epsilon_{\rm b}^{\frac{1}{5}} E_{52}^{\frac{1}{5}} n^{\frac{3}{5}}. & (1.49) \end{aligned}$$

If instead the surrounding medium has a stellar wind profile and its density decreases with the radius as R^{-2}, the Lorentz factor decreases like

$$\Gamma \propto t^{-\frac{1}{4}}. \tag{1.50}$$

We can define the density normalisation parameter $A_\star$ following the medium density profile relation

$$\rho R^2 = A_\star 5 \times 10^{11} \text{ gr cm}^{-1}. \tag{1.51}$$

In this case the equations for the synchrotron characteristic frequencies become

$$\nu_{\rm m} = 1.7 \times 10^{14} {\rm Hz} (1+z)^{\frac{1}{2}} E_{52}^{\frac{1}{2}} \epsilon_{\rm e}^2 \epsilon_{\rm b}^{\frac{1}{2}} t_{\rm days}^{-\frac{3}{2}} \tag{1.52}$$

$$\nu_{\rm c} = 7 \times 10^{11} {\rm Hz} (1+z)^{-\frac{3}{2}} E_{52}^{\frac{1}{2}} \epsilon_{\rm b}^{-\frac{3}{2}} t_{\rm days}^{\frac{1}{2}} A_\star^{-2} \tag{1.53}$$

$$\nu_{\rm a} = 1.5 \times 10^{10} {\rm Hz} (1+z)^{-\frac{2}{5}} E_{52}^{-\frac{2}{5}} \epsilon_{\rm e}^{-1} \epsilon_{\rm b}^{\frac{1}{5}} A_\star^{\frac{6}{5}} t_{\rm days}^{-\frac{3}{5}} \tag{1.54}$$

We can now focus on the shape of the emitted spectrum.

Assume that the source injects electrons with an energy distribution $\mathcal{Q}(\gamma)[\text{ cm}^{-3}\text{ s}^{-1}]$. The continuity equation can be written as

$$\frac{\partial N(\gamma,t)}{\partial t} = -\frac{\partial [N(\gamma,t)\dot{\gamma}]}{\partial \gamma} + \mathcal{Q}(\gamma) \tag{1.55}$$

where $\dot{\gamma}$ is the energy loss for electrons with Lorentz factor γ. The condition that is typically assumed for GRBs is that the electrons are injected with a power law energy distribution $\mathcal{Q}(\gamma) \propto \gamma^{-p}$. The total energy is therefore given by

$$E = \int_{\gamma_m}^{\gamma_{max}} m_e \gamma c^2 \mathcal{Q}(\gamma) d\gamma. \tag{1.56}$$

Depending on the value of p we can have two different scenarios.

$$E \propto \gamma_{\rm m}^{-(p-2)} \quad p > 2 \tag{1.57}$$

$$E \propto \gamma_{\rm max}^{(p-2)} \quad p < 2 \tag{1.58}$$

Typical values of p for GRBs are around $p \approx 2.5$ (see §5 for a comparison with observations).

If we only consider synchrotron emission we can write

$$\dot{\gamma} = -\frac{4}{3} \frac{\sigma_T c U_{\rm B} \gamma^2}{m_{\rm e} c^2} \tag{1.59}$$

and the cooling time in the comoving frame is

$$t_{\rm cool} = \frac{\gamma}{|\dot{\gamma}|} = \frac{3}{4} \frac{m_{\rm e} c^2}{U_{\rm B} c \sigma_T \gamma} \tag{1.60}$$

For times smaller than the cooling time $t_{\rm cool}$, the continuity equation leads to a synchrotron observed spectrum that is well described by the sum of different

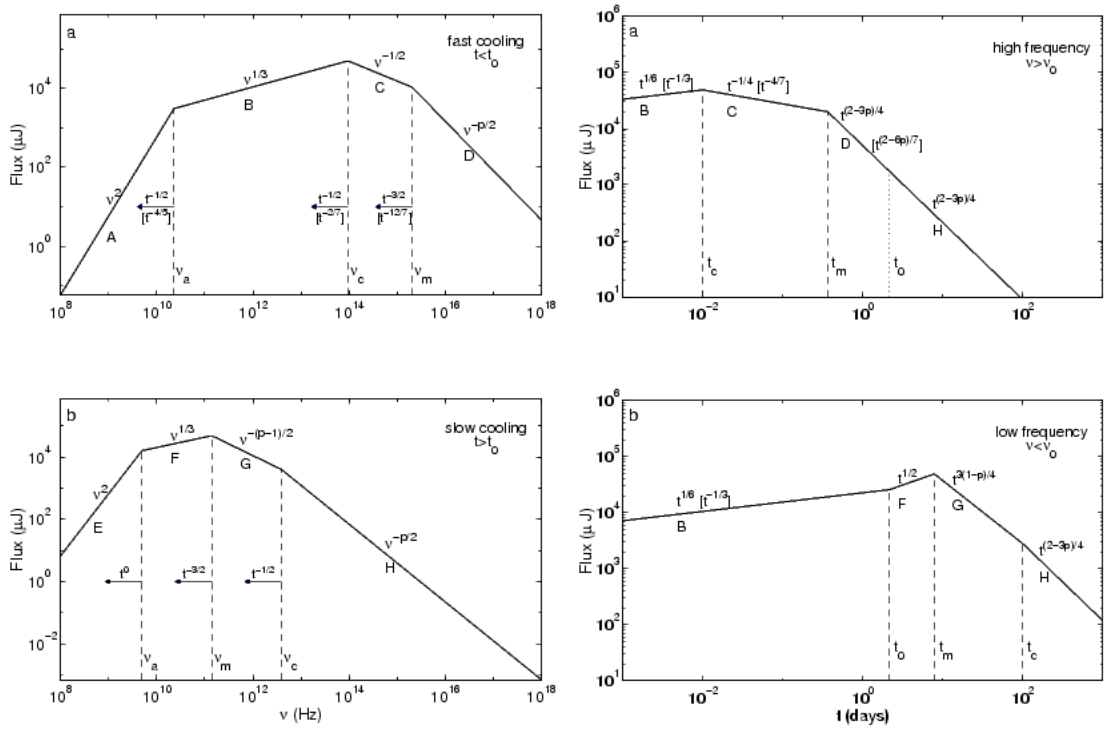

Figure 1.20: Theoretical broad band spectra (left panels) and light curves evolution (right panels) for the fast cooling (upper panels) and slow cooling (lower panel) regimes. This image has been taken from Zhang & Mészáros (2004).

power laws joining at the characteristic frequencies. The slope of the power laws depends only on p.

We have two regimes. When $\gamma_{\rm c} < \gamma_{\rm m}$ we are in the fast cooling regime: most of the injected energy is radiated away. Instead, when $\gamma_{\rm c} > \gamma_{\rm m}$ we are in the slow cooling regime.

In the slow cooling regime we have

$$F(\nu) \propto \begin{cases} \nu^2 & \nu < \nu_{\rm a} \\ \nu^{\frac{1}{3}} & \nu_{\rm a} \leq \nu < \nu_{\rm m} \\ \nu^{-\frac{p-1}{2}} & \nu_{\rm m} \leq \nu < \nu_{\rm c} \\ \nu^{-\frac{p}{2}} & \nu \geq \nu_c \end{cases} \tag{1.61}$$

In the fast cooling regime we have

$$F(\nu) \propto \begin{cases} \nu^2 & \nu < \nu_{\rm a} \\ \nu^{\frac{1}{3}} & \nu_{\rm a} \leq \nu < \nu_{\rm c} \\ \nu^{-\frac{1}{2}} & \nu_{\rm c} \leq \nu < \nu_{\rm m} \\ \nu^{-\frac{p}{2}} & \nu \geq \nu_{\rm m} \end{cases} \tag{1.62}$$

Note that in this case, the spectral shape below $\nu_{\rm c}$ is fixed and does not depend on p.

In fig. 1.20 (from Zhang & Mészáros 2004) the spectral slopes of the synchrotron emission are represented together with the related temporal evolution both in slow cooling and fast cooling regimes.

Temporal decay indices α and spectral slopes β are related ($F_\nu \propto t^\alpha \nu^\beta$ is adopted) in the different cooling regimes. These relations are different depending on the nature of the surrounding medium. They are usually called "closure relations" and, since they connect directly observable quantities, they represent a powerful instrument to check the consistency between the observed data and the theoretical scenario.

In table 1.2 (taken from Zhang & Mészáros 2004), I report the closure relations between the temporal decay α and the spectral index β in various afterglow models.

	β	α $(p>2)$	$\alpha(\beta)$	α $(1<p<2)$	$\alpha(\beta)$
ISM					
Slow Cooling					
$\nu<\nu_a$	2	$\frac{1}{2}$		$\frac{17p-26}{16(p-1)}$	
$\nu_a<\nu<\nu_m$	$\frac{1}{3}$	$\frac{1}{2}$	$\alpha=\frac{3\beta}{2}$	$\frac{p+2}{8(p-1)}$	
$\nu_m<\nu<\nu_c$	$-\frac{p-1}{2}$	$\frac{3(1-p)}{4}$	$\alpha=\frac{3\beta}{2}$	$-\frac{3(p+2)}{16}$	$\alpha=\frac{3(2\beta-3)}{16}$
$\nu>\nu_c$	$-\frac{p}{2}$	$\frac{2-3p}{4}$	$\alpha=\frac{3\beta+1}{2}$	$-\frac{3p+10}{16}$	$\alpha=\frac{3\beta-5}{8}$
ISM					
Fast Cooling					
$\nu<\nu_a$	2	1		1	
$\nu_a<\nu<\nu_c$	$\frac{1}{3}$	$\frac{1}{6}$	$\alpha=\frac{\beta}{2}$	$\frac{1}{6}$	$\alpha=\frac{\beta}{2}$
$\nu_c<\nu<\nu_m$	$-\frac{1}{2}$	$-\frac{1}{4}$	$\alpha=\frac{\beta}{2}$	$-\frac{1}{4}$	$\alpha=\frac{\beta}{2}$
$\nu>\nu_m$	$-\frac{p}{2}$	$\frac{2-3p}{4}$	$\alpha=\frac{3\beta+1}{2}$	$-\frac{3p+10}{16}$	$\alpha=\frac{3\beta-5}{8}$
Wind					
Slow Cooling					
$\nu<\nu_a$	2	1		$\frac{13p-18}{8(p-1)}$	
$\nu_a<\nu<\nu_m$	$\frac{1}{3}$	0	$\alpha=\frac{3\beta-1}{2}$	$\frac{5(2-p)}{12(p-1)}$	
$\nu_m<\nu<\nu_c$	$-\frac{p-1}{2}$	$\frac{1-3p}{4}$	$\alpha=\frac{3\beta-1}{2}$	$-\frac{p+8}{8}$	$\alpha=\frac{2\beta-9}{8}$
$\nu>\nu_c$	$-\frac{p}{2}$	$\frac{2-3p}{4}$	$\alpha=\frac{3\beta+1}{2}$	$-\frac{p+6}{8}$	$\alpha=\frac{\beta-3}{4}$
Wind					
Fast Cooling					
$\nu<\nu_a$	2	2		2	
$\nu_a<\nu<\nu_c$	$\frac{1}{3}$	-$\frac{2}{3}$	$\alpha=-\frac{\beta+1}{2}$	-$\frac{2}{3}$	$\alpha=-\frac{\beta+1}{2}$
$\nu_c<\nu<\nu_m$	$-\frac{1}{2}$	$-\frac{1}{4}$	$\alpha=-\frac{\beta+1}{2}$	$-\frac{1}{4}$	$\alpha=-\frac{\beta+1}{2}$
$\nu>\nu_m$	$-\frac{p}{2}$	$\frac{2-3p}{4}$	$\alpha=\frac{3\beta+1}{2}$	$-\frac{p+6}{8}$	$\alpha=\frac{\beta-3}{4}$
Jet					
Slow Cooling					
$\nu<\nu_a$	2	0		$\frac{3(p-2)}{4(p-1)}$	
$\nu_a<\nu<\nu_m$	$\frac{1}{3}$	$-\frac{1}{3}$	$\alpha=2\beta-1$	$\frac{8-5p}{6(p-1)}$	
$\nu_m<\nu<\nu_c$	$-\frac{p-1}{2}$	$-p$	$\alpha=2\beta-1$	$-\frac{p+6}{4}$	$\alpha=\frac{2\beta-7}{4}$
$\nu>\nu_c$	$-\frac{p}{2}$	$-p$	$\alpha=2\beta$	$-\frac{p+6}{4}$	$\alpha=\frac{\beta-3}{2}$

Table 1.2: Temporal index α and spectral index β in various afterglow models. The convention $F_\nu \propto t^\alpha \nu^\beta$ is adopted. The assumption $\nu_a < \min(\nu_m, \nu_c)$ is made. The jet model applies for the sideways expanding phase, which is valid for both the ISM and wind cases and is usually in the slow cooling regime. This table is taken from Zhang & Mészáros (2004).

Chapter 2

Alternative models of GRB afterglow emission

2.1 The canonical X–ray light curve

The XRT telescope is able to observe GRB X–ray counterparts starting from approximately 100 after the gamma ray trigger. Before the launch of *Swift*, X–ray afterglow observations were available only starting from several hours after the trigger. At these late times the X–ray afterglow light–curves were characterised by smoothly decaying behaviours that were well described by single or broken power–lay decays with $\alpha \sim 1$ and $\alpha \sim 1.6$ before and after the break.

The completely new observational window opened by the fast XRT slew capability unveiled a much more complex scenario. Most of the promptly observed X–ray light–curves are not well described by single or double power law decays. Soon after the *Swift* launch several groups (e.g. Nousek et al. 2006; Zhang et al. 2006; O'Brien et al. 2006, Chincarini et al. 2005) recognised the existence of a "canonical" X–ray light–curve behaviour shown by most of the observed GRBs.

Figure 2.1 shows the synthetic cartoon proposed by Zhang et al. (2006) in order to describe the typical "canonical" light curve behaviour observed by XRT. In summary we have:

0 *Prompt X–ray emission*: observed contemporaneously with the gamma ray detection.

I *Steep phase*: immediately after the end of the gamma ray prompt event the X–ray flux suddenly drops down by more than one order of magnitude. This phase is usually smoothly connected to the prompt emission (Tagliaferri et al. 2005; Barthelmy et al. 2005) and lasts some hundreds/thousands seconds. This early time steep decay phase is usually described by a power–law like temporal behaviour $F(t) \propto t^{-\alpha_{\rm I}}$ with $\alpha_{\rm I} > 3$. The X–ray spectrum

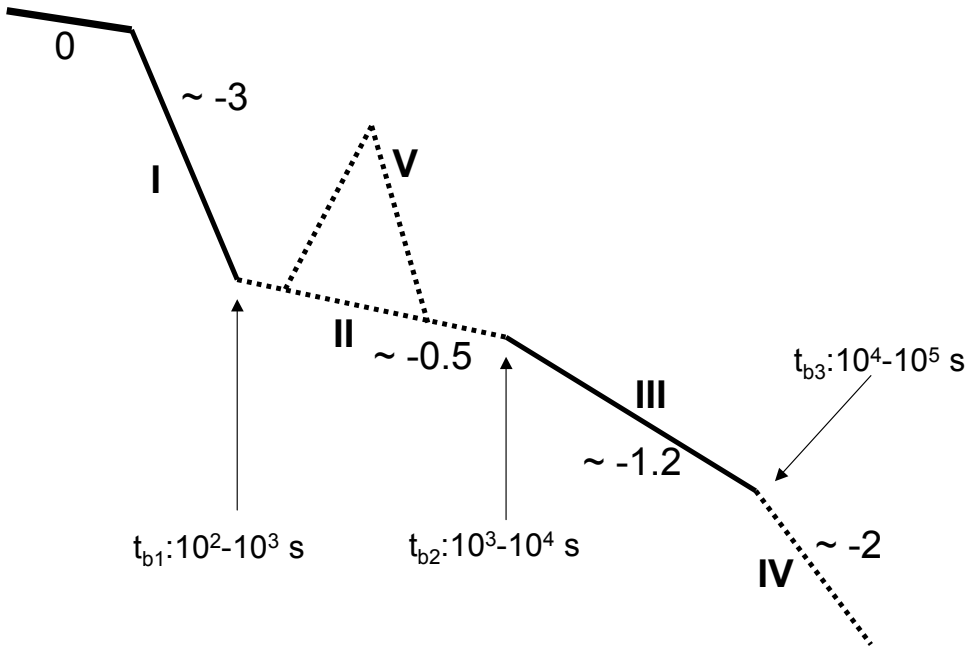

Figure 2.1: Sketch proposed by Zhang et al. (2006) showing the typical "canonical" behaviour observed in the X–ray light curves observed by XRT.

is sometimes observed to evolve during this phase and it is usually different from the one observed at later times (e.g. Butler & Kocevsky 2007).

II *Shallow or "flat" phase*: after the fast early time decline the flux remains almost constant from a few times 10^2 up to $10^3 - 10^4$s, following a power law evolution with $-0.5 < \alpha_{\rm II} < 0.5$. No spectral evolution is usually observed during this phase.

III *Normal steep phase*: the "flat" phase ends with a break in the X–ray light–curve at a characteristic time $T_{\rm A}$ (Willingale et al. 2007). After $T_{\rm A}$ the typical steeper power law decay $\alpha_{\rm III} \sim 1.2$ observed in the pre–*Swift* epoch sets in (De Pasquale et al. 2006b). The X–ray spectra show no evolution at $T_{\rm A}$ and the spectral index is usually the same before and after the break

(Evans et al. 2009)

IV *Post break phase*: Some of the GRBs that have been followed up in the X–rays for a long time show the presence of a further steepening in the X–ray light curve some days/weeks after the trigger. After such a break the temporal decay index becomes $\alpha_{\rm IV} \sim 2$. In the pre–*Swift* era this late time break in the X–ray light curves was usually interpreted as a jet break but nowadays some doubts have been cast out on this interpretation because of the inconsistency of a large number of jet breaks candidates with the closure relations discussed in §1.3.4 (see e.g. Racusin et. al 2009b, Perley et al. 2009).

V *X–ray flaring activity*: About half of GRBs show sudden rebrightnings (flares) in the X–ray light curves characterised by very steep rise and decay slopes and duration $\delta t/t \ll 1$ where t is the time since trigger at which the flare occurs (Burrows et al. 2005; Falcone et al. 2006; Romano et al. 2006, Chincarini et al. 2007).

2.2 Early time steep decay phase interpretation

The early time steep decay (phase I in fig 2.1) is the canonical X–ray light curve phase for which a more widely accepted physical interpretation has been proposed.

In this section I will briefly discuss the so called "curvature effect" (Fenimore et al. 1996; Kumar & Panaitescu 2000; Zhang et al. 2006; Panaitescu et al. 2006), that is thought to be responsible to the steep decay observed in the phase, following the discussion published in Zhang et al. (2006) and Zhang (2007). There are also other possible interpretations (see e.g. Yamazaki et al. (2006), Pe'er et al. (2006)).

The main assumptions of the "curvature effect" are:

- the region where the gamma ray prompt emission is produced is completely disconnected from the region where the afterglow radiation is emitted
- the emission process happening in the prompt emission region ceases abruptly.

These assumptions are consistent with the standard internal–external shock GRB scenario.

If we assume that the jet is confined inside a conical region with an opening angle $\theta_{\rm j}$, the radiation coming from a surface at a radius $R_{\rm cr}$ but from different viewing latitudes $\theta < \theta_{\rm j}$ would reach the observer at different times. The emitted photons would reach the observer at the angle θ at a time

$$t = (1+z)\frac{R_{\rm cr}}{c}\frac{\theta^2}{2} \tag{2.1}$$

If the line of sight is not too close to the jet edge this tail emission lasts for a time

$$t_{\rm tail} = (1+z)\frac{R_{\rm cr}}{c}\frac{\theta_{\rm j}^2}{2} \approx 330{\rm s}\left(\frac{R_{\rm cr}\theta_{\rm j}^2}{10^{13}}\right)\left(\frac{1+z}{2}\right). \quad (2.2)$$

Suppose for simplicity that the jet is in relativistic motion with a constant Lorentz factor Γ. If ν and ν' are the observer and the comoving frame frequencies respectively we have $\nu = \mathcal{D}\nu'$ that becomes:

$$\nu = \mathcal{D}\nu' = 2\Gamma\nu' \quad \theta \ll 1/\Gamma \quad (2.3)$$

$$\nu = \mathcal{D}\nu' = \frac{2}{\Gamma\theta^2}\nu' \quad \theta \gg 1/\Gamma \quad (2.4)$$

and since $t \propto \theta^2$, $\theta \gg 1/\Gamma$, one gets $\nu \propto t^{-1}\nu'$.

If $L'_{\nu'}$ is the comoving surface brightness and β is the observed spectral index, when $1/\Gamma \ll \theta < \theta_{\rm j}$ the observed flux can be written as

$$F_{\nu,t} \propto L'_{\nu'}\mathcal{D}^2 \propto (\nu')^{-\beta}\mathcal{D}^2 \propto \nu^{-\beta}t^{-2-\beta} \quad (2.5)$$

Comparing it with the standard description of the afterglow emission $F_{\nu,t} \propto \nu^{-\beta}t^{-\alpha}$ we can obtain the well known relation for the "curvature" emission (e.g. Kumar & Panaitescu 2000)

$$\alpha = 2 + \beta. \quad (2.6)$$

Zhang et al. (2006) proved that the eq. 2.6 is valid also in the more complex case of a decelerating jet.

This simple relation has the powerful feature to be directly testable since both α and β are observable parameters taking into account two cautions. The first one is that each time the central engine restarts, the clock must be reset to 0. The trigger time is not the correct time to be used as t_0. A wrong identification of t_0 leads to find decay indices that are artificially too steep. The second caution is that the possible contribution of the underlying afterglow emission must be subtracted.

The simple description of the "curvature" emission just described cannot account for the strong spectral evolution observed during the steep decline phase of some GRBs (e.g. Zhang et al. 2007b). Zhang et al. (2007b) interpreted the spectral evolution of some bursts like GRB 060218 as the superposition of a "curvature" emission and an underlying afterglow. This interpretation cannot explain GRBs with strong spectral evolution (e.g. GRB 050724, GRB 060218, and GRB 060614).

2.3 The "flat" phase theoretical interpretations

The shallow decay is the phase of the canonical X–ray light curve that has not already found a convincing theoretical interpretation accepted by the majority of

the GRB scientific community. For this reason several models have bee proposed in the last four years in order to explain its physical origin.

Some of them tried to explain this shallow decay phase with some modifications of the standard external shock afterglow model. In other cases a prolonged activity of the central engine has been invoked. Several models claimed a geometrical origin of this phase while others proposed completely different emission processes.

Since the complexity of the X–ray and optical light curves will be treated in this thesis, in this section I will briefly summarise some of the proposed interpretations. To this aim I will again follow the review by Zhang (2007).

2.3.1 Energy injection from a long lasting central engine activity

Zhang et al. (2006), Nousek et al. (2006), Panaitescu et al. (2006) propose that the shallow decay can be produced by a continuous, long lasting, energy injection into the forward external shock. This interpretation invokes the presence of a long lasting activity of the central engine. This is characterised by a smoothly declining power of the form

$$L \propto t^{-q} \tag{2.7}$$

The details of the dynamical evolution and the radiative processes in this scenario have been discussed by Zhang & Mészáros (2001).

In order for the blast wave total energy to increase with time we should have $q < 1$. The energy in the fireball increases with time as $E_{\rm iso} \propto t^q$. The Γ Lorentz factor and the radius R goes like:

$$\Gamma \propto R^{-\frac{2+q}{2(2-q)}} \propto t^{-\frac{2+q}{8}}; R \propto t^{\frac{2-q}{4}} \quad \text{ISM case} \tag{2.8}$$

$$\Gamma \propto R^{-\frac{2+q}{2(2-q)}} \propto t^{-\frac{q}{4}}; R \propto t^{\frac{2-q}{2}} \quad \text{wind case} \tag{2.9}$$

It is possible to infer the temporal evolution of some important parameters such as:

- the typical synchrotron frequency $\nu_{\rm m}$

$$\nu_{\rm m} \propto t^{-\frac{2+q}{2}} \quad \text{ISM case} \tag{2.10}$$

$$\nu_{\rm m} \propto t^{-\frac{2+q}{2}} \quad \text{wind case} \tag{2.11}$$

- the synchrotron cooling frequency $\nu_{\rm c}$

$$\nu_{\rm c} \propto \Gamma^{-4} t^{-2} \propto t^{\frac{q-2}{2}} \quad \text{ISM case} \tag{2.12}$$

$$\nu_{\rm c} \propto \Gamma^{-4} t^{-2} \propto t^{\frac{2-q}{2}} \quad \text{wind case} \tag{2.13}$$

		no injection		injection	
	β	α	$\alpha(\beta)$	α	$\alpha(\beta)$
ISM	slow cooling				
$\nu < \nu_m$	$-\frac{1}{3}$	$-\frac{1}{2}$	$\alpha = \frac{3\beta}{2}$	$\frac{5q-8}{6}$	$\alpha = (q-1) + \frac{(2+q)\beta}{2}$
$\nu_m < \nu < \nu_c$	$\frac{p-1}{2}$	$\frac{3(p-1)}{4}$	$\alpha = \frac{3\beta}{2}$	$\frac{(2p-6)+(p+3)q}{4}$	$\alpha = (q-1) + \frac{(2+q)\beta}{2}$
$\nu > \nu_c$	$\frac{p}{2}$	$\frac{3p-2}{4}$	$\alpha = \frac{3\beta-1}{2}$	$\frac{(2p-4)+(p+2)q}{4}$	$\alpha = \frac{q-2}{2} + \frac{(2+q)\beta}{2}$
ISM	fast cooling				
$\nu < \nu_c$	$-\frac{1}{3}$	$-\frac{1}{6}$	$\alpha = \frac{\beta}{2}$	$\frac{7q-8}{6}$	$\alpha = (q-1) + \frac{(2-q)\beta}{2}$
$\nu_c < \nu < \nu_m$	$\frac{1}{2}$	$\frac{1}{4}$	$\alpha = \frac{\beta}{2}$	$\frac{3q-2}{4}$	$\alpha = (q-1) + \frac{(2-q)\beta}{2}$
$\nu > \nu_m$	$\frac{p}{2}$	$\frac{3p-2}{4}$	$\alpha = \frac{3\beta-1}{2}$	$\frac{(2p-4)+(p+2)q}{4}$	$\alpha = \frac{q-2}{2} + \frac{(2+q)\beta}{2}$
Wind	slow cooling				
$\nu < \nu_m$	$-\frac{1}{3}$	0	$\alpha = \frac{3\beta+1}{2}$	$\frac{q-1}{3}$	$\alpha = \frac{q}{2} + \frac{(2+q)\beta}{2}$
$\nu_m < \nu < \nu_c$	$\frac{p-1}{2}$	$\frac{3p-1}{4}$	$\alpha = \frac{3\beta+1}{2}$	$\frac{(2p-2)+(p+1)q}{4}$	$\alpha = \frac{q}{2} + \frac{(2+q)\beta}{2}$
$\nu > \nu_c$	$\frac{p}{2}$	$\frac{3p-2}{4}$	$\alpha = \frac{3\beta-1}{2}$	$\frac{(2p-4)+(p+2)q}{4}$	$\alpha = \frac{q-2}{2} + \frac{(2+q)\beta}{2}$
Wind	fast cooling				
$\nu < \nu_c$	$-\frac{1}{3}$	$\frac{2}{3}$	$\alpha = \frac{1-\beta}{2}$	$\frac{(1+q)}{3}$	$\alpha = \frac{q}{2} - \frac{(2-q)\beta}{2}$
$\nu_c < \nu < \nu_m$	$\frac{1}{2}$	$\frac{1}{4}$	$\alpha = \frac{1-\beta}{2}$	$\frac{3q-2}{4}$	$\alpha = \frac{q}{2} - \frac{(2-q)\beta}{2}$
$\nu > \nu_m$	$\frac{p}{2}$	$\frac{3p-2}{4}$	$\alpha = \frac{3\beta-1}{2}$	$\frac{(2p-4)+(p+2)q}{4}$	$\alpha = \frac{q-2}{2} + \frac{(2+q)\beta}{2}$

Table 2.1: Temporal index α and spectral index β in various afterglow models when energy injection is considered as presented in table 2 of Zhang et al. (2006).

- the peak flux density $F_{\rm m}$

$$F_{\rm m} \propto t^{1-q} \quad \text{ISM case} \tag{2.14}$$

$$F_{\rm m} \propto \Gamma^{-2} \propto t^{-\frac{q}{2}} \quad \text{wind case} \tag{2.15}$$

It is possible also to evaluate the dependencies of the temporal index α and of the spectral index β (when the standard convention $F \propto t^{-\alpha}\nu^{-\beta}$ is applied) with q and p (i.e. the electron energy distribution spectral index).

In tab. 2.1 we report these relations as reported by Zhang et al. (2006).

2.3.2 Energy injection from a short lived engine

In this case the energy injection of a short-lived engine (i.e. of duration comparable to that of the prompt phase) can produce shells with a steep power-law distribution of Γ Lorentz factors (Rees & Mészáros 1998).

$$M(>\Gamma) \propto \Gamma^{-s} \tag{2.16}$$

with s larger than 1.

The temporal steepening at $T_{\rm A}$ is explained as a cut-off in the Γ Lorentz factor distribution. Below this cut-off value (of the order of a few tens for a break around 10^2-10^3s) s is smaller than 1 (Zhang et al. 2006).

The two energy injection alternatives cannot be currently distinguished observationally. Both interpret the plateau as afterglow emission from a continuously refreshed shock. One can expect that the two different energy injection scenarios should produce different reverse shock signatures since in the long lasting central engine activity case the reverse shock is fully relativistic while in the varying Lorentz factor case the reverse shock is expected to be non relativistic. Unfortunately the uncertainties in the composition of the central engine outflows produce large uncertainties on the reverse shock observable signatures and therefore it is difficult to distinguish between the two scenarios.

In both cases the energetic (in bulk motion) largely exceeds what required to produce the prompt emission.

2.3.3 Delayed energy transfer to the forward shock

The onset of the afterglow is expected to happen at $t_{\rm dec} = {\rm Max}(t_\gamma, T)$, where t_γ is the time scale in which the fireball collects $\Gamma-1$ of the rest mass of the initial fireball from the ISM and T is the duration of the explosion.

From numerical calculations (Kobayashi & Zhang 2007) it has been evaluated that the transfer of kinetic energy from the fireball to the medium takes some time (of the order of several thousands of seconds). In case of high ratio between Poynting flux and kinetic flux, the energy transfer starts after the reverse shock disappears with a further delay of the energy transfer process (note that for a purely magnetic fireball no reverse shock is predicted).

In this model the shallow decay phase is simply due to this delayed energy transfer from the fireball to the surrounding medium. The strong curvature predicted by this interpretation seems to be consistent with the "dip" observed before the flat phase observed in a few events. On the other hand for those cases with a straight shallow decay light curve, one needs to take into account the steep decay tail to reproduce the observations (Zhang 2007).

2.3.4 Reverse shocks

The shallow decay could be produced as synchrotron emission from the reverse shock if the micro-physical parameters ϵ_e and ϵ_B are much larger than those in the forward shock.

In this situation, the ratio of the X–ray flux produced by the reverse and forward shocks would be dominated by the former. Along these lines, Uhm & Beloborodov (2007) and Genet, Daigne & Mochkovitch (2007) suggested that the X–ray plateau emission is due to the reverse shock running into ejecta of relatively small (and decreasing) Lorentz factors. This requires an appropriate Γ distribution of the ejecta, besides the suppression of the X-ray flux produced by the forward shock.

2.3.5 Time dependent micro-physical parameters

Ioka et al. (2006) proposed some physical interpretations of the shallow decay phase with the aim of avoiding the problem of requiring an unreasonably high gamma-ray efficiency.

In one of those, they proposed a model in which some micro-physical parameters such as the energy fraction that goes into electrons ϵ_e and magnetic field ϵ_B can vary with time.

If the X–ray emission is produced by an electron distribution with a power law index $p \sim 2$ in fast cooling regime, the X–ray luminosity is given by

$$L_X \sim \epsilon_e L \tag{2.17}$$

where L is the bolometric kinetic luminosity.

The X–ray luminosity does not depend on the magnetic energy fraction ϵ_B since $L_X \propto \epsilon_B^{(p-2)/4}$.

Since bolometric luminosity decreases like $L \propto t^{-11}$, a time evolution of the electron energy fraction like

$$\epsilon_e \propto t^{\frac{1}{2}} \tag{2.18}$$

would produce an X–ray flux decay

$$L_X \propto t^{-\frac{1}{2}} \tag{2.19}$$

similar to the typical flat phase decay index.

In this scenario the shallow decay phase ends at a time T_A when ϵ_e is saturated at the value (i.e. $\epsilon_e \sim 0.1 - 1$).

[1] Ioka et al. (2006) mention this relation without derivation. An explicit derivation can be seen in the Master thesis of Daniele Malesani

2.3.6 Prior activity model

In this alternative interpretation Ioka et al (2006) assume that a precursor explosion occurs around 10^4s before the prompt. This precursor ejects mass with Lorentz factor smaller than the one of the main event. Since the precursor is quite weak, the related afterglow emission is too faint to be detected. The faster main event ejecta catches the slower precursor one producing a shock. Ioka et al (2006) show that such a shock produces an emission with bolometric kinetic luminosity that evolves like $L \sim E_{\rm kin}/t \propto t^{-1}$.

When finally the two ejecta merge and interact with the circumburst medium, the standard afterglow sets in.

2.3.7 Up-scattering of forward shock photons

Panaitescu (2008) proposed an alternative model in order to disentangle the X–ray and the optical emission that often show early times chromatic breaks that are not easily explainable with the other proposed models.

The main idea of this interpretation is that the central engine ejects a first fireball. The photons emitted by the forward shock of this fireball are up-scattered by a second shell emitted by the central engine at later times. This delayed emission is responsible for the X–ray plateau observed in the X–rays while is contributing much less in the optical. There is then the possibility to observe chromatic breaks (a $T_{\rm A}$ in the X–rays but not in the optical).

2.3.8 Dust scattering

Long GRBs are predicted to take place inside star forming regions. This location could imply the presence of a large amount of dust in the GRB progenitor surroundings (at distances within $\sim$ 100 pc). From this assumption Shao & Dai (2007) and Shao, Dai & Mirabal (2008) evaluated the possible contribution to the X–ray afterglow of the scattering of X-rays by dust grains showing that the shallow decay phase can be consistent with their predictions of the dust echo in the GRB progenitor surroundings.

This interpretation has some drawbacks. First of all the presence of a large amount of dust in a region within about 100 pc around the progenitor should produce high dust reddening at optical–UV wavelengths that is excluded by the optical-UV spectral energy distributions analysis. A second important drawback is that this model predicts a strong spectral evolution since softer X-rays tend to be scattered at larger angles (implying longer paths and then retarded arrival time with respect to higher energy photons). Intensive X–ray spectral analysis of large samples of GRBs has been carried out in the last years (e.g. Evans et al. 2009, Racusin et al. 2009b) showing that, after the end of the early steep decay phase,

the X–ray afterglows do not show any evidence of spectral evolution during the whole light curve.

2.3.9 Cannonball model

In the so called "cannonball model" (Dar & De Rújula 2000, 2004 and references therein) the full X-ray steep-flat-steep light curve behaviour is produced by the same unique mechanism. In the Cannonball model, long-duration GRBs and their afterglows are produced by bipolar jets of cannonballs ejected in ordinary core collapse supernova explosions. The cannonball radiation observed in the X–rays is due to the sum of thermal bremsstrahlung, line emission and synchrotron radiation from swept-in ISM electrons spiralling in the cannonballs enclosed magnetic field.

Dado, Dar & De Rújula (2006) explained the X–ray canonical light curve in the framework of the cannonball model. The shallow decay phase corresponds to the time where the synchrotron radiation becomes dominant with respect to the bremsstrahlung and line emission mechanisms. The break time $T_{\rm A}$ at the end of the shallow decay phase would correspond to the start of the cannonball deceleration phase.

2.3.10 Fireshell model

In the "fireshell model" (see Ruffini 2008 for a complete review) the whole broad band GRB emission from the gamma ray (precursor and prompt) event to the optical and X–ray afterglow is produced by a baryonic shell (fireshell) interacting with a non-homogeneous circumburst medium.

The emission process is thermal at all times. Once the fireshell reaches a region of low density, $\sim$ 0.03–2 pc away, it decelerates very slowly, giving origin to the plateau phase.

2.3.11 Geometrical models

Off-beam model

Eichler & Granot (2006) proposed an alternative model to explain the shallow decay phase. In this scenario the viewing angle is slightly outside the (rather sharp) edge of the jet (i.e. outside the regions where the energy per solid angle in the external shock is large enough to produce bright afterglow emission). In this condition the early X–ray light curve phase may be a combination of the decaying tail of the prompt emission and the delayed onset of the afterglow emission observed from viewing angles slightly outside the edge of the jet with prominent afterglow emission.

The shallow phase is due to the combination of the emitted flux decrease (due to the deceleration) and the increase of the visible area. At the time at which beaming angle becomes large enough to include the line of sight, the observer starts to see the standard "on beam" evolution. This transition is seen by the observer as a steepening of the light curve at $T_{\rm A}$.

Patchy shell model

Toma et al. (2006) proposed the "Patchy shell model". Their idea is similar to the "off-beam model" proposed by Eichler & Granot (2006).

In this case they considered an inhomogeneous jet with an anisotropic angular energy distribution (i.e. the whole jet consists of multiple sub-jets). Every subject is responsible for a gamma ray and afterglow emission but is observable only when the relativistic beaming is decreased enough to include the observer line of sight. While the jets are decelerating, the number of visible jets increases and the observed light curve shows the typical shallow decay phase. This effect ends when the beaming angle becomes large enough for the whole emitting area to be observable. After that the observed light–curves follows the standard "on beam" evolution.

Two-component jet model

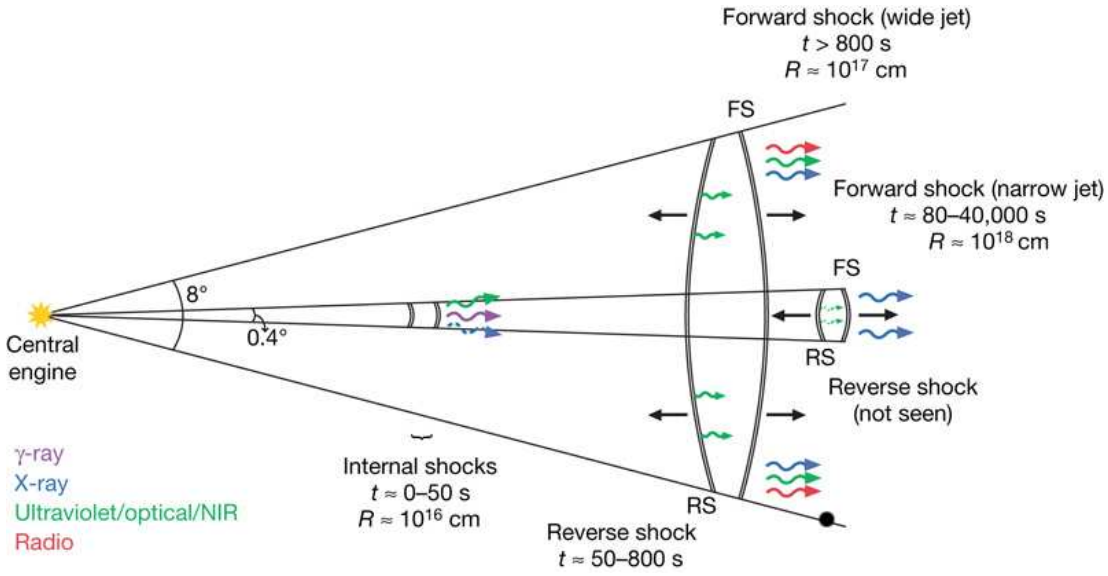

Figure 2.2: Sketch illustrating the application of the two-component jet model for GRB 080319 proposed by Racusin et al. (2008).

In this model the jet is composed by two different components: a narrow and a wider jet. The wider jet is characterised by a smaller Lorentz factor and it

is thought to be responsible for the observed optical emission while the faster narrower jet should produce the observed X–ray emission. This model has been already proposed in order to explain the light curves of some pre–*Swift* events (e.g. GRB 021004 and GRB 030329 (Peng et al. 2005)) and it has been now proposed in order to explain both the X–ray shallow decay phase and the diversity between the observed X–rays and optical light curves (e.g. Oates et al. 2007 for GRB 050802 and Racusin et al. 2009a for GRB 080319b). The latter is explained by the association of the optical and X–ray emission with different jets (wide and narrow respectively). $T_{\rm A}$ instead is nothing but the narrow jet-break and occurs when the Lorentz factor of the narrow jet decreases to $1/\theta_{\rm narrow}$. The interaction of the wide jet to the external medium may be seen as a late rise/bump or a change in the decay slope of the optical bands light curve.

In fig. 2.2 I show a schematic picture proposed by Racusin et al. (2008) in order to explain the spectral and temporal elements of the two-component modelling applied to GRB 080319b. The gamma ray prompt emission is due to the internal shocks in the narrow jet. The optical and X–ray emission are due to the combined effects of the forward and reverse shocks in both the narrow and wide jets. In this case the reverse shock is too faint to be detected.

2.4 Late prompt model

In the second part of this thesis I will focus mainly on the alternative interpretation, i.e. the "late prompt model" proposed by Ghisellini et al. (2007).

In this scenario the central engine, after having emitted most of its power during the gamma ray prompt phase (lasting up to a few hundred seconds), persists producing shells for a long time. This activity is characterised by a smaller power. In order to distinguish it from the early times gamma ray prompt process, they called "late prompt" this late central engine activity. At late times, while the late prompt mechanism is still acting, the forward shock created by the interaction of the shells with the circumburst medium is taking place producing the standard afterglow emission.

In the late prompt model, the early gamma ray prompt emission is produced by the internal energy dissipation of shells of large Γ Lorentz factors. The late prompt emission is thought to be produced by the same mechanism by shells characterised by much smaller Γ Lorentz factors. Smaller Γ factors imply also a smaller observed variability.

The radiation is produced at distances relatively close to the central engine (even less than 10^{13}-10^{14} cm), in a region different from the one where the shells, produced during the early prompt, interact with the circumburst medium producing the standard afterglow.

If the late shells Γ factors decrease in time, the relativistic beaming angle $\theta_{\rm beam}$

increases since

$$\theta_{\rm beam} = \frac{1}{\Gamma}. \tag{2.20}$$

In a first stage the late shells are still fast enough to have

$$\theta_{\rm j} > \theta_{\rm beam} \tag{2.21}$$

where $\theta_{\rm j}$ is the jet opening angle. Therefore only a small fraction of the emitting area is visible by the observer. This area becomes larger and larger with the decreasing of Γ and the intrinsic luminosity decrease is partially compensated by the increase of the visible emitting area. If this process is dominating the observed emission, this effect can explain the shallow decay phase observed in the X–ray light curves. At a certain time $T_{\rm A}$ we have that

$$\theta_{\rm j} = \theta_{\rm beam} = \frac{1}{\Gamma_{T_{\rm A}}} \tag{2.22}$$

and all the emitting area becomes visible by the observer. The increase of $\theta_{\rm beam}$ can not compensate anymore the luminosity decrease and the observed light curve shows a sudden steepening.

Even if the total amount of mass emitted in the late shells is comparable with the one emitted during the early prompt, since the Γ factors are smaller, the total energy emitted in this late phase is smaller then the early prompt one. This is in agreement with the fact that the total energy emitted in the X–rays is only a fraction ($\approx 10\%$) of the energy emitted in gamma rays (Willingale et al. 2007).

In terms of total energetics, the late prompt scenario may be the least demanding for explaining what is observed. In fact, in the refreshed shock scenario, the plateau phase is flat because the shock running into the circumburst medium is energised by the arrival of shells with kinetic energies that overtake the energy of the first shells, which have produced the early prompt emission. Alternatively, in the increasing $\epsilon_{\rm e}$ $\epsilon_{\rm b}$ scenario, the radiation produced during the plateau phase is a small fraction of the carried kinetic energy. Instead, interpreting the plateau phase as late prompt emission, we note that the extra energy created by the central engine in the late phase is less than (or at most comparable to) the total energetics of the shells responsible for the early prompt emission. If the radiative efficiency of the early prompt is large, it can also explain the weakness of the real afterglow emission, since the kinetic energy of the fireball, remaining after the early prompt phase, may be relatively small.

With the late prompt scenario, Ghisellini et al. do not proposed a detailed physical description of the processes that produce the late prompt radiation. However they proposed some theoretical speculations that could be the base for making a first step towards a better understanding of the late prompt physical mechanism. Here I report a few lines directly taken from their paper where they discuss these speculations.

"*After the black hole formation following the core collapse of the progenitor star, the equatorial core material that failed to form the black hole in the first place can form a very dense accreting torus, which can sustain a strong magnetic field, which in turn extracts the rotational energy of the black hole. This accretion phase could correspond to the early prompt phase of the burst. After this phase, some fallback material may also be accreted. This phase of "late accretion" can last for a longer time, with a density of the accreting matter smaller than in the early phases. If so, the magnetic field that this matter can sustain is weaker than before, with a corresponding smaller power extracted from the black hole spin. This may well correspond to production of shells of smaller* Γ *factors. These shells can dissipate part of their energy with the same mechanism of the early ones. Occasionally, the central engine produces a faster than average shell, originating the late flares often observed in the* Swift *X–Ray Telescope light curves.*

One of the most important differences between this model and the other ones discussed in the previous sections, is the fact that the observed broad band light curves are due to the sum of two completely disentangled mechanisms. One is the "standard" forward shock afterglow emission and the other is the radiation produced by the late prompt mechanism. These components can be dominant in different bands so that the optical and X–ray light curves can follow completely different temporal behaviours.

2.4.1 Observed light curves in the late prompt scenario

Focusing on the differences between the optical and X–ray light curves we can have different observed situations:

i The X–rays are dominated by the late prompt emission while the standard afterglow is responsible for the optical light curve. In this case the X–rays do not track the optical bands temporal behaviour. Different temporal decay indices and chromatic breaks can be seen. In particular no jet break is expected in the X–rays and the flat phase is not observed in the optical. This first case is sketched in figure 2.3 from Ghisellini et al. (2007).

ii Both the optical and X–ray observed fluxes are dominated by the late prompt emission. Both light curves should show the shallow decay phase ending with an achromatic break at $T_{\rm A}$. No jet break is expected to be seen. At later times the contribution of the standard afterglow emission could become dominant.

iii Both the optical and X–ray observed fluxes are dominated by the standard afterglow emission. This is the case that well describes the pre-*Swift* GRBs. The observed early times light curves do not show the shallow decay phase. The temporal and spectral parameters follow the standard afterglow closure

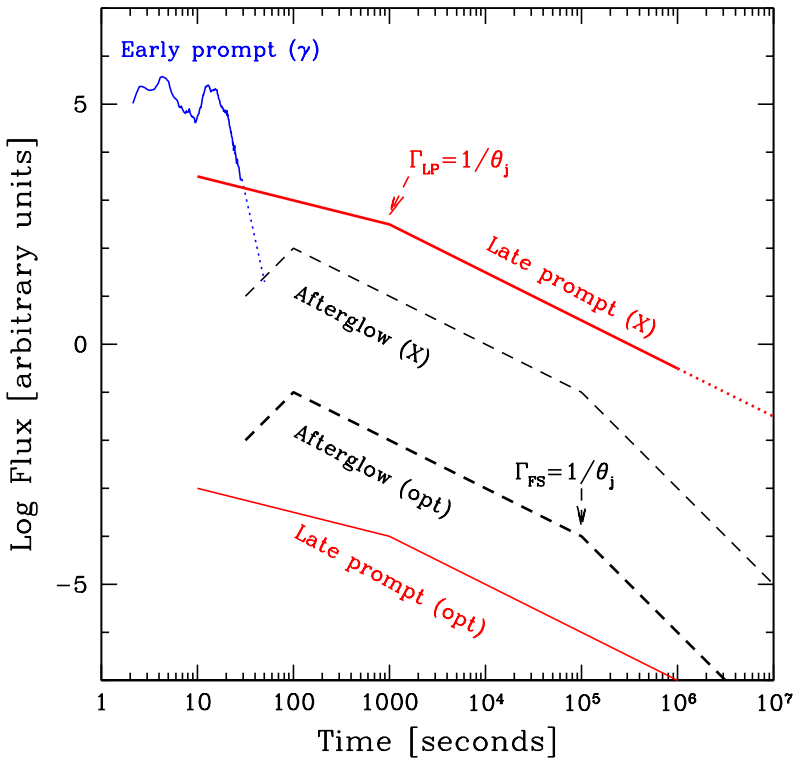

Figure 2.3: Schematic illustration of the different components contributing to the X–ray and optical light curves, as labelled (picture from Ghisellini et al. (2007). Scales are arbitrary. The case illustrated here is only one (likely the most common) possible case, when the X–ray flux is dominated by late prompt emission (solid line; the dotted line corresponds to an extrapolation at very late times), while the optical flux is dominated by the real afterglow (dashed line). $\Gamma_{\rm LP}$ and $\Gamma_{\rm FS}$ indicate the Γ Lorentz factors of the late shells and the forward shocks, respectively.

relations. An achromatic late time steepening of the light curves can be seen at the jet break time.

iv The optical bands are dominated by the late prompt emission while the standard afterglow is responsible of the X–ray light curve. This case is the same described in the first point but with optical and X–rays inverted.

v The afterglow and late prompt emission dominate the light curve in one band only for a fraction of the light curve and we can observe complex light curves also when observing a single band. These cases are the most difficult

to recognise.

Another important characteristic of this model is that there are some observational features that the model predicts and that can be therefore used to test its validity. From the light curves evolution point of view we expect to observe the different cases itemised above. Depending on which component dominates the observed fluxes in the X–rays and in the optical we can test if the presence/absence of jet breaks at late times is consistent with the late prompt scenario.

This modelling can be also be tested from the spectral point of view. When the optical and X–ray observed light curves are dominated by different emission mechanisms, this should have observable consequences in the optical to X–rays spectral energy distribution (SED). The signature of the fact that these bands are dominated by different components is that the optical fluxes in the SED are inconsistent with the extrapolation at lower frequencies of the spectrum observed in the X–ray and vice versa. When instead the optical and X–ray light curves are dominated by the same component, the broad band SED should be consistent with one single emission model connecting the two bands. When there is a transition in the light curve from the domination of one component to another, a spectral evolution should be seen and the optical to X–ray SED should evolve following the previously discussed cases.

In the second part of my thesis I will focus on the possibility to model the broad band optical and X–ray light curves of a sample of long GRBs as the sum of two separate components (i.e. the standard external shock afterglow emission and an additional phenomenological component). I will discuss this choice in the framework of the late prompt scenario finding some results that can represent a first step towards a better description of the physical mechanism that is responsible for the emission of this late prompt component (see §5). I will discuss the nature of the breaks observed in the *Swift* GRB light curves and the problem of the lack of achromatic jet breaks in many of the *Swift* afterglows (see §6). I will finally study the temporal evolution of the X–ray spectra and of the optical to X–ray SEDs of a sample of GRBs in order to test their consistency with the predictions of the two components modelling. I will also discuss the obtained results in the framework of the late prompt scenario (see §7 and §8). These issues have been discussed also by Ghisellini et al. (2009a), Ghisellini et al (2009b), Nardini et al. (2009b), Nardini et al. (2009c), Nardini et al. (2009d).

2.5 X–ray flares

One of the most intriguing discoveries made by *Swift* is the systematic presence of flares in more than half of the observed X–ray light curves. These flares appear as a sudden increase of the observed X–ray flux with respect of the afterglow emission and are characterised by very steep increase and decrease slope. In most

cases, after the end of a flare, the afterglow light curve continues according to the extrapolation of the pre-flare decay. Some events show multiple flares and in some cases the flare fluence can be comparable to the gamma ray prompt one. The X–ray flares are spectrally harder than the underlying continuum (Burrows et al. 2005; Romano et al. 2006b; Falcone et al. 2006), they show a hard–to–soft evolution similar to the one observed during the gamma ray prompt phase and later flares are less energetic and broader (in time) than early flares. *BeppoSAX* observations of some X–ray flares without significant spectral evolution (Piro et al. 2005). This result is strengthened by the broad available spectral coverage (2-700 keV). This suggests the possible existence of two different families of flares, both related to a long duration central engine but related to different emission mechanisms.

All these observed features show that the flaring activity has a different physical origin with respect to the underlying afterglow emission continuum and seem to indicate that they are not related to an external shock origin (Zhang et al 2007, Lazzati & Perna 2007). An internal energy dissipation origin related to a restarting of the central engine seems to better explain the flaring activity for two main reasons. First of all the need to reset the time t_0 when the central engine restarts producing radiation allows to explain the observed very fast rise and decay. Another advantage is that the internal dissipation model is very economical from an energetic point of view while in the refreshed external shock models a large energy budget is needed (Galli & Piro 2007). The injection energy has to be at least comparable to that already in the blast wave in order to have any significant injection signature (Zhang & Mészáros 2002).

The late internal dissipation model of X–ray flares has been tested in a large sample of X–ray flares by Liang et al. (2006). They described the decay phase of the flares (after subtracting the contribution of the underlying continuum emission) as due to "curvature" effect assuming the flare t_0 around the beginning of the flare. This internal late internal dissipation implies that the central engine can remain active up to days after the gamma ray prompt event. Lazzati et al. (2008) found that the average luminosity of X–ray flares as a function of time decays as $\propto t^{-5/3}$. This value is intriguingly similar to the to the time dependence of the the fall-back of material accreting the black hole. This similarity can be due to a link between the flaring activity and the reactivation of the internal engine and will be discussed in section 2.4.

Chapter 3

The intrinsic afterglow luminosities of long GRBs

3.1 Pre-*Swift* results

During the first years after the discovery of the first GRB afterglow (Van Paradijs et al. 1997), the afterglows of different bursts were usually studied was through the comparison of their light–curves in the observer's reference frame, in terms of their fluxes vs. the observed time $t_{\rm obs}$. With the increasing number of known redshifts it has been possible possible to analyse directly the properties of the GRB afterglows in the progenitor rest frame. The easiest way to carry out this analysis is to compare the luminosity light curves of of different bursts, using the rest-frame time $t_{\rm RF} = t_{\rm obs}/(1+z)$. The first attempts in this direction were the studies by Kumar & Piran 2000 and Gendre & Boër 2005, hereafter GB05. These analysis were mainly focused on the X–ray luminosities of a relatively small sample of GRBs with available redshift determination and X–ray observations. However, in these analysis, the intrinsic luminosities in the optical bands were not onsidered. From these earlier studies it appeared that the X-ray afterglow luminosities (calculated at the same rest frame time) were characterised by a dispersion smaller than the dispersion of the total energies radiated during the prompt emission (but see Berger et al. 2003, for a different conclusion). In addition, Boër & Gendre (2000) and GB05 found that the X-ray afterglow luminosities showed a tendency to cluster in two groups (that differ for a factor ~ 30 in luminosity) with a small dispersion within each group (See fig 3.1).

These authors also tried to extend their studies to the optical luminosities. However, the limited size of the sample and the almost unknown optical absorption prevented them to draw any firm conclusion.

These earlier results prompted us to study the behaviour of the optical afterglow luminosities. One of our main motivations was the possibility that what seems to

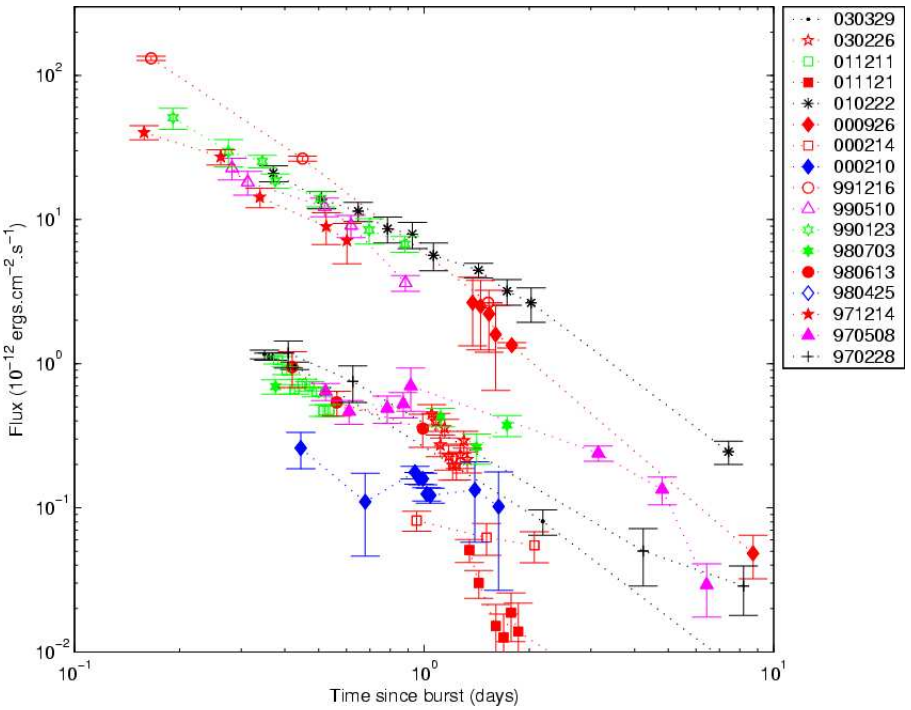

Figure 3.1: X–ray flux light curves of a sample of 17 pre-*Swift* long GRBs re scaled at a common redshift $z = 1$ (Gendre & Boër 2005).

be a "dichotomy" in the X-ray afterglow luminosity distribution could also be present in the optical if the optical and X–ray afterglow emission are due to the same emission process. Such an optical luminosity dichotomy, if discovered, could shed light on the still unexplained nature of the so called "dark GRBs" [1].

De Pasquale et al. (2003), when comparing GRBs (all with detected X-ray afterglow) with and without optical detection, found that "dark" GRBs tend to be fainter in the X-rays, by a factor ~ 5 in flux at the same observed time. In the standard external shock afterglow scenario, we expect a dispersion of the optical luminosities (at a given rest-frame time) even greater than the corresponding dispersion of the X-ray luminosities. This is because electrons emitting X-rays through the synchrotron process cool on a dynamical timescale (sometimes several hours after trigger), and this implies (in the standard synchrotron fireball model) that the emitted X-ray emission is insensitive to the density of the external medium responsible for the external shocks. On the contrary, it is likely that electrons emitting in the optical do not cool in a dynamical timescale (about a day after the prompt phase), so the optical emission does depend on the density of the

[1] In this analysis we follow the definition in which the dark GRBs are GRBs with detected X–ray afterglow for which no optical detection has been obtained even if they have been observed

circumburst material. If the dispersion introduced by this effect is not too large, some sort of "dichotomy" could survive and then flag the existence of two families of GRBs with two different average afterglow luminosities. Dark GRBs could then be thought to belong to the optically underluminous family, and as a consequence, more difficult to be detected in optical (see §1.2.6 for a more complete discussion about this issue).

The following results concern the sample of bursts detected before the launch of *Swift* (so called pre-*Swift* sample hereafter) and they have been published in Nardini et al. (2006).

3.1.1 GRB sample selection

To compare the rest frame optical luminosities of different GRBs, we applied all the relevant cosmological and extinction corrections to the GRB light curves. In particular, one of our selection criteria is that there is a published estimate of the host galaxy dust absorption $A_{\rm V}^{\rm host}$.

We collected from the literature all GRBs with the following information available:

- known spectroscopic redshift z
- detected optical afterglow
- known optical spectral index $\beta_{\rm o}$
- known optical extinction in the host rest frame $A_{\rm V}^{\rm host}$

As of November 24th, 2005 (the *Swift* satellite launch date) the total number of GRBs with measured redshifts is more than 40. 24 of these fulfil our selection criteria. They are listed in Table 3.1. This table includes 13 out of the 17 GRBs present in the list of X–ray afterglows analysed by Gendre & Böer (2005). The 4 missing GRBs are: GRB 970228 (for which there is no estimate of $A_{\rm V}^{\rm host}$), GRB 000210 and GRB 000214 (with no detected optical afterglow), and GRB 980425 (an anomalous GRB associated with the 1998bw supernova).

We collected all the photometric data available both in the literature and in the GRB Coordinates Network (GCN)[2]. Since in the pre-*Swift* epoch the large majority of the optical observations were performed using the $R_{\rm C}$ filter, we used the central frequency of such a filter as a reference for our studies. The observed magnitudes have been corrected for the effect of dust absorption along the line of sight inside our own Galaxy. We corrected the observed optical magnitudes using the on line Galactic extinction calculator (i.e.. `http://nedwww.ipac.caltech.edu/forms/calculator.html`). This calculator exploits the extinction maps obtained by Schlegel (1998).

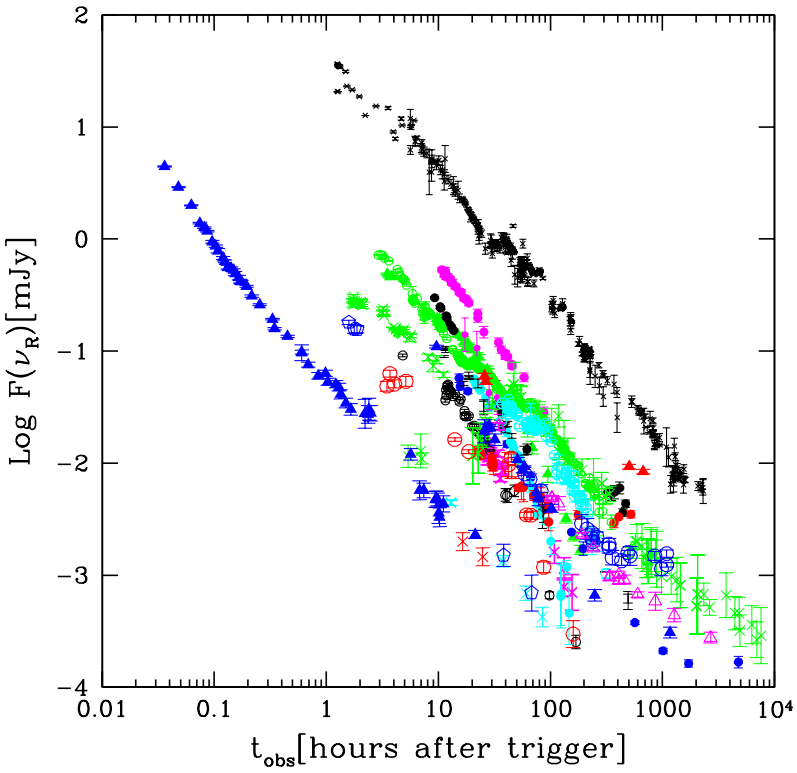

Figure 3.2: Light curves in terms of observed fluxes versus observed time since the burst trigger for the 24 GRBs reported in Table 3.1. Fluxes have been corrected only for galactic extinction. Different colours and symbols correspond to different GRBs. The references for all the plotted data can be found in appendix 10.1.

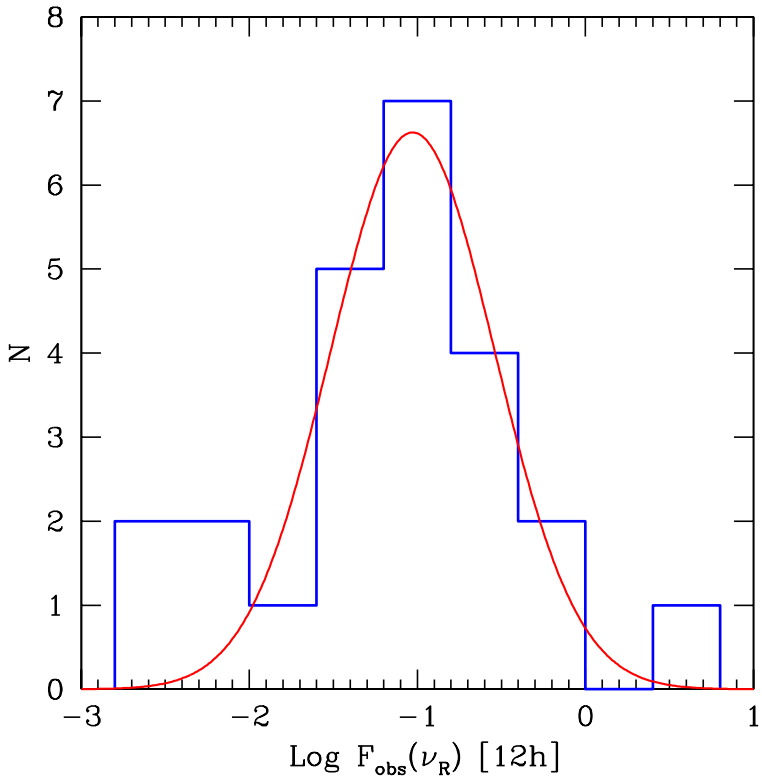

Figure 3.3: Histogram of the observed fluxes (in mJy) in the R–band (Cousin system) 12 hours after the trigger (observer frame). All fluxes have been corrected for the foreground galactic extinction only. Superimposed to the histogram is a Gaussian fit to the data with mean value $\mu = -1.03$ and dispersion $\sigma = 0.48$.

Figure 3.2 shows the behaviour of the observed R-band fluxes as a function of the observed time $t_{\rm obs}$ for all bursts in our sample. In this figure the fluxes are corrected for the Galactic extinction only. In the pre–*Swift* era, the optical observations usually started a few hours after the gamma ray trigger and show a similar typical power-law like behaviour. The observed fluxes at a given time are quite different from one burst to another spanning more than 3 orders of magnitude. In Fig. 3.3 we show the distribution of the observed fluxes at the same observed time. We selected 12 h after the trigger in order to maximise the available data and to avoid long extrapolations. Fitting the distribution of the observed optical fluxes at 12 h with a Gaussian gives a (logarithmic) dispersion of σ= 0.48. Note that the Gaussian fit is poor, and the real distribution could have an even larger dispersion.

The monochromatic optical luminosities can be calculated from the observed monochromatic flux $F(\nu, t)$ by applying the k-correction and time corrections, as

$$L(\nu, t) \; = \; \frac{4\pi d_{\rm L}^2 F(\nu, t)}{(1+z)^{1-\beta+\alpha}} \tag{3.1}$$

where we assumed $F(\nu, t) \propto \nu^{-\beta} t^{-\alpha}$.
We appropriately convert Johnson R magnitudes (λ=6800 Å) into Cousin magnitudes when data in the former filter are given. We have then calculated all monochromatic optical luminosities at the rest frame wavelength of 6400 Å (corresponding to the Cousin R filter central wavelength).

The observed flux $F(\nu_R, t)$ was corrected for both galactic and rest-frame extinction. We calculated the A_λ values for the extinction in the burst's host galaxies evaluated at the wavelength $\lambda = 6400/(1+z)$ Å. A_λ have been calculated assuming the host galaxy extinction curves as described by Pei (1992). For each burst we used the same extinction curve that had been used ifor the $A_{\rm V}^{\rm host}$ estimate (Small Magellanic Cloud like extinction curve for most of them).

There are cases in which different authors find slightly different values for $A_{\rm V}^{\rm host}$ and for $\beta_{\rm o}$, i.e. the de reddened value of the optical spectral index. There is some degeneracy between these two quantities when the available data are poorly sampled and affected by relatively large uncertainties. In most of cases, the method used to find the intrinsic extinction is to assume that the spectrum is a power law, and the fit returns the best values of the spectral index and $A_{\rm V}^{\rm host}$. The two quantities are, however, somewhat correlated, since increasing $A_{\rm V}^{\rm host}$ gives a flatter $\beta_{\rm o}$. A more detailed discussion about the host galaxy dust absorption estimate in the pre-*Swift* era can be found in Kann et al. (2006). In addition, different results can be obtained by using different extinction curves. Therefore, for completeness, we list the different values of $A_{\rm V}^{\rm host}$ and $\beta_{\rm o}$ found by different authors in Table 3.1, and the corresponding value of the optical luminosity. In order to avoid a

[2] `http://gcn.gsfc.nasa.gov/`

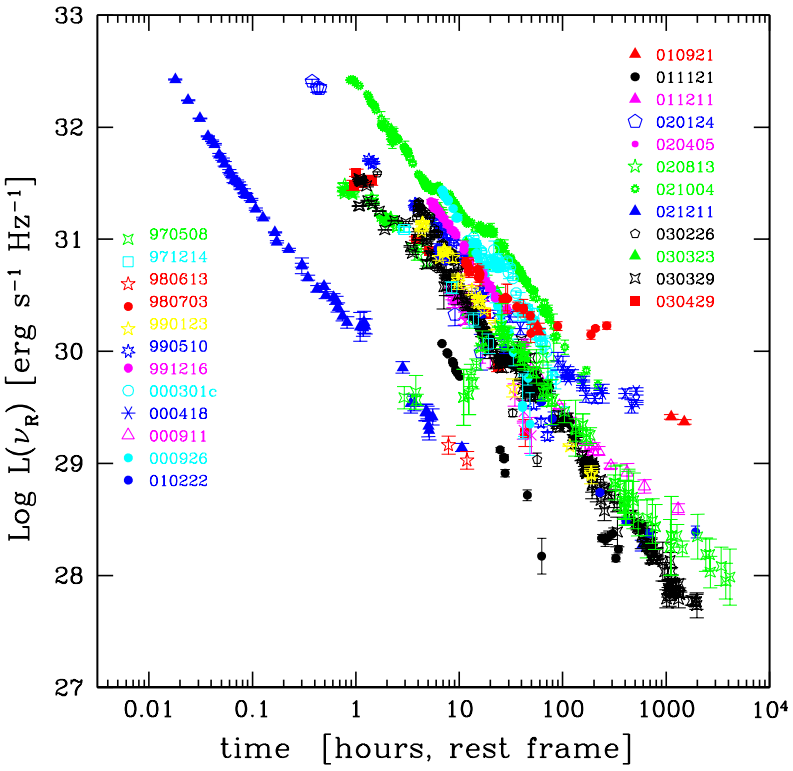

Figure 3.4: Light curves of the optical luminosities L_{ν_R} as a function of the rest frame time. All data have been corrected for extinction (both Galactic and host). The references for the observed magnitudes can be found in the Nardini et al. (2006). The references of the values of the spectral index β_o and the host galaxy absorption can be found in Nardini et al. 2006.

priori assumptions on the relation between optical and X-ray emission based on a particular radiative process model, when multiple choices were available, estimates of A_V^{host} based on the optical data alone were preferred.

3.1.2 Optical luminosities light curves

In Fig. 3.4 we show the light curves in terms of the optical luminosities in the R-band as a function of the rest-frame time. As can be seen, there is a clear clustering of the light curves when corrected for the cosmological and extinction effects with respect to the light curves shown in Fig. 3.2. At a given rest frame time the majority of the the considered bursts but three seem to be characterised by a similar $L_{\nu_R,t}$. The exceptions are GRB 980613, GRB 011121, and GRB 021211,

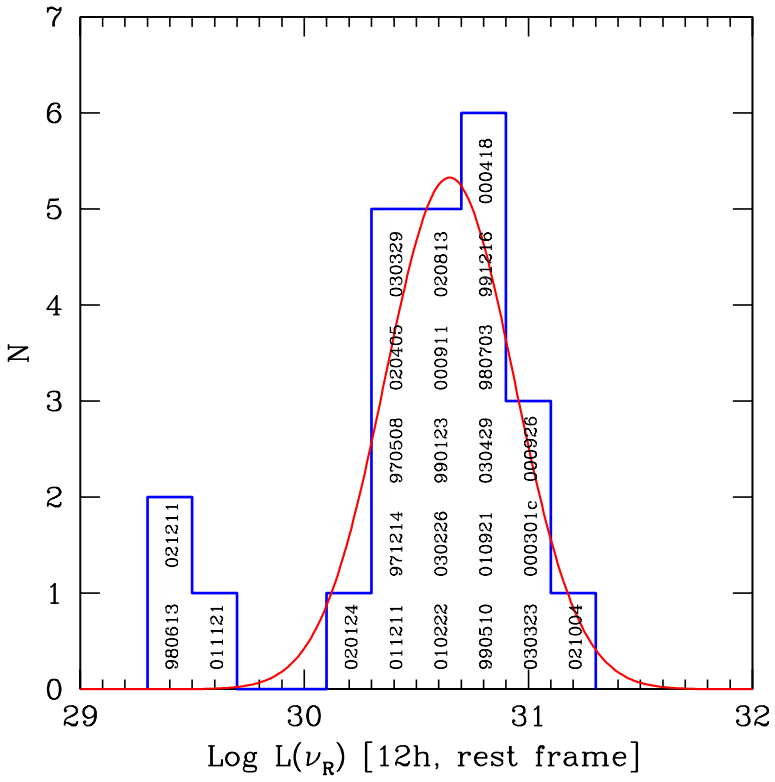

Figure 3.5: Histogram of the monochromatic optical luminosities 12 hours (rest frame) after the trigger for the 24 GRBs reported in Tab. 3.1. Data have been de reddened both for galactic and host extinction. The solid red line represents the Gaussian fit to the data with mean value $\mu = 30.65$ and dispersion $\sigma = 0.28$.

which stand out from the bulk of the other bursts by being underluminous of a factor ∼15.

Some of the light curves shown in fig. 3.4 appear peculiar, in particular:

GRB 970508: the optical light curve of this burst showed an initial brightening followed, approximately at 1 day, by a normal decay. For this reason we calculated L_{ν_R} at 12 h by extrapolating the light curve from the data available starting from ∼30 h (rest frame). The choice of not to extrapolate from later times would make this burst to belong to the "underluminous family" for times earlier than 12 hours.

GRB 020813 and *GRB 030329:* these GRB have an early jet break time (roughly at 4.6 h and 10 h, rest frame, respectively), and we calculate the 12 h luminosity by extrapolating from the light curve before $t_{\rm jet}$. Note that choosing not to extrapolate from earlier times, makes these bursts to fall in the "luminous burst family".

As done for the observed flux distribution, we evaluated the intrinsic luminosities of all the GRBs in our sample at a common rest frame time which we chose to be 12 h. For densely sampled optical light curves, we have directly taken the flux measured at $t_{\rm obs} = 12(1+z)$ h. When this flux was not available, we interpolated between data before and after this time. There are 2 cases (GRB 020813 and GRB 030329) in which a break in the light curve (very likely a jet break) occurs before 12 h (see above). In these cases we have extrapolated the flux from data before the break time.

In Table 3.1 we report, for every GRB in our sample, the redshift, the optical spectral index $\beta_{\rm o}$, the Galactic absorption $A_{\rm V}^{\rm Gal}$ (taken from Schlegel et al. 1998 except for GRB 011121 for which we also report the values quoted in the corresponding references), the host rest frame absorption $A_{\rm V}^{\rm host}$, the absorption $A_{R(1+z)}^{\rm host}$ at the rest-frame frequency $\nu_{R(1+z)}$, the extinction and k-corrected monochromatic luminosity $L_{\nu_R}^{\rm 12h}$ (at the source frame frequency corresponding to the R band) and the references of the optical spectral index and extinction value.

Fig. 3.5 shows the $L_{\nu_R}^{\rm 12h}$ distribution of our bursts. The 24 GRBs separate into two groups: the bulk of GRBs (21 objects) with a 12 h rest frame luminosity distribution spanning less than one order of magnitude, and a second group (3 objects) that appears underluminous by a factor ∼15. The first distribution can be well represented by a Gaussian with an average luminosity $\langle \log L_{\nu_R}^{\rm 12h} \rangle = 30.65 {\rm erg Hz^{-1} s^{-1}}$ and a dispersion $\sigma = 0.28$. The typical error on $\log L_{\nu_R}^{\rm 12h}$ is around 0.1, much less than the 1σ dispersion of the distribution of this quantity. This error has been estimated by propagating the average error on the observed magnitude (0.1), $A_{\rm V}^{\rm host}$ (0.13) and $\beta_{\rm o}$ (0.1). At the time of publishing our results (Nardini et al. 2006), two other groups were working on similar topics. Liang & Zhang (2006) confirmed both the clustering and the bimodality of the optical luminosity light curves with a slightly different sample of long GRBs (they did

not require the knowledge of the host galaxy dust absorption) and Kann et al. (2006) confirmed our results while analysing the rest frame reddening of a large sample of pre-*Swift* long GRB afterglows. Boër & Gendre (2000) have analysed the optical behaviour of 8 pre–*Swift* bursts without applying the de reddening of the extinction of the host (at that time largely unavailable). They did not find any clustering, nor a dichotomy, although (even without correcting for the absorption of the host), they noted that the distribution of the intrinsic optical luminosities was narrower than the distribution of the observed fluxes. The choice of 12 h rest frame is not critical for our results, as can be seen in the left panel of Fig. 3.4, as long as the chosen time is less than the jet break time for most bursts.

The three underluminous bursts, (i.e. GRB 980613, 011121, 021211) that seem to form a separate "family" are more than 4σ dimmer than the majority of bursts. For GRB 011121 and GRB 021211 the two parameters $\beta_{\rm o}$ and $A_{\rm V}^{\rm host}$ have possible different estimates (see Table 3.1). Here we adopted the values reported in the first line of Table 3.1. However, if we consider the other possible choices, the implied $L_{\nu_R}^{\rm 12h}$ would be even smaller, making these two bursts even more inconsistent (more than 4.5σ) with the distribution of the bulk of GRBs. Instead, considering the GRBs with different estimates of $\beta_{\rm o}$ and $A_{\rm V}^{\rm host}$ that fall in the more populated group, the use of the other choices for these parameters would shift their luminosities by less than one σ (except for GRB 980703, for which the shift would be 1.7σ). The three underluminous bursts do not seem to have any distinguishing property for what concerns the optical afterglow other than their smaller optical luminosities: all three have "normal" optical decays, spectral indices and extinction values.

3.1.3 Comparison with other bands

Comparison with the prompt γ ray energetics

Both the clustering of the brighter events luminosities and the hint of bimodality are unexpected in the frame of the "standard" external shock afterglow scenario. In order to better understand the nature of these findings we compared the results we obtained in the optical bands with what can be observed at higher frequencies. First of all we tried to compare the intrinsic optical luminosities with the total energy emitted in gamma rays during the prompt phase $E_{\gamma,\rm iso}$. The latter distribution does not show any evidence either of bimodality or clustering around a typical value. The $E_{\gamma,\rm iso}$ distribution for the bursts in our sample, when fitted with a lognormal function has a much larger dispersion than the $L_{\nu_R}^{\rm 12h}$ one ($\sigma = 0.80$). The upper panel of Fig. 3.6 clearly shows that there is no correlation between $E_{\gamma,\rm iso}$ and $L_{\nu_R}^{\rm 12h}$.

GRB	z	$\beta_{\rm o}$	$A_R^{\rm Gal}$	$A_V^{\rm host}$	$A_{R(1+z)}^{\rm host}$	$\log L_{\nu_R}^{\rm 12h}$
970508	0.835	1	0.13	0	0	30.42
971214	3.418	1.03±0.18	0.04	0.38±0.08	0.99	30.39
980613	1.0964	0.59±0.03	0.23		0.45	29.31
980703	0.966	1.01± 0.01	0.15	1.51±0.11	2.50	30.82
		0.78	0.15	0.90±0.20	1.48	30.34
990123	1.6	0.750± 0.068	0.04	0	0	30.62
990510	1.619	0.49±0.1	0.54	0	0	30.73
		0.55± 0.1	0.48			30.75
991216	1.02	0.58±0.08	1.67	0	0	30.89
000301c	2.0670	0.70±0.09	0.13	0.09±0.04	0.26	30.99
000418	1.1181	0.81	0.08	0.96±0.20	1.69	30.71
000911	1.06	1.3	0.30	0.39	0.69	30.66
000926	2.0375	1.0±0.2	0.06	0.18±0.06	0.53	31.06
010222	1.477	1.07±0.09	0.06	0	0	30.52
		0.89± 0.03		0	0	30.45
		0.5		0.19	0.42	30.46
010921	0.45	p=3.03	0.396	1.16±0.07	1.43	30.77
011121	0.36	0.62± 0.05	1.32	0	0	29.65
		0.76± 0.15	0.97	0	0	29.58
		0.66± 0.13	1.12	0	0	29.53
011211	2.14	0.56± 0.19	0.11	0.08±0.08	0.23	30.36
		0.61± 0.15		0.06	0.177	30.29
020124	3.198	1.32± 0.25	0.14	0	0	30.22
		0.31± 0.43		2.66± 0.16	0.73	29.81
		0.91± 0.14		0	0	30.00
020405	0.69	1.45	0.15	0	0	30.44
020813	1.25	0.85±0.07	0.30	0.12± 004	0.226	30.57
021004	2.3351	0.60± 0.02	0.16	0.15	0.39	31.17
021211	1.004	0.55±0.10	0.07		0.48	29.41
		0.69± 0.14		0	0	29.27
030323	3.3718	0.89±0.04	0.13	0	0	30.92
030226	1.986	0.55	0.05	0.52	0.98	30.59
		0.70±0.03		0	0	30.27
030329	0.1685	0.5	0.07	0.30±0.03	0.29	30.45
		0.8± 0.2		0.12	0.12	30.40
030429	2.66	0.36±0.12	0.165	0.34±0.04	0.99	30.78

Table 3.1: Sample of GRBs with measured redshift z and estimated host extinction $A_V^{\rm host}$. The optical spectral index $\beta_{\rm o}$ and the Galactic R–band extinction $A_R^{\rm Gal}$ are reported. $A_{R(1+z)}^{\rm host}$ represents the host rest frame R–band extinction and $\log L_{\nu_R}^{\rm 12h}$ in units of ergHz^{-1}cm^{-2} is the rest frame R–band luminosity calculated at 12 h (rest frame) according to Eq. 1. References are given for $\beta_{\rm o}$,$A_R^{\rm Gal}$, $A_V^{\rm host}$ and $A_{R(1+z)}^{\rm host}$. References can be found in Nardini et al. (2006).

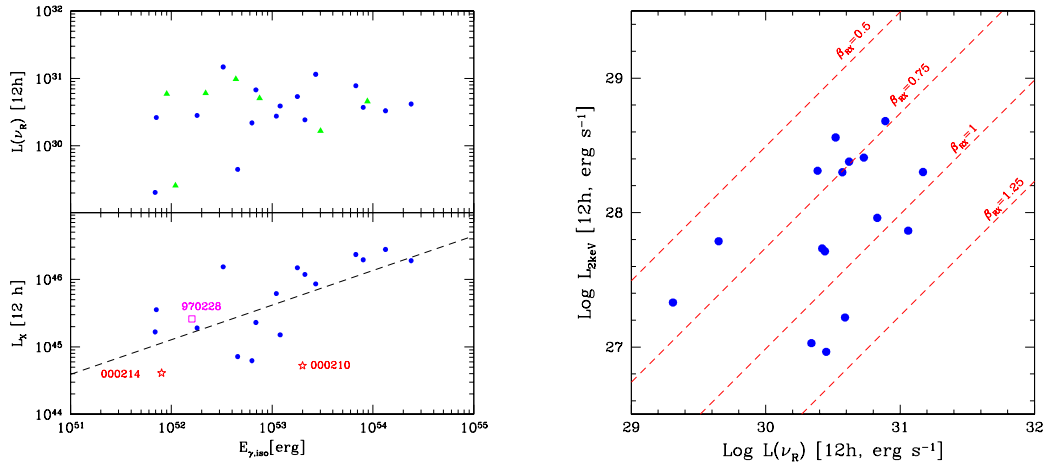

Figure 3.6: **Left**: Optical monochromatic luminosity (top panel) and X–ray [4–20 keV] luminosities (lower panel) at 12 hours after trigger (rest frame time) as a function of the isotropic emitted energy during the prompt phase (integrated between 1 keV and 10 MeV, see Ghirlanda, Ghisellini & Lazzati 2004). Circles corresponds to bursts having both optical and X–ray data. Triangles are GRBs with optical but no X–ray data. Stars are the two GRBs (as labelled) with X–rays but no optical data. We also show GRB 970228, for which there is no information on the amount of extinction in the host (square). The dashed line is the linear regression fit ($\log L_{\rm X} \propto 0.51 \log E_{\gamma,{\rm iso}}$), which has a chance probability $P = 3 \times 10^{-3}$. **Right**: X–ray monochromatic [2 keV, rest frame] luminosity as a function of the optical monochromatic [R band, rest frame] luminosity at 12 hours after trigger. The dashed lines correspond to different broad band spectral indices β_{RX} as labelled.

Comparison with X–ray afterglow luminosities

In their analysis of the X-ray afterglow light curves, Gendre & Boër (2005) found that the distribution of the rest frame $[4-20]$ keV X–ray luminosities is bimodal, clustering around two typical values. We expanded their original long GRBs sample by including three more GRBs: GRB 020405, GRB 020813, GRB 021004. We used some different values of the parameters presented in their original table, as new information became available after the publication of their work. For this reason we have collected the information about the X-ray data in Table 3.1.3, with the appropriate references. We find a more continuous distribution than that of Gendre & Boër (2005), as can be seen in Fig. 3.7, without a clear clustering or a clear separation in two GRB "families". Even if the statistics is small, it is clear from Fig. 3.7 that the distribution of X–ray luminosities is wider than the distribution of the optical luminosities. A Gaussian fit (although poor) gives a

Table 3.2: X–ray properties of the GRBs with known redshift and data collected from the literature. α and β_X are the temporal and spectral power law indices, respectively [i.e. $F(\nu,t) \propto t^{-\alpha}\nu^{-\beta_X}$]. F_X is the observed X–ray flux integrated in the reported energy band and $L^{12h}_{10\mathrm{keV}}$ is the monochromatic X–ray luminosity at 12 h (rest frame) calculated at 10 keV.

GRB	z	α	β_X	F_X 10^{-12} cgs	$t_{\rm obs}$	band keV	$\log L^{12h}_{10\ \rm keV}$
970228	0.695[1]	1.3± 0.1	1.1± 0.3	1.0± 0.2	1d	2–10	26.81
970508	0.835	1.1± 0.1[a]	1.1± 0.3	1.0± 0.4	1d	2–10	26.97
971214	3.418	1.1±0.1	1.2±0.4	0.23±0.05	1d	2–10	27.47
980613	1.096	1.1± 0.2	1	0.27± 0.07	1d	2–10	26.63
980703	0.966	0.9± 0.2	1.8± 0.4	0.48± 0.07	1d	2–10	26.70
990123	1.60	1.35	0.99± 0.07	5.3± 0.2	11h	1.6–10	27.69
		1.44± 0.11	1.00± 0.05	1.8± 0.4	1d	2–10	27.72
990510	1.619	1.4± 0.1	1.2± 0.2	1.2± 0.2	1d	2–10	27.57
991216	1.02	1.6± 0.1	1.2± 0.2	2.58	37h	2–10	27.77
		1.6± 0.1	0.8± 0.5	5.6± 0.3	1d	2–10	27.89
000210	0.846[2]	1.38± 0.03	0.95± 0.15	0.4± 0.06	11h	2–10	26.13
		1.38± 0.03	0.9± 0.2	0.21± 0.06	1d	2–10	26.32
000214	0.42[3]	0.8± 0.5[b]	1.2± 0.3	0.77± 0.08	15h	2–10	26.01
		0.7± 0.3	1.2± 0.5	0.6± 0.2	1d	2–10	26.05
000926	2.066	1.7± 0.5	0.7± 0.2	0.12± 0.1	2.78d	2–10	27.35
010222	1.477	1.33± 0.04	1.01± 0.06	2.7± 0.6	1d	2–10	27.85
011121	0.36	4^{+3}_{-2}	2.4± 0.4	0.6± 0.2	1d	2–10	26.11
011211	2.14	1.3± 0.1	1.2± 0.1	0.03± 0.01	1d	2–10	26.19
020405	0.69	1.9± 1.1	0.72± 0.21	1.36± 0.25	1.71d	0.2–10	27.21
020813	1.25	1.38± 0.06	0.85± 0.04	2.2	1.33d	0.6–6	27.70
021004	2.33	0.9± 0.1	1.01± 0.08	0.63	1.37d	0.6–6	27.60
030226	1.98	2.7± 1.6	0.9± 0.2	0.035± 0.002	1.77d	2–10	26.59
030329	0.168	0.9± 0.3	0.9± 0.2	14.3± 2.9	1d	2–10	26.69

a: 970508 showed a substantial rebrightening, correlated with the optical (Piro et al. 1998). *b*: Antonelli et al. 2000 found $\alpha = 1.41 \pm 0.03$. For GRB 030329 we have calculated the X–ray flux at 12 hours rest frame extrapolating from earlier data, since this GRBs showed a jet break at approximately 10 hours (rest frame time) (see Tiengo et al. 2004). References can be found in Nardini et al. (2006).

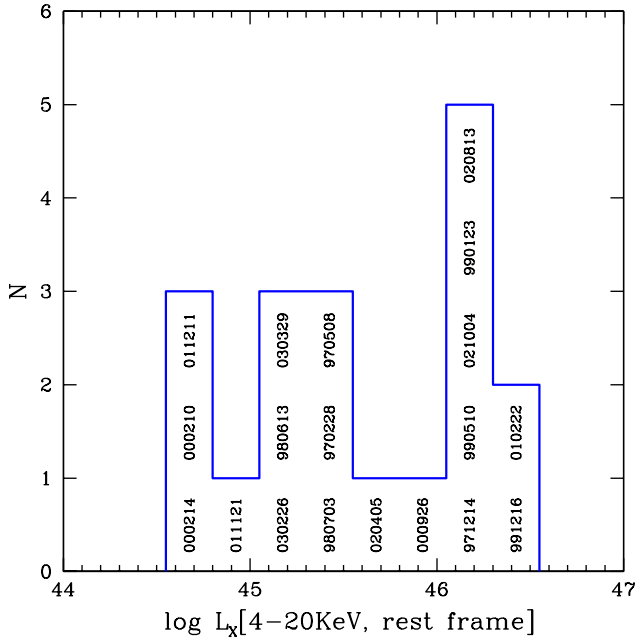

Figure 3.7: Histogram of the X–ray luminosities 12 h (rest frame) after the trigger, calculated in the rest frame band [4 - 20 keV].

dispersion $\sigma = 0.74$.
The right panel of Fig. 3.6 shows the monochromatic [2 keV, rest frame] X-ray luminosity as a function of the optical monochromatic luminosity [R-band] 12 h after trigger, in the rest frame. Dashed diagonal lines correspond to lines of constant broad band spectral indices β_{RX} between the optical (R–band) and the X–ray (2 keV), defined as

$$\beta_{RX} = \frac{\log(L_{\nu_R}/L_X)}{\log(\nu_X/\nu_R)} \tag{3.2}$$

This figure shows that bursts that are more luminous in X–rays tend to have flatter β_{RX} spectral indices (and therefore they are relatively less luminous in the optical) and vice versa. There are two exceptions, both belonging to the dim optical family. This behaviour (flatter β_{RX} for greater L_X) is a necessary condition for having optical luminosities more clustered than the X–ray ones.

Optical to X–rays Spectral Energy Distributions

In the pre-*Swift* era the sampling of the optical and X-ray light–curves was not dense enough to allow a time dependent analysis of the optical to X–ray spectral

energy distributions (SEDs). The quite smooth power law temporal behaviour that characterised the observed optical and X–ray afterglows, and the fact that the richer data samples were available around several hours after the trigger allowed only to interpolate the available luminosities in order to obtain contemporaneous optical to X–rays SEDs at a common rest frame time of 12h after the trigger. In order to compare the SEDs at the same rest frame wavelengths we k-corrected both the optical and X–ray data after having corrected for extinction.
Of the 27 GRBs that we analysed (24 from the optical luminosity sample, 2 with only X–ray data and the peculiar GRB 970228), 17 have both optical and X-rays, 2 have only the X-ray data (GRB 000210 and GRB 000214), and 8 have only the optical data (GRB 000301c, GRB 000418, GRB 000911, GRB 010921, GRB 020124, GRB 021211, GRB 030323, GRB 030429).

In constructing the SED we considered the optical multi band photometry at a time as close as possible to the available X-ray observations. In some cases (i.e. GRB 030226 and GRB 030329), we plotted two SEDs for each burst corresponding to two different observing times or, in the case of GRB 010222, corresponding to two different choices of host galaxy optical extinction. In Fig. 3.8 and Fig. 3.9 we report all the analysed νL_ν SEDs. The references of the data are given in the captions.

Most of the SEDs (11 out of 17 with both optical and X–ray data) seem to be consistent with a broken power law spectral distribution characterised by the presence of a break frequency between the optical and X–ray bands. In the standard synchrotron external shock fireball model this can be ascribed to a common (synchrotron) origin of the optical and X–ray emission by a population of electrons characterized by an energy break (flatter at low energies and steeper at high energies, as expected in the case of incomplete cooling). The quite large uncertainties on the β_o value and the additional uncertainties due to the fluxes extrapolation make the optical and X–ray spectral indices to be consistent with a $\Delta\beta = 0.5$ as predicted if the peak frequency ($\nu_{\rm peak}$) of the νL_ν SED is related to the cooling frequency of the synchrotron emission (see \$ 2.4.1). In two cases the broad band SED can be well described by a single power law connecting the X–ray spectrum with the optical bands. In this case the optical spectral slope is also consistent with β_X. In GRB 021004, the peak frequency $\nu_{\rm peak}$ of the νL_ν SED could be in the IR band, but the overall spectrum is nearly flat in νL_ν. In GRB 020813, $\nu_{\rm peak}$ could lie above the X-ray range.
On the other hand, the remaining 4 GRBs can not be explained in the framework of the simplest synchrotron external shock fireball models. In particular: GRB 000926 shows a steep optical and a flat X-ray spectrum, suggesting that the X-ray flux has a non-synchrotron origin. The same (but less extreme) behavior characterizes the SED of GRB 020405 and the early time SED of GRB 030226. The SED of GRB 010222 is somewhat difficult to classify, since the optical

spectrum could smoothly join the X-ray one if the absorption has been slightly underestimated. Note that GRB 000926 and GRB 010222 are the two bursts lying in between the two groups of X-ray luminosities identified by Gendre & Boër (2005).

3.1.4 Interpretation of the results in the synchrotron external shock fireball model

In order to understand the obtained results, we have to investigate the implications of these two facts: i) for the majority of bursts in our pre-*Swift* sample, $\nu_{\rm peak}$ is between the optical and the X-ray band after a few hours (to a day) from the trigger; ii) the distribution of the optical luminosities is narrower than the distribution of X-ray luminosities.
As previously noted by Panaitescu & Kumar (2000, 2001, 2002) having ν_c between the optical and X–ray bands a day after the trigger implies a relatively small value of ϵ_B (and n). For convenience, we report here Eq. 27 (for homogeneous ISM density) and Eq. 28 (for a r^{-2} wind profile) of Panaitescu & Kumar (2000) for ν_c:

$$\nu_c \,=\, 3.7\times10^{14}E_{53}^{-1/2}n^{-1}(Y+1)^{-2}\epsilon_{B,-2}^{-3/2}t_d^{-1/2} \quad \text{Hz} \tag{3.3}$$

$$\nu_c \,=\, 3.4\times10^{14}E_{53}^{1/2}A_*^{-2}\,(Y+1)^{-2}\,\epsilon_{B,-2}^{-3/2}\,t_d^{1/2} \quad \text{Hz} \tag{3.4}$$

From the above equations, values of ν_c close to 10^{16} Hz require $\epsilon_B \sim 10^{-3}$ or less. The possible dependence of ν_c from the slope of the electron energy distribution is hidden in the $(Y+1)$ term. This term is important if ϵ_B is below some critical value (see discussion in Panaitescu & Kumar 2000).

In order to find the simplest possible reason for the clustering of the optical luminosities, we used again the analytical prescriptions of Panaitescu & Kumar (2000) to construct light curves and spectra at a given time. Fig. 3.10 shows some examples of spectra calculated 12 hours after trigger, assuming for all cases the same kinetic energy ($E = 10^{53}$ erg), the same $\epsilon_B = 10^{-3}$ value, the same $\epsilon_e = 10^{-1}$, and external density ($n = 1$ cm^{-3} for the homogeneous ISM case and $\dot{M} = 3\times10^{-6}M_\odot$ yr^{-1} and $v = 10^3$ km s^{-1} for the wind case). What changes is only the slope of the electron distribution p. As can be seen we indeed obtain in this case that the optical luminosities are distributed in a much narrower range than the X–ray luminosities. This is due to the fact that the cooling frequency changes when changing p as a result of Compton losses being important, decreasing for smaller p. Note also that this is true both for the homogeneous and the wind case.
The observed clustering of the optical luminosities would then require that the kinetic (isotropically equivalent) energy is distributed in a narrow range, as are the equipartition parameters. Furthermore, ϵ_B (and/or the density n) should be small, and the Compton Y parameter relatively large.

The fact that the majority of the optical and X–ray SEDs we analysed are consistent with a broken power law as predicted by the standard model induced us to try to find a possible explanation of the clustering of the optical luminosities and of the differences between the optical and X–ray luminosity distributions in the framework of the synchrotron external shock fireball model. In the following chapters I will discuss in more details the theoretical consequences of the broad band optical and X–rays GRB afterglow analysis taking into account also the new results obtained in the *Swift* era.

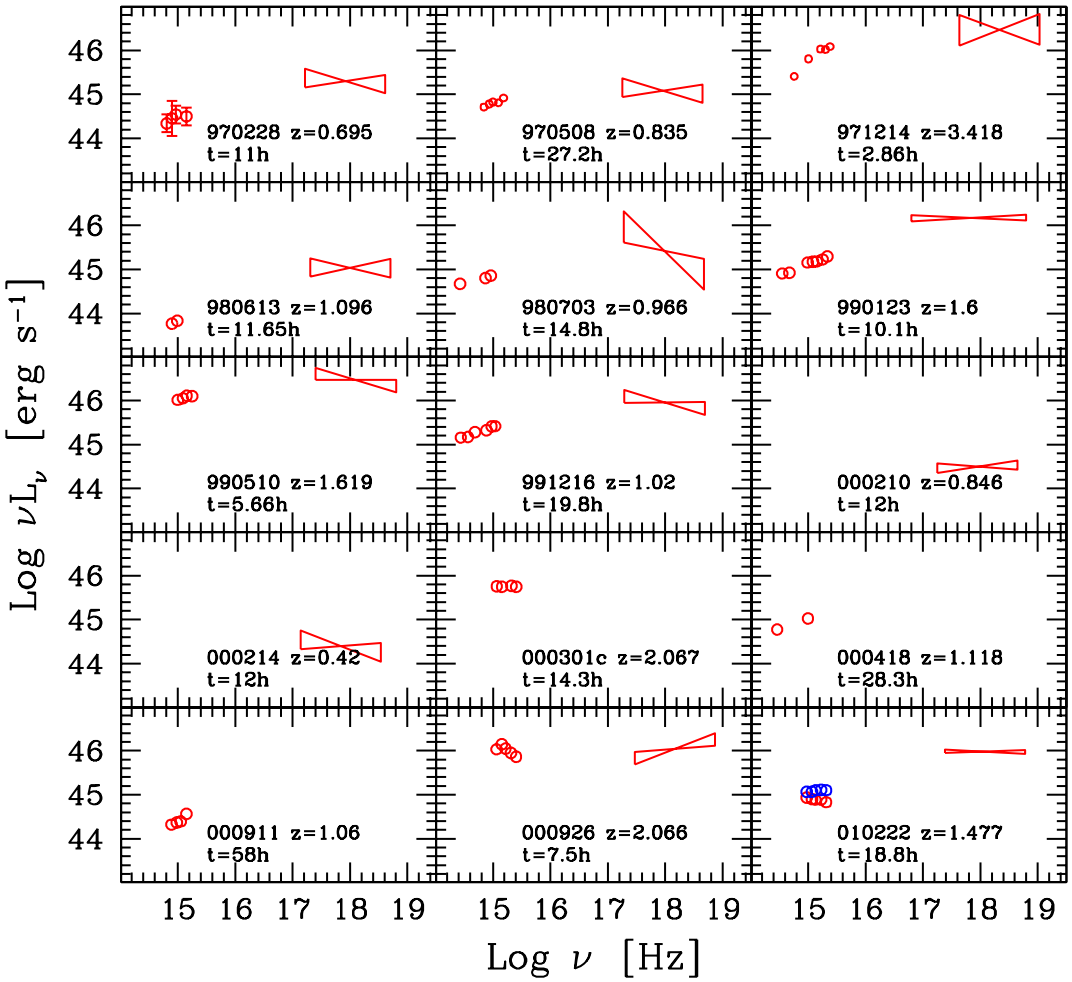

Figure 3.8: Optical to X–ray spectral energy distribution for all GRBs in our pre-*Swift* sample. Data are simultaneous, at the rest frame time labelled in each panel. Sources of data can be found in Nardini et al. (2006).

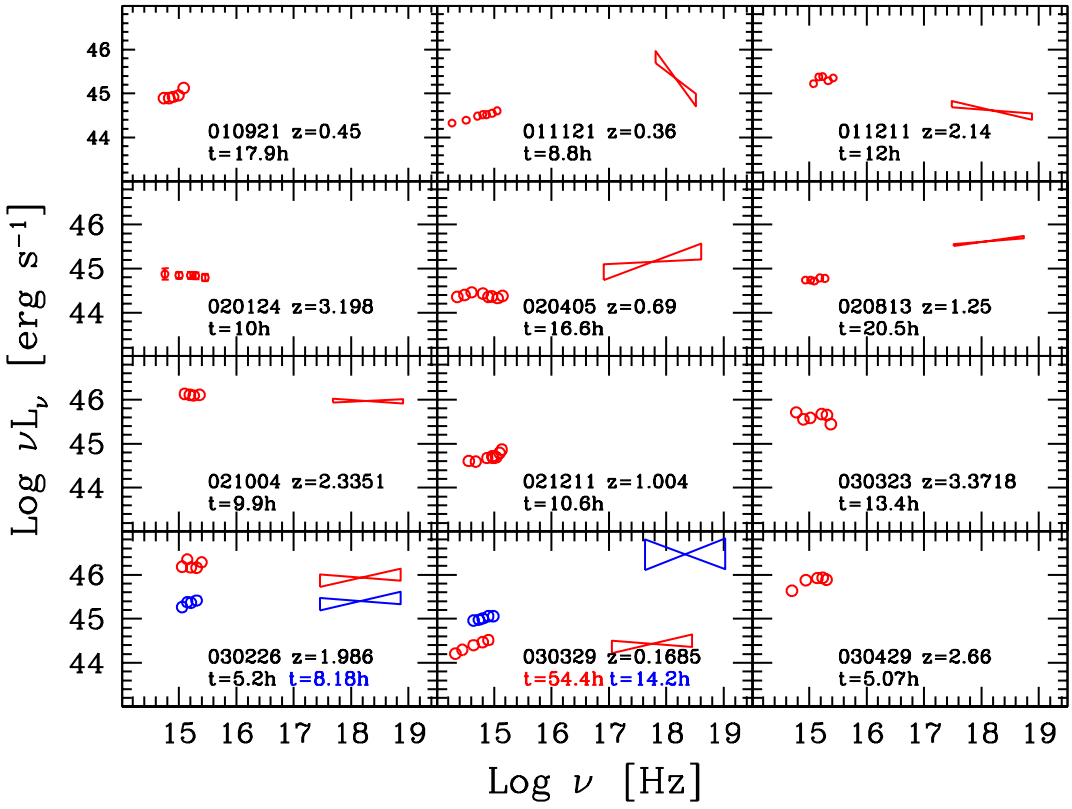

Figure 3.9: Optical to X–ray spectral energy distribution for all GRBs in our sample. Data are simultaneous, at the rest frame time labelled in each panel. Sources of data can be found in 10.1.

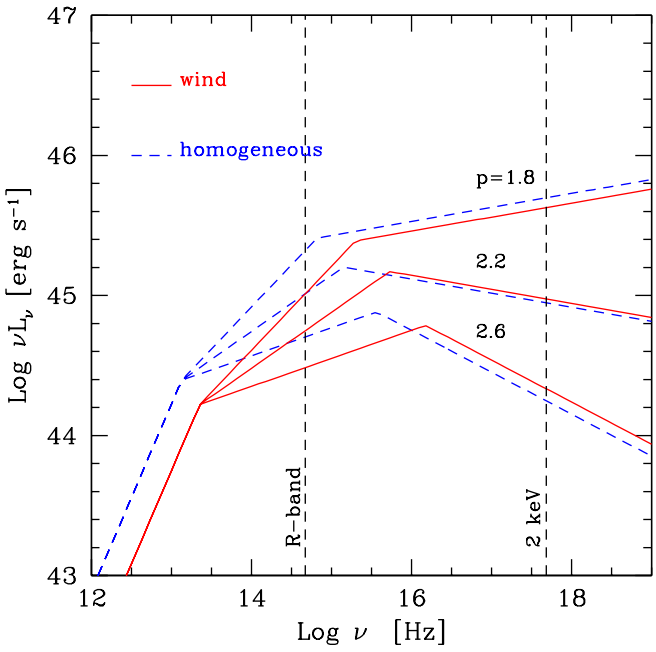

Figure 3.10: Examples of spectra calculated using the prescriptions of Panaitescu & Kumar 2000, at 12 hours after trigger. Dashed lines corresponds to a homogeneous ISM case (with density $n = 1$ cm^{-3}); solid lines to a wind profile of the density (with $\dot{M} = 3 \times 10^{-6} M_{\odot}$ yr^{-1} and wind velocity $v = 10^3$ km s^{-1}. The models differ for the assumed values of p (as labelled).

3.2 Adding *Swift* bursts

3.2.1 *Swift* era luminosity distribution

As discussed in the introduction, the launch of the *Swift* satellite on November 2004 marked a remarkable improvement of the instrumental capabilities in observing the X-rays and optical GRB afterglows. The fast and precise localisation made possible by the presence of XRT on board of *Swift*, increased the number of burst for which a precise measure of the redshift have been obtained. Since the launch of *Swift* up to June 2009 (4.5 years), a redshift have been measured for about 135 GRBs. This number, when compared with the 40 GRB redshifts measured in the 8 years between the first redshift measurement and the *Swift* launch, shows the important step that has been made in the available statistics.

The fast development of the observational capabilities described before, together with the much larger sample of GRBs with known redshift, prompted us to test whether the clustering of the GRB optical luminosities is confirmed by the *Swift* bursts. Melandri et al. (2008), Ceko et al. (2009) and Oates et al. (2009) analysed some samples of *Swift* era GRBs observed with single telescopes (Liverpool and Faulkes Telescopes, Palomar 60 inch telescope, *Swift* UVOT respectively) without requiring the correction for the host galaxy dust absorption and found no evidence for clustering or bimodality of the optical luminosity distribution. Their results are not directly comparable with ours because of the different selection criteria, the missing $A_{\rm V}^{\rm host}$ correction, and the different considered times after the trigger. Because of these differences the absence of clustering and bimodality in their analysis is not in contrast with our findings. We therefore decided to carry an analysis using the same selection criteria as in the Nardini et al. (2006) paper.

We selected all the GRBs with known redshift, published optical spectral index $\beta_{\rm o}$ and host galaxy dust absorption $A_V^{\rm host}$, and well sampled optical light–curves at some hours-days after the trigger (corresponding to a rest frame time of about 12 h). The latter condition is much more restrictive than what expected. Since the *Swift* launch, a big effort has been made in order to obtain a fast optical follow up in the first hours after the trigger in order to study the complex early time afterglow evolution. On the other hand the high GRB detection rate (one every few days or more) and the large amount of observing time spent for the early afterglow observations, made the late times (1-3 days after the trigger) follow up less intense.

In this section I will present the results published in Nardini et al. (2008b). Some bursts fulfilling our selection criteria have been observed after the publication of that paper. In this section these events have been added to the sample. The latter update have been published as a proceeding (Nardini et al. 2009a).

Between the launch of the *Swift* satellite and the end of March 2008 there are

110 detected long GRBs with a reliable redshift determination (absorption redshift, Lyα dropout or widely accepted hosts galaxy redshift). Among them we found a sub sample of 33 GRBs fulfilling all our selection criteria (golden sample) and 20 without a published $A_{\rm V}^{\rm host}$ value but with a late times optical follow up rich enough to give an estimate of the intrinsic luminosity L_{ν_R}. As done for the pre-*Swift* GRB sample we corrected the observed fluxes both for the Galactic and host galaxy dust absorption exploiting the same extinction curves used by the reference authors to calculate $A_{\rm V}^{\rm host}$ (most of the times a Small Magellanic Cloud like extinction curve as discussed by Kann et al. 2006, 2009). Since in the *Swift* epoch XRT observed the X–ray afterglow for almost all the GRBs several groups used contemporaneous UVOT and XRT data in order to evaluate the $A_{\rm V}^{\rm host}$ value from a combined fit of the UVOT and XRT observations assuming that the intrinsic unabsorbed broad band optical to X–ray SED is described either by a single or by a broken power law model with $\Delta\beta = 0.5$ (as predicted in case of synchrotron spectrum with a cooling frequency between the considered bands e.g. Schady et al. 2007). Since in our work we do not want to assume any specific emission mechanism, for GRBs with different $A_{\rm V}^{\rm host}$ estimates in literature we have chosen the $A_{\rm V}^{\rm host}$ values obtained by considering only the optical bands. For a more detailed discussion about this issue see §8.
Even if in the *Swift* sample a richer multi band optical photometry is available, we still used the Cousin R filter in order to compare the results with the pre-*Swift* sample ones. When $R_{\rm C}$ band photometry is not available we converted the observed F_{ν_λ} fluxes into rest frame L_{ν_R} using eq. 3.1.

In fig. 3.11 we plot the rest frame luminosity L_{ν_R} light curves of the complete sample of GRBs with published $A_{\rm V}^{\rm host}$ estimate. The coloured symbols represent the *Swift* era sample (as labelled) while the grey dots represent the pre-*Swift* sample already plotted in fig. 3.4. The new sample shows a much denser photometry coverage at early times (i.e. at $t < 1$ h after trigger). These light curves show that at early times the behaviour is different in different bursts. The light curves become more "regular" and similar at later times when it becomes also similar to the optical decay typical of the pre-*Swift* bursts. At early times there is no clear evidence either of the clustering or bimodality observed in the pre-*Swift* sample at later times. A couple of hours (rest frame) after the trigger the light curves start following the typical power law decay observed before *Swift*. At that time (after about a couple of days after the trigger) the coloured curves cluster into two separate families. A brighter group of GRBs is almost superposed to the pre-*Swift* main family while the remaining faintest GRBs have luminosities smaller or equal to the faintest pre-*Swift* events. The only event that at late times falls between the two main families is GRB 080319b, the so called "naked eye" (Racusin et al. 2008) that, after the very bright prompt optical emission, shows a fast decline phase and at several hours after the trigger has a luminosity comparable to the

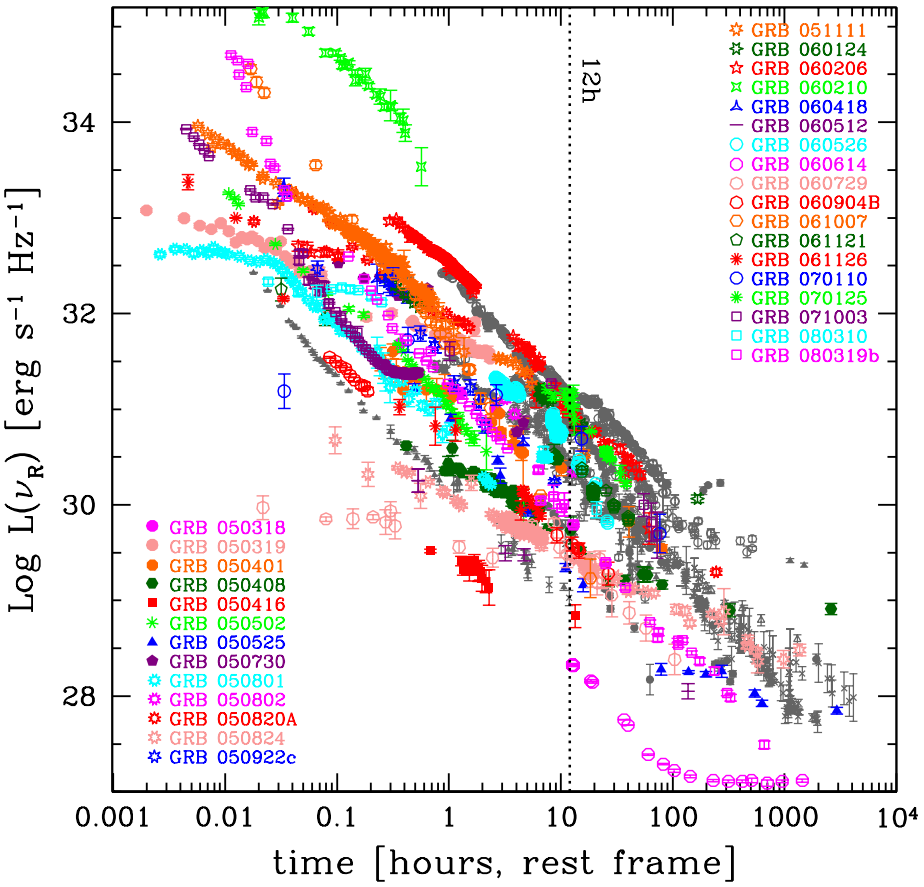

Figure 3.11: Optical monochromatic luminosity log (L_{ν_R}) light curves of long GRBs with a published A_V^{host} estimate. Time is in the rest frame of the source. Grey dots represent the pre-*Swift* sample from Nardini et al. (2006). Coloured points correspond to the *Swift* GRBs, as labelled. The vertical line is at 12 h. References of photometric data can be found in appendix 10.3

ones of the GRBs belonging to the sub–luminous family.

Fig. 3.12 shows the distribution of the luminosities at 12 h for the Swift GRBs superposed to the pre-*Swift* ones. We can see that the *Swift* bursts fully confirm the pre-*Swift* results. Both the clustering of the brighter luminosities and the separation between the luminous and the subluminous families are confirmed. The pre-*Swift* high-luminosity family (Nardini et al. 2006) was well fitted by a lognormal distribution with a mean value of $\log[L_{\nu_R}] = 30.65$ and a dispersion

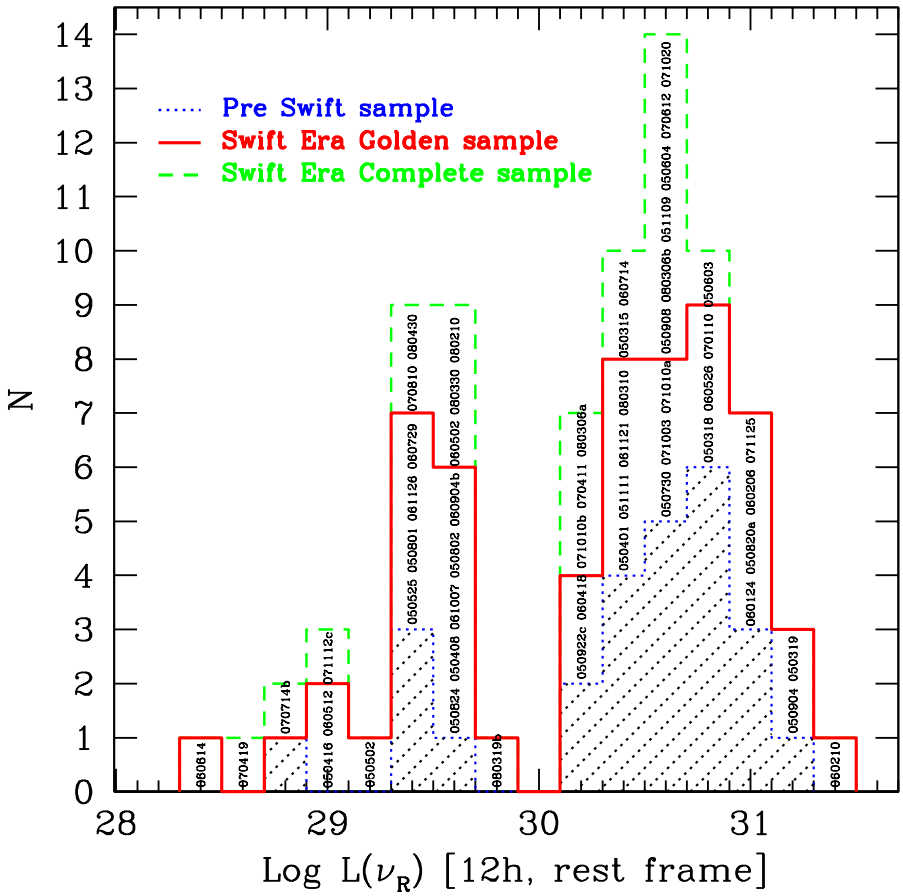

Figure 3.12: Optical luminosity distribution at 12 h rest-frame time. The dashed area shows the pre-*Swift* distribution (Nardini et al. 2006) with the addition of two new GRBs. The continuum red line represents the sum of the pre-Swift bursts and the *Swift* GRBs with published $A_V^{\rm host}$. The dashed green line includes the *Swift* bursts with no published $A_V^{\rm host}$.

$\sigma = 0.28$. The entire sample (*Swift* and pre-*Swift* GRBs) has $\log[L_{\nu_R}] = 30.69$ and $\sigma = 0.29$ (these values become $\log[L_{\nu_R}] = 30.65$ and $\sigma = 0.31$ if we also consider the events without a host extinction estimate). A Kolmogorov-Smirnov (KS) test between the pre-*Swift* and the *Swift* golden sample distributions yields a probability $P \approx 28$ per cent that they come from the same parent population. This probability proves that, from the point of view of the optical luminosities, the pre–*Swift* and the *Swift* era observed GRB populations are very similar despite the

instrumental capabilities evolution occurred after the launch of the *Swift* satellite.

There are several Swift GRBs belonging to the underluminous family and only a single GRB falls into the luminosity gap between the two families. This confirms the existence of a bimodality in the observed optical luminosity distribution. The ratio between the underluminous and the luminous pre-*Swift* GRBs is 5/21 (with the addition of GRB040924 and GRB041006, it was 3/21 in Nardini et al. 2006). For Swift GRBs this ratio becomes closer to unity (i.e. 14/19 for GRBs with known $A_{\rm V}^{\rm host}$ and 20/30 if we include Swift bursts with no published $A_V^{\rm host}$). The improved optical telescopes capabilities (see §4) allowed the detection of a larger number of events with $\log[L_{\nu_R}] < 29.0$ and increased the number of detectable members of the faint family.

As for the pre-*Swift* case Kann et al. (2009) analysed a large sample of *Swift* GRB optical afterglows in order to obtain an estimate of the host galaxy dust absorption from the optical SEDs analysis. Using their $A_{\rm V}^{\rm host}$ estimates confirmed our results showing that the clustering and bimodality in the optical luminosity distribution appear when taking into account all the corrections ($A_{\rm V}^{\rm host}$ and k-correction using the unabsorbed optical spectral index $\beta_{\rm o}$). Therefore no direct comparison is reliable when selecting a sub sample of GRBs when ignoring the effect of the rest frame reddening.

As discussed for the pre-*Swift* sample, there is no clear correlation between the optical and X–ray luminosities. As shown in Fig 3.13, the GRBs belonging to the optically fainter family tend to be characterised by low X–ray luminosities. On the other hand, when we only consider the optically brighter events that cluster around a typical $\log[L_{\nu_R}] = 30.69$ and $\sigma = 0.29$, we can see that their X–ray luminosities spread over a much wider range (between $L_X^{0.3-10keV} = 5 \times 10^{44}$ and $L_X^{0.3-10keV} = 3 \times 10^{47}$ with a dispersion $\sigma = 0.8$). We confirm the results of Gendre, Galli & Boër (2008) that noticed the presence of optically bright events belonging to the X–ray underluminous group.

3.3 Scientific Impact

The clustering of the long GRBs optical luminosities of the majority of events and the bimodality observed in the L_{ν_R} distribution are not easily explainable in the framework of the simplest standard afterglow models and still lack a theoretical interpretation. For this reason, when these results have been confirmed independently by different groups (i.e. Liang & Zhang 2006 and Kann, Klose & Zeh 2006) and when they have been confirmed also in the richer *Swift* era sample (Nardini et al. 2008b, Kann et al. 2009), they triggered the interest of several groups. In the last years several works appeared in order to find possible correlations between the optical luminosity bimodal distribution and other observed features of these GRBs. In this section I will present a brief summary of

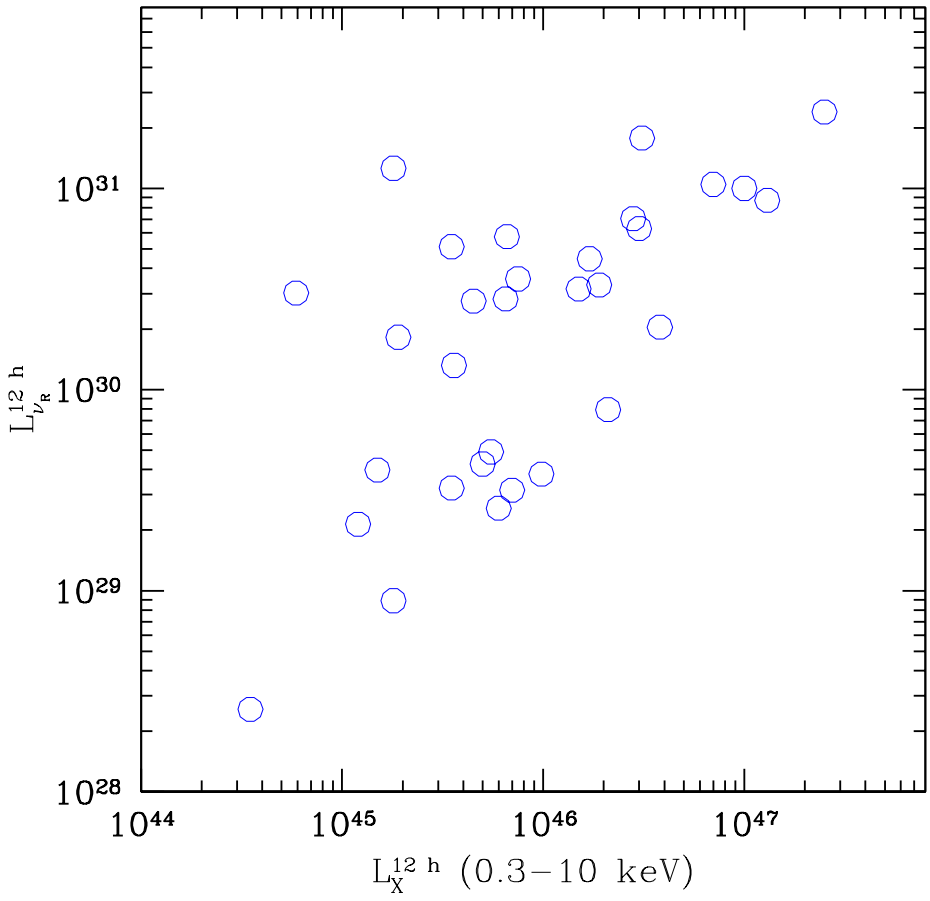

Figure 3.13: Optical luminosities at 12 h rest-frame time versus X–ray luminosities evaluated in the rest frame energy range 0.3-10 keV at 12 h rest frame of the *Swift* GRBs. The optical luminosities are corrected for both Galactic and host galaxy dust absorption and the X–ray luminosities are corrected for Galactic and rest frame $N_{\rm H}$ column densities effects.

the published results.

- Hakkila & Giblin (2006) and Hakkila et al. (2007) analysed the gamma–ray light curve morphology and time lag of a sample of long GRBs and found that optically under luminous events predominantly show single–pulsed gamma ray light–curves. But the number of analysed events was too small to exclude small statistics effects.

- Jakobsson et al. (2008) found a hint of an anti correlation between the

observed optical fluxes and the $N(\mathrm{H_I})$ column densities evaluated by the optical afterglow spectra but there is no such an evidence when comparing the intrinsic rest frame luminosities.

- Borgonovo et al. (2007) studied the temporal properties of the prompt gamma ray emission of a sample of long GRBs with known redshift. They focused in particular on the width of the autocorrelation function (ACF) which has a bimodal distribution in the rest-frame of the source. They tried to test whether this bimodality is somehow correlated with the optical luminosity distribution one. They found that there is "*no correspondence between the ACF bimodality and the bimodality of the afterglow optical luminosity distribution*".

- Porciani, Viel & Lilly (2007) discussed the presence of strong MgII systems in quasars and GRBs. Comparing the number of $\mathrm{Mg_{II}}$ systems with the optical luminosities reported in Nardini et al. (2006), they found that "*the afterglows with more than one Mg_{II} absorbers are, on average, a factor of 1.7 more luminous than the others*". Because of the small statistics the probability that this difference is only due to statistical fluctuation is of the order of 10 per cent. The increased number of well studied GRB afterglows optical spectra with measured $\mathrm{Mg_{II}}$ absorption systems could help in testing this relation.
  On the other hand Sudilovsky et al. (2007) carried a similar test with a sub sample (8 of 14) of the Porciani et al. bursts without finding any significant connection between the afterglow optical luminosities and the number of $\mathrm{Mg_{II}}$ absorption systems.

- Jòhannesson, Björnsson, & Gudmundsson (2008) studied the intrinsic optical luminosity distribution of long GRBs in the framework the standard fireball model. They found good agreement with the observed optical luminosity distribution of the brighter family presented in Nardini et al. (2006) but not with the presence of a separate family of sub luminous event and the inconsistency between the observed optical and X–ray luminosity distributions. They concluded that "*the most likely explanation for this is that the standard fireball model is an incomplete description of the afterglow emission. A more detailed model or possibly an entirely different one is required, where a decoupling of the sources of X–ray and optical radiation is a natural ingredient*".

- Gendre et al. (2008b) analysed the intrinsic infra–red luminosities of a sample of long GRBs. They have shown that both the clustering and the bimodality observed in the optical are confirmed. They also confirmed the differences with the X–ray distribution.

3.4 Summary

- Gendre & Böer (2005) found that the X–ray luminosities of a sample of pre-*Swift* long GRBs tend to cluster in two separate families.

- We studied the de-reddened and k-corrected optical luminosities of a sample of pre-*Swift* long GRBs with known redshift and host galaxy dust absorption. We found that the luminosities at 12 h rest frame after the trigger cluster around a typical value $L_{\nu_R}^{12\mathrm{h}} \approx 30.65$ erg Hz^{-1}s^{-1}. The optical luminosity distribution shows also a hint of bimodality with 3 events having luminosities ~ 30 times smaller than the others.

- The number of events fulfilling our selection criteria strongly increased in after the launch of *Swift*. The GRB optical luminosity distribution, when updated considering the *Swift* GRBs, confirms both the clustering and bimodality observed before. This result appears even more intriguing when considering the different pre-*Swift* and *Swift* GRBs redshift distributions.

- The optical luminosity distribution seems not to be related to what observed in gamma and X–rays.

- The observed bimodality can not be easily explained in the framework of the simplest afterglow emission theoretical models.

Chapter 4

The role of selection effects and the nature of "dark" bursts

In §3 I discussed the results obtained analysing the optical luminosity distribution of the GRBs with known redshift and published estimate of the host galaxy dust absorption. The luminosities of the brighter events seem to cluster around a typical value $\log L_{\nu_R}^{12\mathrm{h}} \approx 30.7$ erg Hz^{-1} s^{-1} with a dispersion $\sigma = 0.3$ while the faintest events seem to belong to a separate underluminous family.

These results opened an interesting discussion about the nature of these findings. Some groups noticed that both the observed clustering and bimodality could be due to observational selection effects (e.g. Porciani et al. 2008, Jòhannesson et al. 2008).

If real, the observed bimodality could have important consequences on the nature of the so called "dark GRB" afterglows, i.e. bursts that are detected in the X–ray band, but not in the optical (See §1.2.6 for a more detailed discussion about this issue). This is true either if the dark GRBs have an intrinsically dim optical afterglow or if the observed optical radiation have been attenuated by a non standard extinction curve (i.e. that can not be identified through the standard analysis of the optical SED curvature). The few underluminous observed events could be the tip of the iceberg of a population of GRBs which are intrinsically less luminous. Therefore, a fraction of dark GRBs could belong to this family whose distance, optical absorption or observing conditions do not allow any optical detection. Because of its potential importance for the understanding of dark bursts, we decided to investigate whether the observed bimodal luminosity distribution of optically bright bursts is due to selection effects (related to the search/detection of GRB optical counterparts) or if it reflects the existence of two GRB populations. The discussion and results reported in this chapter have been presented in two papers published on MNRAS in 2008 (Nardini et al. 2008a & Nardini et al. 2008b). In the first one only the pre-*Swift* GRB sample was considered while in the second the same study has been carried also for the

complete sample discussed in §3.2. In this chapter I will first describe the method we used to test our bimodality as presented in Nardini et al. (2008b) and I will then present the results we obtained discussing also the differences between the pre-*Swift* and *Swift* observational biases.

4.1 The method

The aim of our analysis is test whether the observed optical luminosities clustering and bimodality are due to an intrinsic feature of the optical luminosity function (i.e. there are two separate families of optically bright and optically faint GRBs), to the presence of two different types of host galaxy dust absorption effects (i.e. standard dust reddening and achromatic dust absorption) or are the effect of an observational bias. The fact that some GRBs have much smaller luminosities than the majority of events could in principle be due to a selection effect that prevents to measure optical luminosities in the range between $29.7 < \log L_{\nu_R}^{12h} < 30.2$[erg s^{-1}Hz^{-1}]. In order to test this hypothesis we test whether an intrinsically unimodal luminosity function can generate an observed bimodal luminosity distribution when taking into account all the cosmological and dust absorption effects and accounting for the observing telescopes capabilities.

To this aim we simulate through a Monte Carlo method a sample of GRBs with a redshift distribution traced by the cosmic star formation rate (CSFR, Porciani & Madau 2001), assuming different shapes of their intrinsic optical luminosity function. We also account for different values $A_{\rm V}^{\rm host}$ of dust absorption within the host galaxy for all the simulated events. The corresponding $A_{\nu_R(1+z)}$ value is calculated assuming the standard extinction curves (Pei 1992).

We infer a limiting magnitude distribution obtained by the analysis of the deepest R-band upper limits of all the pre-Swift GRBs with no detection of the optical afterglow. This is the key point of our study: the use of the upper limits on the optical flux to construct the probability that a simulated burst would be detected. It is this probability distribution that allows us to perform, meaningfully, our simulations. We then compare the resulting luminosity distribution of the detectable simulated events with the distribution of the real sample one.
The scope of our simulation is to check if for any conceivable combination of the input assumptions (i.e. luminosity function, extinction and redshift distribution), we can reproduce a simulated sample whose R-band luminosity distribution (12 h rest frame) is consistent with that observed with the observed GRB golden sample.

4.1.1 Optical upper limits of pre-*Swift* dark GRBs

During the pre-*Swift* era, since the first afterglow detection, considered in §3.1, 238 long GRBs have been localized, (within a few hours up to days after the trigger),

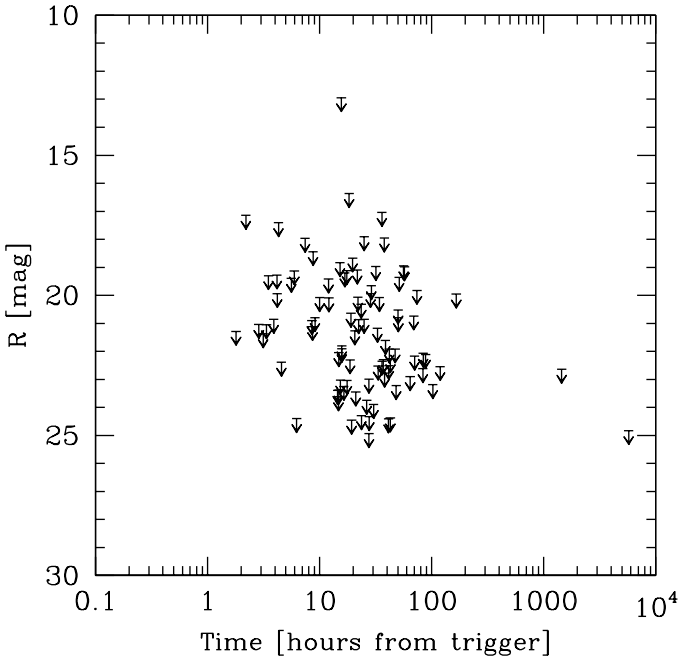

Figure 4.1: Deepest R-band upper limits for all the pre-*Swift* dark bursts. All the data are corrected for the Galactic extinction given in Schlegel et al. (1998). Each upper limit corresponds to a single GRB. For GRBs with several upper limits available in the literature, we report, conservatively, the deepest upper limit evaluated by assuming a standard flux decay light curve (see text). References of photometric data can be found in appendix 10.2

with an accuracy of 1 degree or better. For only 64 of them, an associated optical afterglow was found. For the remaining large fraction the lack of optical data is due to the absence of any optical telescope observation of the source location error box field. We found 111 bursts with at least one optical near-infrared "failed" (i.e. giving only a flux upper limit) observation and among them we consider the 94 GRBs with at least one R-band limiting magnitude.

The non detection of the optical afterglow can in some cases be due to a bad localisation of the gamma-ray source. I these cases the large gamma-ray detector error box should be covered by the optical telescopes. In order to avoid including in our sample events with a large gamma-ray error box uncovered by the optical observation, we discarded the events with an error box larger than 11 arcmin of radius if the R-band observations do not cover at least 80 per cent of the error box area. We found two events which do not satisfy this criterion. Excluding these two events we have:

- 58 events have an error box smaller than 10 arcmin of radius;
- 27 events have the entire error box covered by the observations;
- 4 events have more than 90 per cent of the error box covered;
- three events have more than 80 per cent of the error box covered.

We performed our analysis on these 92 dark GRBs. We often found a large number of R-band upper limits for a single burst obtained at different epochs after the trigger. In these cases, we evaluated the deepest limiting R-band magnitude for each GRB assuming a power law temporal behaviour $F(t) \propto t^{-\alpha}$ with $\alpha = 1$, i.e. the average slope of the detected optical afterglows. Suppose for instance that, for a given burst, there are two upper limits $R > 18$ and 20 at 1 and 24 h after the trigger, respectively. We select $R > 18$ at 1 h as the most stringent, since it corresponds [assuming $F(t) \propto t^{-1}$] to $R > 21.45$ at 24 h.
We corrected the resulting upper limits for the Galactic dust extinction along the line of sight using the absorption maps by Schlegel, Finkbeiner & Davis (1998). For most of the events the amount of Galactic dust absorption is negligible (i.e. smaller than 0.5 magnitudes) but there are some GRBs located close to the Galactic plane that are absorbed by several magnitudes in the R band. For example, along the line of sight of GRB 030501 and GRB 030320, the Galactic dust absorption value A_R (in the R band) is 39 and 20.5 magnitudes, respectively. Such an extinction makes impossible any GRB optical afterglow detection.

In Fig. 4.1, we show the deepest R-band upper limits for all the 92 GRBs of the pre-*Swift* sample, de-reddened for the Milky Way dust absorption[1].

4.1.2 Telescope Selection Function

For the majority of the dark GRBs in our sample, the deepest upper limit is quite constraining. Lazzati et al. (2002), albeit with a smaller sample of bright and dark GRBs, demonstrated that the non–detection of an optical afterglow for most of the optically dark GRBs was not due to adverse observing conditions or delay in performing the observations. They also showed that these events do not have particularly large Galactic absorbing columns. The upper limits we added in our sample are generally deeper than the ones considered by Lazzati et al. (2002), thus confirming their results.

In order to obtain a homogeneous distribution of upper limits, we extrapolated the deepest limiting R-band magnitude for each burst at the common time of 12 h after the burst trigger (observer frame). We again assumed a temporal behaviour of the form $F(t) \propto t^{-\alpha}$ with an index $\alpha = 1$.

[1]The references for the upper limit values are reported in the appendix of Nardini et al. (2008a)

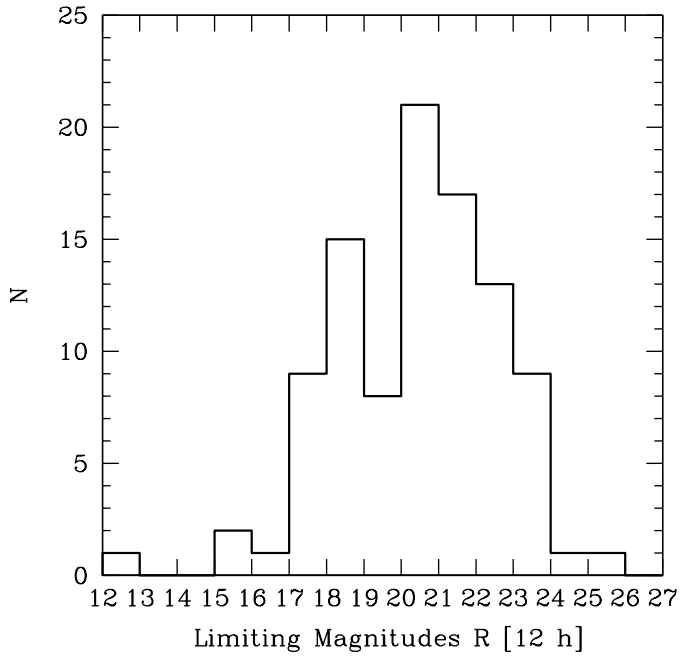

Figure 4.2: Histogram of the deepest R-band pre–*Swift* upper limits (corrected for Galactic extinction) extrapolated at a common time (12 h after the trigger), obtained assuming a temporal behaviour $F(t) \propto t^{-1}$ of the optical afterglow flux. This distribution corresponds to the TSF (see the text).

In Fig. 4.2, we show the distribution of the R-band deepest limiting magnitudes for all the dark GRBs in our pre–*Swift* sample at 12 h after the trigger. These upper limits represent an estimate of the depth at which the afterglow of a dark burst have been searched for. The upper limits we obtained are deeper than the magnitudes of the detected afterglows analysed in §3. This confirms the findings of Lazzati et al. (2002) that proved that the dark GRBs in his sample had not been pointed using telescopes with limiting magnitudes less deep than the optically bright bursts. Thanks to the consistency of the upper limits and the afterglow detections, we can use this distribution to describe the probability distribution for a burst to be observed in the optical with a certain depth. We call this distribution the Telescope Selection Function (**TSF**). We can see in Fig. 4.2 that most of the dark bursts have been observed at 12 h at least down to $R \approx 18$. Sometimes the limiting magnitudes are greater than 24. Only for a small fraction of GRBs, the limiting magnitude is smaller than 15.

4.1.3 The simulated sample

The basic idea of our simulation is to produce, under some assumptions, a population of GRBs which is "subject" to the same TSF that we constructed from the upper limits of dark bursts. The result is a population of observable optical afterglows which can be compared with the real one.

Through this comparison we test the assumptions of the simulated sample:

1. its redshift distribution,
2. the intrinsic luminosity function,
3. the host galaxy extinction.

Redshift distribution

The lack of optical information on the dark GRBs does not allow a direct spectroscopic redshift determination for all but two of them (GRB 000210, Piro et al. 2002; GRB 000214, Antonelli et al. 2000). Assuming that the dark GRBs are related to the same progenitors of the optically detected bursts, we can assume the Cosmic Star Formation Rate (**CSFR**) to represent the redshift distribution of all the GRBs we analyse. Among the three recipes of Porciani & Madau (2001), which differ at redshifts larger than 2, in the following sections we will considered the CSFR#2 (equation 5 in that paper) that has an intermediate high redshift shape. We also run our simulation using the other two CSFR obtaining final results that are in agreement with the ones reported here. The k–correction has been calculated assuming that the optical–ultraviolet afterglow spectrum is a single power law: $F(\nu) \propto \nu^{-\beta}$. The observed spectral index β is usually in the range $0.5 < \beta < 1.1$. We used a value $\beta = 1$ in our simulation but our results are unchanged if we adopt different values in the range $0.5 < \beta < 1.1$ and choosing a different shape for the CSFR (e.g. equations 4 or 6 in Porciani & Madau 2001).

We also tried to test other possible redshifts distribution and to take into account for the observational bias that affects the measure of redshifts in the range between $1.3 < z < 1.9$. At first sight, one can expect that low luminosity objects can be seen preferentially for low redshifts, and highly luminous ones preferentially at high redshifts. A gap in the redshift distribution (due to our ability to measure it) could then in principle produce a fake bimodal luminosity distribution. We tried to mimic the bias by incorporating it in the assumed redshift distribution. We found that the test of the bimodality is not sensitive to a possible "gap" in the assumed redshift distribution. The explanation we found is the following: the above argument can be applied if the gap in redshift is really wide (say 0.3 - 3.5) in such a way that we do not have enough volume to find rare luminous objects in the 0-0.3 redshift bin, while we miss underluminous sources at $z > 3.5$. Furthermore,

we also require a very steep luminosity function, to make luminous objects very rare. A bias between z=1.3 and 1.9 is not wide enough, and z=1.3 already samples most of the accessible volume.

Optical luminosity function

We assumed three different types of distribution of the intrinsic monochromatic luminosities at 12 h after the trigger in the source frame:

i) a lognormal distribution with as free parameters the mean value μ and the dispersion σ,

ii) a top hat distribution with as free parameters the minimum luminosity and the maximum luminosity.

iiI) a power law distribution with as free parameters the minimum luminosity, the maximum luminosity and the index α assuming $N \propto L(\nu_R)^{\alpha}$,

For each luminosity function, we considered several combinations of their free parameters.

A lognormal luminosity function would imply the existence of a typical value of the GRB optical luminosities with an intrinsic dispersion. A top hat distribution implies that there is no preferred value for the optical luminosity. The power law luminosity would instead better mimic the GRB luminosity functions that have been obtained in the literature analysing the GRB logN-logS (see e.g. Firmani et al. 2004). In Nardini et al. (2006) and in §3.1.3 we have shown that there is no correlation between the optical luminosity at 12 h and the luminosity (or total energy) of the burst, therefore we are not guided, in the choice of the optical luminosity function, by what we already know of the luminosity function of the prompt emission of GRBs .

Host galaxy dust absorption

The association of long GRBs with massive progenitors could imply the presence of a large amount of absorbing dust in the source neighbourhood. On the other hand, the analysis of optical–NIR afterglow (SEDs) showed a relatively small amount of reddening due to dust in the host galaxy. The value of $A_{\rm V}^{\rm host}$ in the source frame is usually of the order of a fraction of a magnitude (Kann, Klose & Zeh 2006; see fig. 3 in Nardini et al. 2006), despite the evidence of high $N_{\rm H}^{\rm host}$ column densities obtained from the X–ray spectral analysis (Stratta et al. 2004; Vreeswijk et al. 2004; Jakobsson et al. 2006).

We take into account the host galaxy dust absorption effects on the observable optical luminosities in our simulation. We test different shapes of the intrinsic $A_{\rm V}^{\rm host}$ distributions. The corresponding $A_R^{\rm host}$ (in the rest frame) has been evaluated

using the analytical extinction curves by Pei (1992). Most of the estimated dust absorption in optical GRB afterglows is well described by extinction curves without an evident 2175 Å feature, so we used a Small Magellanic Cloud like extinction curve. In any case, our results are not affected by this choice.

Role of the observing telescopes

The sample of generated events is then assumed to be observed using optical telescopes with a limiting magnitude distribution traced by the TSF at the common (z = 0) time $t_{\rm obs}$ = 12 h. (Note that the effect of Galactic dust absorption is considered within the TSF definition.) All events with redshift larger than about 5 are not observable in the R band because of the Lyα break, therefore they have been considered as dark. In summary:

i) we assume a redshift distribution function, a luminosity distribution and a host galaxy absorption function;

ii) we pick up at random a redshift z a luminosity $L(\nu_R)$ and a host extinction $A_V^{\rm host}$. With these parameters we compute the R(12h) magnitude of the event at 12h in the observer frame;

iii) we pick up at random within the TSF a limiting magnitude $R_{\rm lim}$(12h) for the telescope that observe this event.

iv) We compare R(12h) with $R_{\rm lim}$(12h) to decide if this event is observed or not. Since we are considering the observed R band, all events with redshift greater than 5 are considered undetectable because of the Lyα absorption.

In order to make a statistically meaningful simulation, we repeat the above procedure 1000 times and build up the luminosity distribution of the "observable" events. This distribution can be finally compared with the observed one. Through the comparison between the simulated "detectable" sample and the really observed one we can assign a probability to our set of assumptions. We then repeat this procedure by changing the starting assumptions (e.g. the luminosity and/or absorption distribution).

4.1.4 Comparison with the observed distribution

The luminosity distribution of the simulated GRBs that are observable using the considered TSF has to be compared with the luminosity distribution of the observed GRB afterglows. Some features of the tested intrinsic luminosity functions have been chosen in order to better reproduce the observed distribution. For example, it is necessary to impose an high-luminosity cut-off to the luminosity function at about $\log\left[L(\nu_R)12h\right] \approx 31.2(\mathrm{erg\ s^{-1}Hz^{-1}})$. A GRB with a greater

luminosity would be easily detectable also with a low limiting magnitude for almost all the redshifts smaller than five (see Fig. 4.3). The absence of any observed GRB with such a luminosity therefore sets a constraint to the luminosity function.

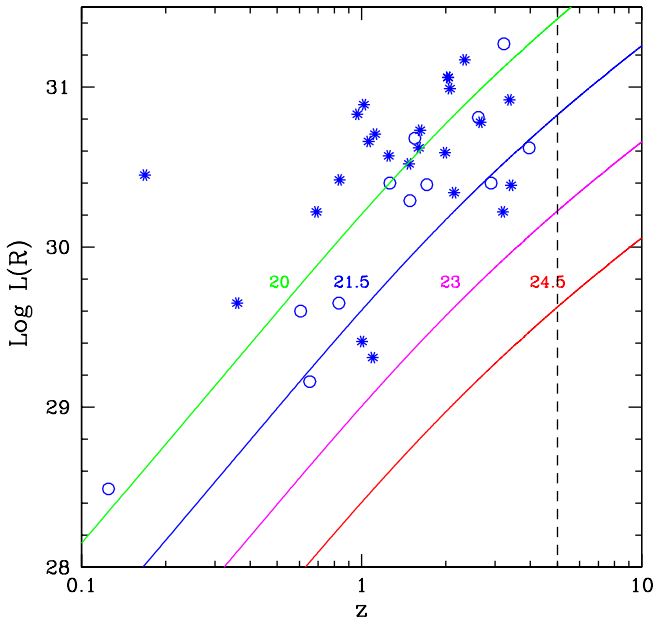

Figure 4.3: Limiting observable intrinsic R-band luminosity as a function of redshift, for different limiting magnitudes. Starred dots represent the luminosities of the GRBs in the sample and circles represent the *Swift* burst luminosities (the *Swift* burst with known $A_{\rm V}^{\rm host}$ observed up to 2008 January). The dashed vertical line at z = 5 corresponds to the Lyα break for the R band.

The method most commonly adopted for comparing two distinct distributions is the two-sample Kolmogorov–Smirnov (K–S) test. This test gives the probability that two discrete data distributions come from the same parent distribution. Unfortunately, given the specific luminosity distribution we are considering, this method has some critical limitations. Indeed (e.g. Press et al. 1992; Ashman, Bird & Zepf 1994), the K–S test is ideal for comparing the median of two distributions but it is not sensitive to the tails of the distributions being compared and it also fails in comparing bimodal with unimodal distributions.
A particular weakness of the K–S test (e.g. Press et al. 1992) is the low sensitivity to the tails of the two distributions being compared. We verified this problem with an example: we extracted randomly "n" points distributed as a Gaussian we also created a cluster of n/10 points at 6 sigma from the centre of the Gaussian.

We then created a new data set extracting $N = 10000$ points distributed as the first Gaussian. If n=50, the K–S test applied to these two (clearly different distributions) yields a probability of 23% that the two distributions come from the same parent distribution. This is much larger than the expected one (the simulation was repeated 500 times and the median value for the probability was 22%). The higher is "n" the lower is the null hypothesis probability, for n=100 $p = 0.13$ and it becomes negligible for n>500 where $p = 10^{-4}$. This example resembles closely our case where we have the luminosity distribution of GRBs made of a Gaussian (the high luminosity population) and a group of points at several sigma from it. The comparison through the K–S test of this real distribution with the simulated ones yields a high probability of the two being drawn from the same parent distribution but only because the K–S is not sensitive to the tail of the real distribution and the number of data points.

Another issue concerning the K-S test is the fact that it might not be a good choice when comparing a bimodal and an unimodal distribution. In order to verify this, we compared the K–S test results with the KMM algorithm described by Ashman, Bird and Zepf , 1994 (ABZ94 hereafter) which was applied (by ABZ94) to test the bimodality of the duration distribution of GRBs. This statistical method is a technique that can be used to detect clustering in data sets and assess its statistical significance. It is usually used to detect bimodalities or multi-modalities in univariate sets. The null hypothesis is that an unimodal parent population is a good description of the observational data and allows to evaluate the improvement in goodness of fit for a multi component modelling relative to the unimodal through the use of the likelihood ratio test statistics.

We generated pairs of Gaussian distributions (with equal dispersion and total number of points). For the number of simulated points and the separation between the two gaussians we used eq. 3.1 and the values reported in table 1 of ABZ94. We compared these simulated bimodal distributions with a unimodal Gaussian that "encloses" the bimodal. We compared the K–S probability (by deriving the median K–S probability of 100 runs, to be consistent with the method adopted by ABZ94) with the one obtained by these authors with the KMM method. We found that the probability obtained from the K–S test is systematically larger (at least a factor of 4) than the one obtained with the KMM method. For example, by simulating n=100 points distributed in two equal Gaussian separated of 3 sigma, we obtain $P_{\rm ks} = 0.03$, $P_{\rm KMM} = 0.001$. The same example but with a 2 sigma separation between the two Gaussian gives $P_{\rm ks} = 0.51$ and $P_{\rm KMM} = 0.133$.

The case studied in our paper is affected by both these problems for two reasons:

i) the luminosity distribution of the sample of GRBs is made of a Gaussian and a small number of bursts at low luminosity (but significantly detached from the more populated high luminosity distribution),

ii) in several cases we are comparing this likely "bimodal" distribution with a

unimodal simulated distribution. A K–S test applied to our case is expected to overestimate the probability that our distribution came from an unimodal one as in the previous example.

These problems urged us to use an alternative statistical analysis that is able to give an estimate of the probability that, starting from an unimodal distribution, we can produce a lack of events similar to the one observed in the real luminosity distribution.

To this aim we adopted the likelihood ratio test (**LRT**) described by Cash (1979). This test represents a good alternative to the χ^2 test in case of small statistics.

The simulation generates a sample of 30 000 GRBs, each with an associated intrinsic luminosity L_{ν_R}, redshift, host galaxy dust absorption $A_{\rm V}^{\rm host}$ and telescope limiting magnitude. The simulation returns the luminosities of the events that have an observer frame flux large enough to be detected by the associated telescope. Through this luminosity distribution, we can predict the number of bursts expected in each bin using the same binning adopted in the histogram plotted in Fig. 3.4. We can then compare these predictions with the observed data by evaluating the factor C (equation 3 of Cash 1979) of the LRT. A large Cash statistic C factor implies the rejection of the model. As a reference value, we adopted $C = 9.2$ which corresponds to a probability of rejection of the model hypothesis of $P_{\rm rej} = 99$ per cent. A simulated distribution can be considered consistent with the observed data with $P_{\rm rej} < 99$ per cent if the obtained C is smaller than 9.2.

4.2 Results of the simulation for the pre–*Swift* sample

4.2.1 Simulation without considering host galaxy dust absorption

We considered different combinations of the parameters characterizing the assumed luminosity distribution (i.e. mean value μ and dispersion σ for the lognormal, luminosity range and slope α for the power law and the luminosity range for the top hat). The results of the simulations are listed in Tab. 4.1.
We found that in none of these cases does the observed luminosity distribution of the simulated samples agree (better than 2 σ) with the observed one. The factor C is always larger than 11.6. In the lognormal cases, a narrow luminosity function that well matches the observed high–luminosity peak returns a large C value because it cannot reproduce the low–luminosity excess. A too wide distribution has, instead, an excess of events with $\log L(\nu_R)^{12\rm h} > 31.2$, in contrast with the observed maximum luminosity.

Table 4.1: Simulation results without considering host galaxy absorption

a	b	C^c	CP^d
G	30.65, 0.25	35.5	$< 10^{-5}$
G	30.20, 0.70	14.8	$6.1 \cdot 10^{-4}$
G	30.50, 0.50	15.4	$4.5 \cdot 10^{-4}$
TH	29.3, 31.2	12.0	$2.5 \cdot 10^{-3}$
PL	29.3, 31.2, -1	11.7	$2.9 \cdot 10^{-3}$
PL	29.3, 31.2, -1.5	11.7	$2.9 \cdot 10^{-3}$
PL	29.3, 31.2, -2	11.6	$3.0 \cdot 10^{-3}$

a) Assumed luminosity distribution: G=Gaussian, TH=top hat, PL=power–law.
b) Parameters G: μ, σ; TH: minimum luminosity, maximum luminosity; PL: minimum luminosity, maximum luminosity, index α assuming $N \propto L(\nu_R)^{\alpha}$.
c) Value of the C factor obtained with the Cash statistics.
d) Cash Probability from eq. 3 of Cash (1979).

Both the power–law and the top–hat distributions are affected by similar problems. The observed high–luminosity cut–off implies an upper bound to the simulated distributions. The low–luminosity end instead does not affect our results. As happens for the lognormal distribution, we are unable to reproduce the observable luminosity distribution, since we always violate some of the observed properties of the distribution shown in Fig. 3.4.

As an illustrative exercise we show in Fig. 4.4 the results obtained by repeating 1000 times the former simulation with 1000 events. We plot the ratio between the number of observed events in the high ($30.2 < \log[L(\nu_R)^{12h}] < 31.2$ over the low ($29.7 < \log L(\nu_R)^{12h} < 30.2$) luminosity bins versus the ratio of the number of observed events in the gap ($29.7 < \log L(\nu_R)^{12h} < 30.2$) and those in the high luminosity range ($30.2 < \log[L(\nu_R)^{12h}] < 31.2$). Note that the the ratios of the simulated samples stand at more than 3σ from the observed one (filled pentagon).

4.2.2 Simulation considering "standard" host galaxy dust absorption

In order to check if the addition of the host galaxy dust absorption allows us to produce a luminosity distribution compatible with the observed one, we tested some different kinds of absorption distributions and extinction curves.

The distribution of $A_{\rm V}^{\rm host}$ estimated for the observed bursts is dominated by low values. A large number of events are consistent with zero absorption and the

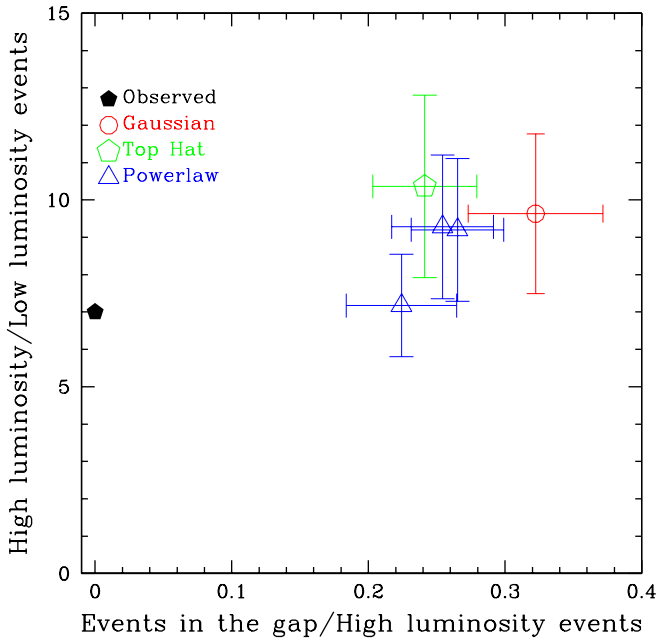

Figure 4.4: Unabsorbed case. Ratio between the number of observed events with $30.2 < \log[L(\nu_R)^{12h}] < 31.2$ and $\log L(\nu_R)^{12h} < 29.7$ versus the observed events with $29.7 < \log L(\nu_R)^{12h} < 30.2$ and $30.2 < \log[L(\nu_R)^{12h}] < 31.2$ for the considered initial luminosity functions in case of host galaxy dust absorption absence. Error bars show 1 σ uncertainties.

majority of them show $A_{\rm V}^{\rm host}$ smaller than one magnitude. This, however, could be due to selection effects, since it is more difficult to detect highly absorbed optical sources.

We first assumed a top–hat $A_{\rm V}^{\rm host}$ distribution, with a minimum $A_{\rm V}^{\rm host}$ =0, and assuming different maximum absorption values (i.e. $A_{V,{\rm Max}}^{\rm host}$= 2, 3, 5 magnitudes). Then, we simulated a power law like $A_{\rm V}^{\rm host}$ distribution (with different slopes and $A_{V,{\rm Max}}^{\rm host}$), which better represents the observed distribution. We finally assumed a single value for the V band extinction in the host galaxy for all bursts [note that this condition in any case implies different values of $A_{\nu_R(1+z)}$]. We also tried a Gaussian distribution, but the results are very similar to those found with the top-hat distribution.

For all these attempts, we have combined the $A_{\rm V}^{\rm host}$ distributions with the different luminosity distributions described in the previous section. The results are listed in Tab. 4.2. In no case were we able to reproduce the observed distribution. We conclude that a continuous absorption distribution, combined with a unimodal luminosity function, is unable to generate an observable GRB

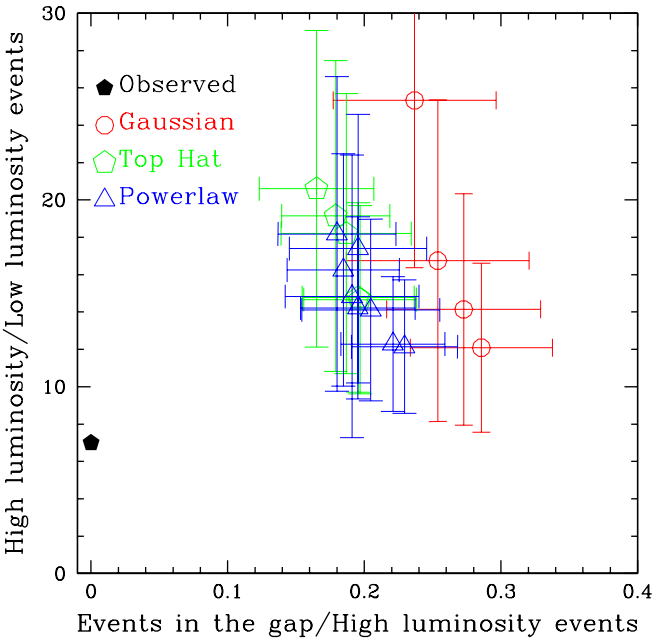

Figure 4.5: Host galaxy absorption case. Ratio between the number of observed events with $30.2 < \log[L(\nu_R)^{12h}] < 31.2$ and $\log L(\nu_R)^{12h} < 29.7$ versus the observed events with $29.7 < \log L(\nu_R)^{12h} < 30.2$ and $30.2 < \log[L(\nu_R)^{12h}] < 31.2$ for the different initial luminosity functions considering the host galaxy dust absorption effects. Error bars show 1 σ uncertainties.

luminosity distribution characterized by an empty gap between the two different luminosity groups. In Fig. 4.5 we show for the absorbed case the same exercise as plotted in Fig. 4.4.

Table 4.2: Simulation results considering different shapes of host galaxy dust absorption distributions.

Luminosity[a] distribution	Parameters[a]	Absorption[b] parameters	C^a	CP^a
G	30.65, 0.25	TH, 2	32.3	$< 10^{-5}$
G	30.20, 0.70	TH, 2	14.4	$7.5 \cdot 10^{-4}$
G	30.50, 0.50	TH, 2	17.1	$1.9 \cdot 10^{-4}$
G	30.65, 0.25	P, 2, -1	35.4	$< 10^{-5}$
G	30.65, 0.25	P, 2, -2	63.8	$< 10^{-5}$
G	30.20, 0.70	P, 2, -1	14.3	$7.8 \cdot 10^{-4}$
G	30.20, 0.70	P, 2, -2	14.7	$6.4 \cdot 10^{-4}$
G	30.50, 0.50	P, 2, -1	15.3	$4.8 \cdot 10^{-4}$
G	30.50, 0.50	P, 2, -2	14.6	$6.8 \cdot 10^{-4}$
G	30.65, 0.28	C, 0.5	34.2	$< 10^{-5}$
G	30.20, 0.70	C, 0.5	13.9	$9.6 \cdot 10^{-4}$
G	30.50, 0.50	C, 0.5	18.2	$1.1 \cdot 10^{-4}$
G	30.65, 0.28	C, 0.7	33.3	$< 10^{-5}$
G	30.20, 0.70	C, 0.7	14.2	$8.3 \cdot 10^{-4}$
G	30.50, 0.50	C, 0.7	17.5	$1.6 \cdot 10^{-4}$
TH	29.3, 31.2	TH, 2	11.6	$3.0 \cdot 10^{-3}$
TH	29.3, 31.2	P,2, -1	12.1	$2.4 \cdot 10^{-3}$
TH	29.3, 31.2	P,2, -2	12.3	$2.1 \cdot 10^{-3}$
TH	29.3, 31.2	C, 0.5	11.8	$2.7 \cdot 10^{-3}$
TH	29.3, 31.2	C, 0.7	12.6	$1.8 \cdot 10^{-3}$
PL	29.3, 31.2, -1	TH, 2	11.0	$4.1 \cdot 10^{-3}$
PL	29.3, 31.2, -1	P, 2, -1	11.5	$3.2 \cdot 10^{-3}$
PL	29.3, 31.2, -1	C, 0.7	10.4	$4.5 \cdot 10^{-3}$
PL	29.3, 31.2, -1	C, 0.5	11.3	$3.5 \cdot 10^{-3}$
PL	29.3, 31.2, -2	TH, 2	10.6	$5.0 \cdot 10^{-3}$
PL	29.3, 31.2, -2	P, 2, -1	11.2	$3.7 \cdot 10^{-3}$
PL	29.3, 31.2, -2	C, 0.5	10.9	$4.3 \cdot 10^{-3}$
PL	29.3, 31.2, -2	C, 0.7	10.7	$4.7 \cdot 10^{-3}$

a) Same notes as in Tab. 4.1.
b) Absorption distributions parameters. TH: maximum absorption in the V band magnitudes (the minimum is set to 0); P: maximum absorption in the V band magnitudes and index α; C: constant absorption $A_{\rm V}^{\rm host}$.

4.2.3 Simulation considering achromatic "grey" host galaxy dust absorption

Already in the pre-*Swift* era, the analysis of the optical to X–ray SEDs of some long GRBs showed an inconsistency between the X–ray spectrum and the contemporaneous optical SED that can not be explained in the framework of the "standard" afterglow scenario. In these cases some groups claimed the presence of an achromatic optical absorption component (Stratta et al. 2005), perhaps due to the small-size grain destruction in the neighbourhood of the GRB (Lazzati, Perna & Ghisellini 2001; Perna & Lazzati 2002). The amount of this absorption could be higher than what is inferred assuming standard dust (even by several magnitudes).We then considered the possibility that a fraction of GRBs can be absorbed with an achromatic extinction curve.

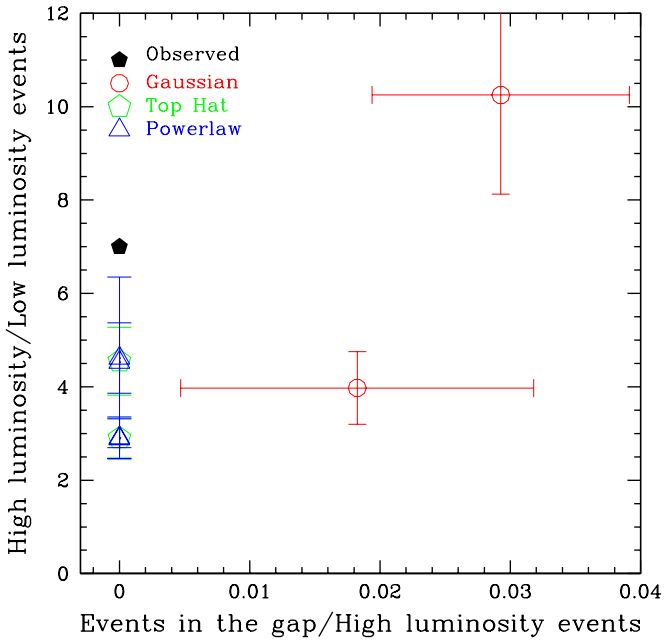

Figure 4.6: Achromatic absorption case. Ratio between the number of observed events with $30.2 < \log[L(\nu_R)^{12h}] < 31.2$ and $\log L(\nu_R)^{12h} < 29.7$ versus the observed events with $29.7 < \log L(\nu_R)^{12h} < 30.2$ and $30.2 < \log[L(\nu_R)^{12h}] < 31.2$ for the different initial luminosity functions in the case of achromatic dust absorption. In all the plotted points we did not consider the contribution of the standard dust absorption. Error bars show 1 σ uncertainties.

Starting with the same luminosity function tested in the previous cases, we associated a further achromatic absorption to a fraction of events. Such an

Table 4.3: Simulation results assuming an achromatic "grey dust" absorption

Luminosity[a] distribution	Parameters[a]	Absorption[a] parameters	Grey dust[b] %	A_λ[c]	C[a]	CP[a]
G	30.65, 0.25	0	60	1.6	6.0	$5.0 \cdot 10^{-2}$
G	30.65, 0.25	0	70	1.6	4.4	0.11
TH	30.2, 31.2	0	60	1.5	5.6	$6.1 \cdot 10^{-2}$
TH	30.2, 31.2	0	70	1.5	4.7	$9.5 \cdot 10^{-2}$
PL	30.2, 31.2, -1	0	70	1.5	2.9	0.24
PL	30.2, 31.2, -2	0	70	1.5	2.6	0.27

a) Same notes as in Tab. 4.2.
b) Fraction of the simulated events with an associated achromatic rest frame absorption (in percentage).
c) Achromatic absorption amount (in $\Delta \log L_{\nu_R}$).

absorption decreases the observable flux and the chance for those events to be detected. When observed, the analysis of the optical SED of these GRBs would not show any evidence of dust absorption. The inferred intrinsic luminosity could therefore be underestimated by a factor equal to the grey absorption amount. The optical luminosity distribution inferred by the observer could appear bimodal even if the real intrinsic luminosity function were unimodal. This last absorption model, when applied in the simulation to a large fraction of events, often returns a luminosity distribution compatible with the observed one.
For the pre-*Swift* era sample, the C factor is always smaller than 9.2. Indeed it is even smaller than 4.6 (P=90 per cent) reaching in some cases very small values with P$<$ 24 per cent. In Tab. 4.3 we present the results of the simulations considering the effect of a possible achromatic host galaxy dust absorption.
We conclude that unimodal luminosity functions can reproduce the observed bimodal luminosity distribution, if strong achromatic absorption is assumed. Similarly to what we have done in Fig. 4.4, we plot in Fig. 4.6 the high to low–luminosity number ratio versus the gap to high-luminosity number ratio. For clarity, we inserted in this plot only the cases with grey absorption, without the addition of a standard dust absorption effect. As can be seen, there are luminosity functions (power law and top hat) which agree with the observed luminosity distribution.

4.3 *Swift* era selection effects and entire sample simulation

In §3.2 we showed that the analysis of the *Swift* era GRBs optical luminosity distribution confirms both the clustering and the hint of bimodality discovered in the pre–*Swift* sample. This result is even more intriguing when considering the already discussed observational revolution occurred after the *Swift* satellite launch. The optical afterglow observational capabilities available in the *Swift* era are very different with respect to the pre–*Swift* ones. Therefore we decided to test whether the observed clustering and bimodality of the optical luminosities are real or due to selection effects taking into account also the *Swift* era late times Telescope Selection Function and applying the method described in the previous chapter also to the entire sample discussed in $ 3.2.

4.3.1 *Swift* era TSF

In order to analyse the possible selection effects affecting the optical observations in the *Swift* epoch, we consider the optical upper limits obtained when the burst, observed and localized by the X-Ray Telescope (XRT) onboard *Swift* , is observed at optical wavelengths but not detected. The main difference with respect to the pre-*Swift* epoch is that now the optical afterglow can be followed even dozen of seconds after the trigger, thanks to UVOT (Ultraviolet/Optical Telescope), the optical–UV monitor onboard Swift, and ground-based robotic telescopes.

For the pre–*Swift* sample we created the distribution of the deepest R–band upper limits of dark GRBs at the observed time of 12 h. These limits were derived by extrapolating, all upper limits for each burst, assuming a time decay $f(t) \propto t^{-\alpha}$ with $\alpha = 1$ (typical value of the optical decay at these time-scales; Zhang 2007). Then we choose the deepest value. These were corrected for the Galactic absorption along the line of sight using Schlegel, Finkbeiner & Davis (1998). This correction accounts for the limitation in the telescope sensitivity affecting the obtained upper limit. The obtained distribution can be considered as the probability, for each burst, to be observed at 12 h with a telescope (and an exposure time) reaching a given magnitude limit. We call it the TSF.

In the pre-*Swift* epoch it was believed that all optical afterglows had a similar decay, while we now know that the situation is more complex. The flat shape of a large number of very early optical afterglows does not allow to use the simple assumption of a single power–law decay lasting from few seconds to days after the trigger. Using very early photometric upper limits in order to extrapolate an upper limit at 12 h by assuming a $f(t) \propto t^{-1}$ decay would lead to a strong overestimate of the latter because that choice does not account for the flatter early time light-curve shape, leading to a too severe constraint on the afterglow flux at later times. To be

conservative we decided not to use the upper limits obtained before 1 h after the trigger in order to determine the deepest upper limit at 12 h to build the TSF. This choice allows us also to better compare the Swift results with the ones obtained in the pre-*Swift* sample. We have chosen 1 h as the minimum time because the optical light curve, which can be flat at earlier times, seems to recover the pre–*Swift* behaviour after this time (see e.g. Kann et al. 2009, Nardini et al. 2008b). Note that 1 h is of the order of the (observer frame) time $T_{\rm A}$ found by Willingale et al. (2007) for the "flat–steep" transition of the X–ray light curves. Note that Gendre, Galli & Boër (2008), in their analysis of X–ray afterglow luminosities, also adopted the choice, similar to ours, of considering data only after $T_{\rm A}$.

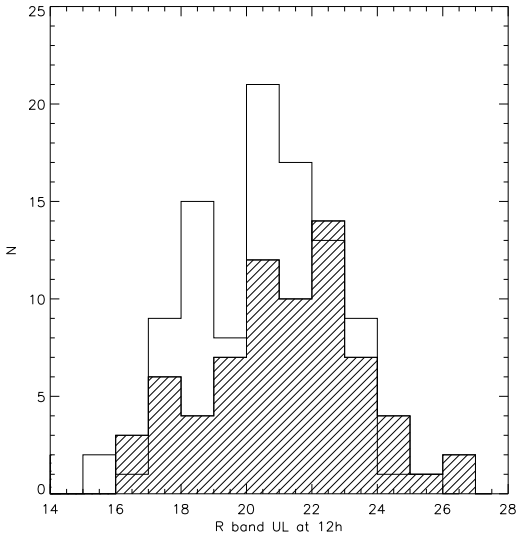

Figure 4.7: Distribution of the deepest R band upper limits (greater than 15) of all dark GRBs, evaluated at 12 hours. The dashed area represents the *Swift* dark GRB sample while the empty area represents the pre–*Swift* sample considered in NGG08. All upper limits are corrected for the Galactic absorption. The plotted distribution is the TSF quoted in the text.

We analysed all the optical limiting magnitudes of the 146 long GRBs without optical detection (updated to 2008 March). The presence on board of *Swift* of the XRT telescope that observes all the detected GRBs, allows a much better localisation of the GRB coordinates with respect to the large error boxes given by the gamma ray instruments in the pre–*Swift* era. This precise localisation allows us to consider all the 126 events without selecting them on the basis of the gamma ray instruments error box coverage (as instead required in §4.1.1). Of these, 20 were not observed in the optical. For the remaining 106 bursts, we found 74 GRBs with at least one useful R-band upper limit. For the other bursts the available data were taken before 1 h. We did not use the unfiltered observation.

If we compare the obtained TSF with the pre-Swift one (see Fig. 4.7) through a KS test, we find that the two distributions are different at the $\sim 2\sigma$ level (the KS null hypothesis probability is 5 per cent).We note that, even if we do not consider the very early upper limits, this new distribution appears slightly deeper than the previous one. Indeed, the mean value of the upper limits at 12 h is 0.9 mag deeper than the pre–*Swift* TSF. This difference decreases to 0.63 if we do not take into account the events with a very weak upper limits (i.e. R–band upper limit < 14). The fraction of very deep upper limits ($R > 24$) moves from 2 to 9.5 per cent.

4.3.2 Full sample simulation

We can now apply the same method described in §4.1 to the full sample of known $A_{\rm V}^{\rm host}$ events shown in Fig. 3.12. This method basically tries to reproduce the luminosity distribution of Fig. 3.12 considering the optical selection effects introduced by the TSF on an assumed intrinsic GRB luminosity function. We simulated 30 000 GRB optical afterglows assuming a redshift distribution (traced by the cosmic star formation rate described by Porciani & Madau 2001), an intrinsic luminosity function, a host galaxy dust absorption distribution and the probability distribution for each burst to be observed with a telescope with a given sensitivity. The latter distribution can be well represented by the TSF obtained above (Fig. 4.7). In order to compare the simulated result with the observed distribution plotted in Fig. 3.12 that includes both the pre–*Swift* and Swift GRBs, we created a combined TSF that includes all the upper limits contained in the two TSFs. This combined TSF is weighted for the number of GRBs observed in the optical in the pre–*Swift* and *Swift* epochs. Considering both the detected and undetected optical afterglows, these are 156 and 249, respectively. We assume that the GRBs of the two samples intrinsically belong to the same distribution and that the differences in the observed distributions are just due to the change of the observing conditions.

The simulation selects all the events whose observable (i.e. taking into account the effects of the redshift of the event and of the host galaxy dust absorption) flux is larger than the upper limit of the assigned telescope. Note that the Galactic absorption is already considered in the upper limit definition and that all GRBs with $z > 5$ are considered undetectable because of the Lyα absorption in the R band. The optical luminosity distribution of the resulting simulated events can be compared with the real one shown in Fig. 3.12.

The number of the events in Fig. 3.12, especially those belonging the underluminous family, strongly increased with respect to the pre-*Swift* sample. Similarly to what we for the pre–*Swift* sample, we compare the simulated and the observed distributions using the Cash (1979) test dividing the observed luminosity range into 11 bins. We reject a model under test if the C factor is larger than 9.2 ($P_{\rm rej} > 99$ per cent) even if in some cases we find C values smaller than 4.6

($P_{\rm rej} = 1 - P_{\rm C} > 90$ per cent). We tested a Gaussian, top hat and power law ($N_L \propto L^{\alpha}$) unimodal luminosity function defined over the same luminosity range of the comparison distribution of Fig. 3.12. The largest observed luminosity gives a strong constraint because more luminous events would have been easily seen. The low-luminosity threshold is less constrained from Fig. 3.12 and it is more affected by observational limits. For a very modest host galaxy dust absorption ($A_V^{\rm host}$) we obtain the following:

i) Top Hat with $28.4 < \log L_{\nu_R} < 31.3$: $P_C = 1.3 \times 10^{-3}\%$;

ii) Power law in the same range and $\alpha = 2$: $P_C = 8.2 \times 10^{-4}\%$;

iii) Gaussian with $\mu = 29.9$, $\sigma = 0.7$: $P_C < 10^{-5}\%$.

Our results show that we cannot reproduce the observed distribution of Fig. 3.12 with a unimodal luminosity distribution of GRBs. This result is almost independent from the assumed dust distribution, if it is standard. We used a Small Magellanic Cloud extinction curve because it seems more appropriate to represent the GRB afterglow host galaxy extinction (Kann, Klose & Zeh 2006; Schady, Mason & Page 2007), but we obtain similar results using the Milky Way and the Large Magellanic Cloud extinction curves.

Much better agreement is obtained either assuming an intrinsic bimodal luminosity function or assigning to most events an additional achromatic dust absorption. Note that this "grey dust" absorption is elusive, and cannot be estimated by the usual technique used to find $A_V^{\rm host}$, namely assuming an intrinsic power–law shape of the optical spectrum. A grey dust extinction has been invoked earlier for explaining some puzzling GRB spectral energy distributions (e.g. Perna & Lazzati 2002; Stratta et al. 2005; Perley et al. 2008).

The best results for the different tested luminosity distributions have been obtained assuming, together with the "grey dust" extinction, a moderate standard reddening modelled with a simple top hat $A_{\rm V}^{\rm host}$ distribution between 0 and 1.8 mag. The best matches between the simulated and the observed distribution are the following:

i) Gaussian $\sigma = 0.30$ $\mu = 30.69$, $A_{grey} = 1.6$[2]: $P_C = 0.9\%$:

ii) Top Hat with $30.1 < \log L_{\nu_R} < 31.3$, $A_{grey} = 1.6$: $P_C = 11.6\%$

iii) Power law in the same range and $\delta = 2$, $A_{grey} = 1.6$: $P = 11.1\%$

The increased number of underluminous observed events with respect to the pre–*Swift* sample gives more information about the shape of the fainter family

[2]Note that A_{grey} is defined in terms of $\Delta \log L_{\nu_R}$ and can be translated in term of units of magnitudes by multiplying A_{grey} for 2.5.

distribution. The Gaussian luminosity case is ruled out because it does not well represent the fainter events distribution (which is now more populated). The simple assumption of adding a strong (about 4 mag) achromatic absorption to about 60 per cent of the events is still producing acceptable results ($P_C \approx 10$–12 per cent). In future, with improved statistics, we will have to better characterize either the fainter family luminosity function (in the case of an intrinsically bimodal function) or the achromatic absorption distribution.

Liang & Zhang (2006) and Kann et al. (2008) noted that the mean redshift of the fainter family is smaller than the more luminous ones. For the present sample the mean redshift of the faint group is $\langle z \rangle = 1.17$ and $\langle z \rangle = 2.4$ for the luminous family.

Also in our simulated sample the observable GRBs belonging to the fainter family have a mean redshift of $\langle z_{faint} \rangle \approx 1.74$ vs $\langle z_{bright} \rangle \approx 2.17$[3], even if their intrinsic redshift distribution is the same. Our simulated faint events seem to be located at larger redshifts with respect to the observed ones while the simulated and observed $\langle z_{bright} \rangle$ are comparable.

In our simulations about 1/3 of the $z < 5$ events are observable and most of the undetectable ones are members of the low luminosity family. This suggests that dark GBRs preferentially are optically underluminous GRBs.

4.4 Discussion on the simulation results

In this study, we analysed the possible importance of observational selection effects on the clustering and bimodality found in the long GRB optical afterglow luminosity distribution.

We have shown that *Swift* bursts confirm the distribution of the luminosities of the optical afterglows observed at a fixed time (12 h) in the rest frame of the source: there are two families, both contained in a narrow luminosity range, and with a gap between the two. The ratio of the averaged luminosities of the two families is about 25 (i.e. $\mu_{\rm faint} = 29.3$, $\mu_{\rm bright} = 30.7$).

We proved that this observed dichotomy is not due to some simple intervening observational selection effects, but it must corresponds to an intrinsic bimodality either of the afterglow luminosity function itself or of the distribution of the absorption, with half of the burst affected only by moderate "normal" (i.e. chromatic) extinction, and the other half dimmed by a further 3–4 mag of "grey" dust absorption.

The first possibility suggests a dichotomy of the intrinsic properties of the burst, while the second suggests a dichotomy of the properties of the GRB environment. We cannot (yet) distinguish between the two possibilities, but an increase of the

[3]These results are obtained in the power–law bimodal scenario but similar results are obtained in all the other cases

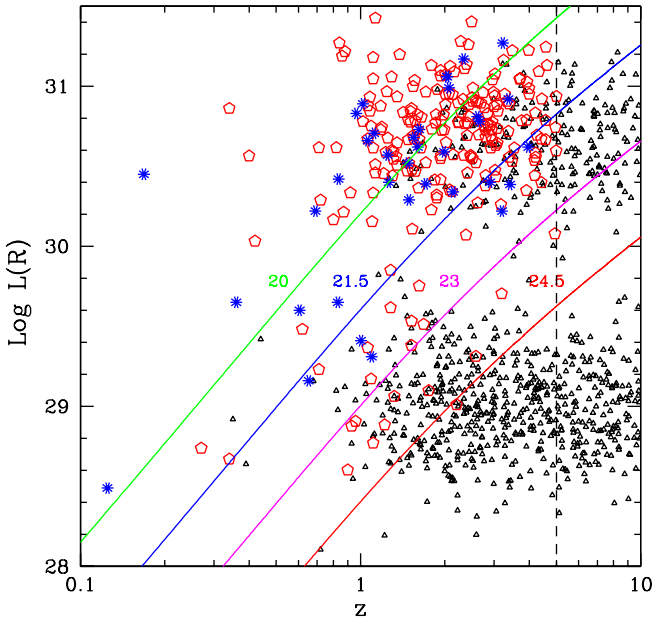

Figure 4.8: Logarithm of the optical luminosity $\log L_{\nu_R}^{12h}$ versus redshift z for the observed GRBs updated with the ones detected by *Swift* (starred dots), for the undetectable simulated events (small triangles) and for the observable simulated events (empty pentagon).

number of GRBs (say, twice as many as we have now, with redshift, well monitored optical afterglow and estimate of the "normal", chromatic, host extinction) will make it possible to well constrain either the slope of the luminosity function or the shape of the grey absorption distribution.

In Fig. 4.8, we superposed the simulated events onto the plot shown in Fig. 4.3. In this case, we simulated two separate Gaussian luminosity functions characterized by the same width but with different mean values (i.e. 30.65 and 29). The starred dots represent the observed values updated with the Swift GRBs, the small triangles represent the non-detectable simulated events and the empty pentagons represent the observable simulated ones. This figure shows how such a bimodal optical luminosity function well reproduces the distribution obtained with the real data.

Note that infrared observations, while surely important and crucial to confirm the existence of the clustering of the high-luminosity burst class and the separation in two luminosity classes, would not discriminate between the two hypotheses mentioned above. In fact, since the grey dust is absorbing the observed infrared

flux (which would be optical or UV in the rest frame) by the same amount as the observed optical one, we could not distinguish between an intrinsic bimodal luminosity distribution and the presence of grey dust. To this end it will be useful in the future to do an extended broadband afterglow analysis of the optically subluminous events. On the other hand, infrared observations and spectroscopy would not be limited to bursts having $z < 5$, and could therefore give important information on the number of bursts above this redshift limit, where the different star formation rates greatly differ. It will then be possible to directly measure the number of bursts which are optically dark because they lie at large redshifts.

During the first 3 yr after the launch of Swift, there have been 167 GRBs with at least one optical afterglow detection. If we define dark GRBs all the events observed, but not detected in the optical, and for which there is an optical upper limit, we find 126 events in these 3 yr, i.e. about 40 per cent of all long GRBs in the Swift epoch. In our simulations about two-third of the $z < 5$ events are undetectable and most of them are members of the low-luminosity family. This overestimate of the number of the simulated dark burst is probably due to the assumption (made for simplicity) that the faint and the bright families have the same shape (even if with different normalizations). With this caveat in mind, we suggest that dark GBRs preferentially are optically underluminous GRBs.

Chapter 5

Optical vs X–ray: a puzzling relation

5.1 Two–component modelling

5.1.1 The complexity of the broad band light–curves of bursts observed by *Swift*

As discussed in § 1, the fast re–pointing capabilities of the *Swift* satellite (Gehrels et al. 2004) allowed to discover the early time afterglow behaviour and its unforeseen complexity. A large fraction of GRBs are characterised by an initial typical steep decay of the X–ray flux, followed by a much shallower decay phase lasting up to $10^3 - 10^4$s. At the end of this "flat" phase, a break in the X–ray light curve occurs (at a time called $T_{\rm A}$ (Willingale et al. 2007)) and the X–ray flux starts to decline as a power law that represents the typical afterglow behaviour observed in the pre–*Swift* era. The optical light–curves instead seem not to trace the behaviour observed in the X–rays in a large number of events.

Both the early time steep decay and the following shallower phase could not be observed before Swift and are not easily explained by the standard afterglow emission model. This complexity therefore triggered the interest of a large number of groups in order to explain this unexpected behaviour and, particularly, the shallow decay phase (see §2 for for a review of the proposed models). Most of the models that have been proposed for explaining the early times X–ray light–curves complexity do not take into account the fact that in a large number of GRBs the optical light–curve do not track the X–ray one. In particular the shallow decay phase that is present in most of the X–ray light–curves is observed only in a small fraction of events. In many GRBs the optical and X–ray light–curves follow different temporal behaviours also at later times and the presence of chromatic breaks is quite a common feature in the *Swift* era.

The inconsistency between the optical and X–ray light–curve evolution prompted us to analyse the rest frame broad band light–curves of a sample of well sampled GRBs and to model them as due to the sum of two separate components excluding the early time steep decay and the flaring activity. The first component is modelled as the "standard" forward shock afterglow component while the second component is treated in a completely phenomenological way with the aim of minimising the number of free parameters and to make a first step towards a more physical modelling.

In the following sections I will discuss our two component modelling following the description given in Ghisellini et al. 2009.

5.1.2 Optical and X–ray light–curves

In order to study the complex temporal behaviour of the *Swift* era afterglow light–curves considering both the X–ray and optical band emission, we selected a sample of long GRBs detected after the *Swift* satellite launch fulfilling the following selection criteria:

i) known redshift,

ii) XRT follow up,

iii) well sampled optical photometry,

iv) published estimate of the host galaxy dust absorption $A_V^{\rm host}$.

These criteria is dictated by the need to determine reliable optical and X–ray intrinsic luminosities, in order to model their time dependent behaviour.

As at the end of March 2008 we found 33 GRBs fulfilling all our selection criteria[1]. When possible, if multiple $A_{\rm V}^{\rm host}$ estimates for an individual burst are present in literature, we choose the one obtained analysing the optical data only, without assuming any connection with the X–rays data as already done for the optical luminosity analysis in §3. Information concerning these 33 GRBs are listed in Table 5.1.2, where we report: redshift, $A_V^{\rm host}$, optical spectral indices $\beta_{\rm o}$ (corrected for extinction), X-ray spectral indices $\beta_{\rm X}$ (again accounting for absorption) and hydrogen column density $N_{\rm H}^{\rm host}$ (at the host) as determined by fitting the X–ray spectrum assuming a simple power law model.

We collected all the multi–band photometric data reported in literature for the GRBs in our sample and converted the observed magnitudes to k–corrected and de–reddened monochromatic luminosities using:

$$L(\nu_0) \;=\; \frac{4\pi d L^2}{(1+z)^{1-\beta_{\rm o}}}\, F(\nu_0), \tag{5.1}$$

[1]For an additional one, GRB 070802, the photometric data set is not yet available

GRB	z	$A_{\rm V}^{\rm host}$	$\beta_{\rm o}$	$\beta_{\rm X}$	$N_{\rm H}^{\rm host}$
050318	1.44	0.68±0.36	1.1±0.1	1.09±0.25	0.4±0.1
050319	3.24	0.11	0.59	0.73±0.05	3.8±2.2
050401	2.8992	0.62±0.06	0.5±0.2	0.89±0.03	16.0±3
050408	1.2357	0.73±0.18	0.28±0.33	1.1±0.1	12.0±3.5
050416A	0.653	0.19±0.11	1.14±0.2	1.04±0.05	6.8±1.0
050525A	0.606	0.32±0.2	0.57±0.29	1.1±0.25	1.5±0.7
050730	3.967	0	0.56±0.06	0.87±0.02	6.8±1
050801	1.56	0	0.6	0.87±0.23	0±0.5
050802	1.71	0.55±0.1	0.72±0.04	0.88±0.04	2.8±0.5
050820A	2.612	0	0.77±0.08	0.94±0.07	6±4
050824	0.83	0.14±0.13	0.45±0.18	1.0±0.1	1.8±0.65
050922C	2.198	0	0.51±0.05	0.89±0.16	0.65±0.27
051111	1.55	0.39±0.11	1.1±0.06	1.15±0.15	8±3
060124	2.296	0	0.73±0.08	1.06±0.06	13±4.5
060206	4.045	0±0.02	0.73±0.05	1.0±0.3	0.4±0.3
060210	3.91	1.14±0.2	1.14±0.03	1.14±0.03	100±12
060418	1.489	0.25±0.22	0.29±0.04	1.04±0.13	1.0±0.4
060512	0.4428	0.44±0.05	0.99±0.02	0.99±0.02	0
060526	3.221	0.04±0.04	0.495±0.144	0.8±0.2	0
060614	0.125	0.05±0.02	0.81±0.08	0.84±0.08	0.15±0.12
060729	0.54	1.05	1.1	1.11±0.01	1.9±0.4
060904B	0.703	0.44±0.05	0.90±0.04	1.16±0.04	4.09±0.13
060908	2.43	0.055±0.033	0.69	0.95±0.15	0.64±0.34
060927	5.47	0.33±0.18	0.64±0.2	0.87	<0.34
061007	1.26	0.48±0.19	1.02±0.05	1.01±0.03	5.8±0.4
061121	1.314	0.72±0.06	0.62±0.03	0.87±0.08	9.2±1.2
061126	1.1588	0	0.93±0.02	1.00±0.07	11±0.7
070110	2.352	0.08	1.1±0.1	1.1±0.1	2.6±1.1
070125	1.547	0.11±0.4	0.58±0.1	1.1±0.1	2±1
071003	1.1	0.209±0.08	0.93±0.04	1.14±0.12	1.1±0.4
071010A	0.98	0.615±0.15	0.76±0.25	1.46±0.2	17.4±4.5
080310	2.42	0.1±0.05	0.6	0.9±0.2	7.0±1
080319B	0.937	0.07±0.06	0.33±0.04	0.814±0.013	1.87±0.13

Table 5.1: The sample. For all bursts we report information taken from the literature (see the references in Ghisellini et al. 2009a), namely: redshift, optical extinction and hydrogen column density at the host ($A_{\rm V}^{\rm host} and N_{\rm H}^{\rm host}$, respectively), and the optical and X–ray indices found after de–absorbing.

where ν_0 is the central frequency of the photometric filter, $d_{\rm L}$ is the luminosity distance and $\beta_{\rm o}$ is the unabsorbed optical spectral index.

The X–ray light curves were taken from the UK Swift Science Data Centre[2] (see Evans et al. 2007 describing how the data were reduced). Also the X–ray 0.3-10 keV XRT light curves have been corrected for the combined effects of both host frame $N_{\rm H}$ and Galactic column densities, using the unabsorbed spectral index $\beta_{\rm X}$ obtained from the X–ray spectral analysis (see Table 5.1.2). The unabsorbed 0.3–10 keV observer frame fluxes $F_{\rm X}$ have been converted to host frame 0.3-10 keV luminosities $L_{\rm X}$ as:

$$L_{\rm X} = \frac{4\pi d_{\rm L}^2}{(1+z)^{1-\beta_{\rm X}}} F_{\rm X}. \tag{5.2}$$

For simplicity, we use the same $\beta_{\rm X}$ for the entire X–ray light curve, neglecting the sudden changes of $\beta_{\rm X}$ sometimes seen during X–ray flares, since the interpretation of the individual flares is beyond the aim of this work. The analysis has been carried out in the GRB host time frame. We therefore re-scale all the observed time intervals by $(1+z)^{-1}$.

In figs. 5.1-5.6 we plot the rest frame k–corrected and de–absorbed optical and X–ray light–curves of all the GRBs in our sample. Even if there are some cases in which the optical and X–ray light–curves track one each other (e.g. GRB 060729, GRB 080310), in most cases the optical and X–ray light–curves follow quite different temporal evolutions showing different temporal indices and chromatic breaks. The canonical "steep–flat–steep" evolution is observed in 13 GRBs X–ray light–curves while it is present in only 3 optical light curves.

5.1.3 Two components light–curve modelling

As mentioned before we modelled the rest frame luminosity light–curves as the sum of two separate components. The first one is modelled as a "standard" forward shock afterglow component following the analytical description given in Panaitescu and Kumar (2000). Since we do not have a complete physical description of the second component we treated it in a completely phenomenological way. In the following discussion this phenomenologically treated component will be simply called Component II.

"Standard afterglow" component

In the Panaitescu and Kumar (2000) description of the standard forward shock afterglow component, the observed emission depends on six parameters:

1. E_0 — the (isotropic equivalent) kinetic energy of the fireball after it has produced the early prompt radiation;

[2] http://www.swift.ac.uk/xrt_curves/

2. Γ_0 — the initial fireball bulk Lorentz factor. It controls the onset of the afterglow, but it does not influence the rest of the light curve. It is then rather undetermined when very early data are not available;

3. n_0 or $\dot{M}_{\rm w}/v_{\rm w}$ — n_0 is the value of the circum–burst medium density if homogeneous, while $\dot{M}_{\rm w}/v_{\rm w}$ (wind mass loss rate over the wind velocity) determines the normalisation of the density in the wind case ($\propto R^{-2}$) profile;

4. $\epsilon_{\rm e}$ — the "equipartition" parameter setting the fraction of the available energy responsible for electron acceleration;

5. $\epsilon_{\rm B}$ — the "equipartition" parameter parametrising the fraction of the available energy which amplifies the magnetic field;

6. p — the slope of the relativistic electron energy distribution, as injected at the shock.

For simplicity, we assume that the highest frequency of the afterglow synchrotron emission is beyond the X–ray range. These are 6 free parameters, if we consider n_0 or $\dot{M}_{\rm w}/v_{\rm w}$ as a single one: in reality, the assumed homogeneous vs wind–like density profile can be considered as an additional degree of freedom.

Phenomenological Component II

This component describes the flat–steep phases observed in the canonical X–ray light–curve. For simplicity, this Component II spectral energy distribution is supposed not to evolve in time. The spectral shape is modelled as a smoothly joining double power–law law written as:

$$\begin{aligned} L_{\rm L}(\nu,t) &= L_0(t)\,\nu^{-\beta_{\rm x}}; & \nu > \nu_b \\ L_{\rm L}(\nu,t) &= L_0(t)\,\nu_{\rm b}^{\beta_{\rm o}-\beta_{\rm x}}\nu^{-\beta_{\rm o}}; & \nu \leq \nu_{\rm b}, \end{aligned} \tag{5.3}$$

where L_0 is a normalisation constant. L_0 by itself is not treated as a free parameter. Instead, we take it as the 0.3–10 keV luminosity $L_{\rm LX}$ of the Component II emission at the time $T_{\rm A}$:

$$L_{\rm LX}(T_{\rm A}) = \int_{0.3}^{10} L_{\rm L}(\nu, T_{\rm A})d\nu \tag{5.4}$$

with ν in keV. Again for simplicity we assume that any cut–off frequency, at high as well as at low energies, is outside the IR–optical/X—ray frequency range.

The temporal evolution is assumed to be described by a smooth broken power law breaking at a time $T_{\rm A}$ and characterised by a pre break temporal index $\alpha_{\rm fl}$

and and a post break decay index $\alpha_{\rm st}$. The analytical form of the Component II temporal evolution is therefore written as:

$$L_{\rm L}(\nu,t) \;=\; L_{\rm L}(\nu,T_{\rm A})\,\frac{(t/t_{\rm A})^{-\alpha_{\rm fl}}}{1+(t/t_{\rm A})^{\alpha_{\rm st}-\alpha_{\rm fl}}}. \tag{5.5}$$

To summarise, the free parameters reproducing the Component II emission are:

1. $\beta_{\rm X}$ — the Component II emission spectral index in X–rays;
2. $\beta_{\rm o}$ — the Component II emission spectral index of the in the IR–optical;
3. $\nu_{\rm b}$ — the break frequency between the optical and the X–rays;
4. $L_{\rm LX}(T_{\rm A})$ — the 0.3–10 keV luminosity of the Component II emission at the time $T_{\rm A}$;
5. $\alpha_{\rm fl}$ — the decay index for the shallow phase, before $T_{\rm A}$
6. $\alpha_{\rm st}$ — the decay index for the steep phase, after $T_{\rm A}$;
7. $T_{\rm A}$ — the time when the shallow phase ends.

These are 7 free parameters. It is worth stressing that, despite of their number, these are rather well constrained by observations. When the Component II emission dominates, $\alpha_{\rm fl}$, $\alpha_{\rm st}$, $T_{\rm A}$ can be directly determined as well as one spectral index (usually $\beta_{\rm X}$, since the Component II emission is usually dominating in the X–ray range). Some degeneracy is present between $\nu_{\rm b}$ and $\beta_{\rm o}$, both of which control the importance of the optical flux due to the late prompt component: the same optical flux can for instance be reproduced assuming a steeper (flatter) $\beta_{\rm o}$ and a larger (smaller) $\nu_{\rm b}$, as the ratio between the 0.3-10 keV X–ray luminosity and the $\nu_{\rm o}L(\nu_o)$ optical luminosity of the late prompt is proportional to $\nu_{\rm b}^{\beta_{\rm X}-\beta_{\rm o}}$.

Modelling caveats

As our treatment is necessarily simplified, simply parametrising the Component II emission, we analyse below the most important (or drastic) assumptions, trying to outline their effects.

- The afterglow calculations are based on the prescriptions by Panaitescu & Kumar (2000). In their analytical treatment the curvature of the emitting shell is neglected. The inclusion of the time delay between the emission times of photons received at any observer time would smooth out any relatively sharp feature of the light curve (especially when the injection or cooling frequency crosses the considered band). However the derived light curves are sufficiently accurate for the purposes of the present work.

- Almost all of the calculations of the afterglow light curves assume that ϵ_e and ϵ_B are constant in time. This is likely to be just a rough approximation, since the physical conditions at the shock front change in time (Γ as well as the density measured in the comoving frame do change). As such a temporal dependence is not known or predicted, we are forced to adopt this simplification.

- The afterglow emission is assumed to be isotropic, therefore no jet breaks can be reproduced in the calculated light curves. Since the presence/absence of jet break is a fundamental topic of this work it will be discussed in §6.

- The spectrum of the Component II emission is assumed to be constant in time, in the observer frame. This is likely to be the most critical approximation, adopted just to minimise the number of free parameters. One might speculate that if this component originate by shells with decreasing bulk Lorentz factor (as in the models by Uhm & Beloborodov 2007, Genet, Daigne & Mochkovitch 2007 and Ghisellini et al. 2007), then it is likely that the observed break frequency ν_b would also decrease in time (if constant in the comoving frame). While this would not affect the X–ray light curves (if ν_b is below the X–ray window even at early times), the optical emission would become relatively more important as time goes on. For instance, a plateau in the X–rays could correspond to a rising optical light curve. This suggests a possible observational test. Assume to select a burst in which both the optical and the X–ray light curves are dominated by the Component II emission. If ν_b decreases in time, we should see two effects. First, the optical plateau should be shallower than the X–ray one (since the X–ray to optical flux ratio decreases as $\nu_b^{\beta_x-\beta_o}$). Secondly, when ν_b crosses the optical band, we should see a spectral steepening, since the decreasing ν_b acts as a cooling break. After ν_b has crossed the optical band, the optical and the X–ray fluxes should lie on the same power–law.

- The low and high frequency cut–offs of both the afterglow and Component II emission have been neglected as free parameters. The late emission spectrum might have a high frequency cut-off in the X–ray band. Given the current status of the X–ray observations, that do not detect such a cut–off, this simplification is reasonable.

- The Component II emission is assumed to last forever, while, of course, it will die away after some time. This may happen, however, at very late times, when any X–ray or optical observations are not any longer feasible or when the GRB emission cannot be detectable (in the optical, emission can be dominated by the host galaxy or sometimes by a supernova associated to the burst).

- Flares, re–brightenings and/or bumps in the light curve are not accounted for. In our scenario, these are separated components, though in practice, their presence makes the choice of what data points to "fit" a bit subjective.

A final remark. Due to the above caveats, the values of the parameters for a single source may be subject to rather large uncertainties. In this sense the *distributions* of parameter values are much more meaningful. We could badly model an individual source, but the general conclusions could be right, if some coherence is found for the parameters of the entire sample.

5.1.4 The light–curves

Figs. from 5.1 to 5.6 show the X–ray and optical light curves of the 33 GRBs together with the results of the modelling: dotted lines refer to the Component II emission, dashed ones to the afterglow component and the solid lines to their sum.

The parameters inferred from the modelling of the light curves are reported in Tables 5.2 and 5.3, together with a tentative classification of the bursts according to the dominant contribution: "A" stands for afterglow, "L" for Component II and "X" and "O" refer for X–ray and optical, respectively. For instance, XL–OA indicates that the X–ray flux is dominated by the Component II , and the optical by the afterglow. When both type of emissions are comparable, we use "M", for mix. This also comprises the case when one component dominates in one time interval, and the other in another time interval. The number of bursts which can be described within these categories is summarised in Table 5.1.4. The X–ray flux is dominated by the Component II emission or a mixture of late prompt and afterglow for the majority of GRBs, the opposite being true for the optical emission. Out of our 33 events, the most common cases are XM–OA (10 GRBs, namely a mix in the X-rays and afterglow in the optical) and XL–OM (eight GRBs, namely Component II in the X–rays and a mix in the optical).

The overall result is that both components have comparable relevance in most cases. This can be seen as a direct consequence of the different slopes of the light curves: since the Component II is flatter than the afterglow up to $T_{\rm A}$, and often steeper after this time, it is likely that the Component II emission dominates or contributes around $T_{\rm A}$ even in the optical. Conversely, the afterglow may dominate or be important at very early and late times (if there is no jet break). In other words, the similar contribution of both the components is the cause of the complex X–ray–optical behaviour observed.

GRB	$E_{0,53}$	Γ_0	n_0	ϵ_e	ϵ_B	p
1	2	3	4	5	6	7
050318	10	100	2	1.e-2	2.2e-4	2.5
050319	0.5	300	1.e-8	1.e-2	1.e-4	2.
050401	1.2	350	10	1.e-4	1.e-2	1.65
050408	2	200	3	1.e-3	3.e-2	2.8
050416A	0.6	200	3	1.e-4	8.e-5	1.67
050525A	1	100	1.e-8	1.e-3	2.e-2	2.3
050730	5	300	8	5.e-3	7.e-4	2.3
050801	0.2	100	1.e-8	1.5e-2	7.e-4	2.4
050802	3	200	3	2.e-2	2.e-4	2.3
050820A	4	120	10	1.e-3	1.e-2	1.85
050824	0.7	100	1	2.e-4	3.e-3	1.75
050922C	10	250	2	2.e-3	1.2e-3	2.4
051111	5	120	5.e-9	1.e-3	1.e-3	2.1
060124	5	110	3	5.e-3	6.e-4	2.
060206	4	180	2	5.e-2	6.e-4	2.6
060210	80	100	1.e-8	5.e-3	8.e-4	2.15
060418	5	200	10	1.e-3	1.e-2	2.3
060512	3	200	10	1.2d-4	1.e-3	2.15
060526	4	300	10	3.e-4	6.e-3	1.9
060614	0.03	100	1	2.e-3	2.e-5	2.
060729	0.5	110	3	4.e-3	1.e-3	2.3
060904B	0.3	100	3	2.8e-2	4.e-4	2.15
060908	1	400	10	2.e-3	3.e-3	2.3
060927	8	220	30	3.e-3	1.e-4	2.3
061007	60	200	1.e-8	3.e-3	3.e-4	2.6
061121	6	110	3	4.e-4	1.e-2	2.
061126	3	100	1.e-8	1.e-3	2.e-4	2.5
070110	3	100	1	5.e-4	6.e-3	1.8
070125	4	300	1	1.3e-2	6.e-2	2.65
071003	4	100	1.e-8	1.e-3	1.5d-4	2.3
071010A	5	120	3	3.e-4	6.e-3	2.
080310	1	120	6	1.e-3	7.e-3	1.95
080319B	50	400	10	1.e-3	8.e-4	2.7

Table 5.2: Input parameters for the afterglow component (columns 2–7). Col 1: Burst Id; Col 2: Fireball kinetic energy (after the early prompt emission, in units of 10^{53} erg); Col 3: Initial bulk Lorenz factor; Col 4: density of circum–burst medium: values equal or larger than 1 are for a homogeneous density; values much smaller than 1 correspond to a wind like profile; the listed value is $\dot{M}_w/v_w$, where $\dot{M}_w$ is the mass loss rate in $M_\odot$/yr and v_w is the wind velocity in km s^{-1}. Col. 5 and 6: equipartition parameters ϵ_e and ϵ_B; Col 7: slope of the assumed relativistic electron distribution;

GRB	$\nu_{\rm b}$	$\beta_{\rm X}$	$\beta_{\rm o}$	$\alpha_{\rm fl}$	$\alpha_{\rm st}$	$T_{\rm A}$	$L_{\rm A}$	Class
1	8	9	10	11	12	13	14	15
050318	1.e16	1.1	0.0	0.0	2.0	2.e3	434	XM-OA
050319	1.e15	0.75	0.6	0.2	1.6	7.e3	623	XL-OM; XA early
050401	7.e16	0.9	-0.1	0.6	1.8	1.75e3	3.7e3	XM-OA
050408	6.e16	1.1	0.28	0.0	1.2	7.e3	133	XL-OM
050416A	7.e16	1.1	0.4	0.0	1.8	2.e3	17	XA-OA
050525A	5.e15	1.1	0.0	0.0	1.65	2.e3	133	XL-OA; XA early
050730	4.e16	0.9	0.15	0.2	2.6	2.5e3	1.3e4	XL-OM; XA late
050801	2.e16	0.9	0.1	0.0	1.5	1.e3	112	XL-OA; XA early
050802	1.e16	1.1	0.0	0.0	1.8	1.5e3	667	XM-OA
050820A	5.e16	1.1	0.0	-0.2	1.6	2.5e3	5.e3	XM-OA
050824	1.e16	1.1	0.0	0.0	1.2	1.e4	3.33	XA-OA
050922C	2.e16	1.1	0.5	0.0	1.5	8.e2	1334	XL-OM; XA early
051111	2.e15	1.1	0.5	-0.1	1.5	5.e2	1.e3	XM-OM
060124	2.e16	1.1	0.1	0.2	1.6	9.e3	1.7e3	XL-OM; XA early
060206	4.e16	1.1	0.1	-0.3	1.5	2.5e3	5.e3	XL-OM
060210	1.5e16	1.25	1.25	0.0	1.7	2.8e2	3.1e4	XA-OL
060418	2.e16	1.1	0.1	0.1	1.6	2.8e2	4.3e3	XL-OA
060512	1.e15	1.1	0.5	0.0	1.3	8.e2	3.33	XA-OA
060526	8.e15	1.1	0.6	0.0	1.9	6.e3	167	XM-OM
060614	5.e16	1.1	0.6	-0.5	2.1	4.5e4	0.5	XL-OL; XA-OA early
060729	2.e15	1.1	0.5	-0.1	1.4	3.5e4	50	XL-OL; XA-OA early
060904B	2.e16	1.1	0.0	0.5	1.6	1.3e3	100	XM-OA; OL early
060908	6.e15	1.1	0.4	0.3	1.5	3.e2	500	XM-OA
060927	3.e16	1.1	0.0	0.0	1.7	4.e2	2.7e3	XM-OA
061007	8.e15	1.1	0.0	0.0	1.75	5.e1	3.e5	XM-OA
061121	2.e16	1.1	0.0	0.0	1.65	1.5e3	1.e3	XM-OA
061126	1.e16	1.1	0.0	0.0	1.45	3.e3	300	XL-OM
070110	5.e16	1.1	0.0	0.0	1.7	1.e3	1.e3	XA-OA
070125	1.e15	1.6	1.6	-0.4	2.2	5.e4	0.3	XA-OM
071003	1.e16	1.1	0.8	-0.7	1.7	1.5e4	50	XL-OM; XA early
071010A	5.e15	1.1	0.0	-0.3	1.4	2.e4	17	XL-OA; XA early
080310	1.e16	1.1	0.4	-0.5	1.7	1.3e3	1.3e3	XM-OA; OM mid
080319B	6.e16	1.1	-0.1	0.0	1.65	4.e1	1.3e6	XL-OA

Table 5.3: Input parameters for the Component II emission (columns 8–14). Col 1: Burst Id; Col. 8: spectral break of the late prompt emission (in Hz); Col. 9 and 10: high and low energy spectral indices of the late prompt emission; Col. 11 and 12: decay slopes of the late prompt emission, before and after $T_{\rm A}$ listed in Col. 13 (in sec); Col. 14: luminosity (in units of 10^{45} erg s^{-1}) in the 0.3–10 keV energy range of the late prompt emission, at the time $T_{\rm A}$; Col. 15: Burst classification (see text).

Dominating component	number of events	notes
XL	15	
XA	6	
XM	12	
OL	3	
OA	19	
OM	11	
XL–OL	2	both with XA–OA very early
XA–OA	4	
XM–OM	2	
XL–OA	5	3 bursts with XA early
XA–OL	1	
XM–OL	0	
XM–OA	10	1 with OL early, one with OM mid
XA–OM	1	
XL–OM	8	4 with XA early, 1 with XA very late

Table 5.4: Number of sources dominated by different components: XA (OA): X–ray and optical flux dominated by the Afterglow emission; XL (OL): X–ray and optical flux dominated by the Component II emission; XM (OM): X–ray and optical fluxes where the Component II and afterglow emission are relevant.

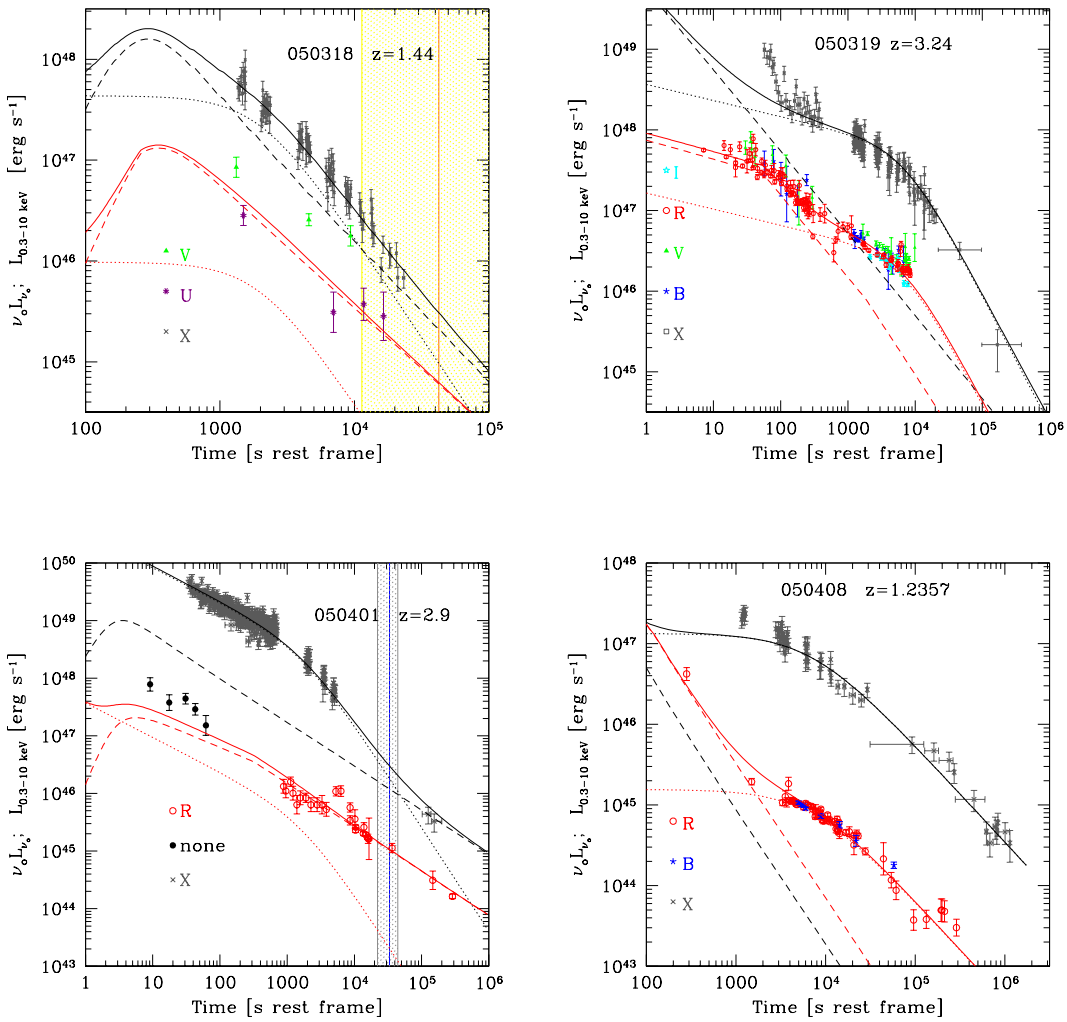

Figure 5.1: X–ray (in grey) and optical (different symbols, as labelled) light curves. Lines indicate the model fitting: afterglow (dashed), Component II (dotted) and their sum (solid). Black lines refer to the X–rays, red for the optical. The vertical blue line (and shaded band) correspond to the rest frame jet break times (and their 3σ uncertainty). Grey lines and stripes correspond to jet break times as reported in the literature (references are listed in Ghirlanda et al. 2007), yellow lines and stripes refer to jet times expected if the burst followed the Ghirlanda relation. These are shown only for bursts with measured $E_{\rm peak}$, the peak energy of the prompt emission. References of photometric data can be found in appendix 10.3

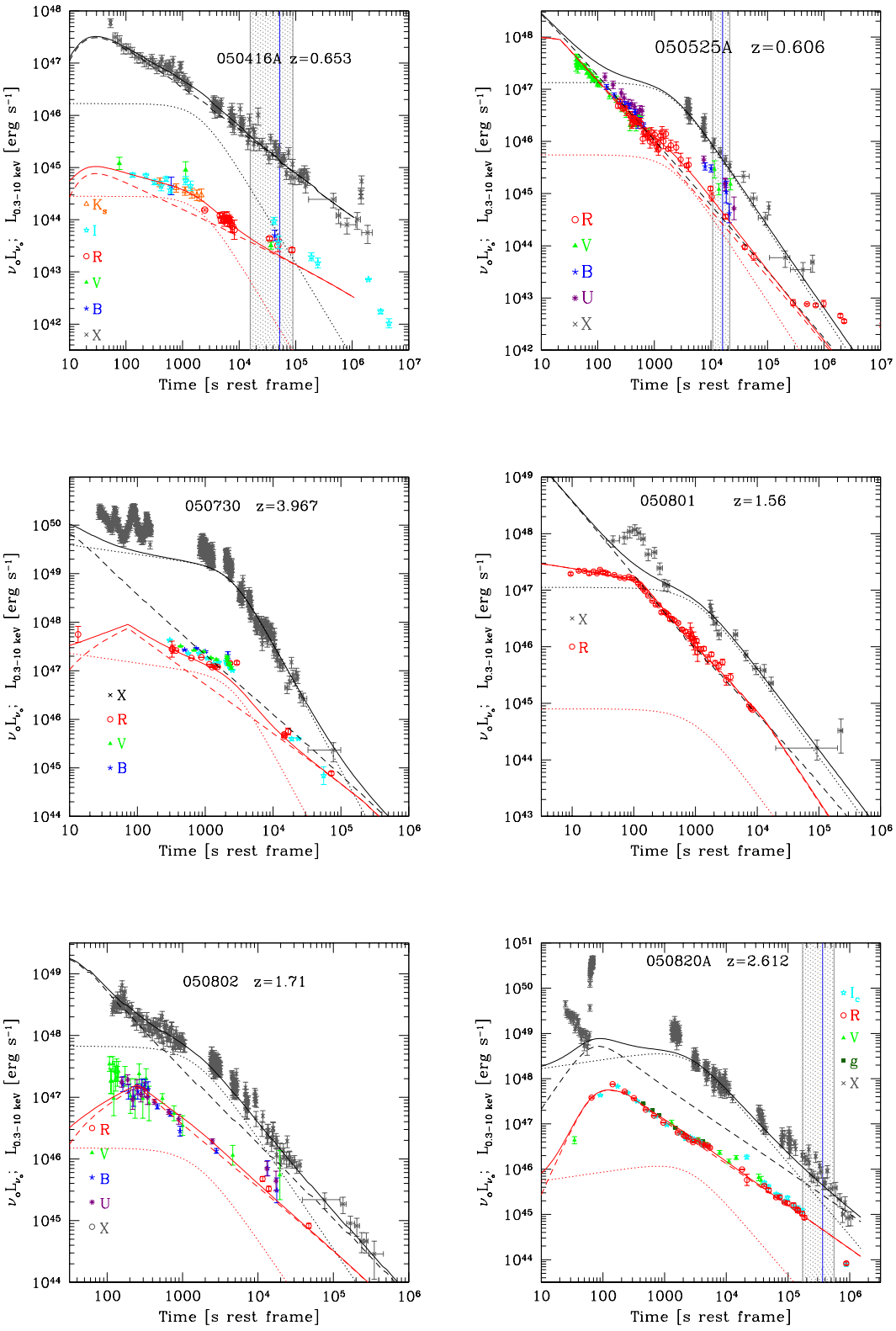

Figure 5.2: Same notes as in Fig 5.1

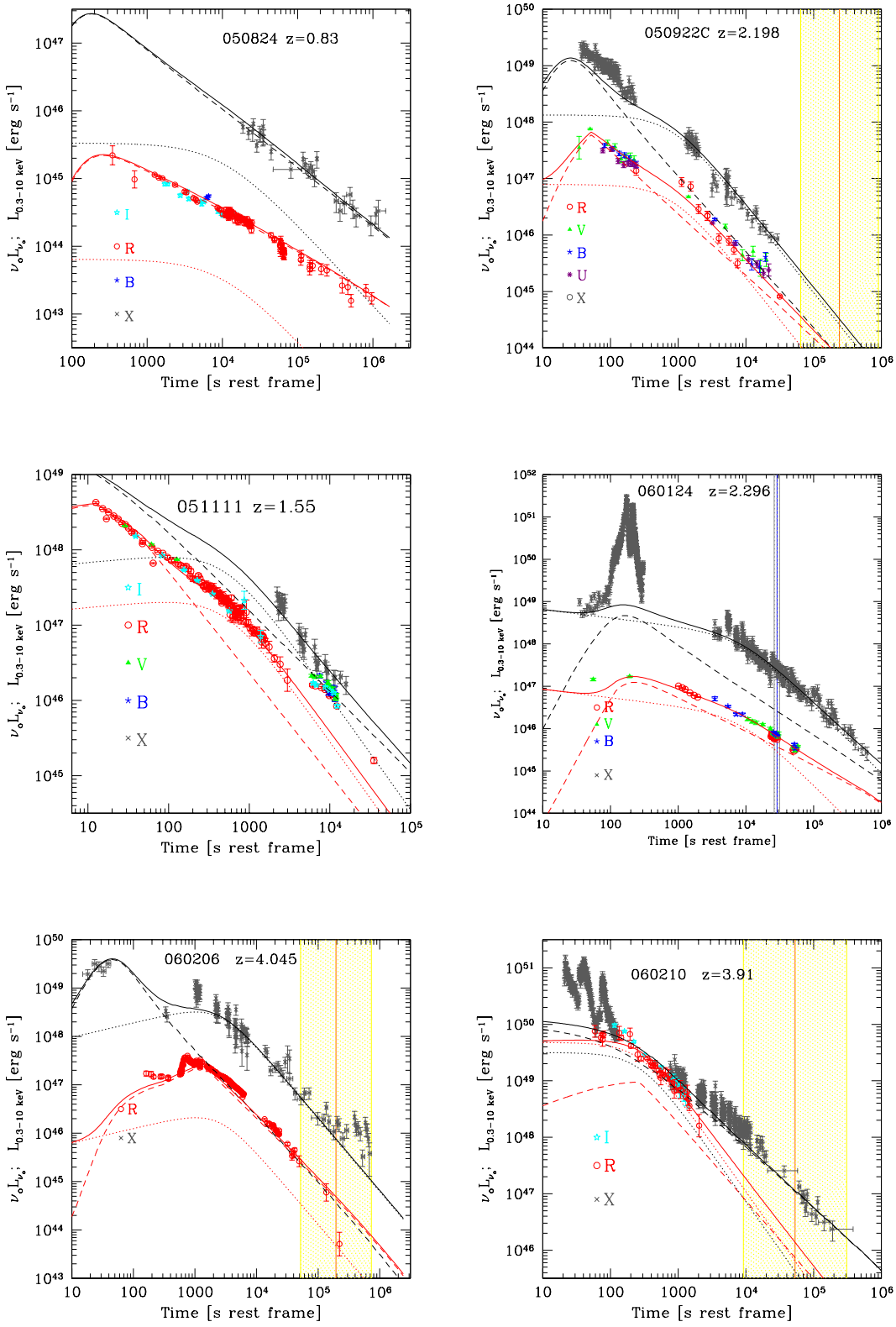

Figure 5.3: Same notes as in Fig 5.1

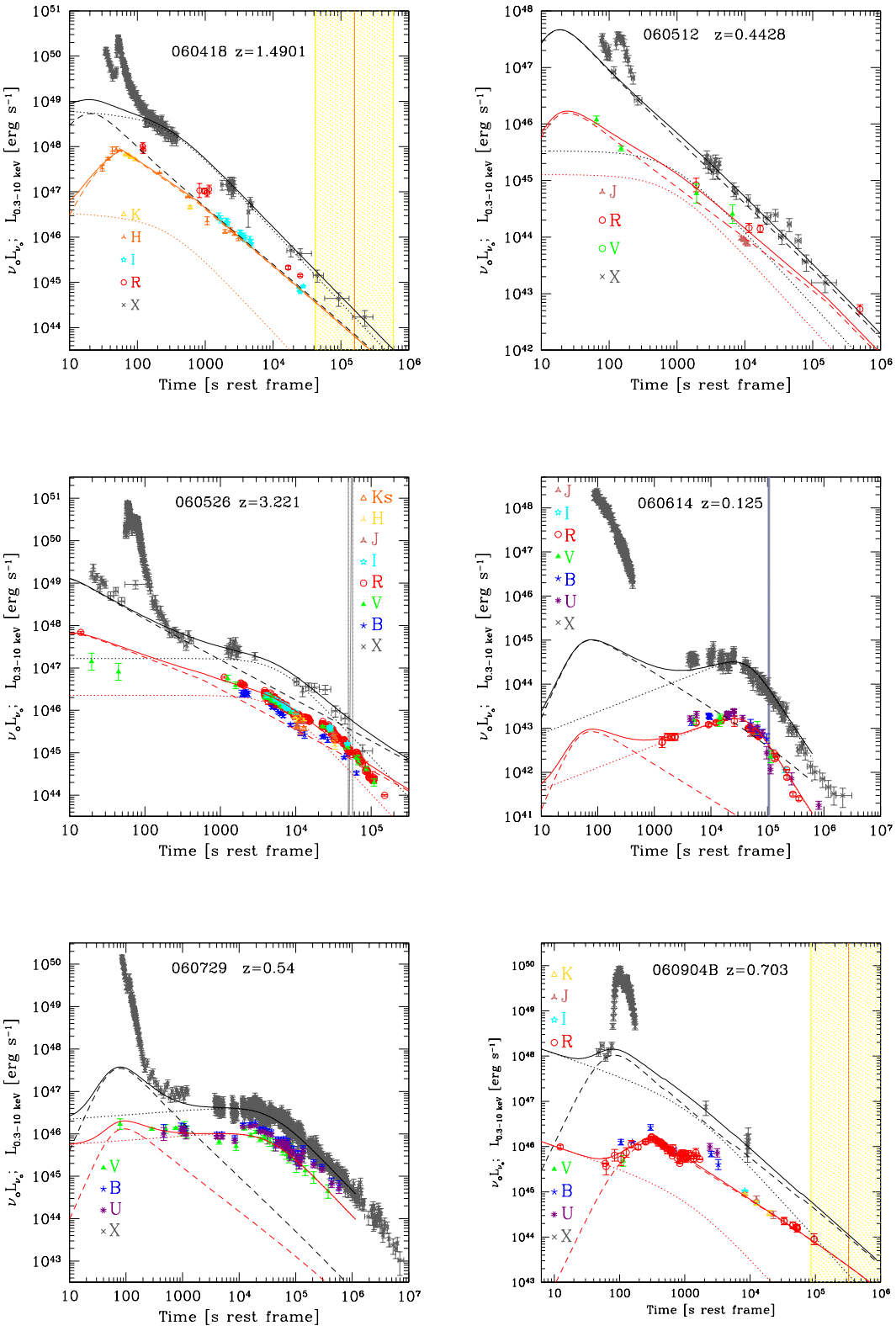

Figure 5.4: Same notes as in Fig 5.1

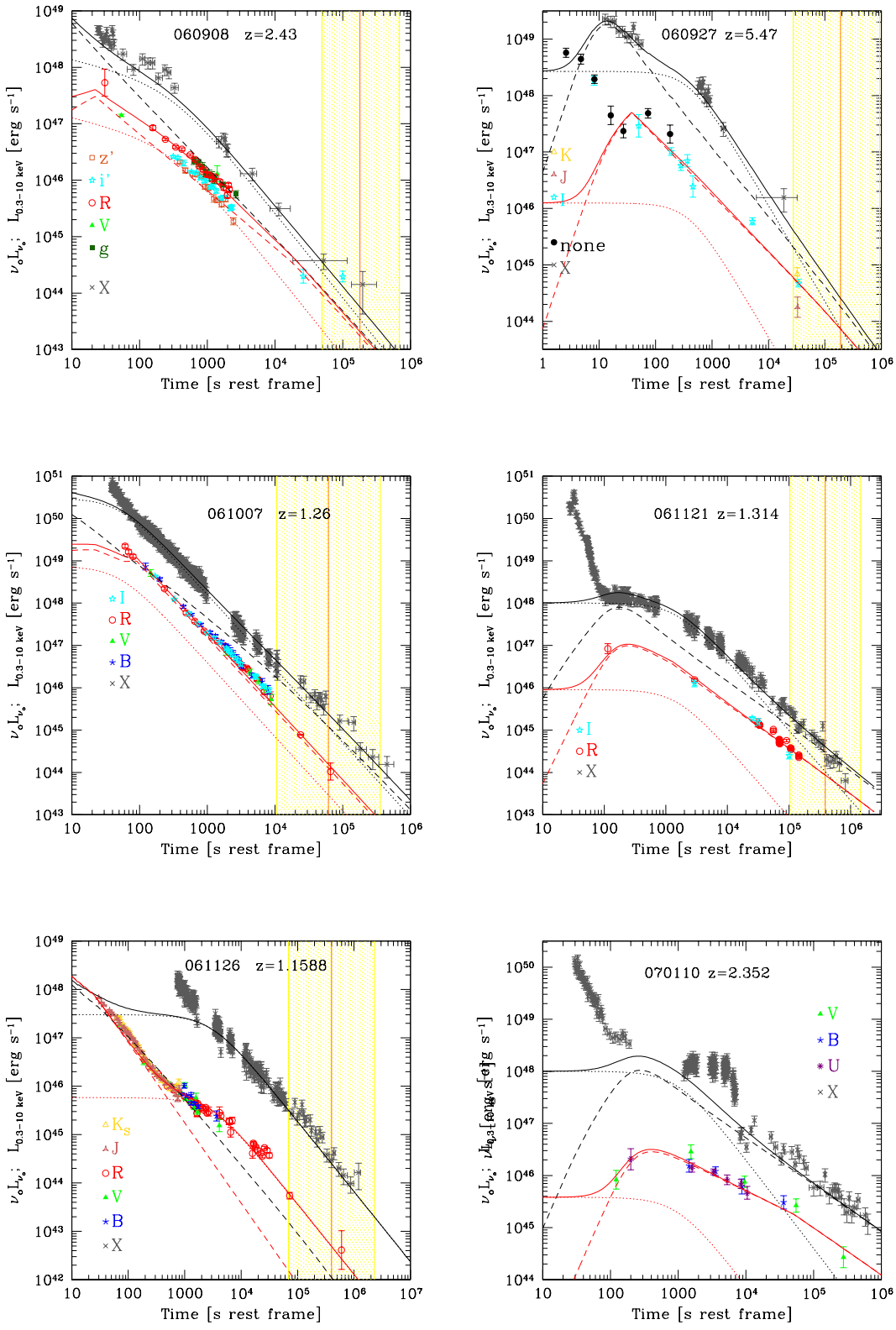

Figure 5.5: Same notes as in Fig 5.1

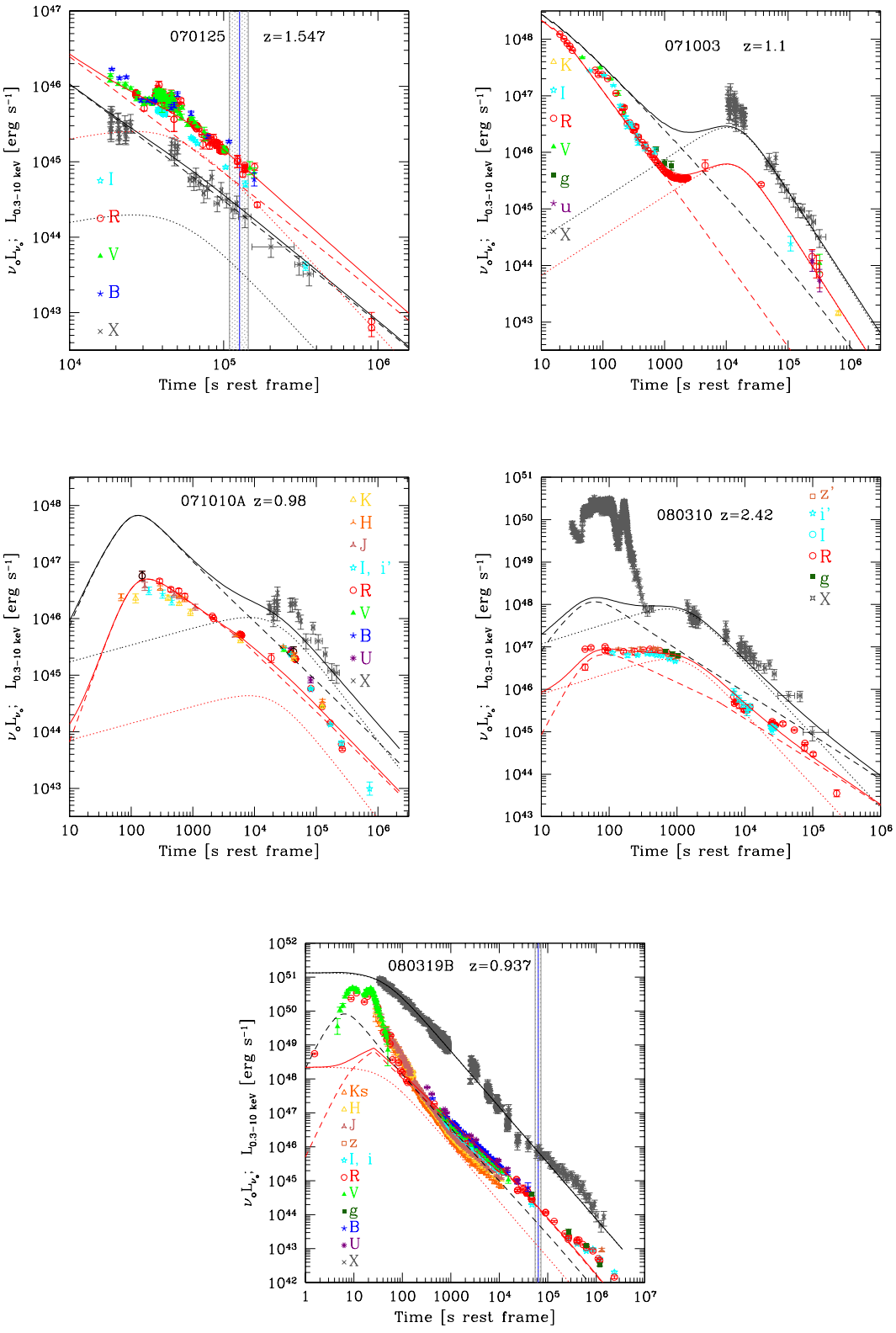

Figure 5.6: Same notes as in Fig 5.1

5.1.5 Modelling parameters distributions

Figs. 5.10 and 5.11 show the distribution of all our input parameters. For comparison, in these figures we report the values found by Panaitescu & Kumar (2002) for 10 pre–*Swift* bursts. Note that Panaitescu & Kumar (2002) give the collimation corrected value for the isotropic kinetic energy of the fireball after the early prompt phase. We have then divided this value by $(1 - \cos\theta_{\rm j})$ to get the isotropically equivalent value of E_0 to be compared with the values found for our bursts. Note that Γ_0 does not affect the properties of the afterglow after its onset, and is therefore not an important parameter for Panaitescu & Kumar (2002), who are fitting data taken much later than the afterglow onset (with the exception of GRB 990123). The afterglow parameters found for our bursts are rather standard, being similar to the ones obtained by Panaitescu & Kumar (2002) (see also Panaitescu & Kumar 2001a,b). The distribution of the circumburst density n_0 is narrower for the bursts in our sample, while the distributions of $\epsilon_{\rm e}$ and $\epsilon_{\rm B}$ are centred on smaller values.

In our interpretation the X–ray luminosity in the majority of cases is not produced by the afterglow, which is thus less energetic.

Most (25 out of 33) afterglows can be consistently described by the interaction of the fireball with a homogeneous medium. This is especially the case when the optical light curve indicates the onset of the afterglow itself (i.e. a very early rising phase), that cannot be reproduced with a wind-like density profile. The latter, in fact, produces almost flat optical light curves in the early phases. The homogeneous densities are very narrowly distributed around a mean value of $n_0 \sim 3$ cm^{-3}.

For eight GRBs (see Table 5.2), a better modelling can be achieved invoking a wind-like density profile. All but one of these eight bursts can be modelled with a value of the ratio of the mass loss rate and the wind velocity of $\dot{M}_{\rm w}/v_{\rm w} = 10^{-8}$ $(M_\odot$ yr$^{-1})/($km s$^{-1})$ that can correspond to $\dot{M}_{\rm w} = 10^{-5}$ $M_\odot$ yr^{-1} and $v_{\rm w} = 10^3$ km s^{-1}. The remaining burst require half of this value. Similarly to what had been found by Panaitescu & Kumar (2002) the afterglow parameters distribution are quite broad, i.e. they do not cluster around typical values. Exceptions are the density n_0 and the bulk Lorentz factor Γ_0.

Also the distributions of some Component II parameters (i.e. $T_{\rm A}$, $L_{T_{\rm A}}$ and $\nu_{\rm b}$) are rather broad, while $\beta_{\rm o}$ and the temporal slopes $\alpha_{\rm fl}$ and $\alpha_{\rm st}$ are more narrowly distributed. The values of $T_{\rm A}$ range from 10^2 to 10^4 s or more (in the rest frame), and are (anti–)correlated with the Component II luminosity at $T_{\rm A}$, as shown in Fig. 5.8. This confirm the correlation found by Dainotti, Cardone & Capozziello (2008). This results in a narrow distribution of $T_{\rm A} L_{T_{\rm A}}$ (Fig. 5.11).

The distributions of $\beta_{\rm o}$ and $\nu_{\rm b}$ must be taken with caution, since the model fixes only their combination, and only in a few GRBs they can be constrained separately (i.e. when the optical light curve is dominated by the Component II

emission and the spectral index during this phase is known).

The distribution of $\alpha_{\rm st}$ is intriguing, since it is centred around a mean value of 1.6. This is very close to 5/3, the predicted decay of the accretion rate of fall–back material (see also §5 where this point is discussed in more depth). The values of $\alpha_{\rm st}$ cluster around 0.

In Fig. 5.11 we show the distribution of $T_{\rm A}L_{T_{\rm A}}$, and in Fig. 5.8 we show $T_{\rm A}L_{T_{\rm A}}$ as a function of $E_{\rm iso}$. The two quantities are correlated (albeit poorly) and the energy contained in the late prompt emission (of which $T_{\rm A}L_{T_{\rm A}}$ is a proxy) is at most comparable with $E_{\rm iso}$. More frequently $T_{\rm A}L_{T_{\rm A}}$ is one or two orders of magnitude smaller than $E_{\rm iso}$, in agreement with the findings by Willingale et al. (2007).

Fig. 5.11 shows also the distribution of $E_{\rm iso}/[E_0 + E_{\rm iso}]$. This ratio represents η, the fraction of the total energy of the fireball required to produce the observed early prompt radiation. In the right panel of Fig. 5.7 this fraction is shown as a function of $E_{\rm iso}$. Although there is a weak positive correlation, the mean value is well defined and corresponds to $\eta \sim 0.1$.

5.1.6 Energetics

As the X–ray luminosity $L_{\rm X}$ is found to be often dominated by the late prompt emission, it does not provide a proxy for the afterglow bolometric luminosity. Since $L_{\rm X}$ exceeds what observed in the other spectral bands, the estimated luminosities and total energetics produced by the afterglow are radically smaller than what simply inferred from $L_{\rm X}$.

This exacerbates the problem of understanding why the prompt emission is larger than the afterglow one, if the former is dissipated in internal shocks. In fact, while in external shocks, believed to be responsible for the afterglow, the whole fireball kinetic energy is available, in internal shocks only a fraction of the relative kinetic energy between two colliding shells can be dissipated as radiation. If such fractions are similar, the "bolometric afterglow fluence" is expected to be a factor ∼10 larger than the bolometric early prompt fluence. The opposite is observed, and the discrepancy is more extreme if $L_{\rm X}$ provides only an upper limit to the afterglow contribution, as in our interpretation.

Bearing in mind that it is often dangerous to claim correlations between luminosities or energetics, since both quantities are function of redshift, we can compare the left with the right panel of Fig. 5.7. It can be seen that the correlation between the Component II energetics measured by $T_{\rm A}L_{T_{\rm A}}$ and $E_{\gamma,{\rm iso}}$ is stronger than the correlation between the kinetic energy (after the gamma ray prompt) E_0 and $E_{\gamma,{\rm iso}}$. A least square fit yields $[T_{\rm A}L_{T_{\rm A}}] \propto E_{\gamma,{\rm iso}}^{0.86}$ (chance probability $P = 2\times10^{-7}$), and $E_0 \propto E_{\gamma,{\rm iso}}^{0.42}$ (chance probability $P \sim 10^{-3}$). If the $T_{\rm A}L_{T_{\rm A}}$–$E_{\gamma,{\rm iso}}$ relation is not a mere product of the common redshift dependence (which however should also affect the E_0–$E_{\gamma,{\rm iso}}$ relation) this suggests that the early and the late

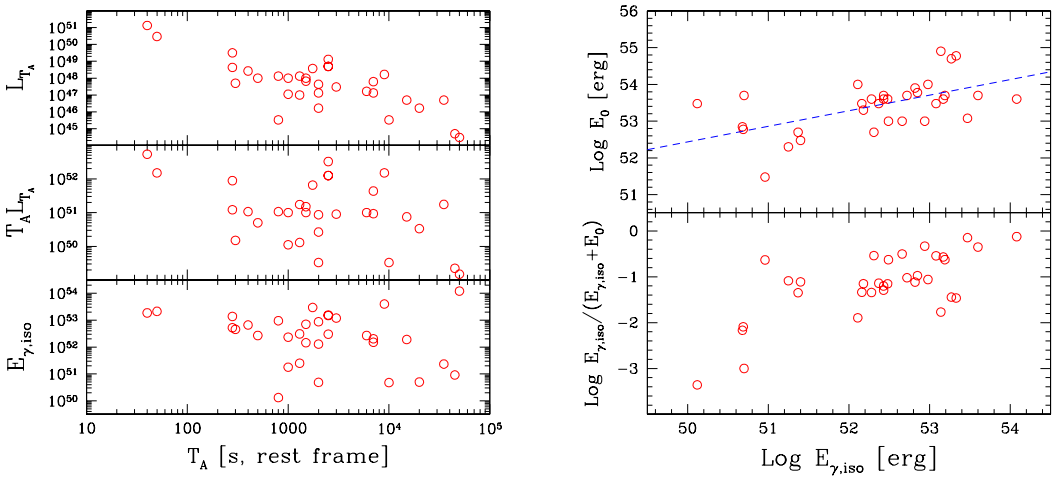

Figure 5.7: *Left panel*: The luminosity of the late prompt emission L_{T_A} (in erg s^{-1}) at T_A, the corresponding energy $T_\mathrm{A}L_{T_\mathrm{A}}$ (in erg) and the isotropic energy $E_{\gamma,\mathrm{iso}}$ (in erg) as functions of T_A. Note that L_{T_A} anti–correlates with T_A, in such a way that the energy $T_\mathrm{A}L_{T_\mathrm{A}}$ has a relatively narrow distribution (see also the corresponding histogram in Fig. 5.11. *Right top panel*: the kinetic energy E_0 after the prompt emission as a function of $E_{\gamma,\mathrm{iso}}$. The dashed line is a least square fit, yielding $E_0 \propto E_{\gamma,\mathrm{iso}}^{0.42}$ (chance probability $P \sim 10^{-3}$, excluding GRB 070125). *Right bottom panel*: the efficiency of the prompt emission estimated as $E_{\gamma,\mathrm{iso}}/(E_{\gamma,\mathrm{iso}}+E_0)$ as a function of $E_{\gamma,\mathrm{iso}}$. There seems to be weak correlation, in the sense that weaker bursts would have the smaller efficiency. See the corresponding distribution in Fig. 5.11. Here and in the other figures, the plotted values of $E_{\gamma,\mathrm{iso}}$ are neither bolometric nor K–corrected, but refer to the observed 15–150 keV range.

prompt phases of emission are related.

In Fig. 5.9 (top panel) $\epsilon_\mathrm{e}E_0$ (which can be considered as an upper limit to the bolometric afterglow luminosity) is compared to $E_{\gamma,\mathrm{iso}}$, the energetic of the gamma ray prompt emission as measured in the 15–150 keV band (rest frame). $E_{\gamma,\mathrm{iso}}$ exceeds the afterglow energetics by almost two orders of magnitudes. In the bottom panel of the same figure $\epsilon_\mathrm{e}E_0$ is plotted against the energetics of the Component II emission E_late, approximated by the quantity $T_\mathrm{A}L_{T_\mathrm{A}}$. These quantities do not correlate, suggesting that they are two separated components.

To summarise: all indications gathered from the analysis of the energetics suggest that what we have called "Component II" is a phenomenon not related to the afterglow, but it is more connected to the same engine producing the early prompt. Furthermore, the energetics associated to the afterglow emission is on average a small fraction of the total energy of the burst.

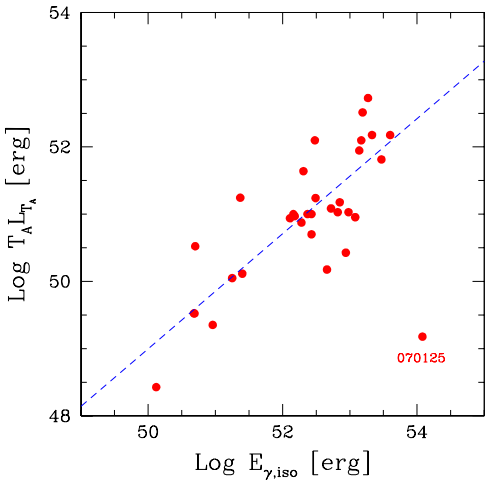

Figure 5.8: Energy of the Component II emission, estimated as $T_{\rm A}L_{T_{\rm A}}$, as a function of the isotropic energy of the prompt emission, $E_{\gamma,{\rm iso}}$. The dashed line corresponds to the least square fit, $[T_{\rm A}L_{T_{\rm A}}] \propto E_{\gamma,{\rm iso}}^{0.86}$ (chance probability $P = 2 \times 10^{-7}$, excluding the outlier GRB 070125).

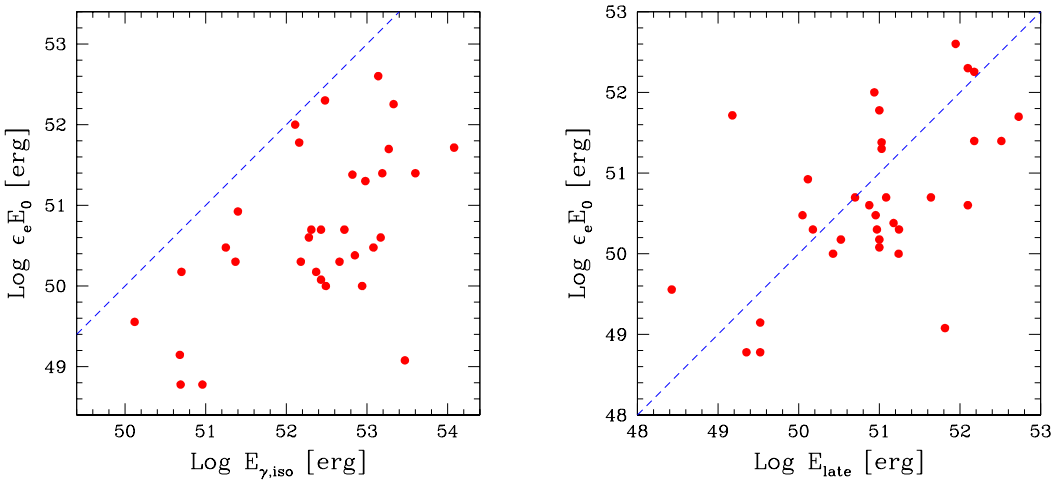

Figure 5.9: The energetics of the afterglow component, estimated as $\epsilon_e E_0$, as a function of: (top panel) $E_{\gamma,{\rm iso}}$, the energetics of the prompt emission as measured in the 15–150 keV band (rest frame) (top panel) – the dashed line corresponds to equal values; (bottom panel) $E_{\rm late}$, the energetics of the late prompt emission, as measured in the (rest frame) 0.3–10 keV band and approximated by $T_{\rm A}L_{T_{\rm A}}$.

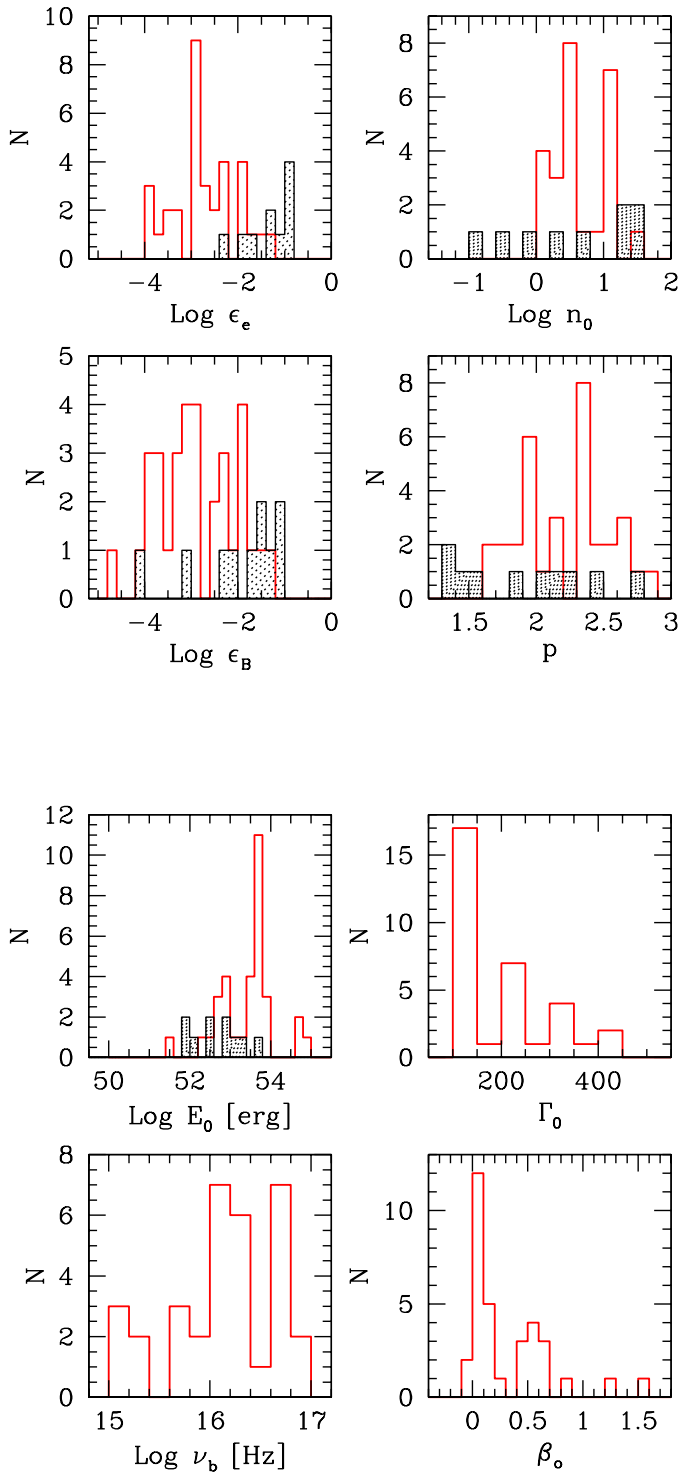

Figure 5.10: Top four panels: distribution of the values of the micro-physical parameters ϵ_e and ϵ_B homogeneous density n_0 and electron slope p. Bottom four panels: distribution of the isotropically equivalent initial kinetic energy E_0, bulk Lorentz factor Γ_0, break frequency $\nu_b$and optical spectral index for the Component II emission β_0. The hatched areas correspond to the distribution of parameters found by Panaitescu & Kumar (2002) fitting the afterglow of 10 pre–*Swift* bursts. They are shown for comparison.

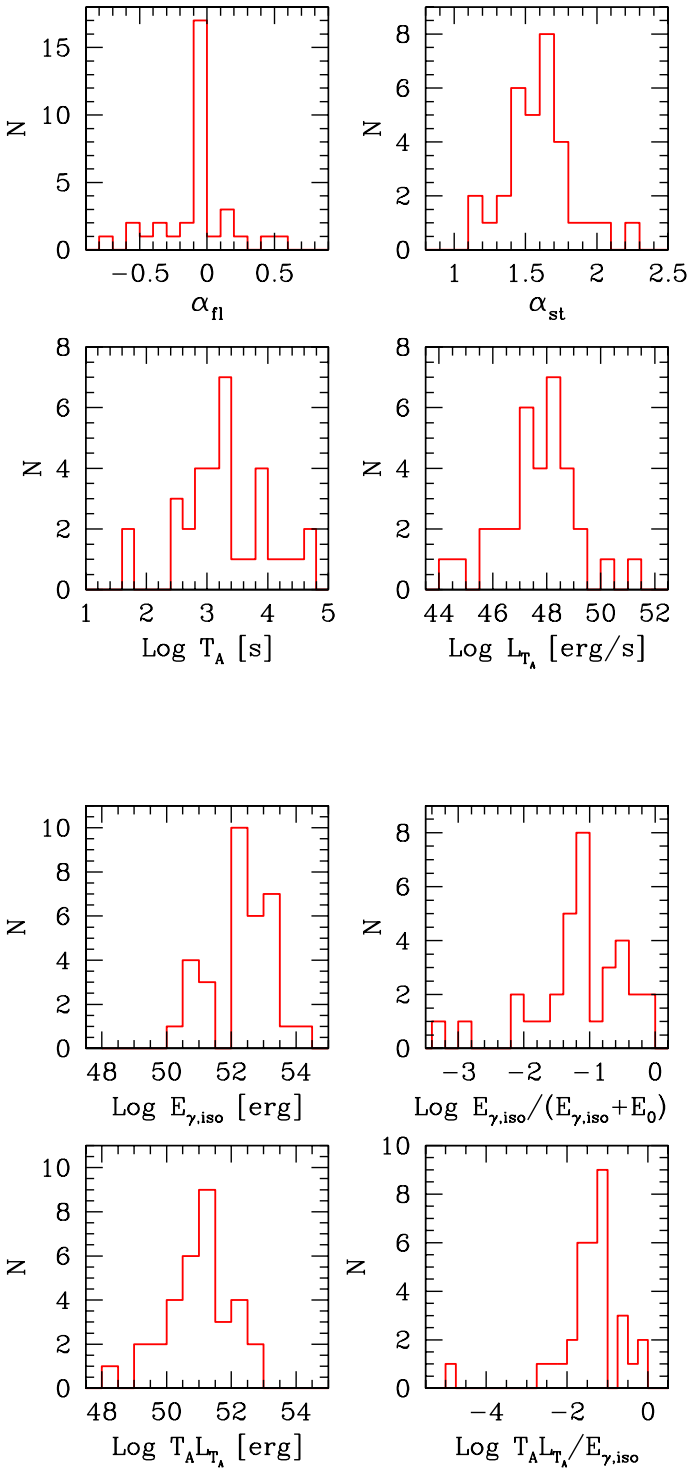

Figure 5.11: Top four panels: distributions of the decay indices of the Component II emission, $\alpha_{\rm fl}$ and $\alpha_{\rm st}$, of $T_{\rm A}$ and of the 0.3–10 keV luminosity at the time $T_{\rm A}$. Bottom four panels: distributions of the isotropic energy $E_{\gamma,{\rm iso}}$ of the early prompt radiation, of the ratio $E_{\gamma,{\rm iso}}/(E_{\gamma,{\rm iso}} + E_0)$, which provides an estimate of the efficiency of the prompt emission; of the energy $T_{\rm A}L_{T_{\rm A}}$, and of the ratio $T_{\rm A}L_{T_{\rm A}}/E_{\gamma,{\rm iso}}$.

5.2 A first step towards a more physical model?

The two components modelling I presented in the previous sections allows us to well represent the broad band optical and X–ray light–curves of all the GRBs in our sample. In order to have this good agreement with the observed light–curves behaviour we had to consider a additional component to the standard forward shock afterglow emission. In our light–curves analysis this second component is treated in a fully phenomenological way with the aim of minimising the number of free parameters but when looking at the Component II parameters distributions we can infer some information that can help us in making a first step towards a more physical description of this additional component. As discussed in the introduction, there has been already a blooming of theoretical ideas, but a general consensus has not yet been reached. Our findings can shed some light and help to discriminate among the different proposals. In this section I will again follow the physical interpretation that we proposed in Ghisellini et al. (2009a, 2009b).

The distributions of these parameters are not particularly clustered around mean values, except for the time decay slopes $\alpha_{\rm fl}$ and $\alpha_{\rm st}$ (see below). However, this should not be taken as a potential problem for the proposed idea, since even the well established afterglow model, when applied to the optical and X–ray afterglows of pre–Swift GRBs, yield broad parameter distributions (see Fig. 5.10 and Panaitescu & Kumar 2002).

The most important results of our analysis is the found distribution of $\alpha_{\rm st}$, the decay index of Component II after $T_{\rm A}$.

From our modelling the steep decay of the late prompt emission can be described by a power–law with slope $\alpha_{\rm st} \sim 1.6$. This is intriguingly similar to the time dependence of the mass accretion rate during the fall–back phase, and to the average decay of the X–ray flare luminosity, as analysed by Lazzati, Perna & Begelman (2008). This is *not* the average decay slope observed: the X–ray and optical light curves are flatter than $L(t) \propto t^{-5/3}$ (see Fig. 5.13), but this is due to the contribution, especially at early and late times, and in the X–rays, of the afterglow contribution. Fig. 5.14 shows the results of our light curve modelling for the optical and X–rays bands.

The late prompt light curves are indeed steeper, on average, than the sum of the two components that reproduce the data. We consider this as a main result of our analysis, because it suggests that the late prompt emission can be interpreted as due to the late time accretion on to a black hole of fall-back mass, namely material that failed to reach the escape velocity from the exploding progenitor star, and falls back.

According to analytical results (Chevalier 1989) and numerical simulations (e.g. Zhang et al. 2007), the accretion rate decreases in time as $t^{-\frac{5}{3}}$, and can continue for weeks, enough to sustain late prompt emission even at very late times. Our finding also agrees with that obtained by Lazzati et al. (2008) by analysing X-ray

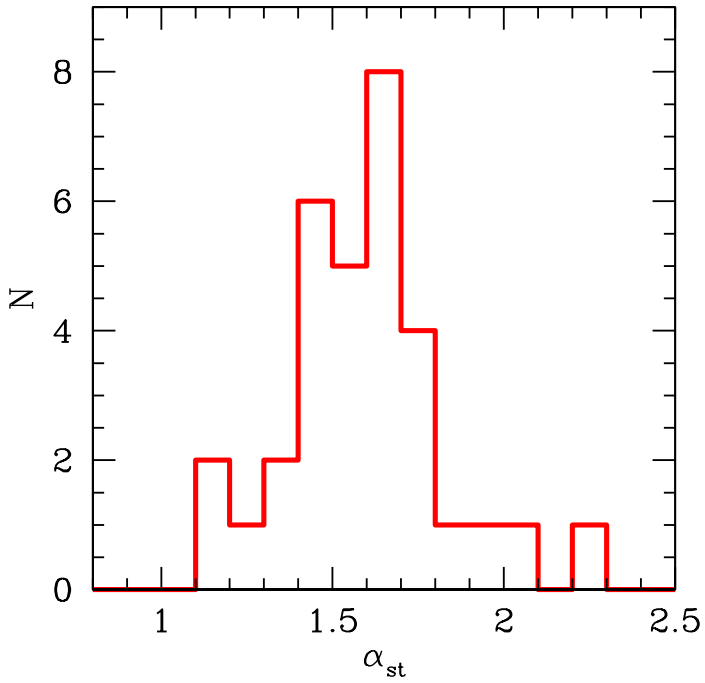

Figure 5.12: The distribution of the decay index α_{st} of the second component. This is the decay index after T_A. Note that the α_{st} distribution is well clustered around the value 5/3 (see text).

flares. They found that the average luminosity of X-ray flares, for a sample of GRBs with known redshift, also decays like $t^{-\frac{5}{3}}$.

Such an agreement then suggests that both the X–ray flares and the late prompt emission have a common origin, related to the accretion of the fall-back material. It remains to be explained why this phase is observed after T_A that in some cases can be as long as 10^4 s or more, while the simulations predict a quasi-constant accretion rate for $10^2 - 10^3$ s (MacFadyen, Woosley & Heger 2001). There are at least two possibilities. The first one is suggested by the simulations of Zhang et al. (2007) (see their fig. 2) which include the effect of the reverse shock running through the fall-back material. When the reverse shock reaches the inner base, the material is slowed down, and thus the accretion rate is enhanced. The asymptotic $t^{-\frac{5}{3}}$ phase can thus be delayed. The second possibility has been suggested by Ghisellini et al. (2007): even if the total flux produced by the late prompt phase is decaying at the rate $t^{-\frac{5}{3}}$, a decreasing Γ implies that the observed emission comes from an increasing surface ($\propto \Gamma^{-2}$), making the observed decay flatter than $t^{-\frac{5}{3}}$, until, at T_A, $\Gamma \sim 1/\theta_j$. After T_A, the whole emitting surface contributes to the

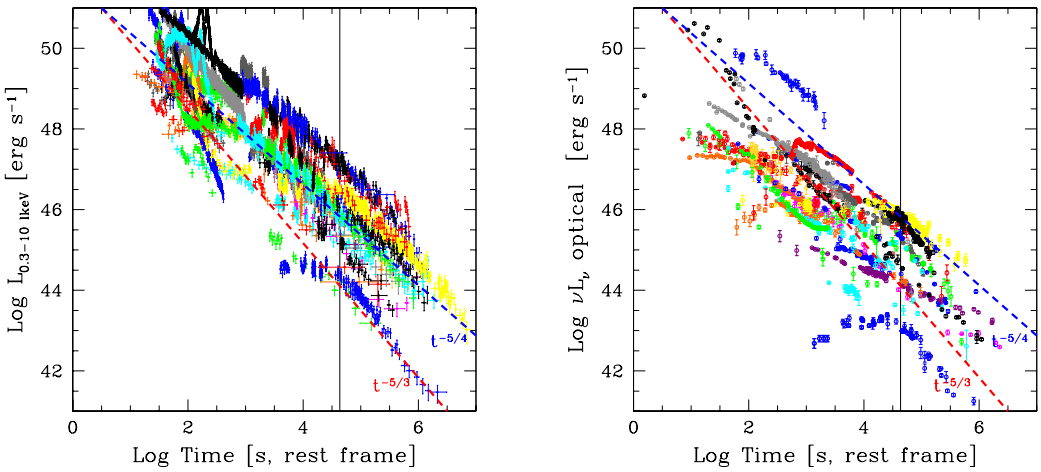

Figure 5.13: The light curves of all the 33 GRBs in the X–rays (left panel) and optical (right panel). For comparison, the dashed lines correspond to $t^{-5/4}$ and $t^{-5/3}$, as labelled. Especially in the X–rays, the luminosity profile seems to be flatter than $t^{5/3}$ and closer to a $t^{-5/4}$ decay. However, this behaviour is due to the contribution in some GRBs of the afterglow emission at late times, flattening the overall light curve. See Fig. 5.14 for comparison.

detected flux, and the flux decreases as $t^{-\frac{5}{3}}$.

Fig. 5.14 shows that the sum of the late prompt and afterglow emission makes the optical fluxes to cluster. This occurs because the late prompt emission, though usually not dominant in the optical, becomes dominant in case of subluminous events. This effect avoids reaching low optical luminosities and narrows the distribution of the optical luminosities at a given time . The vertical dotted line in the figure corresponds to the time (12 h) at which we (Nardini et al. (2006, 2007, 2008, 2009a), Liang & Zhang (2006) and Kann, Klose & Zeh (2006)) found a remarkable clustering of the optical luminosities around two well separated values. However, the total optical luminosities (right-hand bottom panel of Fig. 5.14) are more dispersed than the afterglow ones (middle bottom panel).

The Component II parameters analysis inspired us in Ghisellini et al. (2009a) and Ghisellini, Nardini & Ghirlanda (2009) to try to construct a simple heuristic scenario. I will here briefly report the discussion we proposed in Ghisellini, Nardini & Ghirlanda (2009). A rapidly rotating black hole is formed after the death of a massive star. The large angular momentum of the material surrounding the black hole prevents this material to immediately fall inside the black hole driving the formation of a very dense torus that, because of viscosity and angular momentum conservation, spreads allowing the accretion to start. This accretion phase corresponds to the "real" gamma ray prompt emission, possibly mediated

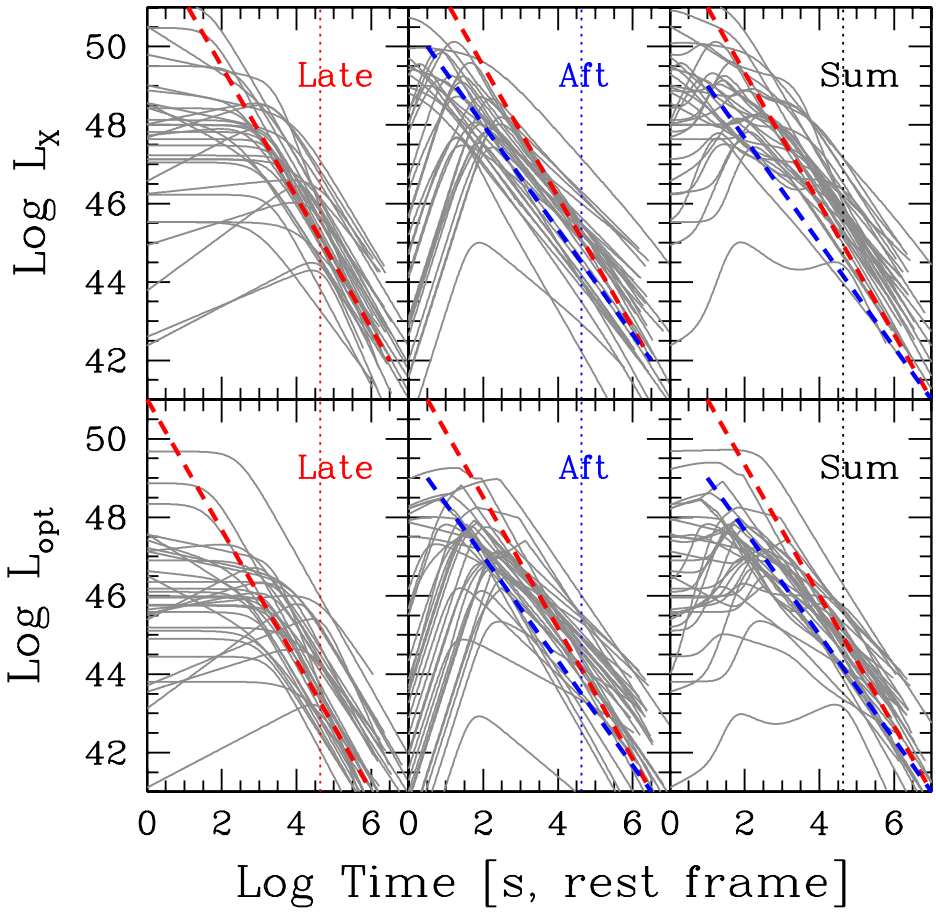

Figure 5.14: The light curves, as inferred from the modelling, for the 33 GRBs in the X–ray (top panels) and optical (bottom panels) bands. The late prompt (left panels), afterglow (middle panels) and total (left panels) emission are shown. The vertical dotted lines correspond to 12 hours. Note that the total optical luminosity at 12 hours is more clustered than the late prompt and afterglow luminosities. The dashed lines in the left panels correspond to $L \propto t^{-5/3}$, while in the middle and right panels also decays $L \propto t^{-5/4}$ are shown for reference.

by the strong magnetic field formed in the vicinity of the black hole, making the Blandford & Znajek mechanism at work. We need to extract only a few per cent of the total energy that can be extracted from a two solar masses maximally rotating black hole that is of the order of 10^{54} erg. After the accretion of the dense torus (gamma ray prompt event) the discontinuity shown by the observed X–ray light–

curve during the early time steep phase, should be associated to a discontinuity in the accretion rate. This discontinuity could be associated to the transition from the end of the accretion of the material of the dense torus and the beginning of the accretion of the fallback material that persists accreting at a reduced rate following the typical fallback profile. A reduced accretion most likely corresponds to a reduced magnetic field in the vicinity of the black hole, and so to a reduced capacity to extract the spin energy of the black hole. Superposed to this continuous accretion, the fragmentation of the accreting material, can produce some suddenly increased accretion. This mechanism could be responsible to the emission of the flares often observed in the X–ray light–curves.

The association of our light–curves modelling Component II emission with the "late prompt" radiation proposed by Ghisellini et al. (2007) (see also §2.4), should be intended as a first possible link with a physical description of this phenomenologically treated component. This choice is strengthened by the intriguing similarity between the late times Component II temporal index and the predicted decay of the accretion rate of fallback material onto the black hole.

Here I present an illustrative example of the possibility to use our modelling to better discriminate different theoretical model. The proposed scenario can be contrasted with the alternative idea that GRBs are characterized by two jets with different opening angles (see the introduction). In the latter interpretation, if the line of sight lies within the wide cone but outside the narrow one, the emission from the narrow jet will be observable when Γ has decreased to $\Gamma \sim 1/\theta_{\rm v}$ and the corresponding afterglow light curve can reproduce the flat-steep-flat behaviour and present a break (at $T_{\rm A}$). However, it is hard to explain why the flat-steep-flat trend is not observed in the optical, as in a (narrow jet) afterglow the optical and X–ray fluxes should temporally track each other. The "late prompt" scenario appears to provide a better interpretation of the data.

Chapter 6

Jet breaks

6.1 *Swift* era jet break issue

A currently hot debate concerns the absence of jet breaks in the light curves of GRB afterglows.

Gamma Ray Bursts emit an isotropically equivalent energy up to a few 10^{54} erg, i.e. more than one solar rest mass (e.g. Amati et al. (2002)). For example GRB 080916c located at redshift 4.35 emitted during the prompt gamma ray event an isotropic equivalent energy $E_{\gamma,\mathrm{iso}} = 6.5 \times 10^{54}$ erg that corresponds to about $4\mathrm{M}_{\odot} \times c^2$ (Greiner et al. 2009). The true energy budget is reduced to more reasonable levels if their emission is collimated into jets (e.g. Frail et al. (2001)). Indeed, theory and observations suggest that GRBs are jetted sources. The jet aperture angle, $\theta_{\mathrm{j}} \sim 5 - 10$ degrees, manifests itself through a steepening of the light curve, the so called jet break. When the bulk Lorentz factor Γ of the GRB ejecta becomes $\Gamma < 1/\theta_{\mathrm{j}}$, a break in the afterglow light curve is observed because the geometric collimation of the jet "prevails" over the relativistic beaming. The measure of the time of the break, t_{jet}, allows to derive θ_{j} under the standard afterglow model assumptions (Rhoads 1997; Chevalier & Li (2000)).

The jet break was routinely observed in the pre–*Swift* era, but it is elusive now in *Swift* bursts, which are much well sampled in the early afterglow phases. Because of its geometrical origin the jet break is expected to be achromatic and therefore should show up as a light curve steepening appearing contemporaneously in the optical and in the X–rays. As discussed in the previous sections, in the *Swift* era most of the optical and X–ray light–curves do not track each other and only in a few cases achromatic breaks have been observed in the *Swift* –era GRBs. This has cast doubts about the real presence of jet breaks, on the amount of collimation and on the real energetics of GRBs.

Unless we accept that GRBs are isotropic sources, but with an extremely large energy, one possible answer is that jet breaks do exist but we are missing them.

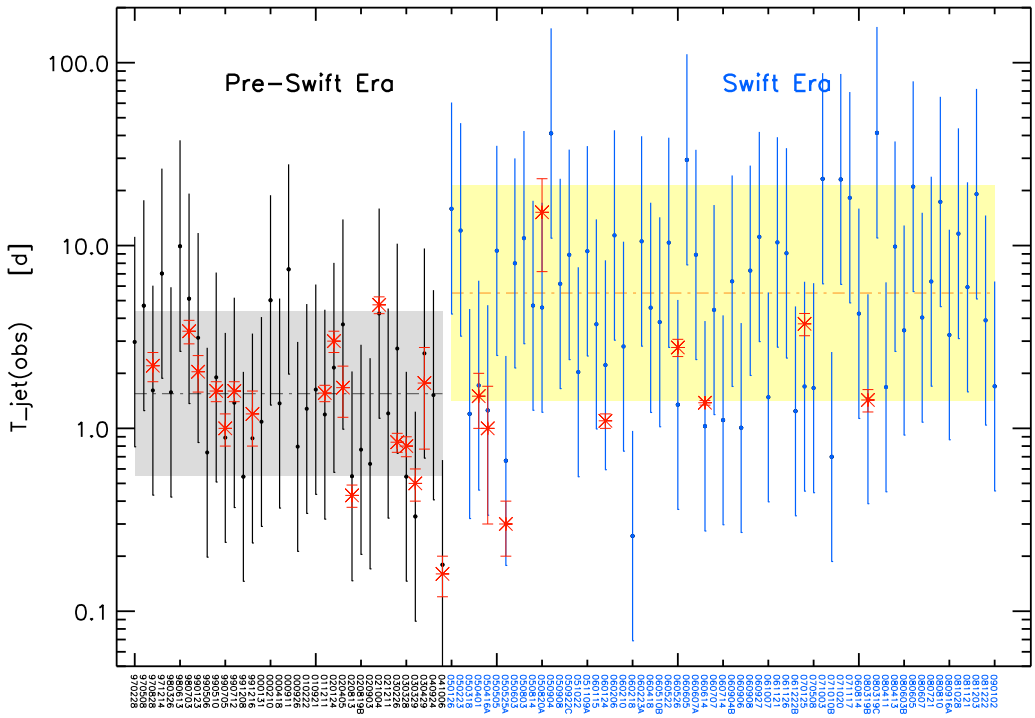

Figure 6.1: Jet break times (observer frame) for all the bursts (updated to Jan 2009) with measured redshifts and well constrained peak energy. Filled points are the jet break predicted with the aid of the $E_{\rm peak} - E_\gamma$ correlation (Ghirlanda et al. 2004). Shaded regions show the 1σ dispersion around the average values of $t_{\rm jet}$ for the "Pre–*Swift* Era" (i.e. before the *Swift* launch in Nov. 2004) and in the "*Swift* Era". Red crosses are the real measured jet break times. Note the lower number of jet breaks measured (red crosses) in the *Swift* –Era wrt the Pre–*Swift* era. Note also that the $t_{\rm jet}$ in *Swift* bursts is expected at later times with respect to the Pre-Swift bursts. This is mostly due to the higher redshift of *Swift* bursts. This motivates the "hunting" of jet break times in the Optical light curve at late times.

In order to measure $t_{\rm jet}$ two conditions should be met:

(i) the light curve should be sampled before and well after the time of the jet break (which occurs systematically at later times for *Swift* bursts with respect to pre–*Swift* events (see Fig. 6.1[1]);

(ii) the light curve should be the "standard" afterglow emission of the burst, because the jet break is a feature of the afterglow emission.

[1]Image inserted thanks to the courtesy of Giancarlo Ghirlanda and inserted in Ghiranda et al. (ESO-VLT proposal period 84A) and in Nardini et al. (INAF-TNG proposal period AOT20)

These conditions are fulfilled by the GRBs belonging to the sample we analysed in this chapter and within the proposed two components modelling scheme, some light can be shed on the puzzling issue about jet breaks.

6.2 Jet break issue in the two components light–curves modelling

In the scenario we propose, the light–curve comprises two components of which only the afterglow one should present a jet break (at $t_{\rm jet}$). It follows that jet breaks should be more often detectable in the optical, rather than being achromatic, and the after-break slopes may be shallower than predicted by the closure relations. The second component is due to a completely different mechanism with respect to the standard afterglow emission and no jet break is therefore expected if the light curve is dominated by Component II. If for example this component is produced by a mechanism like the one described in the "late prompt" scenario, no break is expected after $T_{\rm A}$. In such a case no information about the jet collimation angle can be inferred by the shape of the light curve.

In the two components modelling of the optical and X–ray light curves we can identify different cases related to the observation of jet breaks:

i) **No jet breaks**. When the flux is dominated by the Component II emission in both the optical and X–ray bands, jet breaks may become unobservable. The Component II emission (at least after a few thousand seconds) does so for six GRBs of the sample (namely GRB 050319, GRB 050408, GRB 060614, GRB 060729, GRB 061126 and GRB 071003). Therefore, for these bursts, no jet break is predicted to be visible if the late prompt light curve continues unbroken for a long time if the late prompt component instead breaks, we might erroneously interpret this as a jet break.
An example is GRB 060729 shown in the left panel of Fig. 6.2.

ii) **Achromatic jet breaks**. Vice-versa, an achromatic jet break should be observed when both in the optical and X–ray light curves the afterglow emission prevails, at least when the jet break is likely to occur. 16 GRBs of the sample could show such an achromatic break (GRB 050318, GRB 050401, GRB 050416A, GRB 050802, GRB 050820A, GRB 050824, GRB 060512, GRB 060904B, GRB 060908, GRB 060927, GRB 061121, GRB 070110, GRB 070125, GRB 071010A, GRB 080310 and GRB 080319B). Emission in several of these bursts, although dominated by afterglow emission, especially in the X–ray band, at late times, still comprises a relevant contribution from the Component II. Therefore, the steepening of their light curve after $t_{\rm jet}$ should be shallower than what the standard afterglow theory predicts.

See for example the case of GRB 050820a shown in the right panel of Fig. 6.2. In this case the optical light curve is dominated by the "standard afterglow" up to late times and a clear jet break is observed. The X–rays light curve, instead, is dominated by the second component only at early times. The "standard afterglow" becomes dominant in the X–rays only at later times unveiling the possible presence of an achromatic break.

iii) **Chromatic jet breaks**. When the Component II is dominating in one band, and the afterglow in the other, a jet break should be visible only in the afterglow dominated band. According to our findings, a jet break could be present in the optical but not in the X–rays band in nine GRBs (GRB 050525A, GRB 050730, GRB 050801, GRB 050922C, GRB 060124, GRB 060206, GRB 060418, GRB 060526 and GRB 061007). Instead, two GRBs (GRB 051111 and GRB 060210) could show a jet break in X–rays but not in the optical.
Consider as an example the case of GRB 060124, shown in the bottom panel of Fig. 6.2. The optical bands are dominated by the "standard afterglow" and shows a break. The X–ray emission is dominated by the Component II and the light curve after $T_{\rm A}$ can be well fitted by a single power law without requiring any further break. Note that in the pre–*Swift* era the X–ray observations were not as dense a the optical light curves. Therefore most of the pre–*Swift* jet breaks have been observed only in the optical bands.

In Figs 5.1–5.6, we indicate the time at which a jet break has been reported to be detected or the time at which a jet break is expected to be seen if the burst were to follow the $E_{\rm peak} - E_\gamma$ (Ghirlanda) relation (Ghirlanda, Ghisellini & Lazzati 2004, updated in Ghirlanda et al. 2007) (see the figure caption). The latter ones are estimated only for bursts with measured $E_{\rm peak}$, the peak energy of the $\nu F\nu$ spectrum of the proper prompt emission. We found no contradictory cases (i.e. an observed jet break occurring in a Component II dominated GRB), except for GRB 060614. When late time optical photometry is available and the optical light curve is dominated by the standard afterglow the observed jet breaks are consistent within errors with the predictions of the Ghirlanda relation.

There are some additional bursts for which the presence of a jet break has been claimed in the literature. For instance, in GRB 050319, Cusumano et al. (2006) suggest that the break in the X-ray light curve at 27000 s (observed time) could be a jet break, but also discuss the problems with this interpretation due to the unusual pre and post break slopes. In our scheme, the observed break simply corresponds to $T_{\rm A}$.

For GRB 050730, Pandey et al. (2006) consider the change of slopes at $\sim$0.1 d (observed time) in the optical light curve as indicative of a jet break. In our interpretation, instead, the change of the flux decay slope is due to the late prompt emission providing a relevant contribution after $\sim 3 \times 10^3$ (rest frame time).

Malesani et al. (2007) claim the presence of a possible jet break in the optical light curve of GRB 070110 at ∼5 d (observed time). According to our findings, this can indeed be a jet break that should also be visible in X–rays.

In the light curves examined here, there are also a few examples of slope changes that could be jet breaks, but for which we could not find any report in the literature. The optical light curve of GRB 060206 may be one of such cases (see the last optical point in Fig. 6.2). For this GRB, the presence of the jet break is expected only in the optical, since the X-rays are dominated by the late prompt component. Note that the corresponding $t_{\rm jet}$ would make this burst consistent with the Ghirlanda relation (see the vertical grey line in Fig. 6.2).

Another example is visible in the X-ray flux decay of GRB 061121, at $\sim 10^5$ s (rest frame, see Fig. 5.5). Unfortunately, there are no optical data at this late time to confirm it. Again, if this is a jet break, the burst would be consistent with the Ghirlanda relation (see the vertical grey line in Fig. 5.5).

Also in GRB 071010, there could be a jet break in optical, after $\sim 10^5$ s (rest frame, see Fig. 5.6) but its interpretation is difficult because of an optical/X–ray flare occurring just before. Finally, for GRB 080310, a steepening of the optical light curve after $\sim 10^5$ s (rest frame, see Fig. 5.6) could be a jet break, as also supported by a steepening in the X–ray light curve, i.e. (marginally) dominated by the afterglow component.

6.3 Observative proposals

As already discussed, the big effort has been made in order to obtain a fast optical follow up in the first hours after the trigger in order to study the complex early time afterglow evolution. On the other hand the high GRB detection rate (one every few days or more) and the large amount of observing time spent for the early afterglow observations, made the late times (1-3 days after the trigger) follow up strategy less intense. This lack of long lasting optical follow ups prompted us in participating in two calls for proposals for observing time at the ESO-VLT and INAF TNG telescopes with the aim of testing the presence/absence of jet break steepening in the optical GRB light curves.

In appendix 10.4 I will report part of the Nardini et al. INAF-TNG proposal (Period AOT20 (Aug09–Jan10)) that has been recently approved.

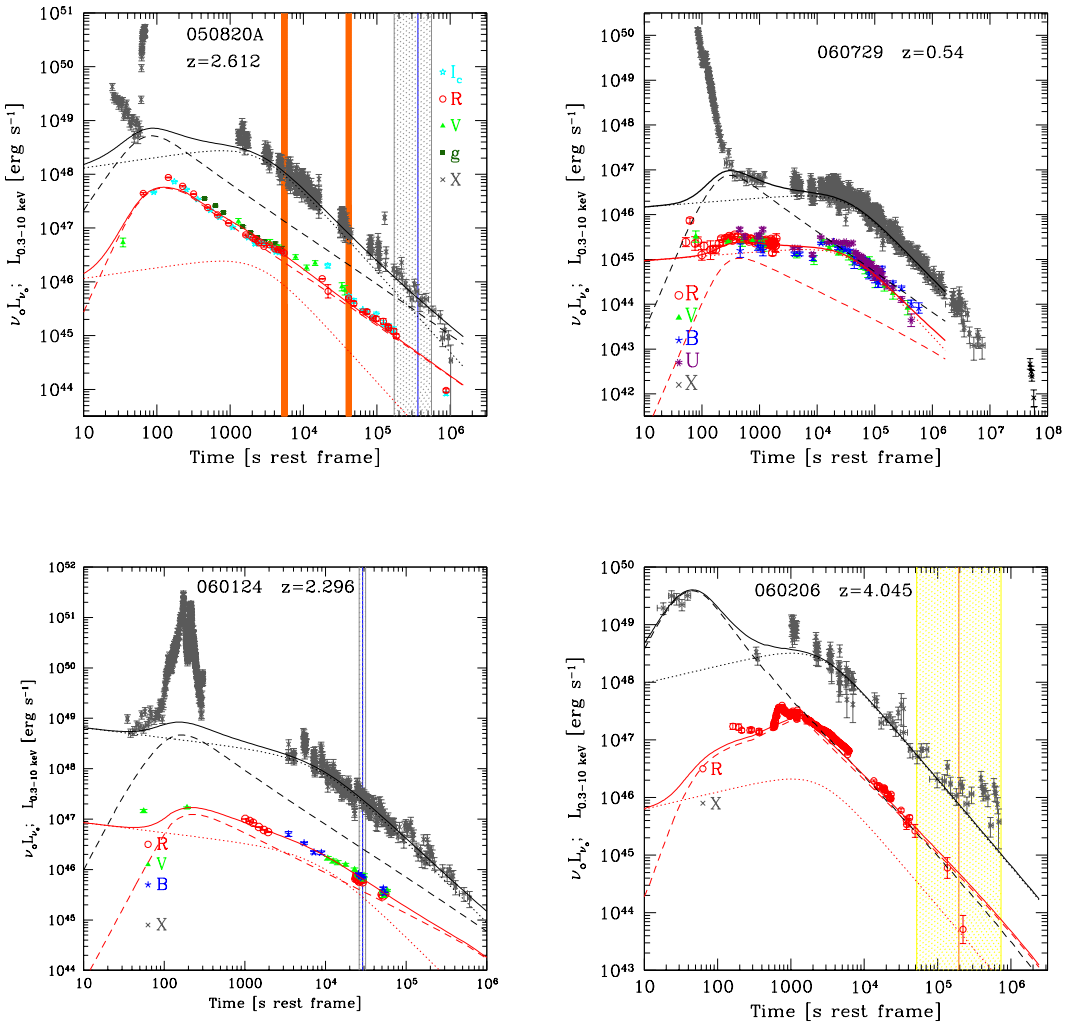

Figure 6.2: *Top right panel* X–ray (in grey) and optical (different symbols, as labelled) light curve of GRB 060729. Same notation as in Fig. 5.1. Lines indicate the model fitting: afterglow (dashed line), Component II (dotted line) and their sum (solid line). Black lines refer to the X–rays, light grey (red in the electronic version) for the optical. Both the optical and the X–rays are dominated by the Component II. There is no evidence for an achromatic jet break. *Top left panel* X–ray (in grey) and optical (different symbols, as labelled) light curve of GRB 050820a. Grey lines and stripes correspond to jet break times as reported in the literature. Both the optical and the X–rays are dominated by the "standard afterglow". Clear evidence of a break in the optical and hint of a shallower achromatic break in the X–rays. *Bottom left panel* X–ray and optical light curve of GRB 060124. The optical bands are dominated by the "standard afterglow" and show the presence of a jet break while the X–ray emission is dominated by the Component II and the light curve after $T_{\rm A}$ can be well fitted by a single power law without requiring any further break. *Bottom right panel* X–ray and optical light curve of GRB 060206.

Chapter 7

Breaks in the X–ray spectra and the $N_{\rm H}^{\rm host}$ / $A_{\rm V}^{\rm host}$ relation

7.1 Spectral predictions of the two components light curves modelling

In §5 I discussed a scenario in which the observed optical and X–ray light curves are produced by the sum of two separate components. The first component is due to the standard external forward shock afterglow emission, the other one is described in a completely phenomenological way and is produced by a completely different mechanism with respect to the standard afterglow emission. For simplicity we called this additional emission Component II.

In §5 I focused on the broad band modelling of the GRBs light curves temporal evolution. Such a modelling contains some information about the spectral shape of both the standard afterglow (see Panaitescu & Kumar 2000) and of the Component II (see eq. 5.3) but in that first stage these parameters where optimised in order to better fit the broad band light curve and no comparison has been done with the observed optical and X–ray spectra.

If the optical and the X–ray emission are produced by different processes, the spectra of these two components must break between these bands in order to avoid the mechanism that is dominating in the X–rays to interfere with the observed optical emission and vice versa. On the other hand, a spectral break (e.g. the cooling break frequency of the synchrotron emission mechanism) between the optical and X–ray bands is sometimes expected also in the standard afterglow scenario (see for example Fig. 3.8 and 3.9). For the light curves modelling we assumed for simplicity that the break frequency of the second component always falls between the optical and the X–ray bands. However, in some cases this break could fall inside the observed XRT energy range, namely 0.3–10 keV. If effectively detected, this break can give precise information on the break frequency location

and on the low energy spectral index. These additional constraints make the bursts with an observed break in the X–ray spectrum the best candidates for checking the consistency between the optical to X–ray SEDs and the light curves modelling.

In order to test our model also from the spectral point of view, we analysed the X–ray time resolved spectra and, when possible, the evolution of the optical to X–ray spectral energy distribution.

In this section I will discuss our XRT spectral analysis following the description proposed in Nardini et al. (2009b,c,d).

7.2 Searching for breaks in the X–ray spectra

7.2.1 The sample

In order to test the presence of breaks in the X–ray spectra, we analysed all the XRT spectra of the 33 GRBs belonging to the same sample considered in §5. (i.e. we require the knowledge of the GRB redshift, a good photometric coverage, *Swift* XRT observations and a published estimate of the host galaxy dust absorption $A_V^{\rm host}$for long GRBs observed by *Swift* before the end of March 2008). As done in §5 when different values of $A_{\rm V}^{\rm host}$ are reported in the literature we choose the estimate derived from a direct analysis of the optical spectral energy distribution rather then that obtained by a combined analysis of the optical to X–ray SEDs. When only the latter is available we discuss the effects of possible alternative solutions. This will be done through a direct analysis of the optical to X–ray spectral energy distributions in the following sections.

For the construction of the SEDs we selected time intervals not affected by prompt or high latitude emission or flaring activity in order to avoid the contribution of these further additional components.

7.3 XRT data reduction and spectral analysis

We analysed the XRT data of the events in the sample with the *Swift* software package *v2.9* distributed with HEASOFT (*v6.6*). The XRT data were reprocessed with the XRTPIPELINE tool[1]. The spectra were extracted in both WT and PC mode with the standard grade, applying, when required, the correction for pileup (Moretti et al. 2005, Romano et al. 2006; Vaughan et al. 2006). The extraction was in boxes (WT mode) or circular regions (PC mode) of typical widths as discussed in Evans et al. (2009). Background spectra were extracted in same-sized regions far from the source. For all of the spectra we created Ancillary

[1]Part of the XRT software, distributed with HEASOFT package: `http://heasarc.gsfc.nasa.gov/heasoft/`

Response Files with the `xrtmkarf` tool and used the calibration database updated to December 2008. The spectra were re-binned in order to have a minimum of 20 counts per energy channel (15 for the faintest events) and energy channels below 0.3 keV and above 10 keV were excluded from the analysis. The XSPEC(*v11.3.2*) software was used for the analysis. For bursts with particularly bright X-ray emission we also performed a time resolved spectral analysis in order to check for the possible spectral evolution. Since we are not considering XRT data that are simultaneous to the BAT γ–ray detection, the steep early phase and the flaring activity are not considered.

7.3.1 Single absorbed power law model

Following the conventional analysis of X-ray GRB spectra we fitted all the spectra with a model composed by a power–law with two absorption components at low energies, `wabs` and `zwabs`. The first one corresponds to the Galactic absorption and its column density $N_{\rm H}^{\rm gal}$ is fixed to the Galactic value (from Kalberla et al. 2005 and Dickey & Lockman 1990). The second absorption is due to the material located at the redshift of the source and its column density $N_{\rm H}^{\rm host}$ is left free to vary. The 90% confidence intervals on the best fit parameters are obtained with the `error` command in XSPEC. All the spectra returned a good fit with such a model, with reduced χ^2/dof close to unity. The best fit parameters are in a good agreement both with the results of the automatic XRT data analysis tool available on line[2] developed by Evans et al. (2008, 2009) and with the values reported in the literature (summarised also in Tab. 1 of G09). Note that discrepancies might arise due to possible differences in the time intervals chosen for the extraction of the spectra. The results of the fits are reported in Tab. 7.1.

7.3.2 Broken power law model

In order to test for the presence of possible spectral breaks within the XRT energy range we selected the GRBs whose spectra have high signal-to-noise, namely those which, after energy rebinning, had a minimum of 50 energy channels. This choice, on average, corresponds to a minimum of 1000 counts per spectrum. We found 20 events fulfilling this condition. In the excluded 13 cases (i.e. GRB 050319, GRB 050408, GRB 050525a, GRB 050801, GRB 050824, GRB 051111, GRB 060512, GRB 060526, GRB 060904b, GRB 060927, GRB 070125, GRB 071010a and GRB 080310) the spectrum in the considered time intervals has too low S/N for fitting a broken power–law model which has two more free parameters (i.e the spectral index of the second power-law component and the energy break between the two

[2] `http://www.swift.ac.uk/xrt_spectra/`

GRB	z	$t_{\rm start} - t_{\rm end}$ s after trigger	$\beta_{\rm X}$	$N_{\rm H}^{\rm host}$ 10^{21} cm^{-2}	$\chi^2_{\rm R}$ (dof)	$A_{\rm V}^{\rm host}$ magnitudes
050318	1.44	3.3×10^3-6.3×10^4	1.1±0.1	0.5±0.4	0.89 (80)	0.68±0.36
050319	3.24	5.0×10^3-1.1×10^5	1.06±0.12	4.±4.	0.76 (46)	0.11
050401	2.8992	1.3×10^2-8.5×10^3	0.88±0.04	15.6±1.9	1.056 (273)	0.62±0.06
050408	1.2357	2.6×10^3-7.1×10^4	1.15±0.16	12.2±2.8	1.36 (37)	0.73±0.18
050416A	0.653	3.5×10^2-1.5×10^5	1.01±0.11	5.8±1.1	0.88(74)	0.19±0.11
050525A	0.606	5.9×10^3-7.4×10^4	1.1±0.17	2.1±1.1	0.86 (32)	0.32±0.2
050730	3.967	1.5×10^4-1.4×10^5	0.62±0.08	4.8±4.8	1.24 (95)	0.01±0.005
050801	1.56	6.5×10^2-5.2×10^4	0.84±0.20	0±0.07	0.66 (14)	0
050802	1.71	4.8×10^2-9.3×10^4	0.86±0.08	1.8±1.0	1.055 (159)	0.55±0.1
050820A	2.612	4.7×10^3-5.9×10^4	0.99±0.06	3.3±2.2	0.98 (143)	0.065±0.008
050824	0.83	6.6×10^3-1.0×10^5	0.87±0.18	0.6±0.6	0.95 (32)	0.14±0.13
050922C	3.221	1.1×10^2-4.5×10^2	1.02±0.07	3.6±2.2	1.00 (115)	0
051111	1.55	5.6×10^3-5.3×10^4	1.21±0.19	6.1±3.0	0.80 (36)	0.39±0.11
060124	2.296	3.4×10^4-1.2×10^5	1.02±0.08	7.6±2.5	0.81 (107)	0
060206	4.045	5.1×10^3-3.5×10^4	1.29±0.15	15.3±9.5	0.99 (87)	0±0.02
060210	3.91	3.8×10^3-5.8×10^4	1.10±0.06	17.5±5.0	1.015 (185)	1.1±0.2
060418	1.489	2.6×10^2-6.7×10^2	0.87±0.09	4.2±1.7	0.86 (91)	0.25±0.22
060512	0.4428	3.7×10^3-2.3×10^5	0.97±0.18	0.2±0.2	1.39 (17)	0.44±0.05
060526	3.221	7.4×10^2-7.6×10^3	0.95±0.13	6.±6.	0.59 (31)	0.04±0.04
060614	0.125	4.4×10^3-2.8×10^4	0.79±0.09	0.3±0.3	0.98 (66)	0.05±0.02
060729	0.54	1.7×10^4-1.8×10^5	1.05±0.02	0.9±0.2	1.01 (290)	0.
060904B	0.703	1.0×10^3-4.1×10^4	1.10±0.12	2.7±1.2	0.86 (40)	0.44±0.05
060908	2.43	1.5×10^2-1.9×10^3	0.84±0.11	2.±2.	1.09 (60)	0.055±0.033
060927	5.47	1.0×10^2-6.1×10^3	0.9±0.2	0.5±0.5	0.75 (15)	0.33±0.18
061007	1.26	2.0×10^2-2.1×10^3	0.91±0.02	5.6±0.3	1.054 (480)	0.54±0.32
061121	1.314	2.0×10^2-1.8×10^4	1.01±0.08	7.3±1.3	0.88 (121)	0.72±0.06
061126	1.1588	1.8×10^3-1.5×10^4	0.81±0.11	5.6±1.2	1.08 (143)	0
070110	2.352	4.0×10^3-4.5×10^4	1.12±0.07	2.6±1.5	0.875 (129)	0.08
070125	1.547	4.7×10^4-1.3×10^5	0.97±0.2	1.7±1.7	0.88 (21)	0.11±0.04
071003	1.604	2.2×10^4-4.2×10^4	1.95±0.12	0.7±0.7	1.20 (47)	0.209±0.08
071010A	0.98	3.4×10^4-9.1×10^4	1.43±0.5	13.5±7.0	0.52 (11)	0.615±0.15
080310	2.42	1.7×10^4-5.2×10^4	0.85±0.1	3.0±3.0	1.11 (36)	0.1±0.05
080319B	0.937	5.6×10^2-1.7×10^3	0.80±0.01	1.6±0.1	1.35 (610)	0.07±0.06

Table 7.1: Results of the single power–law fitting. For each GRB we report: the redshift, the time interval in which the spectrum was extracted, the unabsorbed spectral index $\beta_{\rm X}$, the hydrogen column density at the host $N_{\rm H}^{\rm host}$, the reduced χ^2 and number of degrees of freedom, the host galaxy visual extinction $A_{\rm V}^{\rm host}$ taken from the literature, and the references for redshift and $A_{\rm V}^{\rm host}$. References can be found in Nardini et al. (2009d).

power-laws) with respect to the single power-law model with galactic and intrinsic absorption.

Also for the broken power–law model we considered the two absorption systems. The break energy $E_{\rm b}$ between the low and high energy power–laws spectral indices ($\beta_{\rm X,1}$ and $\beta_{\rm X,2}$, respectively) was left free to vary in the 0.3-10 keV energy range. Clearly a significant broken power–law fit should result in statistically different $\beta_{\rm X,1}$ and $\beta_{\rm X,2}$. Therefore no pre–determined relation between the model parameters was assumed (as done for instance if the emission process is assumed to be synchrotron i.e. $\beta_{\rm X,1} = \beta_{\rm X,2} - 0.5$).

The broken power–law with a free rest frame $N_{\rm H}^{\rm host}$ model (hereafter ABP) has 5 free parameters while the absorbed single power–law model (hereafter AP) has 3 free parameters that are a subset of the ABP model ones. The models are nested with a progression of 2 free parameters so an ABP model fitting is considered an improvement of the AP model one if $\Delta\chi^2 = \chi^2_{\rm AP} - \chi^2_{\rm ABP} > 5.4$ (90% confidence). A similar choice was also done by Butler & Kocevsky (2007): they considered as acceptable a more complex model (with an additional free parameter) if $\Delta\chi^2 > 2.7$.

In 7 events (i.e. GRB 050802, GRB 050820a, GRB 060210, GRB 060729, GRB 061007, GRB 061126, GRB 080319b) the fit with the ABP model resulted in an acceptable χ^2/dof and the 5 free parameters of the ABP model were constrained with acceptable uncertainties (i.e. a χ^2 minimum is found inside the parameters definition range also considering their uncertainties). Usually both the high energy photon index ($\beta_{\rm X,2}$) and $E_{\rm b}$ are well constrained (typical errors of about 0.1 and 0.15, respectively) while $\beta_{\rm X,1}$ and $N_{\rm H}^{\rm host}$ are affected by larger, but still acceptable, uncertainties (about 0.2 and 50%, respectively see Tab. 7.3.2). For all the 7 events the improvement of the ABP fit with respect to the AP one yields a $\Delta\chi^2 = \chi^2_{\rm AP} - \chi^2_{\rm ABP} > 5.4$ (i.e. a 90% significant improvement).

In 8 cases (i.e. GRB 050318, GRB 050401, GRB 050416a, GRB 050922c, GRB 060614, GRB 060908, GRB 070110, GRB 071003) the ABP model is not preferred to the AP one, either because $\beta_{\rm X,1}$ is equal to $\beta_{\rm X,2}$ within their errors or $E_{\rm b}$ results outside the considered energy range.

In 5 GRBs (i.e. GRB 060124, GRB 060206, GRB 061121, GRB 050730, GRB 060418) although the χ^2 of the ABP model is lower than that of the AP model, the improvement of the fit is not statistically significant.

We re-analysed the spectra of these 5 events assuming an ABP model with 4 parameters, namely with $N_{\rm H}^{\rm host}$ frozen to the value estimated from $A_V^{\rm host}$ assuming that the $A_V^{\rm host}$ – $N_{\rm H}^{\rm host}$ relation reported by Schady et al. (2007) (their Eqs. 1, 2 or 3). For each burst we choose the conversion corresponding to the extinction curve adopted to obtain the $A_V^{\rm host}$ from the analysis of its optical SED.

In tab. 7.3.2 we report the best X–ray spectral fit parameters values for these 5 events and the related reduced χ^2 ($\chi^2_{\rm R}$). For all of these events we obtain a good fit to the data with $\chi^2_{\rm R}$ values close to unity like in the AP case.

GRB	z	$N_{\rm H}^{\rm host}$ 10^{21} cm^{-2}	$\beta_{\rm X,1}$	$E_{\rm b}$ keV	$\beta_{\rm X,2}$	$\chi^2_{\rm R}$ (dof)	prob
050802	0.55	0.6±0.6	$0.58^{+0.13}_{-0.14}$	$1.64^{+0.63}_{-0.64}$	0.95±0.12	0.99 (157)	$6.5e^{-3}$
050820A	2.612	$2.2^{+2.2}_{-2.2}$	$0.63^{+0.15}_{-0.20}$	$1.05^{+0.70}_{-0.33}$	1.00±0.07	0.947 (141)	$7.7e^{-2}$
060210	3.91	$4.^{+7}_{-4}$	$0.59^{+0.32}_{-0.22}$	$1.15^{+0.23}_{-0.17}$	1.12±0.07	0.99 (183)	$8.5e^{-2}$
060729	0.54	$0.^{+0.2}_{-0}$	$0.53^{+0.24}_{-0.09}$	$1.13^{+0.13}_{-0.10}$	1.04±0.04	0.97 (288)	$2.9e^{-3}$
061007	1.26	$3.0^{+0.9}_{-0.9}$	$0.02^{+0.36}_{-0.34}$	$0.80^{+0.04}_{-0.05}$	0.86±0.02	1.02 (478)	$3.9e^{-4}$
061126	1.1588	$1.7^{+3.6}_{-1.7}$	$-0.16^{+0.82}_{-1.2}$	$1.05^{+0.27}_{-0.21}$	0.74±0.08	1.056 (141)	$9.8e^{-2}$
080319B	0.937	$0.7^{+0.2}_{-0.2}$	$0.49^{+0.08}_{-0.10}$	$1.14^{+0.08}_{-0.08}$	0.81±0.01	1.27 (608)	$8.6e^{-9}$

Table 7.2: Results of the fit of the X–ray spectra with the absorbed broken power–law for the 7 bursts for which we were able to well constrain all the model parameters. For each burst we report: the redshift, the host galaxy $N_{\rm H}^{\rm host}$ column density, the low energy spectral index $\beta_{\rm X,1}$, the break energy $E_{\rm b}$, the high energy spectral index $\beta_{\rm X,2}$, and the reduced χ^2 with the related degrees of freedom in parenthesis. The last column represents the F test probability obtained comparing the AP and the ABP models. Note that the energy spectral index $\beta = \Gamma - 1$. The analysed spectra have been extracted in the same time intervals reported in the third column of Tab. 7.1.

GRB	z	$N_{\rm H}^{\rm host}$ 10^{21} cm^{-2}	$\beta_{\rm X,1}$	$E_{\rm b}$ keV	$\beta_{\rm X,2}$	$\chi^2_{\rm R}$ (dof)
050730	3.967	0	$0.36^{+0.23}_{-0.27}$	$1.00^{+0.6}_{-0.25}$	$0.75^{+0.09}_{-0.09}$	1.22 (94)
060206	4.045	0	$0.03^{+0.62}_{-1.4}$	$0.63^{+0.18}_{-0.11}$	$1.23^{+0.12}_{-0.12}$	0.98 (86)
060124	2.296	0	$0.47^{+0.14}_{-0.19}$	$1.27^{+0.27}_{-0.25}$	$1.05^{+0.1}_{-0.1}$	0.81 (107)
060418	1.489	0	$-0.23^{+0.5}_{-0.6}$	$0.79^{+0.2}_{-0.09}$	$0.81^{+0.08}_{-0.07}$	0.85 (90)
061121	1.314	1.44	$-0.89^{+0.46}_{-0.65}$	$0.79^{+0.09}_{-0.08}$	$0.89^{+0.06}_{-0.06}$	0.88 (120)

Table 7.3: Absorbed broken power law model fitting results obtained fixing the value of $N_{\rm H}^{\rm host}$ column density to the value derived from the optical extinction through Eq. 1 presented in Schady et al. (2007). For each burst we report: redshift, host galaxy $N_{\rm H}^{\rm host}$ column density, low energy spectral index $\beta_{\rm X,1}$, break energy $E_{\rm b}$, high energy spectral index $\beta_{\rm X,2}$, and the reduced χ^2 with the related degrees of freedom in parenthesis. The analysed spectra have been extracted in the same time intervals reported in the third column of Tab. 7.1.

As the AP parameters are no more a subset of the parameters of this model (i.e. they are not nested models), the $\Delta\chi^2$ does not provide statistical information on the fit improvement (e.g. Protassov et al. 2002).

7.4 Rest frame column density excess

A first result that we want to highlight concerns the values of $N_{\rm H}^{\rm host}$ obtained from the fit with the AP model.

It has been already pointed out (e.g. Galama & Wijers 2001, Stratta et al. 2004, Schady et al. 2007) that the $N_{\rm H}^{\rm host}$ derived from the fit of the X–ray spectra are usually quite large (up to a few $\times 10^{22}$ cm^{-2}), so that the optical reddening estimated for the same events is often one or two orders of magnitude smaller than what expected from the $N_{\rm H}^{\rm host}$. Indeed, this discrepancy is present also in our GRBs.

Fig. 7.1 reports several events with an optical extinction significantly smaller than the value predicted by assuming a $N_{\rm H,X}$ vs. A_V relation (e.g. Eqs. 1, 2 or 3 in Schady et al. 2007). Despite the large uncertainties of some cases, the discrepancy is particularly evident in some highly X–ray absorbed cases with $N_{\rm H}^{\rm host} > 5 \times 10^{21}$ cm^{-2} and $A_V^{\rm host} < 1$.

From the observational point of view the large $N_{\rm H}^{\rm host}$ derived from the fitting of the X–ray spectrum corresponds to a deficit of counts below approximately 1 keV with respect to the extrapolation of a single power–law model. In principle, this deficit could instead be due to an intrinsically curved or a broken power–law spectrum. For the 7 GRBs for which the ABP model gave a better fit (with respect to the AP model) we can check if the obtained values of $N_{\rm H}^{\rm host}$ are in agreement with the optical extinction $A_V^{\rm host}$. Fig. 7.2 shows the values of $N_{\rm H}^{\rm host}$ obtained with the ABP model fitting versus $A_V^{\rm host}$ (filled circles).

For comparison, also the $N_{\rm H}^{\rm host}$ values obtained with the AP model fitting (empty squares) are reported. The solid lines represent the Milky Way and Small Magellanic Cloud like relations as in Fig. 7.1. For 5 GRBs the uncertainties on $N_{\rm H}^{\rm host}$ are quite large, making these values consistent with zero, i.e. they must be considered as upper limits. These limits, always smaller than the $N_{\rm H}^{\rm host}$ values obtained with the AP model, are consistent with the observed $A_V^{\rm host}$. For the remaining 2 GBRs (GRB 060210 and 080319b), however, the values of $N_{\rm H}^{\rm host}$ are still somewhat larger than what expected by the standard gas-to-dust relation, though the disagreement is less pronounced.

As discussed above, we re–analysed the spectra of 5 GRBs in which the ABP model was not required, but we were not able to well constrain its model parameters (i.e. GRB 050730, GRB 060206, GRB 060124, GRB 060418, GRB 061121), fixing $N_{\rm H}^{\rm host}$ to the values derived from the standard $N_{\rm H,X}$ versus A_V relations. Also in these cases an acceptable fit to the data ($\chi^2_{\rm red} \approx 1$) was found.

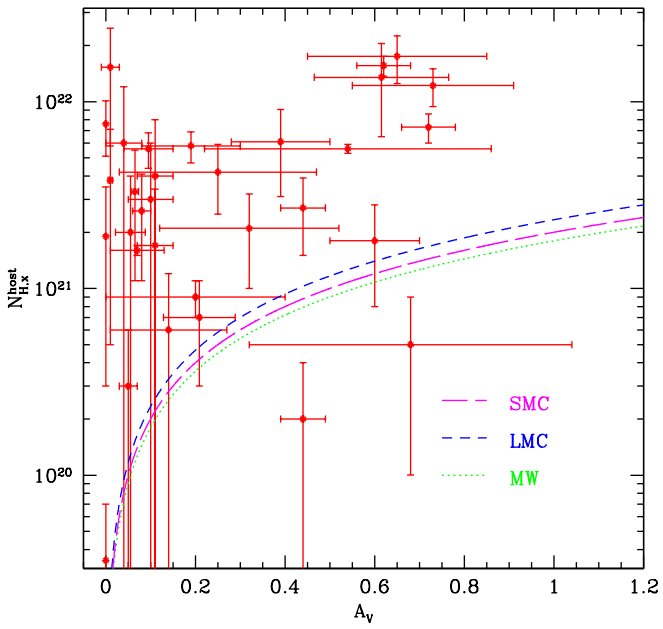

Figure 7.1: Rest frame column densities $N_{\rm H}^{\rm host}$ (obtained from fitting a single power–law model to the X–ray data) versus the visual extinction $A_V^{\rm host}$ in the GRB host galaxy for all 33 GRBs of the sample. The three curved lines correspond to the $N_{\rm H,x}$ versus A_V relations observed in the Milky Way and in the Small Magellanic Cloud as described by Eqs. 1, 2 or 3 in Schady et al. (2007).

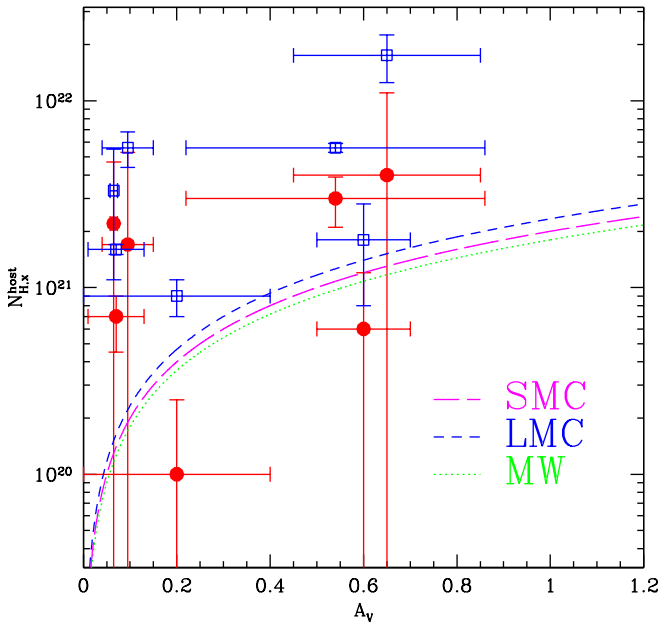

Figure 7.2: Rest frame column densities $N_{\rm H}^{\rm host}$ versus visual extinction $A_V^{\rm host}$ for the 7 GRBs in which a broken power–law model gave an acceptable fit (see text). Filled circles represent the column densities obtained from an absorbed broken power law fit to the XRT spectra with the local absorption fixed to the Galactic $N_{\rm H}^{\rm Gal}$ values while empty squares represent the $N_{\rm H}^{\rm host}$ obtained from a single power law fitting for the same events. The two curved lines represent the $N_{\rm H,x}$ versus A_V relations observed in the Milky way and in the Small Magellanic Cloud as described by Eq.1 , Eq. 2, or Eq. 3 in Schady et al. (2007).

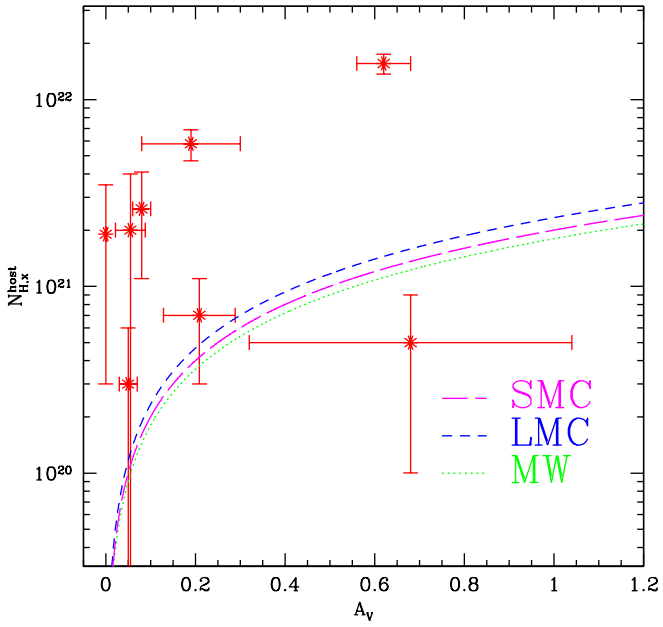

Figure 7.3: Rest frame column densities $N_{\rm H}^{\rm host}$ versus the visual extinction $A_V^{\rm host}$ obtained from the AP model for the events where the ABP model is not required. The two curved lines represent the $N_{\rm H,x}$ versus A_V relations observed in the Milky Way and in the Small Magellanic Cloud as described in Schady et al. (2007).

No a priori relation between $\beta_{X,1}$ and $\beta_{X,2}$ was assumed and the extremely hard $\beta_{X,1}$ obtained for GRB 061121 and GRB 060418 cannot be easily accounted for by the standard emission processes. Given the uncertainties in the inferred $N_{\rm H}^{\rm host}$, we then fixed or constrained the value of $\beta_{X,1}$ in two ways: i) assuming the relation $\Delta\beta = \beta_{X,1} - \beta_{X,2} = 0.5$; ii) $\beta_{X,1} = 0$. In both cases the best fit returns the same $\chi^2_{\rm R}$ value. For GRB 061121 the derived columns are $N_{\rm H}^{\rm host} = 0.58^{+0.20}_{-0.13} \times 10^{21}$ cm^{-2} ($\Delta\beta = 0.5$) and $N_{\rm H}^{\rm host} = 0.44^{+0.32}_{-0.13} \times 10^{21}$ cm^{-2} ($\beta_{X,1} = 0$), while for GRB 060418 $N_{\rm H}^{\rm host} = 0.28^{+0.2}_{-0.16\times10^{21}}$ cm^{-2} ($\Delta\beta = 0.5$) and $N_{\rm H}^{\rm host} \leq 0.25 \times 10^{21}$ cm^{-2} ($\beta_{X,1} = 0$). We conclude that for these two bursts the data cannot robustly constrain the low energy spectral slope as an acceptable fit can be obtained for not so extreme values of $\beta_{X,1}$. The column densities obtained in these cases are intermediate between the ones obtained through the ABP and the AP models, in agreement with what found by Schady et al. (2007) when assuming $\Delta\beta = 0.5$.

While the presence of an intrinsic break in the emitted X–ray spectrum can solve or mitigate the problem of an excess of $N_{\rm H}^{\rm host}$ with respect to the optical reddening for a fraction of events, this can not be considered as a general solution

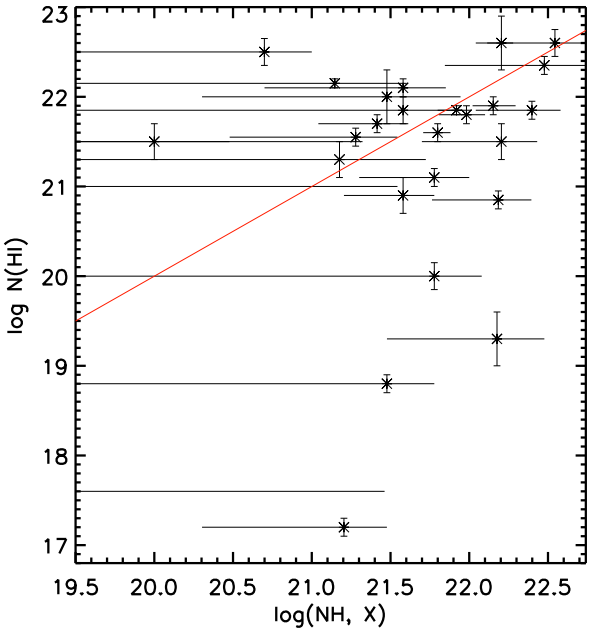

Figure 7.4: Rest frame column densities $N_{\rm H}^{\rm host}$ evaluated from the soft X–ray absorption (assuming solar metallicity) versus the $N_{\rm H_I}$ column densities evaluated from the dumped Lyα optical spectra (data from Fynbo et al. 2009). The red line indicates solar metallicity ($Z = Z_{\odot}$).

of this issue, on the basis of different indications.

As the excess is observed in a large fraction of GRBs, this would imply that the observed X–ray spectrum is almost always a broken power law, with a break in the rather narrow 0.5–1.5 keV energy range, even if the redshifts of these bursts are different. This is unlikely.

Furthermore we can directly exclude the presence of a spectral break inside the observed XRT spectrum for about half of the analysed events. In general, these events have an intermediate/high $N_{\rm H}^{\rm host}$ (when fitted with the AP model; see Fig. 7.3 compared to Fig. 7.2).

A particularly strong support to the fact that an excess is indeed present at least in some GRBs is given by the case of GRB 050401, for which we get $N_{\rm H}^{\rm host} = (1.56\pm0.19)\times10^{22}$ cm^{-2} when fitting the AP model. Watson et al. (2006) discussed in details this GRB and found that, together with the high $N_{\rm H}^{\rm host}$ evaluated from the X–ray spectral fitting, this burst is characterised by a very large damped Lyα absorber (DLA) with $\log N_{\rm H_I} = 22.6 \pm 0.3$. The direct analysis of the optical spectrum allows to evaluate an $A_V^{\rm host} = 0.62\pm0.06$, much smaller than that inferred from the $N_{\rm H}^{\rm host}$ column density. They also put limits on the possible presence of achromatic "grey" dust absorption from the analysis of the optical/X–ray SED, which are still inconsistent with $N_{\rm H}^{\rm host}$. They also discuss the possibility to have

an environment for GRB 050401 characterised by little dust with high metallicity.

GRBs are known to be characterised by high neutral hydrogen column densities (Jensen et al. 2001; Fynbo et al. 2001; Hjorth et al. 2003) that are usually larger than the ones measured in QSOs (Vreeswijk et al. 2004). Watson et al. (2007) showed that in GRBs there is no correlation between the $N_{\rm H}^{\rm host}$ column density evaluated from the soft X–ray absorption analysis and the $N_{\rm H_I}$ column densities estimated by the optical spectral analysis of dumped Lyα GRBs.

This useful comparison between the soft X–ray $N_{\rm H}^{\rm host}$ absorption and the dumped Lyα $N_{\rm H_I}$ column densities estimate is affected by an observational limitation. In order to study the Lyα absorption line (rest frame wavelength $\lambda = 1216$ Å) with the available ground based optical spectrometers, a GRB must be located at a redshift larger than 2. On the other hand the estimate of the $N_{\rm H}^{\rm host}$ column density becomes more difficult at high redshifts since the neutral oxygen edge at 0.52 keV falls outside the observed XRT 0.3–10 keV energy range and at redshifts larger than 2, only an intrinsic only $N_{\rm H}^{\rm host}$ lager than $\sim$ a few $\times 10^{21}$ can be measured and therefore in only a small fraction of GRBs this comparison can be done.

Presently the number of GRBs fulfilling these requests is increased. Using the $N_{\rm H_I}$ column densities of a much larger sample of events taken from Fynbo et al. (2009) I confirm this finding as shown in fig. 7.4.

The soft X–ray absorption is mainly due to the presence of α chain elements in gas and solid phases, in particular to the neutral oxygen edge at 0.52 keV and in order to infer from it a $N_{\rm H}^{\rm host}$ column density we need to assume a metal to gas ratio. The UV Lyα absorption instead, is a direct measurement of the $N_{\rm H_I}$ column density. The fact that there is no correlation in fig. 7.4 implies that the metallicities of GRB environments are quite different. In some cases we also confirm that in our sample the high metal to gas ratios seem to imply that the metalicities of some bursts are above the solar value (see Watson et al. 2007).

I also tried to compare the $N_{\rm H_I}$ column densities estimated by the optical spectral analysis of dumped Lyα with the host galaxy dust reddening $A_{\rm V}^{\rm host}$. The results are plotted in fig. 7.5 and clearly show that there is no correlation between the two sets. We note that, also in this case, quite large $N_{\rm H_I}$ column densities correspond to small values of $A_V^{\rm host}$, confirming that the amount of dust around the progenitor, inferred from the reddening analysis, is very small.

We can now confirm some typical GRB environment features. They are characterised by high metal (α chain elements) column densities (inferred from the $N_{\rm H}^{\rm host}$ estimate) with respect to the neutral hydrogen column densities inferred from the dumped Lyα spectra. On the other hand these high metal column densities do not correspond to high amount of dust since there are very small host galaxy reddening $A_{\rm V}^{\rm host}$ values. This result can be explained by assuming a non standard achromatic "grey" dust absorption due to a dust grain distribution dominated by

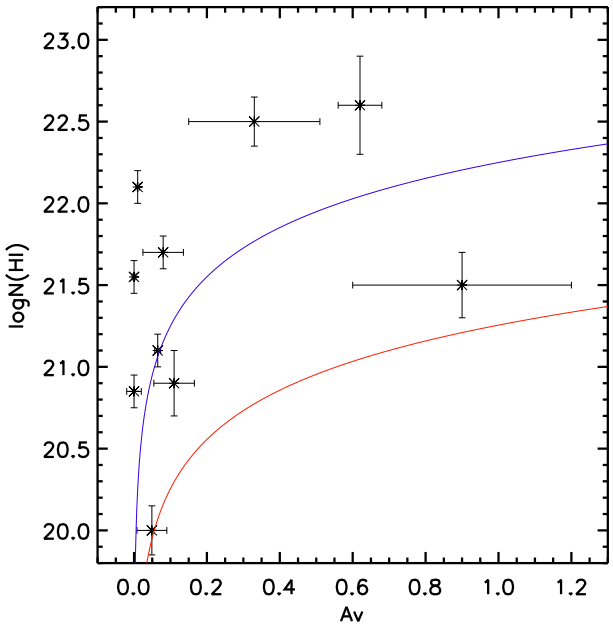

Figure 7.5: $N_{\rm H_I}$ column densities evaluated from the dumped Lyα optical spectra versus the host galaxy dust reddening $A_V^{\rm host}$. The solid lines represent the $N_{\rm H}^{\rm host}$ vs $A_{\rm V}^{\rm host}$ column densities following Schady et al. 2007.

larger grain sizes, but this hypothesis is sometimes excluded by the GRB afterglow broad band SED (Watson et al. 2006). A high metal column with little extinction could be also due by the destruction of the dust in the progenitor surroundings or by an unexpected small dust formation in spite of the strong star formation activity that should take place in GRB location region.

All these results do not lead to any clear result and should be accompained by an extensive analysis of the optical-UV high resolution spectra of a large sample of GRB afterglows (see e.g. Vreeswijk et al. 2007). It is clear that the connections between these quantities are complex and should be considered with care.

Chapter 8

Optical to X–rays SEDs: testing the unifying view of GRB afterglows

8.1 Optical to X–ray SEDs consistency check

In §7 we analysed the 0.3–10 keV XRT spectra of all the GRBs in our sample and we found the possible presence of a spectral break in 7 events. For these events we know where the spectral break $\nu_{\rm b}$ is located and what is the value of the low energy (i.e. at frequencies smaller than $\nu_{\rm b}$) $\beta_{\rm X,1}$ (see tab. 7.3.2). This additional information allows us to well constrain the spectral energy distribution of the component that is dominating in the X–rays (when assuming an intrinsic broken power law spectrum). In these 7 cases we can therefore infer the optical fluxes that are expected extrapolating at larger wavelengths the low energy X–ray spectral index. These predicted fluxes can be then compared with the contemporaneously observed optical magnitudes in order to test whether the observed optical radiation is consistent with having being produced by the same radiative emission that is dominating in the X–ray band. We can finally test whether the results obtained through this optical to X–rays SED analysis is consistent with what our two components light curves modelling predicts.

When we analyse contemporaneously the optical and X–rays temporal evolution and the spectral energy distribution of a GRB in which we identified the presence of a break inside the XRT observed energy range, we can have the 3 different scenarios shown in fig. 8.1:

- *Top panel in fig. 8.1* Both the optical and X-ray light curves are dominated by the Component II emission showing parallel light curves.
  In this case we expect that the optical bands are consistent with the extrapolation of the low energy X–ray spectral index.

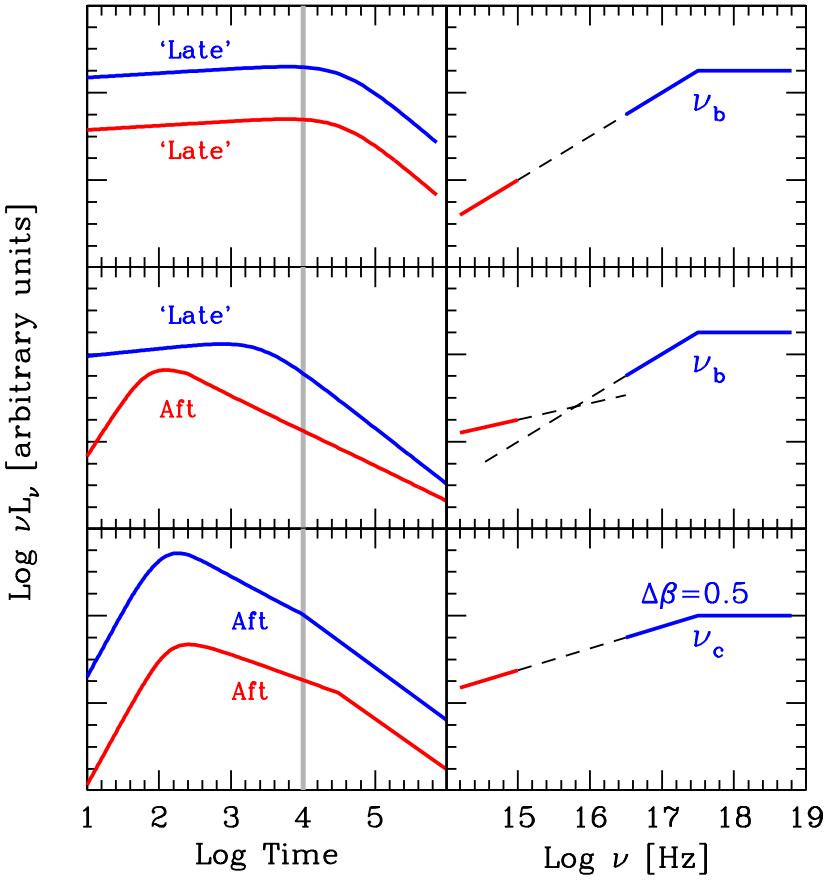

Figure 8.1: Sketch illustrating the possible different cases. The left panels refer to the X–ray (upper curves) and optical (lower curves) light–curves. The right panels refer to the corresponding expected optical to X–ray SED. The bottom right panel shows the standard "afterglow–afterglow" case, with a cooling break time appearing first in the X–ray light curve. The vertical grey line illustrates the time of the extraction of the SED. The ν_b frequency is the break frequency of the Component II, while ν_c refers to the cooling frequency.

- *Mid panel in fig. 8.1* One band (usually the X–rays) light curve is dominated by the Component II emission while the other (usually the optical) is dominated by the "standard afterglow".
  In this case, as predicted by the two components modelling, the SED should show that the low energy extrapolation of the X–ray spectrum does not interfere with the observed optical bands.

- *Bottom panel in fig. 8.1*: Both the optical and X-ray light curves are dominated by the "standard afterglow" emission.
  In this case the spectral break detected in the X–ray spectrum is probably the cooling break frequency ν_c of the synchrotron emission that is passing through the observed XRT energy range. The optical bands are consistent with the extrapolation of the low energy X–ray spectral index. In this scenario the high and low energy spectral indices are not independent and must satisfy the relation $\Delta\beta = \beta_{X,2} - \beta_{X,1} = 0.5$. If in a homogeneous medium environment the cooling frequency decreases enough to reach the observed optical bands during the observed light curve, we expect to observe a later time chromatic break in the optical light curve. After this break the optical to X–ray SED should be well described by a single power law.

In the following we discuss 6 of the 7 GRBs separately as done in Nardini et al. (2009d). The remaining one is GR 080319b, the so called 'Naked eye" GRB. Because of its complexity that has already been discussed in literature (see e.g. Racusin et al. 2009), we are planning to analyse it in details in a forthcoming paper (Nardini et al. in prep.). I anticipate that no event shows an optical to X–rays SED that is inconsistent with the presence of a break in the XRT band and the two component interpretation.

8.2 Individual cases

8.2.1 SEDs extraction

For each burst we select epochs where simultaneous optical photometry and XRT observations are available in order to have the largest number of simultaneous photometric points and to avoid (if possible) flux extrapolations. This requirement limits the number of optical to X–ray SED we consider for each burst.

The X–ray spectrum is obtained using a time interval around the selected epoch in order to have at least 50 energy bins and it is re normalised to the 0.3–10 keV flux obtained by the light curve. When the optical and X–ray bands light curves track each other one single SED is considered. When instead the optical and X–ray light curves follow different temporal behaviours we extracted more SEDs in order to test different phases of the light curve.

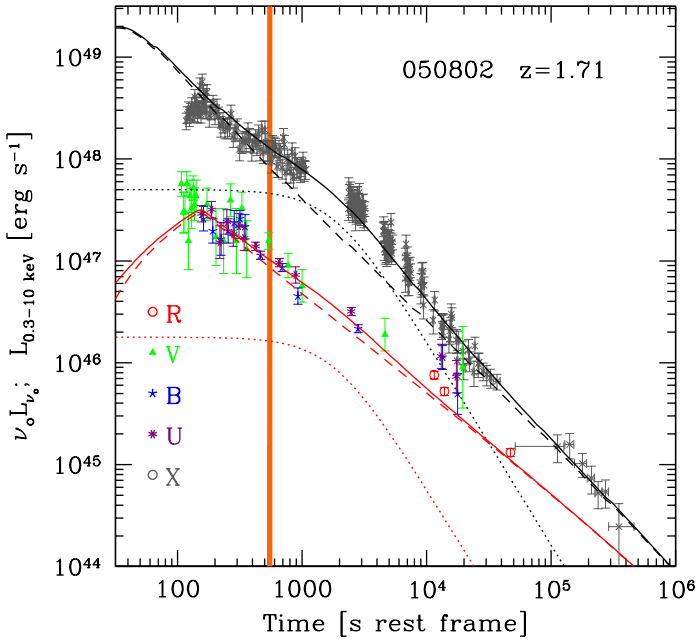

Figure 8.2: X–ray (in grey) and optical (different symbols, as labelled) light curves of GRB 050802 (in the rest frame time). Lines indicate the model fitting: afterglow component (dashed line), "late prompt" one (dotted line) and their sum (solid line). Black lines refer to the X–rays, red to the optical. The vertical line marks the time at which the SED is extracted.

The X–ray SED is corrected for both the Galactic $N_{\rm H}$ ad the host galaxy $N_{\rm H}^{\rm host}$ reported in tab. 7.3.2. The observed optical magnitudes have been corrected for the Galactic reddening $A_V^{\rm Gal}$ ad for the host galaxy $A_V^{\rm host}$. The choice of the value of $A_{\rm V}^{\rm host}$ is discussed in every single event. The unabsorbed fluxes have been then re-scaled to the flux at the selected time using the temporal decay index describing the optical light curve around that epoch.

8.2.2 GRB 050802

The optical light curve photometric data are mainly from Oates et al. (2007) together with later time R band data from GCNs (Pavlenko et al. 2005, Fynbo et al. 2005). The *Swift* UVOT filters UVM2 and UVW2 are strongly affected by Lyα dumping and are not considered. The X–ray light curve has been modelled as the combination of "standard afterglow" emission dominating at early and at late times (before 400 s and after about 10 ks, rest frame) and "late prompt" emission dominating in between. The "standard afterglow" component instead describes

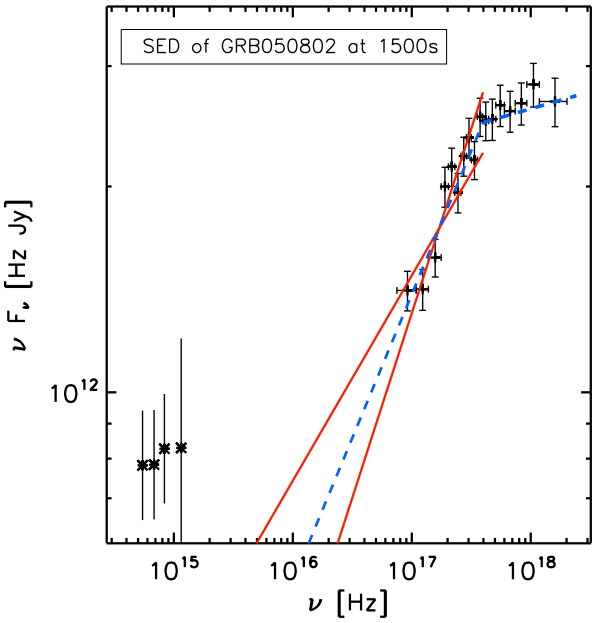

Figure 8.3: Optical to X–ray νF_ν SED of GRB 050802 extracted around 1500 s (observed time, corresponding to 560 s rest frame) after trigger. The dashed line shows the best fit (with the ABP model) to the X–ray spectrum (spectra parameters are reported in Tab. 7.3.2) and the solid lines are the uncertainties on the slope of the low energy spectral index $\beta_{\rm X,1}$.

the evolution of the optical flux during the whole period of the follow up (see Fig. 8.2).

We extracted the optical to X–ray SED around an observed time of 1500s (560 s rest frame) when the optical and X–ray fluxes are dominated by different components. Schady et al. (2007) estimated a non negligible host galaxy dust absorption ($A_{\rm V}^{\rm host} = 0.55 \pm 0.1$) on the basis of a Milky Way extinction curve and assuming a power–law spectrum connecting the optical and X–ray bands. By considering the optical bands alone we find a similar $A_{\rm V}^{\rm host} = 0.6$ with an optical spectral index $\beta_{\rm o} \approx 0.9$.

The SED, plotted in Fig. 8.3, is consistent with the optical and the X–ray emission being dominated by different components with a spectral break falling in the observed XRT energy range, as indeed obtained from the X–ray spectral analysis. Note that the X–ray spectra shown in this section have been "de-absorbed" both for the galactic and the host frame (when present) contributions.

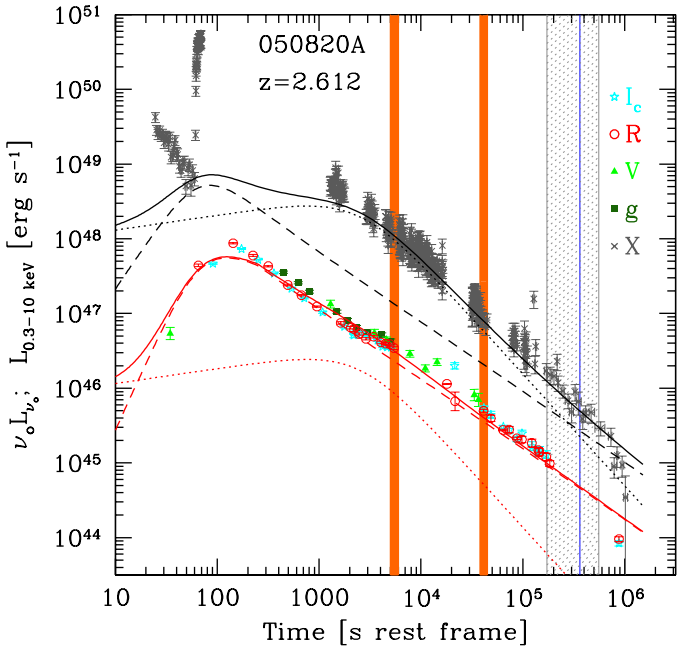

Figure 8.4: Top panel: X–ray and optical light curves of GRB 050820a (rest frame time). Same notation as in Fig. 8.2. The thin vertical line represents the jet break time with its estimated errors (see Ghirlanda et al. 2007 and references therein). The thick vertical lines mark the times at which the SEDs are extracted.

8.2.3 GRB 050820a

The photometric data are from Cenko et al. (2006a, 2009). *Swift*/BAT triggered on a precursor about 200 s before the main event (Cenko et al 2006a, Burlon et al. 2009). Our reference time is set at the trigger time and we do not consider the prompt X–ray emission detected before the end of the main γ–ray event. The X–ray light curve is dominated by the "late prompt" component up to 200 ks (720 ks in the observer frame), and by a "standard afterglow" component after then. The "standard afterglow" emission instead prevails during the entire duration of the optical light curve but in a time interval around 5 ks (18 ks observer frame) where its contribution becomes comparable with the "late prompt" one (see Fig. 8.4).

We extracted two SEDs in order to test the modelling at two different light curve phases. The first one at about 20 ks in the observer frame ($\sim$ 5500 s rest frame) where the "late prompt" gives the maximum contribution in the optical light curve and the available photometry is richer (I_c, R_c, V, g and B bands). Cenko et al. (2006a) estimated a $\beta_{\rm o} = 0.77$ with negligible host galaxy dust absorption while Kann et al. (2009) inferred an $A_{\rm V}^{\rm host} = 0.065 \pm 0.008$. We used the latter estimate and obtained $\beta_{\rm o} \approx 0.7$. This first SED is plotted in Fig. 8.5 and shows that the optical flux lies slightly above the extrapolation of the broken power law that best describes the XRT spectrum, but as the uncertainties on $\beta_{\rm X,1}$ are quite large the optical flux is fully consistent with the extrapolation.

As mentioned at 5500 s (rest frame) the optical flux is due to a similar contribution of the "standard afterglow" and the "late prompt" component. The cooling frequency is already redward of the considered optical bands and the "standard afterglow" has $\beta_{\rm o} = 0.92$ (corresponding to an emitting particle distribution with slope $p = 1.85$). In the "late prompt" component modelling, the low energy spectral index is instead $\beta_{\rm o} = 0.45$ (see Eq. 3 in G09), consistent within errors with $\beta_{\rm X,1}$. The intermediate value of the observed optical slope is thus consistent with the predictions of the two component modelling.

We considered a second SED at about 150 ks after the trigger (observer frame, corresponding to 41 ks rest frame). In this phase the X–ray light curve is dominated by the "late prompt" while the "standard afterglow" dominates the optical emission. The combined SED is plotted in the bottom panel of Fig. 8.5 and confirms the proposed scenario: the optical data are at this time much brighter than what predicted by the extrapolation (with slope $\beta_{\rm X,1}$) of the X–ray spectrum to the optical bands . Even though at these late times there are only 3 available photometric points (I_c, R_c and V band) and the V band flux is affected by a large error, the optical SED is well fitted by a softer $\beta_{\rm o} = 0.95$ that is closer to the value predicted for the "standard afterglow" component.

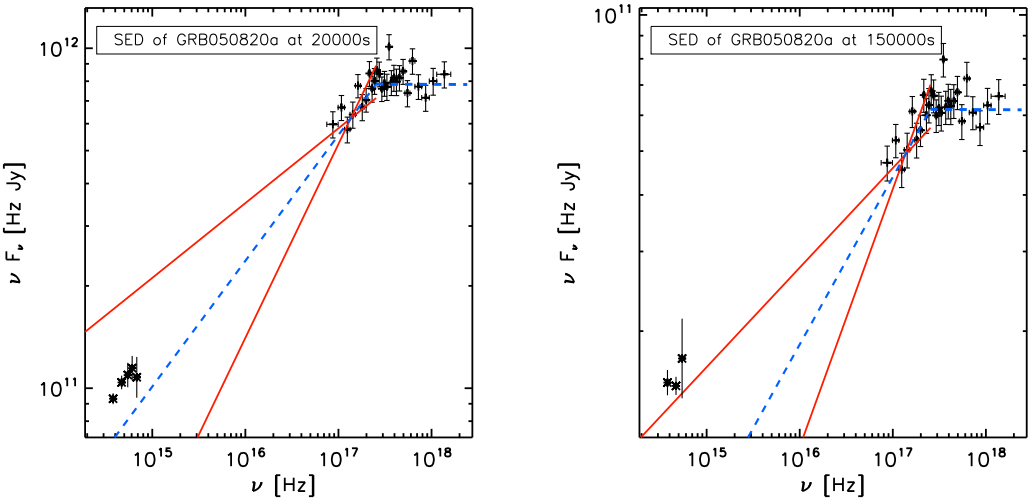

Figure 8.5: *Left and Right panels*: Optical to X–ray νF_ν SED of GRB 050820a extracted around 20 ks (left) and around 150 ks (right) after trigger in the observer frame (corresponding to 5.5 ks and 41.5 ks in the rest frame). The dashed line shows the best fit (with the ABP model) to the X–ray spectrum (spectra parameters are reported in Tab. 7.3.2) and the solid lines are the uncertainties on the slope of the low energy spectral index $\beta_{\rm X,1}$.

8.2.4 GRB 060210

The optical afterglow has been observed in the R and I bands (photometric data from Curran et al. 2007), while, because of the high redshift, smaller wavelengths bands are not observable due to the Lyα limit. The X–ray light curve shows an intense flaring activity at early times and it is dominated by the "late prompt" component at later times. The optical light curve is sampled only up to ∼2000 s rest frame (∼ 9800 s observer frame) and is dominated by the "standard afterglow" emission, as shown in Fig. 8.6. Since fluxes in only two optical bands are available it is not possible to infer the value of $A_{\rm V}^{\rm host}$ from the optical photometry. Curran et al. (2007) found a very soft observed spectrum, after correction for Galactic extinction and Lyα absorption: the optical spectral index $\beta_{\rm o}^{\rm obs} = 3.1$ at 5000 s (observer frame). Assuming that the optical and X–ray emission are produced by the same mechanism they inferred two possible values of the host galaxy dust extinction, assuming either a single or a broken power–law joining the optical and the X–ray data.

We extracted 3 SEDs at 600, 4500, 6500 s (observer frame; see Fig. 8.7). In the two component modelling the optical and X–ray emission would be due to different components, to account for their different temporal behaviours. Thus $A_{\rm V}^{\rm host}$ cannot be inferred from the optical to X–rays SED. If we assumed a $\beta_{\rm o} \approx 0.5$ then $A_{\rm V}^{\rm host} \approx 0.65$, a value similar to the mean Small Magellanic Cloud–like

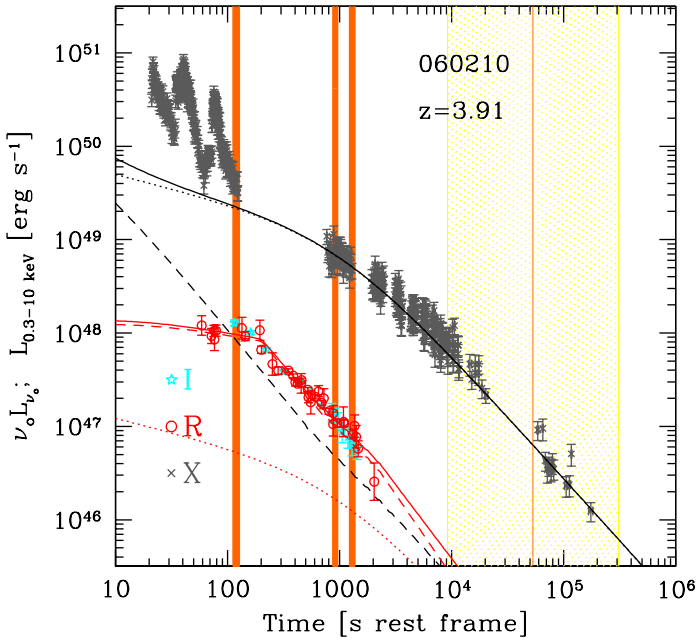

Figure 8.6: X–ray (in grey) and optical (different symbols, as labelled) light curves of GRB 060210 (in the rest frame time). Same notation as in Fig. 8.2. The vertical line and stripes indicate the jet times expected if the burst followed the $E_{\rm peak}$ vs. E_γ "Ghirlanda relation" (Ghirlanda et al. 2007) (see text). The vertical lines mark the time at which the SEDs are extracted.

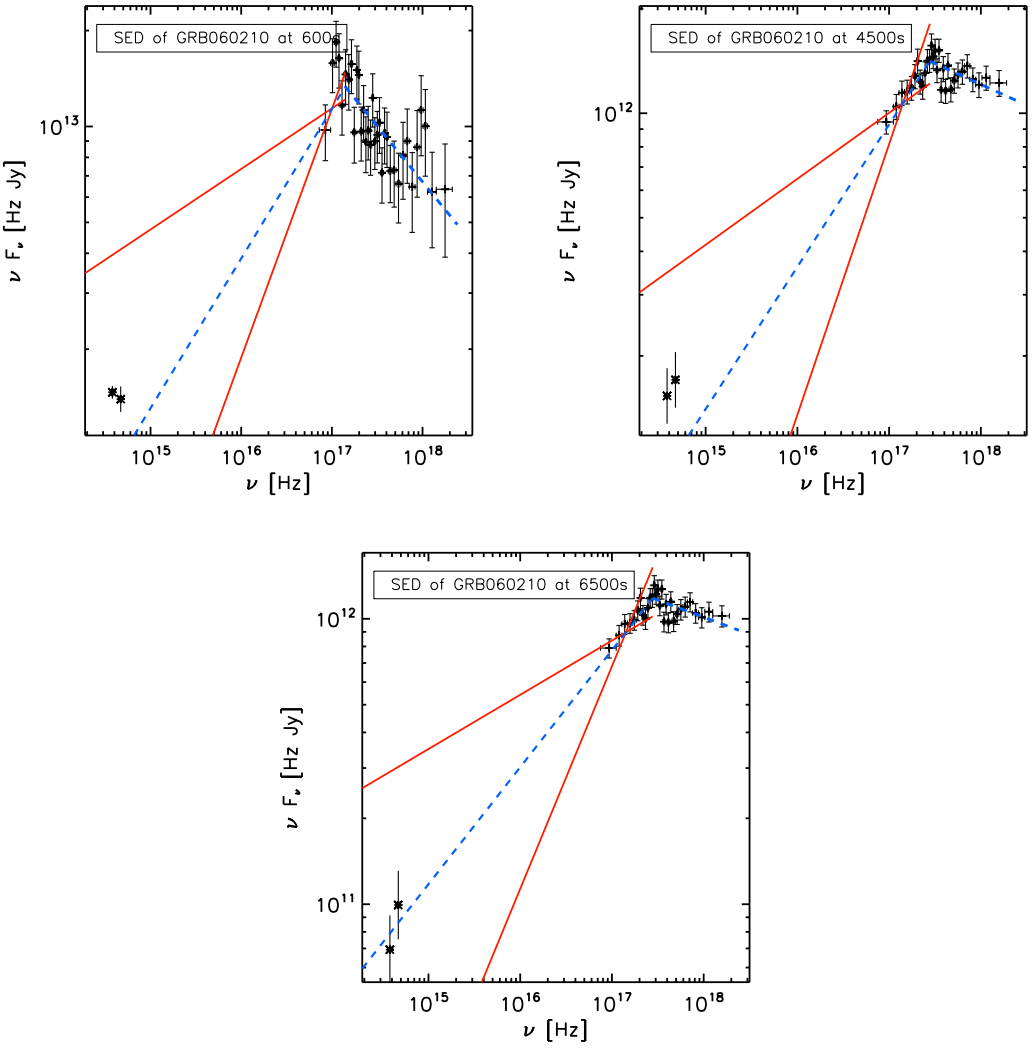

Figure 8.7: Optical to X–ray νF_ν SED of GRB 060210 extracted at three selected times. The dashed lines are the best fit value of $\beta_{X,1}$ and the solid lines represent the errors as given in Tab. 7.3.2. The top and the bottom panels show the SEDs at 600 and 4500 s after trigger (observed time, corresponding to 120 and 916 s in the rest frame). The bottom panel shows the SED 6500 s after trigger (observed time, corresponding to 1300 s in the rest frame). The dashed line shows the best fit (with the ABP model) to the X–ray spectrum (spectra parameters are reported in Tab. 7.3.2) and the solid lines are the uncertainties on the slope of the low energy spectral index $\beta_{X,1}$.

$E_{\rm B-V} = 0.27$ obtained by Curran et al. (2007) in the broken power–law case. This correspond to the correction applied to the SEDs plotted. The large error on $\beta_{\rm X,1}$, and the paucity of photometric data do not allow to draw any firm conclusion on this burst.
The optical to X–ray SED at 4500 and 6500 s (observer frame) are consistent with an unique broken–power law SED, at odds with the different optical to X–ray temporal behaviour. The optical SED at 600 s appears harder ($\beta_{\rm o} \approx 1$), possibly consistent with the passage of a cooling frequency through the optical bands in a wind like scenario. Since the X–ray spectral break does not shift in energy significantly during the considered time interval, it is possible to exclude that the different optical and X–rays temporal behaviour is simply due to a moving cooling frequency.

No break is observed in the X–ray light curve. In particular, one can estimate the expected jet break time if the GRB was to follow the so called "Ghirlanda relation" (Ghirlanda et al. 2007). However the lack of evidence for such a break is consistent with the light–curve modelling as the X–ray flux is indeed dominated by the "late prompt" emission at the time when the jet break is expected. No data are available at such time in the optical band where the jet break should have been detectable, due to the dominance of the "standard afterglow" component.

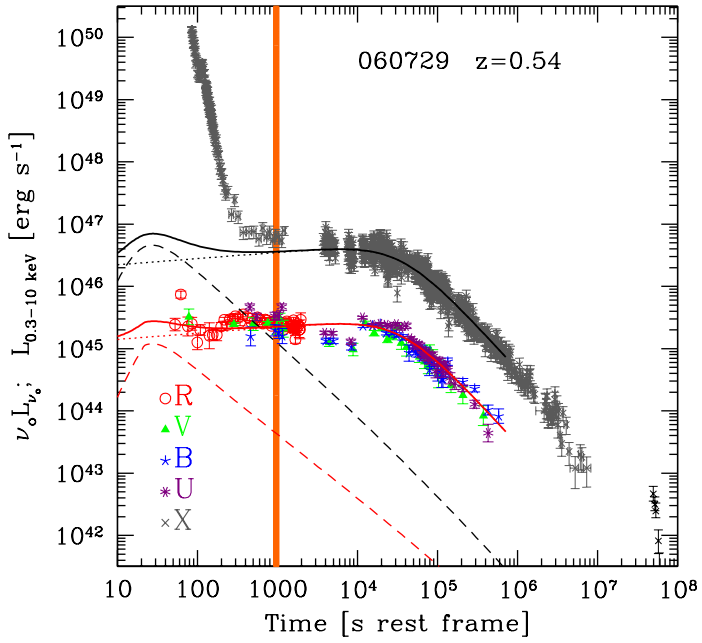

Figure 8.8: X–ray (in grey) and optical (different symbols, as labelled) light curves of GRB 060729 in rest frame time. Same notation as in Fig. 8.2. The vertical line represents the time at which the SED is extracted

8.2.5 GRB 060729

The UVOT data in 6 filters are from Grupe et al. (2007) while the ROTSE R band photometry is from Rykoff et al. (2009).

After a steep decay in X–rays for about 400 s, the optical and X–rays light curves track each other and are characterised by a long lasting ($\sim$ 50 ks) shallow decay phase. Following an achromatic break, a steeper flux decay phase is observed in X–rays up to about 10^7 s after the burst (Grupe et al. 2009). The light–curves are dominated by the "late prompt" component with no significant evolution of the optical to X–ray flux ratio as can be seen in Fig. 8.8. As a consequence, the optical to X–ray SED is not expected to evolve in time.

Fig. 8.9 shows that the optical flux at about 1500 s is indeed consistent with the extrapolation to the optical band of the broken power law X–ray spectrum. The SED does not require any additional host galaxy dust absorption, but the quality of the optical–UV SED is not good enough to constrain the $A_{\rm V}^{\rm host}$.

It is possible to consider SEDs at later times based on the UVOT data (the R band photometry covers only the first XRT orbit). It is possible to notice from the right panel of fig.8.9 showing the optical to X–ray SED at 20 ks (observer frame)

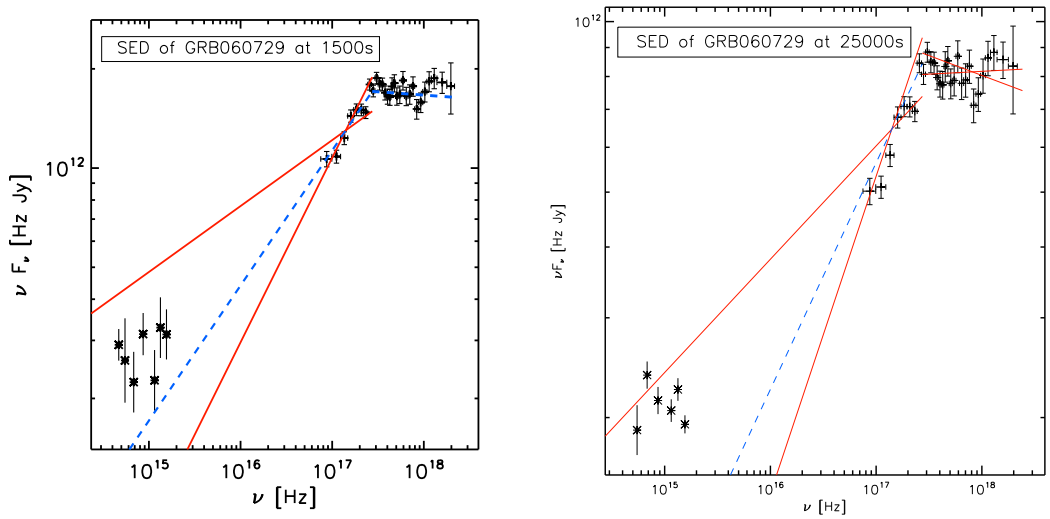

Figure 8.9: *Left and Right panels*: Optical to X–ray νF_ν SED at about 1500 s after trigger in the observer frame (970 s rest frame). The dashed and solid lines show respectively the best fit (with the ABP model) to the X–ray spectrum (the spectral parameters are reported in Tab. 7.3.2) and the uncertainties on the slope of the low energy spectral index $\beta_{X,1}$

that neither the optical to X–ray flux ratio nor the optical colour significantly evolve.

8.2.6 GRB 061007

The photometric data are from Mundell et al. (2007) (I, R, V and B bands) and Rykoff et al. (2009) (ROTSE R band). After a steeper flux decay lasting about 90 s (rest frame), the X–ray light curve declines following a single power–law for the whole observed time. The optical flux instead shows a fast rise (by about 2 orders of magnitude) in the first 40 s followed by a simple power–law decay up to about 60 ks rest frame (see Fig. 8.10). The first R band fluxes are simultaneous with the γ–ray prompt emission, and the rise between the first and second detection is faster than t^5, hardy explainable with any standard emission mechanism.

In the two component modelling the optical light curve (after the end of the prompt phase, i.e. $\sim$ 50s in the rest frame) is dominated by the "standard afterglow" emission.

According to this interpretation, there would be a flux excess simultaneous with the BAT γ–rays emission both in the optical and X–rays bands. The single power–law X–ray decay phase after the end of the γ–ray detection would be dominated by the "late prompt" component. Thus the X–ray and optical fluxes would be dominated by two different components, despite the similarity of the light curves

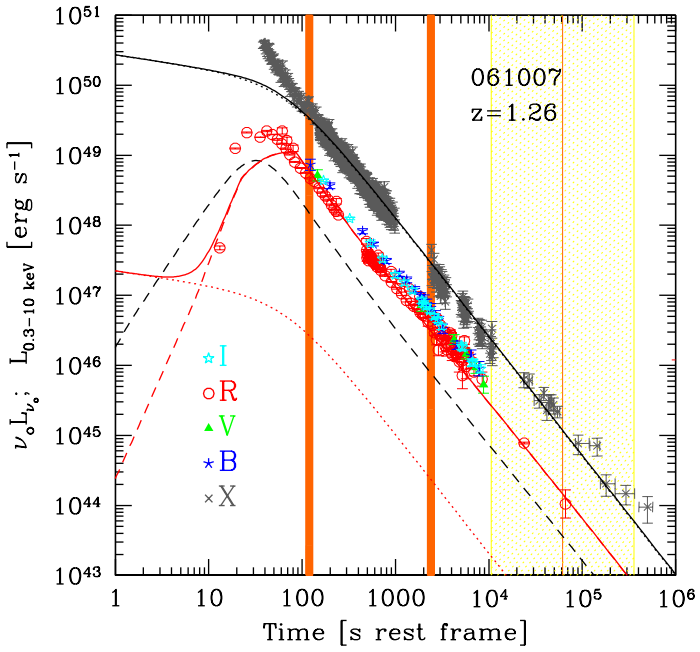

Figure 8.10: X–ray and optical light curves of GRB 061007 in rest frame time. Same notation as in Fig. 8.2. The vertical line and stripes indicate the jet times expected if the burst followed the $E_{\rm peak}$ vs. E_γ "Ghirlanda relation" (Ghirlanda et al. 2007) (see text). The vertical lines mark the times at which the SEDs are extracted.

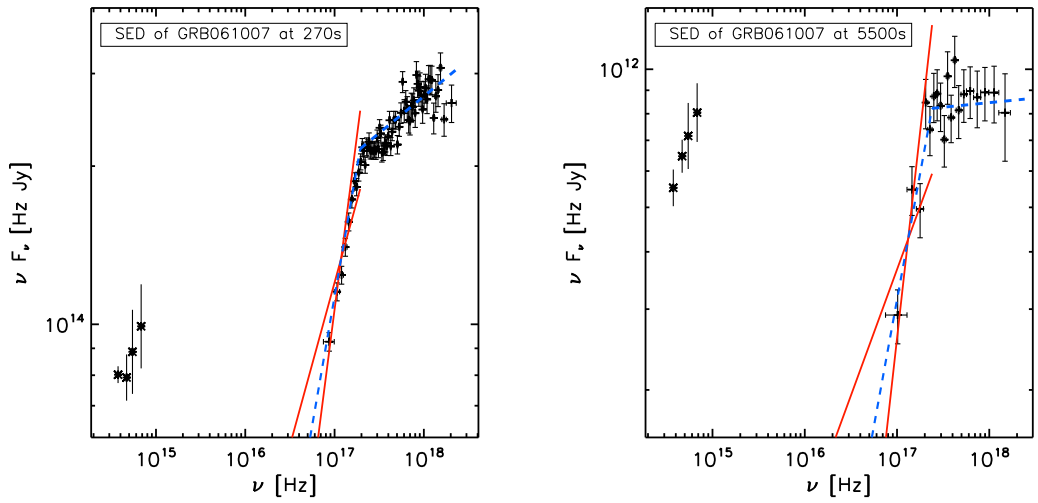

Figure 8.11: Optical to X–ray νF_ν SED at about 270 s (Left) and 5500 s (Right) after trigger in the observer frame (corresponding to 120 s and 2.4 ks in the rest frame). The dashed and solid lines show respectively the best fit (with the ABP model) to the X–ray spectrum (the spectral parameters are reported in Tab. 7.3.2) and the uncertainties on the slope of the low energy spectral index $\beta_{X,1}$.

after ∼100 s (rest frame), requiring a hard "late prompt" $\beta_{X,1}$ in order for this emission not to significantly contribute to the observed optical flux.

The optical fluxes have been corrected for a host galaxy dust extinction $A_V^{host} = 0.54 \pm 0.30.3$ (Kann et al. 2009). We considered two SEDs at the times where all of the four photometric bands are simultaneously available: the first one at about 270 s (observed frame), immediately after the beginning of the simple power–lax X–ray decay, and the second one at about 5.5 ks (observed frame). In both cases the hard $\beta_{X,1}$ implies a negligible contribution of the X–ray component in the optical band, supporting the proposed interpretation. (see the left and right panels of Fig. 8.11).

The X–ray light curve does not show any slope variation in correspondence to the expected jet break time obtained in the assumption that the GRB follows the "Ghirlanda relation". Once again this is in agreement with the "late prompt" dominated nature of the X–ray flux. The jet break should instead be visible in the optical, but unfortunately there are no observations after 150 ks (observer frame) to confirm or rule out this prediction.

8.2.7 GRB 061126

A very dense photometric sampling is available for GRB 061126 (Perley et al. 2008, Gomboc et al. 2008). After a steeper decay the X–ray light curve follows

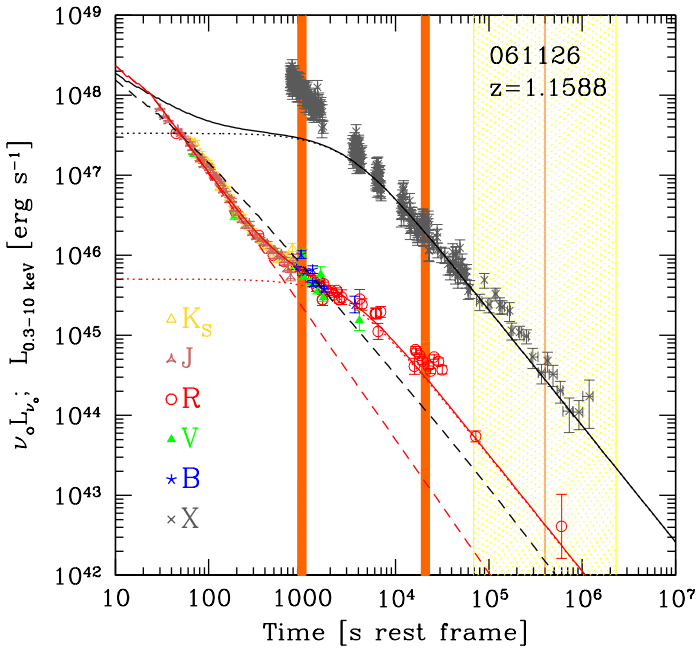

Figure 8.12: X–ray (in grey) and optical (different symbols, as labelled) light curves of GRB 061126 in rest frame time. Same notation as in Fig. 8.2. The vertical line and stripes indicate the jet times expected if the burst followed the $E_{\rm peak}$ vs. E_γ "Ghirlanda relation" (Ghirlanda et al. 2007) (see text). The vertical lines mark the times at which the SEDs are extracted.

a single power–law flux decay for the whole observed time. The IR–optical–UV light curve instead shows a more complex behaviour, as shown in Fig. 8.12.

We modelled the power–law decay of the X–ray light curve as a "late prompt" component. The optical bands is accounted for by a sudden transition from a "standard afterglow" dominated early time to a "late prompt" dominated late time behaviour. If correct, this scenario would imply a spectral evolution from a two components to a single component optical–to–X–ray SED. We would also expect an evolution of β_o at the time of transition between the two components.

We extracted two SEDs, plotted in the middle and bottom panels of Fig. 8.13. The first one (left panel) corresponds to ∼2000 s (observer frame) and is obtained using 8 contemporaneous photometric bands (U, B, V, R, I, J, H, and Ks). At this time the optical spectrum is well fitted by a single power law with $\beta_o = 0.94 \pm 0.05$, and no host galaxy dust absorption is required. This is in agreement with the findings by Perley et al. (2008). The optical spectrum slope is inconsistent with the X–ray spectrum. We examined a second SED at 45 ks (observer frame; right panel of Fig. 8.13) when both the optical and X–ray light curves are dominated by the "late prompt" component. At that time only 4 optical bands are available (I_c, R_c, V and B), and the spectrum is still well fitted by a single power–law without host galaxy dust absorption, but the spectral index is harder than at earlier times (i.e. $\beta_o = 0.54 \pm 0.1$). The right panel of Fig. 8.13 reveals that not only the optical fluxes but also the optical slope are now consistent with the extrapolation from the X–rays (with slope $\beta_{X,1}$).

As predicted by the light curve modelling, the optical spectral index evolves after the transition from standard afterglow to late prompt emission, with the SED becoming consistent with a single dominating component.

We can contrast our interpretation with the alternative one proposed by Gomboc et al. (2008), who suggested that the presence of some dust absorption at early times could account for the optical spectrum being consistent with a broken power–law optical–to– X–ray SED. At later times the SED could be fitted with a similar broken power–law but without the need of any host galaxy dust absorption. Thus in the Gomboc et al. (2008) scenario a change in dust absorption would be required to interpret the optical spectral and broad band SED evolution.

Also for this burst we can evaluate the expected jet break time in the hypothesis that the GRB follows the "Ghirlanda relation". However, at the corresponding epoch both the optical and X–ray emission are dominated by the late prompt contribution and thus no jet break would be observable. This is indeed in agreement with the absence of a break in the observed light curves, although the observations end soon after the predicted jet break time.

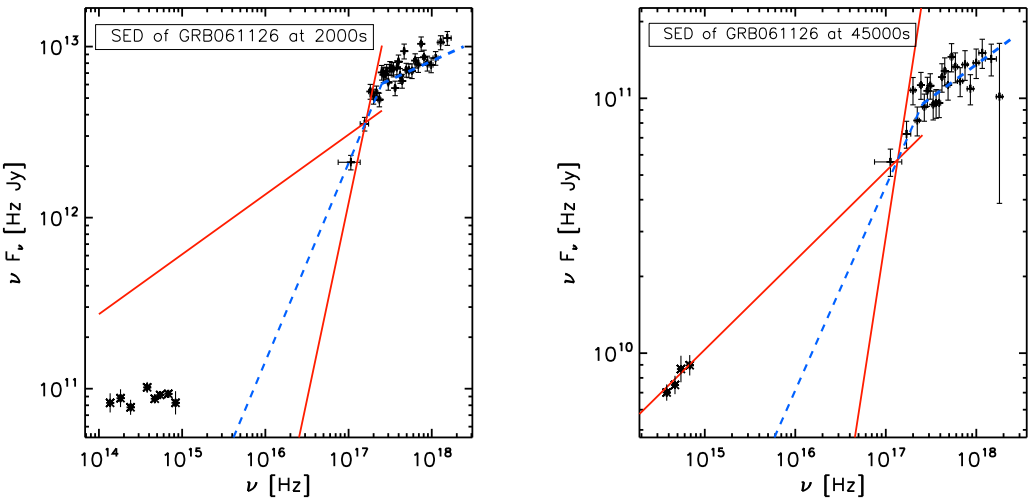

Figure 8.13: Optical to X–ray νF_ν SED of GRB 061126 extracted around 2200 s (mid) and around 45 ks (bottom) after trigger in the observer frame (corresponding to 1000 s and 21 ks in the rest frame). The dashed line shows the best fit (with the ABP model) to the X–ray spectrum (spectra parameters are reported in Tab. 7.3.2) and the solid lines are the uncertainties on the slope of the low energy spectral index $\beta_{\rm X,1}$.

8.3 Conclusions

We analysed the *Swift* XRT data of a sample of 33 long GRBs selected by G09 to have known redshift, published estimate of the host galaxy dust absorption and good XRT and optical follow up.

If the XRT 0.3–10 keV spectra are modelled as a single power law, we confirm that the host frame $N_{\rm H}^{\rm host}$ column densities are rather large when compared to the values of the host galaxy dust absorption inferred from the optical analysis, according to " standard" extinction laws (see also Schady et al. 2007, Stratta et al. 2004).

For the 15 brightest bursts we could model the X–ray data with a broken power law, and in 7 cases we find evidence of a spectral break. In such cases the required $N_{\rm H}^{\rm host}$ is in turn smaller than for the single power–law fitting and is marginally consistent with the column estimated by the optical extinction. However, in other 8 bright GRBs the X–ray spectrum does not show any break and some of them do require a large value of $N_{\rm H}^{\rm host}$. Therefore the presence of an intrinsic curvature in the spectrum cannot be considered as a general solution for the "excess" of $N_{\rm H}^{\rm host}$ commonly found in GRB X–ray spectral analysis.

In order to test the interpretation by G09 that the X-ray and optical light curve complex behaviour can be interpreted as due to the contributions to the

emission by two different components, we combine the results of the light curve de-convolution with the X–ray and broad band spectral properties at different times.

In particular we checked whether the presence of a break in the XRT spectra is consistent with what has been observed in the optical bands by studying the time dependent optical to X–rays SEDs of the GRBs for which a spectral break was found.

We found that all the events are consistent with the presence of a break in the XRT spectra and the evolution of the broad band SEDs appears to support the predictions of the two components scenario, even in the presence of complex light curve behaviours.

Consistency is also found in relation with the (lack of) evidence for jet breaks in the light curves, whose break time is estimated by assuming that the Ghirlanda relation holds for all GRBs (Ghirlanda et al. 2007). Indeed light curves are observed to steepen in correspondence with the jet break time only when the light curve is dominated by the "standard afterglow" emission while no break is detected if the other component is dominating.

Further testing of the two–component modelling requires to extend the simultaneous multi–band optical follow–up at later times (i.e. several days after the trigger), when the typical expected R band magnitudes are around 24–25. Such an intensive and long lasting multi–band follow up could allow us: i) to search for possible optical spectral index evolution when a different component becomes dominant (as in the case of GRB 061126); ii) to test for the presence (absence) of jet breaks in "standard afterglow" ("late prompt") dominated optical light–curves in a larger sample of events, presumably shedding light also on the jet geometry and energetics.

Chapter 9

Summary and conclusions

9.1 Summary of the obtained results

In the first part of my thesis (see §3) I studied the intrinsic optical luminosity distribution of the long GRB afterglows. After correcting for the distance and for the effects of the host galaxy dust absorption I found that, even if the observed optical fluxes differ widely from burst to burst, the intrinsic de-reddened and k-corrected optical luminosities of most GRBs tend to cluster around a typical value. Selecting a common rest frame time $t = 12$h after trigger, the distribution of the optical luminosities of most GRBs (taking as a reference the central R band wavelength in the rest frame) clusters around $\log[L_{\nu_R}^{12\mathrm{h}}] = 30.71$erg Hz^{-1}s^{-1} with dispersion $\sigma = 0.31$.

I found also that the observed optical luminosity distribution is bimodal. Indeed, the remaining GRBs that do not cluster around $\log[L_{\nu_R}^{12\mathrm{h}}] = 30.71$ erg Hz^{-1}s^{-1}, seem to form a separate less luminous family. This second group lies at more than 4σ from the main group being under luminous by a factor $\sim$30.

This result appears even more interesting when comparing the optical luminosity distribution with what observed in the other bands. The prompt gamma ray energy distributions do not show any evidence of clustering or bimodality and there is no clear correlation between the gamma ray properties of these events a their optical luminosities. The same happens when considering the X–ray afterglow luminosities. Even if Gendre et al. (2005, 2007) found hints of clustering and bimodality also in the X–ray afterglow luminosity distributions, there is no direct connection between what we see in the optical and in the X–rays with some optically bright GRBs belonging to the fainter X–ray luminosity family. In §3.1.4 I also discuss these results in the framework of the standard external shock fireball model.

I showed that we are able to reproduce a clustering in the optical luminosities

together with a wider X–ray luminosity distribution of the optically brighter events in the standard afterglow model framework, under the strong and quite ad hoc assumptions that all the GRBs have almost the same initial kinetic energy and similar micro-physical parameters (e.g. $\epsilon_{\rm e}$ $\epsilon_{\rm b}$). This is obtained, imposing the cooling frequency to fall between the optical and X–ray bands, simply modifying the value of the electron energy spectral index p. Even if it is possible to find such a justification of the clustering of the optical luminosities in the standard afterglow model framework, the bimodality in the optical luminosity distribution is much harder to explain.

The clustering and bimodality have been found in a sample of GRBs that have been observed in the optical bands and, in principle, these results could be affected by some observational biases due for example to instrumental selection effects.

For this reason I studied how the observational selection biases affect the observed afterglow properties. I tried to disentangle the evidences of the afterglows from the effect of the observational selection effects. This study is discussed in §4. I considered dark GRBs (i.e. GRBs for which no optical afterglow has been detected even if they have been followed up with good observing conditions and even if they have been detected in the X–ray band). I analysed the limiting magnitudes of the failed optical observations of the dark GRBs finding the probability for each GRB to be observed with a certain limiting magnitude.

Through a Montecarlo simulation I then proved that both the observed clustering and bimodality are not simply due to selection effects but convey important information regarding the nature of the afterglow emission.

I then studied the importance of the presence of dust inside the GRB host galaxy when interpreting the observed results. In particular I focused on the importance of the effects of the host galaxy dust absorption. I tested whether the effects of standard dust extinction in the GRB host galaxies can mimic the observed clustering and bimodality starting from an unimodal luminosity function. I found that this is not the case. The clustering and bimodality observed in the distribution of optical afterglow luminosities can be explained either with an intrinsic bimodality in the optical luminosity function or with the presence of a strong achromatic "grey" dust absorption that cannot be identified through the standard methods for estimating $A_V^{\rm host}$.

As a consequence, my results suggest that optically dark GRBs can either belong to an optically sub luminous family or be affected by a strong achromatic dust absorption. In §1.2.6 I also compared some other properties of the optically dark GRBs with the ones with observed optical afterglows finding that they appear fainter in the X–rays and that they are usually characterised by higher $N_{\rm H}$ column densities in excess to the Galactic value bat since there is no clear correlation between the host galaxy $N_{\rm H}$ column density and the optical dust absorption, these results can not lead to a conclusive solution between the two proposed scenarios

(i.e. intrinsic bimodality or grey dust).

In the second part of my thesis I focused on the complex relation between the optical and the X–rays light curves characteristics. *Swift* is able to observe the optical and the X–rays afterglow evolution starting a few tens of seconds after the gamma ray trigger. The observations at such early times showed that the the light curve evolution is much more complex than what expected before the launch of *Swift* and it cannot be explained by the standard afterglow models.

Since I had already studied the complex relation between the optical and X–ray afterglow luminosities I was particularly interested in the fact that in a large number of GRBs the optical and X–ray light curves do not track one other and the broad band light curves evolution was not consistent with the standard model predictions.

I therefore collaborated in Ghisellini et al. (2009) in proposing an alternative view of the optical and X–ray GRB afterglow emission. In §5 I discuss the alternative scenario in which the broad band optical to X–ray spectral evolution is due to the sum of two separate emission mechanisms. We analysed the rest frame de-absorbed and K-corrected optical and X–ray light curves of a sample of 33 GRBs with known redshift and optical extinction at the host frame. We modelled their broadband behaviour as the sum of the standard forward shock emission due to the interaction of a fireball with the circum–burst medium and an additional component. The latter component (called Component II) is treated in a completely phenomenological way with the aim of minimising the free parameters. The idea is to test if we are able to well describe the observed optical and X–ray light curves behaviour and then try to use the Component II parameter distributions in order to make a first step towards the construction of a more physical scenario.

In §5 I show that we are able to reproduce the observed light curves despite their complexity and diversity. Most of the X–ray light curves are dominated by this additional Component II while the optical emission is usually dominated by the standard afterglow process. In §5 I discuss also the distribution of the parameters that we used to model the light curves.

The distributions of the second component parameters show some interesting features. In particular the values of the post break second component decay index $\alpha_{\rm steep}$ cluster around 1.6: this is remarkably close to 5/3 that is the predicted decay of the accretion rate of fallback material onto the black hole. It is also the average decay of the X–ray flare luminosity. This result strongly suggests that Component II can be interpreted as due to the late time accretion of fallback mass, namely material that failed to reach the escape velocity from the exploding progenitor star, and falls back.

We also found an interesting correlation between the total energy emitted in γ–rays during the prompt event $E_{\gamma,\rm iso}$ and the energetics of the second component. This correlation is stronger than the one between $E_{\gamma,\rm iso}$ and the kinetic fireball

energy E_0, implying that it is not simply due to the common redshift dependence.

These results seems to be in agreement with the predictions of the late prompt model (Ghisellini et al. 2007) described in §2.4 and discussed in §5. Apart from this possible theoretical interpretation, the two–component model that we are proposing has the important characteristic to disentangle the standard afterglow emission from a Component II that has a completely different origin. This choice has a fundamental impact on one of the most discussed topic in the *Swift* era: the lack of achromatic jet breaks in the optical–X–ray light curves.

The lack of jet breaks has important implications on different GRB related fields. First of all, if the observed emission is produced by a standard afterglow mechanism, the lack of jet breaks implies that GRB are not collimated into jets but emit isotropically. In this scenario the total energy emitted by the burst is about two orders of magnitudes larger than in the case of collimated GRBs reaching values of a few $\times 10^{54}$ erg (several $M_{\odot}c^2$). The measure of the break time allows to evaluate the collimation corrected gamma ray energy and this quantity has important implications on the possible use of GRBs as cosmic rulers (Ghirlanda et al. 2004b, Nava et al. 2007). The lack of jet breaks detection opened therefore a fervent discussion on these attempts to use GRBs in cosmology. In the scenario we are proposing, the second component is due to a completely different mechanism with respect to the standard afterglow emission and no jet break is therefore expected if the light curve is dominated by the second component. We therefore analysed all the light curves of the GRBs in our sample and we are able to explain the presence of chromatic breaks in the light curves (when only one band is dominated by the standard afterglow and the other is dominated by Component II) and to account for the lack of jet breaks observations without requiring isotropic emission (and therefore huge energy releases) when Component II is dominating. This point is discussed in §6.

The two components model can be also tested from the spectral point of view. If the optical and the X–ray emission are produced by different processes, the two components spectra must break between these bands in order to avoid that the mechanism that is dominating in the X–rays interferes with the observed optical emission and vice versa. I therefore checked if such a break can sometimes fall within the observed XRT energy range (see §7). When this occurs (i.e. in 7 cases in our sample), the fact to have directly measured the break energy and the low energy spectral index makes these events the best candidates to test the two component light–curve modelling from a spectral point of view.

As discussed in §8, in the cases in which a break is found in the X–ray spectrum, it is possible to analyse the simultaneous optical to X–ray spectral energy distributions and to test whether they are consistent with the predictions of the two-component light curves modelling predictions. We found that all the events are found to be fully consistent with what predicted by our model.

In §8 I also discussed the fact that in many GRBs large $N_{\rm H}^{\rm host}$ column densities have been found from the analysis of the X–ray spectra. This seems to be in contradiction with the fact that very small $A_{\rm V}^{\rm host}$ amount of dust extinction have been found from the optical SED analysis. The presence of a spectral break in the X–ray spectrum could mitigate the $N_{\rm H}^{\rm host}$ requirement. In §8 I show that, even if the required amount of $N_{\rm H}^{\rm host}$ is smaller in the cases in which I find a break within the XRT energy range, large values of $N_{\rm H}^{\rm host}$ are found also in the bursts where the spectral break is excluded and therefore the large values oh $N_{\rm H}^{\rm host}$ in GRBs is still an open issue.

9.2 Conclusion

In the 7 years between the first GRB afterglow detection and the launch of the *Swift* satellite, there was a widely diffused agreement on the physical mechanism responsible for the afterglow emission of long GRBs.

According to this picture, the central engine is active only for the duration of the prompt, powered by accretion of the part of the core of the progenitor star that failed to originate the black hole.

In this scenario the gamma–ray prompt emission is associated to the "internal shocks" between shells produced by the central engine with different Lorentz factor. The forward shock produced by the "external shock" between the ejected relativistically expanding material with the material surrounding the GRB progenitor is, instead, responsible for the emission of the whole afterglow radiation. The optical and X–ray afterglows are therefore produced by the same process and in the same location.

The optical and X–ray observations that were available at that time (usually starting some hours after the gamma ray trigger) were in a good agreement with the predictions of the model that became the standard scenario for our comprehension of the GRB phenomenon.

The remarkable instrumental development that followed the launch of the *Swift* satellite opened a new window on the GRB science. Much better sampled optical and X–ray light curves are now observed starting from a few tens of seconds after the gamma ray trigger. The standard scenario is not able to account for the complexity of the light curves that we now observe in these bands.

This prompted the development of alternative scenarios to explain the GRB afterglow emission in the light of the new observational evidences. Most of them try to explain the *Swift* GRB afterglow observations with some modifications of the standard GRB paradigm, maintaining the basic assumption that the optical and X–ray afterglow emission are produced by the same process and in the same emitting region. In many cases these models focused on the X–ray flux behaviour overlooking the expected optical properties.

I instead decided to contemporaneously study the GRB afterglow properties in the optical and X–ray bands. In my studies on the afterglow luminosities I found that the clustering and bimodality in the optical luminosity distribution are not directly connected with what we observe in the X–rays and cannot be explained in the standard afterglow scenario. In the analysis of the optical to X–ray light curves and SEDs that I carried with the group I am working with we tried, for the first time, to contemporaneously model the evolution of the optical and the X–ray fluxes of a relatively large sample of GRBs. We were led to consider that two different mechanisms are at work.

The inconsistency between the optical and X–rays luminosity distributions, together with the success of the two-component model that we proposed, allows us to propose a new view on the nature of the broad band GRB afterglow emission. Two separate emission mechanisms coexist, both emitting at the observed optical and X–ray frequencies.

In this new picture, (called late prompt scenario) the internal engine activity lasts for a much longer time with respect to the standard model. After the "standard" prompt phase, in which the central engine produces the high Lorentz factor shells that are responsible for the gamma–ray prompt emission, this central engine does not turn off (as in the standard model). Its activity persists for a much longer time, keeping on producing shells with less power and smaller Lorentz factors than before. These late time shells can produce a long lasting radiation that competes with the standard forward shock afterglow emission.

The existence of the late prompt *and* of the standard forward shock emission can account for the very complex afterglow behaviour we observe.

The long lasting central engine activity is sustained by the accretion of the material that failed to reach the escape velocity from the exploding progenitor star, and falls back. Accretion of fall back material can last for a very long time (even weeks-months after the explosion) and its possible presence is strengthened by the similarity between the temporal evolution of the late prompt component and the expected time profile of the accretion rate of the fall back material.

The main conclusion is to have shown that the paradigm that the optical and X–ray afterglow emission are produced by the same mechanism is not appropriate any longer for describing the observations. A new view is now needed, in which separate mechanisms coexist producing the observed radiation.

We therefore moved from a scenario in which the activity of the central engine lasts for only a few hundreds of seconds, and where the interaction of the expanding material with the interstellar medium is responsible for the long lasting broad band afterglow emission, to a different picture in which the central engine remains active for a much longer time, sustained by the fall back material accretion, producing a late time optical and X–ray radiation that competes with the external shock (standard) afterglow emission.

The two-component model has been tested on a sample of 33 GRBs. In order to confirm our scenario, a larger sample of densely observed events is needed. When this will be available, we will verify if sub classes of events (with respect to e.g. redshift, prompt gamma–ray energy, afterglow luminosity) have similar properties and we can see if the correlation between the energetics of the early and late prompt still holds.

It has been noted that the X–ray flares are probably related to fragmentation of the fall back material. The origin of the X–ray flares is therefore probably connected with the late prompt mechanism. Also the average flare luminosity decays as $t^{-5/3}$, but this intriguing result is based only on a dozen of GRBs. A systematic study of this issue will soon be possible using larger samples and such a study should be useful in order to verify the connection between X–ray flares and late prompt emission.

In our scenario, a jet break in the optical and X–ray light curve can be seen only if the observed fluxes are dominated by the standard afterglow emission. In the last years only a few GRBs have been observed in the optical until late times after the trigger. A much denser late time (at least some weeks–one month after trigger) optical follow up is needed for a larger number of GRBs in order to verify if the two component model predictions are in agreement with the lack/presence of achromatic breaks in the optical light curves. Since the two component modelling is able to tell which component is dominating in the optical band, these late time optical observations represent a important observational test of the model.

Chapter 10

Appendix

10.1 References for the data plotted in Fig. 3.2 and in Fig. 3.4

- GRB 970508: Garcia et al, 1998; Sokolov et al., 1998; Vietri et al., 1998.
- GRB 971214: Diercks et al., 1998.
- GRB 980613: Hjorth et al., 2002.
- GRB 980703: Bloom et al., 1998, Castro–Tirado et al., 1999, Vreeswijk et al., 1999.
- GRB 990123: Odewahn et al., 1999, (IAUC 7094); Zhu et al, 1999, (IAUC 7095); Zhu et al., 1999, (GCN 204); Lachaume et al., 1999, (IAUC 7096); Ofek et al., 1999, (GCN 210); Maury et al.,1999, (IAUC 7099); Garnavich et al., 1999, (GCN 215); Masetti et al., 1999, (GCN 233); Sagar et al., 1999, (GCN 227); Yadigaroglu et al., 1999, (GCN 242); Veillet, 1999, (GCN 253); Veillet, 1999, (GCN260).
- GRB 990510: Harrison et al., 1999; Israel et al., 1999.
- GRB 991216: Garnavich et al., 2000; Halphern et al., 2000.
- GRB 000301c: Jensen et al., 2001; Bhargavi et al., 2000.
- GRB 000418: Berger et al., 2001.
- GRB 000911: Price et al., 2002; Lazzati et al., 2001; Masetti et al., 2005.
- GRB 000926: Fynbo et al., 2001.
- GRB 010222: Galama et al., 2003.

- GRB 010921: Price et al., 2002, ApJ, 571,L121.
- GRB 011121: Greiner et al., 2003b; Garnavich et al., 2003.
- GRB 011211: Jakobsson et al., 2003.
- GRB 020124: Hjorth et al., 2003; Berger et al., 2002.
- GRB 020405: Price et al., 2002, (GCN 1326); Price et al. 2002 (GCN 1333); Gal–Yam et al., 2002, (GCN 1335); Hjorth, 2002, (GCN 1336).
- GRB 020813: Laursen & Stanek, 2003; Urata et al., 2003; Li et al., 2003.
- GRB 021004: Bersier et al., 2003; Pandey et al., 2003; Holland et al., 2003.
- GRB 021211: Holland et al., 2004; Pandey et al., 2003b; Li et al., 2003, b; Fox et al., 2003.
- GRB 030323: Vreeswijk, et al., 2004.
- GRB 030226: KLose S. et al., 2004; Pandey et al., 2004.
- GRB 030329: Lipkin et al., 2004; Torii et al., 2003; Torii, 2003, (GCN 1986); Rykoff, 2003, (GCN 1995); Gal–Yam, 2003, (GCN 1999), Klose et al., 2003, (GCN 2000); Burenin et al., 2003a, (GCN 2001); Lipunov et al., 2003, (GCN 2002); Martini et al., 2003, (GCN 2012); Masi et al., 2003, (GCN 2016); Halpern et al., 2003, (GCN 2021); Zharikov et al., 2003, (GCN 2022); Burenin et al., 2003b, (GCN 2024); Rumyantsev et al, 2003a, (GCN 2028); Klose et al., 2003b, (GCN 2029); Bartolini et al., 2003, (GCN 2030); Lipkin et al., 2003, (GCN 2034); Stanek et al., 2003b, (GCN 2041); Lipkin et al., 2003b, (GCN 2045); Burenin et al., 2003c, (GCN 2046); Zeh et al., 2003, (GCN 2048); Lipkin et al., 2003, (GCN 2049); Burenin et al., 2003d, (GCN 2051); Burenin et al., 2003e, (GCN 2054); Fitzgerald et al., 2003a, (GCN 2056); Price, 2003, (GCN 2058); Lipkin et al., 2003c, (GCN 2060); Li et al., 2003, (GCN 2063); Pavlenko et al., 2003a, (GCN 2067); Fitzgerald et al., 2003b, (GCN 2070); Price & Mattei, 2003 (GCN 2071); Cantiello et al., 2003, (GCN 2074); Zharikov et al., 2003b, (GCN 2075); Ibrahimov et al., 2003a, (GCN 2077); Burenin et al., 2003f, (GCN 2079); Sato et al., 2003, (GCN 2080); Pavlenko et al., 2003b, (GCN 2083); Ibrahimov et al., 2003b, (GCN 2084); Khamitov et al., 2003a, (GCN 2094); Lee et al., 2003, (GCN 2096); Pavlenko et al., 2003c, (GCN 2097); Ibrahimov et al., 2003c, (GCN 2098); Urata et al., 2003, (GCN 2106); Khamitov et al., 2003b, (GCN 2108); Lyuty et al., 2003, (GCN 2113); Suzuki et al., 2003, (GCN 2116); Khamitov et al., 2003c, (GCN 2119); Rumyantsev et al., 2003b, (GCN 2146); Ibrahimov et al., 2003c, (GCN 2160); Zharikov et al., 2003c, (GCN 2171);

Semkov, 2003, (GCN 2179); Ibrahimov et al., 2003d, (GCN 2191); Kindt, et al., (GCN 2193); Khamitov et al., 2003d, (GCN 2198); Ibrahimov et al., 2003e, (GCN 2219); Pizzichini at al., 2003, (GCN 2228); Stanek et al., 2003c (GCN 2244); Stanek et al., 2003d, (GCN 2259); Burenin et al., 2003g, (GCN 2260); Zharikov et al., 2003d, (GCN 2265); Ibrahimov et al., 2003f, (GCN 2288); Khamitov et al., 2003e, (GCN 2299).

- GRB 030429; Jakobsson et al., 2004b.

10.2 References for the upper limits of the dark burst plotted in fig. 4.1

GRB970111: Castro-Tirado et al. (1997);
GRB970228: Odewahn et al. (1997);
GRB981220: Pedersen et al. (1999);
GRB990217: Palazzi et al. (1999a);
GRB990506: Vrba et al.(1999);
GRB990527: Pedersen et al. (1999b);
GRB990627: Rol et al. (1999);
GRB990704: Rol et al. (1999b);
GRB990806: Greiner et al. (1999);
GRB990907: Palazzi et al. (1999b);
GRB991014: Uglesich et al. (1999);
GRB991105: Palazzi et al. (1999c);
GRB991106: Jensen et al. (1999);
GRB000115: Gorosabel et al. (2000a);
GRB000126: Kjernsmo et al. (2000);
GRB000210: Gorosabel et al. (2000b);
GRB000307: Kemp et al. (2000);
GRB000323: Henden et al. (2000a);
GRB000326: Pedersen et al. (2000);
GRB000408: Henden et al. (2000b);
GRB000416: Price et al. (2000a);
GRB000424: Uglesich et al. (2000);
GRB000508B: Jensen et al. (2000a);
GRB000519: Jensen et al. (2000b);
GRB000528: Palazzi et al. (2000a);
GRB000529: Palazzi et al. (2000b);
GRB000607: Masetti et al. (2000a);
GRB000615: Stanek et al. (2000);
GRB000616: Bartolini et al. (2000);
GRB000620: Gorosabel et al. (2000c);
GRB000623: Gorosabel et al. (2000d);
GRB000801: Palazzi et al. (2000c);
GRB000812: Masetti et al. (2000b);
GRB000830: Jensen et al. (2000c);
GRB001018: Bloom et al. (2000);
GRB001019: Henden et al. (2000c);
GRB001025: Fynbo et al. (2000);
GRB001105: Castro Ceron et al. (2000);

GRB001109: Greiner et al. (2000);
GRB001120: Price et al. (2000b);
GRB001204: Price et al. (2000c);
GRB001212: Zhu (2000);
GRB010103: Dillon et al. (2001);
GRB010119: Price et al. (2001d);
GRB010126: Masetti et al (2001);
GRB010213: Zhu (2001);
GRB010220: Berger et al. (2001b);
GRB010324: Oksanen et al (2001);
GRB010326A: Price et al. (2001e);
GRB010326B: Pandey et al. (2001);
GRB010412: Price et al. (2001f);
GRB010629: Halpern et al. (2001);
GRB011019: Komiyama et al. (2001);
GRB011030: Rhoads et al. (2001);
GRB011212: Saracco et al. (2001);
GRB020127: Castro Cerón et al. (2002a);
GRB020409: Price et al. (2002b);
GRB020418: Gorosabel et al. (2002a);
GRB020531: Dullighan et al., (2002);
GRB020603: Castro Cerón et al. (2002b);
GRB020604: Gorosabel et al. (2002b);
GRB020625: Price et al. (2002c);
GRB020812: Ohashi et al. (2002);
GRB020819: Levan et al. (2002);
GRB021008: Castro-Tirado et al. (2002);
GRB021016: Durig et al. (2002);
GRB021112: Schaefer et al. (2002);
GRB021113: Kawabata et al. (2002);
GRB021201: Garnavich et al. (2002);
GRB021204: Ishiguro et al. (2002);
GRB021206: Pedersen et al. (2003);
GRB021219: Castro-Tirado et al. (2002b);
GRB030204: Nysewander et al. (2003);
GRB030320: Gal-Yam et al. (2003b);
GRB030413: Schaefer et al. (2003);
GRB030414: Lipunov et al. (2003);
GRB030416: Henden et al. (2003);
GRB030501: Klotz et al. (2003);
GRB030823: Fox et al. (2003b);

GRB030824: Fox et al. (2003c);
GRB030913: Henden et al (2003b);
GRB031026: Chen et al. (2003);
GRB031111: Silvey et a. (2003);
GRB040223: Gomboc et al. (2004);
GRB040228: Sarugaku et al. (2004);
GRB040403: de Ugarte et al. (2004);
GRB040624: Fugazza et al., (2004);
GRB040701: de Ugarte et al. (2004b);
GRB040810: Price et al. (2004);
GRB040812: Cobb et al. (2004);
GRB040825A: Jensen et al. (2004);
GRB040825B: Gorosabel et al. (2004);
GRB041015: Isogai et al. (2004);
GRB041016: Kuroda et al. (2004);
GRB041211: Monfardini et al. (2004);

10.3 Phometric data references for the *Swift* GRBs plotted in figs. 3.11, 5.1, 5.2, 5.3, 5.4, 5.5, 5.6

- GRB 050318: Still et al. (2005);
- GRB 050319: Woźniak et al. (2005), Mason et al. (2006), Quimby et al. (2006), Huang et al. (2007), Kamble et al. (2007);
- GRB 050401: Rykoff et al. (2005), De Pasquale et al. (2005), Watson et al. (2006), Kamble et al. (2008);
- GRB 050408: Foley et al. (2006), de Ugarte Postigo et al. (2007);
- GRB 050416a: Holland et al. (2007), Soderberg et al. (2007);
- GRB 050525a: Torii & BenDaniel (2005); Malesani et al. (2005), Chiang et al. (2005), Mirabal, Bonfield & Schawinski (2005), Homewood et al. (2005), Haislip et al. (2005), Green et al. (2005), Klotz et al. (2005a), Blustin et al. (2006);
- GRB 050730: Sota et al. (2005), Holman, Garnavich & Stanek (2005), Burenin et al. (2005), Klotz et al (2005b), D'Elia et al. (2005a), Bhatt & Sahu (2005), Kannappan et al. (2005), Pandey et al. (2006);
- GRB 050801: Monard (2005), Fynbo et al. (2005b), Rykoff et al. (2006);
- GRB 050802: Pavlenko et al. (2005), Fynbo et al. (2005c), Oates et al. (2007);
- GRB 050820a: Cenko et al. (2006a);
- GRB 050824: Sollerman et al. (2007);
- GRB 050922c: Norris et al. (2005), Jakobsson et al. (2005), Andreev & Pozanenko (2005), Durig & Price (2005), Henych et al. (2005), Novak (2005), Piranomonte et al. (2005), D'Elia et al. (2005b), Covino et al. (2005), Li et al. (2005);
- GRB 051111: Butler et al. (2006), Yost et al. (2007);
- GRB 060124: Romano et al. (2006a), Misra et al. (2007);
- GRB 060206: Woźniak et al. (2006), Stanek et al. (2007), Curran et al. (2007b);

- GRB 060210: Stanek et al. (2007), Curran et al. (2007), Cenko et al. (2009);

- GRB 060418: Melandri et al. (2006a), Cobb (2006a), Jelínek Kubánek & Prouza(2006), Koppelman (2006), Chen et al. (2006), Hafizov et al. (2006), Karimov (2006), Molinari et al. (2007);

- GRB 060512: Mundell & Steele (2006), Cenko (2006a), Milne (2006), De Pasquale & Cummings (2006), Cenko & Baumgartner (2006), Sharapov Djupvik & Pozanenko (2006);

- GRB 060526: Campana et al. (2006b), French & Jelinek (2006), Covino et al. (2006), Lin et al. (2006), Brown et al. (2006), Khamitov et al. (2006a), Morgan & Dai (2006), Khamitov et al. (2006b), Rumyantsev & Pozanenko (2006), Kann & Hoegner (2006), Khamitov et al. (2006c), Baliyan et al. (2006), Khamitov et al. (2006d), Khamitov et al. (2006e), Terra et al. (2006), Khamitov et al. (2006f), Rumyantsev et al. (2006), Dai et al. (2007), Thöne et al. (2008);

- GRB 060614: French et al. (2006), Schmidt Peterson & Lewis (2006), Cobb et al. (2006), Fynbo et al. (2006), Della Valle et al., (2006), Gal-Yam et al. (2006), Mangano et al. (2007);

- GRB 060729: Grupe et al. (2007);

- GRB 060904b: Skvarc (2006), Oates & Grupe (2006), Mescheryakov et al. (2006), Cobb & Bailyn (2006), Greco et al. (2006), Soyano Mito & Urata (2006), Huang et al. (2006), Asfandyarov Ibrahimov & Pozanenko (2006), Klotz et al. (2008);

- GRB 060908: Nysewander et al. (2006), Antonelli et al. (2006), Morgan et al. (2006), Cenko et al. (2009);

- GRB 060927: Guidorzi et al. (2006), Torii (2006a), Ruiz-Velasco et al. (2007);

- GRB 061007: Mundell et al. (2007);

- GRB 061121: Page et al. (2006), Melandri et al. (2006b), Uemura Arai & Uehara (2006), Marshall Holland & Page (2006), Halpern Mirabal & Armstrong (2006a), Cenko (2006b), Torii (2006b), Halpern Mirabal & Armstrong (2006b), Efimov Rumyantsev & Pozanenko (2006a), Halpern& Armstrong (2006a), Halpern& Armstrong (2006b), Efimov Rumyantsev & Pozanenko (2006b), Cobb (2006b);

- GRB 061126: Perley et al. (2008a), Gomboc et al. (2008);

- GRB 070110: Malesani et al. (2007), Troja et al. (2007);

- GRB 070125: Cenko & Fox (2007), Xing et al. (2007), Uemura Arai & Uehara (2007), Greco et al. (2007), Yoshida Yanagisawa & Kawai (2007), Terra et al. (2007), Mirabal Halpern & Thorstensen (2007), Updike et al. (2008), Chandra et al. (2008);

- GRB 071003: Perley et al. (2008b), Cenko et al. (2009);

- GRB 071003: Covino et al. (2008a); Cenko et al. (2008);

- GRB 080310: Milne & Williams (2008a), Covino et al. (2008b), Chen et al. (2008), Garnavich Prieto & Pogge (2008a), Yoshida et al. (2008), Kinugasa (2008), Garnavich Prieto & Pogge (2008b), Urata et al. (2008a), Wegner et al. (2008), Hill et al. (2008), Cenko et al. (2008);

- GRB 080319b: Li et al. (2008a), Milne & Williams (2008b), Urata et al. (2008b), Li et al. (2008b), Cwiok et al. (2008), Covino et al. (2008c), Wozniak et al. (2008), Swan Yuan & Rujopakarn (2008), Jelínek et al. (2008), Novak (2008), Krugly Slyusarev & Pozanenko (2008), Perley & Bloom (2008), Tanvir et al. (2008), Bloom et al. (2008).

10.4 Nardini et al. INAF-TNG proposal (Period AOT20 (Aug09–Jan10))

As already discussed, the big effort has been made in order to obtain a fast optical follow up in the first hours after the trigger in order to study the complex early time afterglow evolution. On the other hand the high GRB detection rate (one every few days or more) and the large amount of observing time spent for the early afterglow observations, made the late times (1-3 days after the trigger) follow up strategy less intense. This lack of long lasting optical follow ups prompted us in participating in two calls for proposals for observing time at the ESO-VLT and INAF TNG telescopes with the aim of testing the presence/absence of jet break steepening in the optical GRB light curves.

In this section I will report part of the Nardini et al. INAF-TNG proposal (Period AOT20 (Aug09–Jan10)) that has been recently approved.

10.4.1 Scientific aim

We propose to observe the optical light curve, starting about 3 days after the burst prompt detection, of 3 bright GRBs. These bursts will be selected to belong to class (A) or (B):

A) bursts whose optical emission after ∼1 day is standard afterglow (forward shock) while the X–ray (at the same epochs) is dominated by the Component II emission.

B) bursts dominated by the Component II emission in both the X–ray and Optical bands.

according to their early time multi-band emission.

These two examples can represent a fundamental test for our model: the detection of a jet break in case (A) and the non detection of a jet break in (B) would prove the correctness of the model. Indeed, $t_{\rm jet}$ is a feature of the standard afterglow emission and, then, it should be observed only when the light curve is dominated by the afterglow component.

We expect to detect the jet break in burst of class (A) while no break is expected in class (B). Our primary aims are to measure the jet breaks and to test how two different emission components, i.e. the classical afterglow and the Component II, "compete" in the GRB X–ray and Optical light curves.

Our aim is to distribute at least three deep observations across the time interval when the jet break is most likely to happen, i.e. between 3 and 20 days. The last observation is particularly important to detect the host galaxy in order to subtract its contribution and better constrain tjet (e.g. Ghirlanda et al. (2007)). The bursts will be selected on the basis of

i) their early time optical light curve (reconstructed by collecting the data distributed through the GCN within 1 day),

ii) their early time X–ray light curve (through the analysis of the Swift/XRT data, publicly available soon after the GRB detection).

For the selection we will follow a general rule. Bursts belonging to the class (A) have a typical early decay with a non prominent shallow phase: the temporal decay index of the optical light curve, $t^{-\alpha}$, is typically $\alpha \geq 1.0$. Bursts belonging to class (B) show an early time shallow decay phase also in the optical band. The shallow decay is the signature of the Component II emission and in these cases there are good chances that it still dominates the optical emission at later epochs, if the afterglow component is fainter. Class (B) GRBs will be selected for having $\alpha \leq 0.7$. This selection, however, is only a guideline. Our goal is to search for jet breaks in the late time optical emission.

10.4.2 Observational strategy and justification of requested time

Fig. 6.1 shows that in the *Swift* era the rate of jet break measurements is much lower than in the pre–*Swift* era and that the few detections of breaks in *Swift* GRBs

are mostly early time breaks. Jet breaks of *Swift* bursts are expected at later times as a consequence of the larger average redshift sampled by *Swift* . The prevailing interest in observing the early afterglow phase up to 1 day, at the expense of sampling the late time optical light curve (up to 10-20 days) when the jet break should happen, in part accounts for the lack of jet break measurements. However, despite the network of robotic telescopes dedicated to the optical follow up of the GRB counterparts, observations at $t > 2-3$ days are sometimes missing in a large fraction of *Swift* era events.

We expect that out of ∼60 GRBs/yr optically bright detected by Swift, ∼8 will be observable with TNG in a 6 months time scale. We expect that for about 3 we will have enough early time information and will be bright enough to activate the ToO. We need 3 sets of observations for each of the 3 GRBs.

A) The first set consists in a V and R band observation around 3 days after the trigger. At that time the observed magnitudes in these bands have typical values between 20 and 22 as shown in Fig. 1 in Kann et al. 2009. (1.5 h for each burst for a total time requirement of 4.5 h evaluated using the on line exposure time calculator for DOLORES by assuming the fainter of the two magnitude values).

B) The second set consists in a V and R band observation around 8 days after the trigger. At that time the observed magnitudes in these bands have typical values between 22 and 24. (2.5 h for each burst for a total time requirement of 7.5 h).

C) The third observation is planned around 20 days after the trigger and consists in a single deep R band observation in the direction of the afterglow in order to constrain the late time temporal decay index when the R band light curves magnitudes have typical values between 22 and 25 and possibly detect the GRB host galaxy. (3 h for each burst for a total time requirement of 9 h).

The scientific goal allows a certain flexibility on the exact observation dates. This can make this proposal less impacting on the TNG observations schedule. Therefore, set A can be carried out between 2 and 4 days after the trigger, set B can be carried out between 6 and 10 days after the trigger, and set C can be carried out between 20 and 40 days after the trigger.

Our observation strategy will provide five photometric points distributed between ∼3–20 days (i.e. the typical interval where jet breaks are expected in Swift bursts as shown by the shaded yellow region of Fig. 6.1).

We ask for observations in the V and R filters which are the most sampled in the early phases and test the light curve achromaticity. With this strategy we will be able to combine our late time photometric points with early time observations

distributed through the GCN. We will complement our analysis of the optical late time light curve with the public available XRT X–ray data.

At later times the optical light curve could be contaminated by an underlying supernova emission but we expect that the SN contribution will enter starting at ~ 40 days ($< z > \approx 2$). We can cope with it also thanks to the flexibility of the late time observation.

List of Figures

List of Tables

Bibliography

[-] Abdo A.A., et al., 2009, Science, 323, 1688

[-] Akerlof, C. W. et al. 2003, PASP, 115, 132

[-] Amati et al., 2000, Science, 290, 953

[-] Amati L., Frontera F., Tavani M. et al. 2002, A&A, 390, 81

[-] Andersen E. et al. 2000, A&A, 364, L54

[-] Andreev M. & Pozanenko A., 2005, GCN, 4016

[-] Antonelli L. A. et al., 2000, ApJ, 535, 39

[-] Antonelli L. A. et al., 2000b, ApJ, 545, L39

[-] Antonelli L.A., Covino S., Testi V., 2006, GCN, 5546

[-] Asfandyarov I., Ibrahimov M. & Pozanenko A., 2006, GCN, 5741

[-] Ashman K. M., Bird C. M., & Zepf S. E., 1994, AJ, 108, 2348

[-] Atwood W.B., et al., 2009, ApJ., 697, 1071

[-] Band D., Matteson J., Ford L., et al., 1993, ApJ, 413, 281

[-] Barthelmy, S. D. et al., 2005, ApJ 635, L133

[-] Bartolini, C., Gualandi, R., Guarnieri, A., Piccioni, A., Palazzi, N., Pian, E. & Masetti, N., 2000, GCN, 714

[-] Bartolini, G., Guarnieri, A., Piccioni, A., Gavazzi, G., Gualandi, R., Pizzichini, G., Ferrero, P., 2003, GCN 2030

[-] Beloborodov, A.M., Stern, B.E., Svensson, R., et al., 2000, ApJ, 535, 158

[-] Berger E., Diercks A., Frail D.A., et al., 2001, ApJ, 556, 556

[-] Berger, E., Frail, D.A., Price, P.A., Bloom, J.S., Galama, T.J., Kudritzki, R. & Bresolin, F., 2001b, GCN, 958

[-] Berger E., Kulkarni S.R., Bloom J.S., et al., 2002, ApJ, 581, 981

[-] Berger, E., Kulkarni, S. R., & Frail, D. A. 2003, ApJ, 590, 379

[-] Bersier, Stanek, K.Z., Winn, L.N., et al., 2003, ApJ, 584, L43

[-] Bhatt B.C. & Sahu D.K., 2005, GCN, 3775

[-] Björnsson, E.H., Gudmundsson, G & Johannesson, G., 2004, ApJ, 615, 77

[-] Bhargavi S.G., & Cowslk 2000, ApJ, 545, L77

[-] Blandford R.D., & Znajek R.L., MNRAS, 1977, 179, 433

[-] Bloom, J.S., Frail, D.A., Kulkarni, S.R., et al., 1998, ApJ, 508, 21

[-] Bloom, J.S., Diercks, A., Kulkarni, S.R., Harrison, F.A., Behr, B.B. & Clemens, J.C., 2000, GCN, 915

[-] Bloom J.S., Djorgovski S.G., & Kulkarni S.R., 2001, ApJ, 554, 678

[-] Bloom J.S., Frail D.A., & Kulkarni S.R. 2003, ApJ, 594, 674

[-] Blustin A.J., Band D., Barthelmy S., et al., 2006, ApJ, 637, 901

[-] Bloom J.S., Perley D. & Li W., 2008, ApJ submitted (arXiv:0803.3215v2)

[-] Boella, G., Butler, R.C., Perola, G.C., Piro, L., Scarsi, L. & Bleeker, J.A.M., 1997, A&A, 122, 299

[-] Boër, M., & Gendre, B. 2000, A&A, 361, L21

[-] Brown P.J., Campana S., Boyd P.T. & Marshall F.E., 2006, GCN, 5172

[-] Burenin, R., Denissenko, D., Pavlinsky, M., et al., 2003a, GCN 2001

[-] Burenin, R., Sunyaev, R., Pavlinsky, M., et al., 2003b, GCN 2028

[-] Burenin, R., Sunyaev, R., Pavlinsky, M., et al., 2003c, GCN 2046

[-] Burenin, R., Sunyaev, R., Pavlinsky, M., et al., 2003d, GCN 2051

[-] Burenin, R., Sunyaev, R., Pavlinsky, M., et al., 2003e, GCN 2079

[-] Burenin, R., Sunyaev, R., Denissenko, D., et al., 2003f, GCN 2054

[-] Burenin, R., Sunyaev, R., Denissenko, D., et al., 2003g, GCN 2260

[-] Burenin R., Tkachenko A., Pavlinsky M., et al., 2005, GCN, 3718

[-] Burlon D. et al., 2008, ApJ, 685, L19

[-] Burrows,D. N. et al., 2005, Science, 309, 1833

[-] Borgonovo L., et al., 2007, A&A, 465, 765

[-] Butler N.R., Li W., Perley, D., et al., 2006, ApJ, 652, 1390

[-] Butler N.R. & Kocevsky D., 2007, ApJ, 663, 407

[-] Campana, S., et al. 2006, Nature, 442, 1008

[-] Campana S., Barthelmy S.D., Burrows D.N., et al., 2006b, GCN, 5163

[-] Cantiello, M., Dolci, M., Maiorano, E., Masetti, N., Palazzi, E. & Broccato, E., 2003, GCN 2074

[-] Cash W., 1979, ApJ, 228, 939

[-] Castro Ceron, J.M., Castro-Tirado, A.J., A. Henden, A., et al., 2000, GCN, 894

[] Castro Cerón, J.M., Gorosabel, J., Amado, P., 2002a, GCN, 1775

[] Castro Cerón, J.M., Pedani, M., Gorosabel, J. & Castro-Tirado, A.J., 2002b, GCN, 1413

[-] Castro-Tirado, A.J. & Gorosabel, J., 1997, IAUC, 6598

[-] Castro–Tirado, A.J., Zapatero–Osorio, M.R., Gorosabel, J., et al., 1999, ApJ, 511, L85

[-] Castro-Tirado, A.J., Klose, S., Wisotzki, L., Greiner, L., Castro Ceron, J.M. & Gorosabel, J., 2002, GCN, 1642

[-] Cenko S.B., Kasliwal M., Harrison F. A., et al., 2006a, ApJ, 652, 490

[-] Cenko S.B., 2006b, GCN, 5844

[-] Cenko S.B., Baumgartner W.H., 2006, GCN, 5156

[-] Cenko S.B. & Fox D.B., 2007, GCN, 6028

[-] Cenko S. B. et al., 2009, ApJ, 693, 1484

[-] Chandra P., Cenko S.B., Frail D.A., 2008, ApJ., 683, 924

[-] Chen, A.C., Ting,H.C., Lin, H.C., Huang, K.Y., Kinoshita, D., Ip, W.H., Urata, Y. & Tamagawa, T., 2003, GCN, 2436

[-] Chen B.A., Lin C.S., Huang K.Y., Ip W.H. & Urata Y., 2006, GCN, 4982

[-] Chen B.A., Huang L.C., Huang K.Y. & Urata Y., 2008, GCN, 7395

[-] Chevalier R. A., 1989, ApJ, 346, 847

[-] Chevalier & Li, ApJ, 2000, 536,195

[-] Chiang P.S., Huang K.Y., Ip W.H., Urata Y., Qiu Y., & Lou Y.Q. 2005, GCN, 3486

[-] Chincarini G. et al., 2007, ApJ, 671, 1903

[-] Chornock R., Foley R.J., Filippenko A.V., Papenkova M.,Weisz D., & Garnavich P., 2003, IAU Circ, 8114

[-] Cobb, B.E. & Bailyn, C.D., 2004, GCN, 2642

[-] Cobb B.E., 2006a, GCN, 4972

[-] Cobb B.E., 2006b, GCN, 5878

[-] Cobb B.E. & Bailyn, C.D., 2006, GCN, 5525

[-] Cobb B. E., Bailyn C. D., van Dokkum P. G., & Natarajan P., 2006, ApJ., 651, L85

[-] Costa, E., Frontera, F., Heise, J., et al., 1997, Nature, 387, 783

[-] Covino S., Piranomonte, S., Fugazza D., Fiore F., Maleani G., Tagliaferri G., Chincarini G. & Stella L., 2005, GCN, 4046

[-] Covino S., Israel G.L., Ghinassi F. & Pinilla N., 2006, GCN, 5167

[-] Covino S., D'Avanzo P., Klotz A., et al., 2008a, MNRAS, 388, 347

[-] Covino S., Tagliaferri G., Fugazza D. & Chincarini G., 2008b, GCN, 7393

[-] Covino S., D'Avanzo P., Fugazza D. et al., 2008, GCN, 7446

[-] Cusumano G. et al., 2006, ApJ, 639, 316

[-] Curran P. A. et al., 2007, A&A, 467, 1049

[-] Curran P. A., van der Horst A. J., Wijers R.A.M.J., et al., 2007b, MNRAS, 381, L65

[-] Cwiok M., Dominik W., Kasprowicz G., et al., 2008, GCN, 7445

[-] D'Elia V., Melandri A., Fiore F., et al., 2005a, GCN, 3746

[-] D'Elia V., Piranomonte S., Fiore F., et al., 2005b, GCN, 4044

[-] Dai X., Halpern J.P., Morgan N.D., Armstrong E., Mirabal N., Haislip J.B., Reichart D. E. & Stanek K. Z., 2007, ApJ, 658, 509

[-] Dainotti M. G., Cardone V. F., Capozziello S., 2008, MNRAS, 391, L79

[-] Dado S., Dar A., & De Rújula A., 2005, ApJ, 646, L21

[-] Dar A., & De Rújula A., 2000, preprint (astro-ph/0008474)

[-] Dar A., & De Rújula A., 2004, Phys. Rep., 405, 203

[-] De Pasquale, M., Piro, L., Perna, R., et al. 2003, ApJ, 592, 1018

[-] De Pasquale M., Beardmore A.P., Barthelmy S.D., et al., 2006b, MNRAS, 365, 1031

[-] De Pasquale M., et al., 2006, A&A, 455, 813

[-] De Pasquale M. & Cummings J., 2006, GCN, 5130

[-] de Ugarte Postigo, A., Sota, A., Gorosabel, J. & Castro-Tirado, A.J., 2004, GCN, 2571

[-] de Ugarte Postigo, A., Tristram, P., Sasaki, Gorosabel, J., Yock, P. & Castro-Tirado, A.J., 2004, GCN, 2621

[-] de Ugarte Postigo A., Fatkhullin T.A., Jóhannesson G. et al., 2007, A&A, 462, L57

[-] Della Valle, M., et al. 2006, Nature, 444, 1050

[-] Dermer, C. D., & Mitman K. E., 1999, ApJ, 513, L5.

[-] Dezalay, J. P., J. P. Lestrade, C. Barat, R. Talon, R. Sunyaev, O. Terekhov, & A. Kuznetsov, 1996, ApJ., 471, L27

[-] Dickey J.M., & Lockman F.J., 1990, ARA&A, 28, 215

[-] Diercks, A., Deutsch, E.W., Castander, F.J., et al., 1998, ApJ, 503, L105

[-] Dillon, B. & Dellinger, J., 2001, GCN, 911

[-] Durig D.T. & Price T., 2005, GCN, 4023

[-] Dullighan, A., Monnelly, G., Butler, N., Vanderspek, R., Ford, P. & Ricker, G., 2002, GCN, 1411

[-] Durig, D.T., Shroyer, E.W., Shukla, P.P. & West, D., 2002, GCN, 1644

[-] Eichler D., & Granot J., 2006, ApJ, 641, L5

[-] Efimov Y., Rumyantsev V. & Pozanenko A., 2006a, GCN, 5850

[-] Efimov Y., Rumyantsev V. & Pozanenko A., 2006b, GCN, 5870

[-] Evans P.A., Beardmore A.P., Page K.L., et al., 2009, MNRAS submitted (arXiv:0812.3662v1)

[-] Falcone, A. D. et al., 2006, ApJ, 641, 1010

[-] Fenimore, E. E., J. J. M. in 't Zand, J. P. Norris, J. T. Bonnell, & R. J. Nemiroff, 1995, ApJ, 448, L101

[-] Fenimore, E. E., Madras, C. D. & Nayakshin, S., 1996, ApJ 473, 998

[-] Fernandez-Soto A., et al., 2009, GCN, 9222

[-] Firmani C., Avila-Reese V., Ghisellini G., Tutukov A., 2004, ApJ, 611, 1033

[-] Fishman G.J., et al. 1994, ApJS, 92, 229

[-] Fitzgerald, J.B. & Orosz, J.A., 2003a, GCN 2056

[-] Fitzgerald, J.B. & Orosz, J.A., 2003b, GCN 2070

[-] Foley R.J., Perley D.A., Pooley D., et al., 2006, ApJ, 645, 450

[-] Ford L. A., D. L. Band, J. L. Matteson, M. S. Briggs, G. N. Pendleton, R. D. Preece, W. S. Paciesas, B. J. Teegarden, D. M. Palmer, B. E. Schaefer, T. L. Cline, G. J. Fishman, et al., 1995, ApJ., 439, 307

[-] Fox D.W., Price P.A., Soderberg A.M., et al., 2003, ApJ, 586, L5

[-] Fox, D.B., & Hunt, M.P., 2003b, GCN, 2365

[-] Fox, D.B., & Hunt, M.P., 2003c, GCN, 2369

[-] Frail D.A., et al. 2001, ApJ, 562, L55

[-] Frail, D.A., Kulkarni, S.R., Nicastro, S.R., Feroci, M. & Taylor, G.B., 1997, Nature, 389, 261

[-] French J. & Jelinek M., 2006, GCN, 5165

[-] French J., Melady G., Hanlon L. & Jelinek M., 2006, GCN, 5257

[-] Fugazza, D., D'Avanzo, P., Tagliaferri, G., et al., 2004, GCN, 2617

[-] Fynbo, J.P.U., Moller, P., Milvang-Jensen, B., et al., 2000, GCN, 867

[-] Fynbo J.P.U., Gorosabel J., Dall T.H., et al., 2001, A&A, 373, 796

[-] Fynbo J.P.U., et al., 2003, A&A, 406, L63

[-] Fynbo J.P.U., Hjorth, J., Jensen, B.L., Jakobsson P.,Moller P. & Näränen J., 2005a, GCN, 3136

[] Fynbo J.P.U., Jensen B.L., Hjorth J., Woller K.G., Watson D., Fouque P. & Andersen M.I., 2005b, GCN, 3736

[-] Fynbo J.P.U., Jensen, B.L., Hjorth, J. et al., 2005c, GCN, 3756

[-] Fynbo J.P.U., Watson, D., Thöne C., et al., 2006, Nature, 444, 1047

[-] Fynbo J.P.U., et al., 2008, GCN, 8225

[-] Fynbo, J. P. U., Jakobsson, P., Prochaska, J.X., Malesani, D., Ledoux, C., de Ugarte Postigo A., **Nardini, M.**, et al., 2009, ApJS submitted (pre-print arXiv:0907.3449v1)

[-] Gal–Yam A., Ofek E.O. & Lipkin Y., 2002, GCN, 1335

[-] Gal–Yam, A., Ofek, E.O. & Lipkin, Y., 2003, GCN, 1999

[] Gal-Yam, A. & Ofek, E.O., 2003b, GCN, 1946

[-] Gal-Yam, A., et al. 2006, Nature, 444, 1053

[-] Galama T. J., et al., 1998, Nature, 395, 670

[-] Galama T. J., & Wijers R. A. M. J., 2001, ApJ, 549, L209

[-] Galama T.J., Reichart D., Brown T.M., et al., 2003, ApJ, 587, 135

[-] Galli A., & Piro L., 2007, A&A, 475, 421

[-] Garcia,M.R., Callanan, P.J., Moraru, D., 1998, ApJ, 500, 105

[-] Garnavich, P.M., Jha, Stanek, K.Z. & Garcia, M., 1999, GCN 215

[-] Garnavich, P.M., Jha, S., Pahre, M.A., Stanek, K.Z., Kirshner, P.R., Garcia, M.R., Szentgyorgyi, A.H. & Tonry, J., 2000, ApJ, 543, 61

[-] Garnavich, P. & Quinn, J., 2002, GCN 1746

[-] Garnavich P.M., Matheson T., Olszewski E.W., Harding P., & Stanek K.Z., 2003a, IAU Circ., 8114, 1

[-] Garnavich P.M., Stanek K.Z., Wyrzykowski L., Infante L., Bendek E., et al. 2003b, ApJ, 582, 924

[-] Garnavich P., Prieto J.L. & Pogge R., 2008a, GCN, 7409

[-] Garnavich P., Prieto J.L. & Pogge R., 2008b, GCN, 7414

[-] Gehrels N. et al., 2004, ApJ, 601, 1005

[-] Gehrels N. et al., 2006, Nature, 444, 1044

[-] Gendre, B., & Boër, M. 2005, A&A, 430, 465

[-] Gendre, B., Galli, A., & Boër, M. 2008, ApJ, 683, 620

[-] Gendre B., Pelisson S., Boër M., Basa S., & Mazure A., 2008b, A&A, 492, L1

[-] Genet F., Daigne F., & Mochkovitch R., 2007, MNRAS, 381, 732

[-] Ghirlanda G., Celotti A., & Ghisellini G., 2002, A&A, 393, 409

[-] Ghirlanda G., Ghisellini G., & Lazzati D., 2004, ApJ, 616, 331

[-] Ghirlanda G., et al., 2004, ApJ, 613, 13

[-] Ghirlanda G., Nava L., Ghisellini G., & Firmani C., 2007, A&A, 466, 127

[-] Ghisellini G., Ghirlanda G., & Tavecchio F., 2007, MNRAS, 382, L77

[-] Ghisellini G., et al., 2007, ApJ, 658, 75

[-] Ghisellini G., **Nardini M.**, Ghirlanda G., & Celotti A., 2009a, MNRAS, 393, 253

[-] Ghisellini G., **Nardini M.**, & Ghirlanda G., arXiv:0908.0732v1

[-] Gomboc, A., Marchant, J.M., Smith, R.J., Mottram, C.J. & Fraser, S.N., 2004, GCN, 2534

[-] Gomboc et al., 2008, ApJ, 687, 443

[-] Gorosabel, J., Henden, A., Castro-Tirado, A.J., et al., 2000c, GCN, 734

[-] Gorosabel, J., Pascual, S., Gallego, J., et al., 2000d, GCN, 735

[-] Gorosabel, J., Hjorth, J., Jakobsson, P., et al., 2002, GCN, 1419

[-] Gorosabel, J., Hjorth, J., Jensen, B.L., Pedersen, H., Jakobsson, P., Fynbo, J. & Andersen, M.I., 2002b, GCN, 1429

[-] Gorosabel, J., Jensen, B.L., Hjorth, J., Fogh Olsen, L., Christensen, L., Andersen, M.I. & Jaunsen, A.O., 2000b, GCN, 547

[-] Gorosabel, J., Pascual, S., Gallego, J., et al., 2000d, GCN, 735

[-] Gorosabel, J., Vrba, F., Henden, A., et al., 2000, GCN, 563

[] Gorosabel, J., Hjorth, J., Jakobsson, P., et al., 2002a, GCN, 1419

[] Gorosabel, J., Hjorth, J., Jensen, B.L., Pedersen, H., Jakobsson, P., Fynbo, J. & Andersen, M.I., 2002b, GCN, 1429

[-] Greiner, J., Pompei, J., Els, S., et al., 1999, GCN, 396

[-] Greiner, J., Stecklum, B., Klose, S., et al., 2000, GCN, 887

[-] Gorosabel, J., de Ugarte Postigo, A., Miranda, L.F., Jelinek, M., Pereira, C.B., Castro Cerón, J.M. & Aceituno, J., 2004, GCN, 2675

[-] Greco G., Terra F., Bartolini C., et al., 2006, GCN, 5526

[-] Greco G., Terra F., Bartolini C., et al., 2007, GCN, 6047

[-] Green D.W.E., Della Valle M., Malesani D., Benetti S., Chincarini G., Stella L., & Tagliaferri G., 2005, IAUC, 8696.1

[-] Greiner J., Peimbert M., Estaban C., Kaufer A., Vreeswijk P., et al., 2003. GCN, 2020

[-] Greiner, J., Guenther E., Klose S. & Schwarz, R., 2003b, GCN, 1886

[-] Greiner J., Clemens C., Krühler T., et al., 2009, A&A., 498, 89

[-] Grupe D. et al., 2007, ApJ, 662, 443

[-] Grupe D. et al., 2009, submitted, (arXiv:09031258)

[-] Guidorzi C., Bersier D., Melandri A., et al., 2006, GCN, 5633

[-] Hafizov B., Sharapov D., Pozanenko A. & Ibrahimov M., 2006, GCN, 4990

[-] Haislip J., MacLeod C., Nysewander M., et al., 2005, GCN, 3568

[-] Hakkila J. & Giblin T.W., 2006, ApJ., 646, 1086

[-] Hakkila J. et al., 1994, ApJ, 422, 659

[-] Hakkila, J., D. J. Haglin, G. N. Pendleton, R. S. Mallozzi, C. A. Meegan, & R. J. Roiger, 2000, ApJ., 538, 165.

[-] Hakkila J., et al. 2007, ApJs, 169, 62

[-] Halpern, J.P., Uglesich, R., Mirabal, N., et al., 2000, ApJ, 543, 697

[-] Halpern, J.P. & Mirabal, N., 2001, GCN, 1079

[-] Halpern, J.P., Mirabal, N., Bureau, M., Fathi, K., 2003, GCN 2021

[-] Harrison, F.A., Bloom, J.S., Frail, D.A., et al., 1999, ApJ, 523, 121

[-] Henden, A., Castro-Tirado, A.J. & Castro Ceron, J.M., 2000a, GCN, 621

[-] Halpern J.P., & Armstrong E., 2006a, GCN, 5851

[-] Halpern J.P., & Armstrong E., 2006b, GCN, 5853

[-] Halpern J.P., Mirabal N. & Armstrong E., 2006a, GCN, 5840

[-] Halpern J.P., Mirabal N. & Armstrong E., 2006a, GCN, 5847

[-] Henden, A., Luginbuhl, C., Canzian, B., 2000b, GCN, 633

[-] Henden, A., Kaiser, D., Hohman, D., Pason, R. & Aquino, B., 2000c, GCN, 858

[-] Henden, A. & Oksanen, A., 2003, GCN, 2392

[-] Henden, A., Silvay, J., Moran, J., Soule, R., Reichart, D., Schaefer, J., Canterna, R. & Scoggins, B., 2003b, GCN, 2250

[-] Henych T., Kocka M., Hroch F., Jelinek M. & Hudec R., 2005, GCN, 4026

[-] Hill J., Ragazzoni R., Baruffolo A. & Garnavich P., 2008, GCN, 7523

[-] Holland S.T., Weidinger M., Fynbo J.P.U., et al., 2003, AJ, 125, 2291

[-] Holland S.T., Bersier D., Bloom J.S., et al., 2004, AJ, 128, 1955

[-] Holland S.T., Boyd P.T., Gorosabel J., et al., 2007, AJ, 133, 122

[-] Holman M., Garnavich P., & Stanek K.Z., 2005, GCN, 3716

[-] Homewood A., Hartmann D.A., Garimella K., Henson G., McLaughlin J., & Brimeyer A., 2005, GCN, 3491

[-] Hjorth J., 2002, GCN 1336

[-] Hjorth, J., Thomsen, B., Nielsen, S.R., et al., 2002, ApJ, 576, 113

[-] Hjorth, J., et al. 2003, ApJ, 597, 699

[-] Hjorth J., Sollerman J., Møller P., Fynbo J.P.U., Woosley S.E., et al. 2003b, Nature, 423, 847

[-] Horváth, I., 1998, Ap. J., 508, 757

[-] Huang K.Y., Ip W.H., Lee Y.S. & Urata Y., 2006, GCN, 5549

[-] Huang K.Y., Urata Y., Kuo P. H. et al., 2007, ApJ, 654, L2

[-] Hurley, K., Sari, R., Djorgovsky, S.G., 2003, Compact Stellar X-Ray Sources, Cambridge University Press, pre-print (arXiv:astro-ph/0211620v2)

[-] Ibrahimov, M.A., Asfandiyarov, I.M., Kahharov, B.B., Pozanenko, A., Rumyantsev, V. & Beskin, G., 2003a, GCN 2077

[-] Ibrahimov, M.A., Asfandiyarov, I.M., Kahharov, B.B., Pozanenko, A., Rumyantsev, V. & Beskin, G., 2003b, GCN 2084

[-] Ibrahimov, M.A., Asfandiyarov, I.M., Kahharov, B.B., Pozanenko, A., Rumyantsev, V. & Beskin, G., 2003, GCN 2098

[-] Ibrahimov, M.A., Asfandiyarov, I.M., Kahharov, B.B., Pozanenko, A., Rumyantsev, V. & Beskin, G., 2003c, GCN 2160

[-] Ibrahimov, M.A., Asfandiyarov, I.M., Kahharov, B.B., Pozanenko, A., Rumyantsev, V. & Beskin, G., 2003d, GCN 2191

[-] Ibrahimov, M.A., Asfandiyarov, I.M., Kahharov, B.B., Pozanenko, A., Rumyantsev, V. & Beskin, G., 2003e, GCN 2219

[-] Ibrahimov, M.A., Asfandiyarov, I.M., Kahharov, B.B., Pozanenko, A., Rumyantsev, V. & Beskin, G., 2003f, GCN 2288

[-] Ioka K., Toma K., Yamazaki R., & Nakamura T., 2006, A&A, 458, 7

[-] Ishiguro, M., Sarugaku,Y., Nonaka, H., Kwon, S.M., Nishiura, S., Mito, H. & Urata, Y., 2002, GCN, 1747

[-] Israel, G.L., Marconi, G., Covino, S., et al., 1999, A&A, 348, L5

[-] Jakobsson P., Hjorth J., Fynbo J.P.U., et al., 2003, A&A, 408, 941

[-] Jakobsson P. et al., 2004, ApJ, 617, L21

[-] Jakobsson, P., Hjorth, J., Fynbo, J.P.U., et al., 2004b, A&A, 427, 785

[-] Jakobsson P., Paraficz D., Telting J., Fynbo J.P.U., Jensen B.L., Hjorth J. & Castro Cerón J.M., 2005, GCN, 4015

[-] Jakobsson P. et al., 2006, A&A, 460, L13

[-] Jakobsson P., Vreeswijk P.M., Hjorth J., Malesani D., Fynbo J.P.U., & Thöne C., 2007, GCN 6952

[-] Jelínek M., Kubánek P. & Prouza M., 2006, GCN, 4976

[-] Jelínek M., Castro-Tirado A.J., Chantry V. & Plá J., 2008, GCN, 7476

[-] Jensen, B.L., Pedersen, H., Hjorth, J., Larsen, S. & Costa, E., 1999, GCN, 440

[-] Jensen, B.L., Pedersen, H., Hjorth, J., et al., 2000a, GCN, 670

[-] Jensen, B.L., Pedersen, H., Hjorth, J., Gorosabel, J., Dall, T.H. & O'Toole, S., 2000b, GCN, 679

[-] Jensen, B.L., Pedersen, H., Hjorth, J., Gorosabel, J., Fynbo, J.P.U. & Nowotny, W., 2000c, GCN, 788

[-] Jensen B.L., Fynbo J.U., Gorosabel J., Hjorth J., et al., 2001 A&A ,370, 909

[-] Jensen, B. L., et al. 2001, A&A, 370, 909

[-] Jensen, B.L., Cassan, A., Dominis, D., et al., 2004, GCN, 2686

[-] Jòhannesson G., Björnsson G., & Gudmundsson E.H., 2008, A&A, 472, L29

[-] Kalberla P.M.W., Burton W.B., Hartmann D., Arnal E.M., Bajaja E., Morras R., & Pöppel W.G.L., 2005, A&A, 440, 775

[-] Kawabata, T., Ayani, K., Yamaoka, H., Kawai, N. & Urata, Y., 2002, GCN, 1700

[-] Kamble A., Resmi L. & Misra K., 2007, ApJ, 664, L5

[-] Kamble A., Misra K., Bhattacharya D. & Sagar R., 2008, MNRAS submitted (arXiv0806.4270K)

[-] Kann D. A., Klose S., Zeh A., 2006, ApJ, 641, 993

[-] Kann D. A., et al. 2009, ApJ, submitted (arXiv:0712.2186)

[-] Kannappan S., Garnavich P., Stanek K.Z., Christlein D. & Zaritsky D., 2005, GCN, 3778

[-] Karimov R., Hafizov B., Pozanenko A. & Ibrahimov M., 2006, GCN, 5112

[-] Kawabata K.S., Deng J., Wang L., Mazzali P., Nomoto K., et al., 2003, ApJ, 593, L19

[-] Kemp, J. & Halpern, J.P., 2000, GCN, 609

[-] Kennea J.A., et al., 2006, GCN, 4776

[-] Khamitov, I., Aslan, Z., Golbasi, O., et al., 2003a, GCN 2094

[-] Khamitov, I., Bikmaev, I., Parmaksizoglu, M., et al., 2003d, GCN 2198

[-] Khamitov, I., Bikmaev, I., Galeev, A., et al., 2003e, GCN 2299

[-] Khamitov, Parmaksizoglu, M., Bikmaev, I., et al., 2003b, GCN 2108

[-] Khamitov, Parmaksizoglu, M., Uluc, K., et al., 2003c, GCN 2119

[-] Khamitov I., Bikmaev I., Sakhibullin N., et al., 2006a, GCN, 5173

[-] Khamitov I., Bikmaev I., Sakhibullin N., et al., 2006b, GCN, 5177

[-] Khamitov I., Bikmaev I., Sakhibullin N., et al., 2006c, GCN, 5183

[-] Khamitov I., Bikmaev I., Sakhibullin N., et al., 2006d, GCN, 5186

[-] Khamitov I., Bikmaev I., Sakhibullin N., et al., 2006e, GCN, 5189

[-] Khamitov I., Bikmaev I., Sakhibullin N., et al., 2006f, GCN, 5193

[-] Kindt, L., Andersen, H.H. & Jakobsen, A., 2003, GCN 2193

[-] Kinugasa K., 2008, GCN, 7413

[-] Kjernsmo, K., Jaunsen, A., Saanum, OE, Jensen, B.L., Hjorth, J., Pedersen, H. & Gorosabel, J., 2000, GCN, 533

[-] Klebesadel R.W., Strong I.B., & Olson R.A., 1973, ApJ., 182, L85

[-] Klose, S., Hoegner, C. & Greiner, J., 2003, GCN 2000

[-] Klose, S., Hoegner, C. & Greiner, J., 2003b, GCN 2029

[-] Klose S., Greiner J., Rau A., et al., 2004, AJ, 128, 1942

[-] Klotz,A. & Boër, M., 2003, GCN, 2224

[-] Klotz A., Bo´er M., Atteia J.L., Stratta G., Behrend R., Malacrino F., & Damerdji Y., 2005, A&A, 439, L35

[-] Klotz A., Bo´er M., & Atteia J.L., 2005b, GCN, 3720

[-] Klotz A., Gendre B., Stratta, G., et al., 2008, A&A, 483, 847

[-] Klotz, A., Boer, M., Atteia, J. L., & Gendre, B. 2009, A.J., 137, 4100

[-] Komiyama, Y., Kosugi, G., Kobayashi, N., et al., 2001, GCN, 1128

[-] Koppelman M., 2006, GCN, 4977

[-] Koshut, T., et al. 1995, ApJ, 452, 145

[-] Kouveliotou, C., C. A. Meegan, G. J. Fishman, N. P. Bhat, M. S. Briggs, T. M. Koshut, W. S. Paciesas, and G. N. Pendleton, 1993, Ap. J. Lett., 413, L101.

[-] Kouveliotou, C., T. Koshut, M. S. Briggs, G. N. Pendleton, C. A. Meegan, G. J. Fishman, & J. P. Lestrade, 1996, Proceedings of the 3rd Huntsville Symposium, 384, 42

[-] Kobayashi, S. & Zhang, B. 2007, ApJ, 655, 973

[-] Krimm H.A., et al., 2009, GCN Report 211.2

[-] Krugly Y., Slyusarev I. & Pozanenko A., 2008, GCN, 7519

[-] Kumar, P. & Panaitescu, A., 2000, ApJ, 541, L51

[-] Kumar, P. & Panaitescu, A., 2008, MNRAS, 391, L19

[-] Kumar, P., & Piran, T. 2000, ApJ, 535, 152

[-] Kuroda, D., Yanagisawa, K & Kawai, N., 2004, GCN, 2818

[-] Lachaume, R. & Guyon, 1999, IAUC 7096

[-] Laursen L.T. & Stanek K.Z., ApJ, 597, L107

[-] Lazzati, D. 2005, MNRAS, 357, 722

[-] Lazzati D., Covino, S. Ghisellini G., et al., 2001, A&A, 378, 996

[-] Lazzati D., Covino S., & Ghisellini G., 2002, MNRAS, 330, 583

[-] Lazzati, D., Ghisellini, G. & Celotti, A., 1999, MNRAS, 309, 13

[-] Lazzati D., & Perna R., 2007, MNRAS, 375, L46

[-] Lazzati D., Perna R., Begelman M. C., 2008, MNRAS, 388, L15

[-] Lazzati D., Perna R., Ghisellini G., 2001, MNRAS, 325, 19

[-] Lee, B.C., Lamb, D.Q., Tucker, D.L. & Kent, S., 2003, GCN 2096

[-] Levan, A., Burud, I., Fruchter, A., Rhoads, J., van den Berg, A., Homan, J., Rol, E. & Tanvir, N., 2002, GCN, 1517

[-] Levesque E., et al. 2009, GCN, 9264

[-] Li W., Filippenko A.V., Chornoch R. & Jha S., 2003b, ApJ, 586, L12

[-] Li, W., Chornock, R., Jha, S. & Filippenko, A.V., 2003, GCN 2063

[-] Li W., Jha S., Filippenko A.V., Bloom J.S., Pooley D., Foley R.J. & Perley D.A., 2005, GCN, 4095

[-] Li W., Bloom J.S., Chornock R., Foley R.J. Perley D.A. & Filippenko A.V., 2008a, GCN, 7430

[-] Li W., Chornock R., Perley D.A. & Filippenko A.V., 2008b, GCN, 7438

[-] Liang E., & Kargatis V, 1996, Nature, 381, 49

[-] Liang E. & Zhang B., 2006, ApJ, 638, L67

[-] Liang, E.W. et al., 2006, ApJ, 646, 351

[-] Lin C.S., Huang K.Y., Ip W.H. & Urata Y., 2006, GCN, 5169

[-] Lipkin, Y.M., Ofek, E.O., Gal–Yam, Mandelson, H., 2003, GCN 2034

[-] Lipkin, Y.M., Ofek, E.O., Gal–Yam, Leibowitz, E.M., Mandelson, H., 2003b, GCN 2045

[-] Lipkin, Y.M., Leibowitz, E.M., Ofek, E.O., Kaspi, S., Gal–Yam, A., Mandelson, H., 2003c, GCN 2060

[-] Lipkin, Y.M., Ofek, E.O., Gal–Yam, A., 2004, ApJ, 606, 381

[-] Lipunov, V., Krylov, A., Kornilov, V., et al., 2003, GCN 2002

[-] Lipunov, L., Krylov, A., Kornilov, V., et al., 2003, GCN, 2157

[-] Lithwick Y., & Sari R., 2001, ApJ, 555, 540

[-] Lyuty, V. & Metlov, V., 2003, GCN 2113

[-] MacFadyen A. I., Woosley S. E., Heger A., 2001, ApJ, 550, 410

[-] Malesani D., Piranomonte D., Fiore F., Tagliaferri G., Fugazza D., & Cosentino R., 2005, GCN, 3469

[-] Malesani D., Fynbo J. P. U., Jaunsen A. O., Vreeswijk P. M., 2007, GCN, 6021

[-] Mangano V., Holland S.T., Malesani D., et al., 2007, A&A, 470, 105

[-] Marshall F.E., Holland S.T. & Page K.L., 2006, GCN, 5833

[-] Martini, P., Berlind, P., Stanek, K.Z., Garnavich, P.,, 2003, GCN 2012

[-] Mescheryakov A., Burenin R., Pavlinsky M., et al., 2006, GCN, 5524

[-] Masetti, N., Palazzi, E., Pian, E., et al., 1999, GCN 233

[-] Masetti, N., Palazzi, E., Pian, E., et al., 2000, GCN, 720

[-] Masetti, N., Palazzi, E., Pian, E., Cosentino, R., Ghinassi, F., Magazzú, A. & Benetti, S., 2000b, GCN, 774

[-] Masetti, N., Palazzi, E., Pedani, M., Magazzu, A., Ghinassi, F. & Pian, E., 2001, GCN, 926

[-] Masetti, N., Palazzi, E., Pian, E., et al., 2005, astro-ph, 0504592

[-] Masi, G., Mallia, F., Tagliaferri, U., Jensen B.L., Hijorth, J., Andersen, M.I., 2003, GCN 2016

[-] Mason K.O., Blustin A.J., Boyd P. et al, 2006, ApJ, 639, 311

[-] Matheson T., Garnavich P., Hathi N., Jansen R., Windhorst R., et al. 2003a, GCN, 2107

[-] Matheson T., Garnavich P., Olszewski E.W., Harding P., Eisenstein D., et al., 2003b, GCN, 2120

[-] Matheson T. 2004. In Cosmic Explosions in Three Dimensions: Asymmetries in Supernovae and Gamma-Ray Bursts, ed. PHöflich, P. Kumar, J.C. Wheeler, p. 351. Cambridge, UK: Cambridge Univ. Press

[-] Maury, A., Boér, M. & Chaty, S., 1999, IAUC 7099

[-] McBreen S., F. Quilligan, B. McBreen, L. Hanlon, and D. Watson, 2001, A&A, 380, L31

[-] Meegan C.A., et a., 1992, Nature, 355, 143

[-] Melandri A., Gomboc A., Mundell C.G., et al., 2006a, GCN, 4968

[-] Melandri A., Guidorzi C., Mundell C.G., et al., 2006b, GCN, 5827

[-] Metzger, M.R., Djorgovski, S.G., Kulkarni, S.R., Steidel, C.C., Adlberger, K.L., Frail, D.A., Costa, E. & Frontera, F., 1997, Nature, 387, 878

[-] Milne P.A.& Williams G.G., 2008a, GCN, 7387

[-] Milne P.A.& Williams G.G., 2008b, GCN, 7432

[-] Mirabal N., Bonfield D., & Schawinski K., 2005, GCN, 3488

[-] Mirabal N., & Halpern J.P., 2006, GCN, 4792

[-] Mirabal N., Halpern J. & Thorstensen J.R., 2007, GCN, 6096

[-] Misra K., Bhattacharya D., Sahu D.K., Sagar R., Anupama G.C., Castro-Tirado A.J., Guziy S.S. & Bhatt B.C., 2007, A&A, 464, 903

[-] Molinari E., et al., 2007, A&A, 469, L13

[-] Monard B., 2005, GCN, 3728

[-] Monfardini, A., Guidorzi, C., Mottram, C.J. & Mundell, C., 2004, GCN, 2852

[-] Moretti A., Campana S., Mineo T., et al., 2005, SPIE, 5898, 360

[-] Morgan N.D. & Dai X., 2006, GCN, 5175

[-] Morgan N.D., Vanden Berk, D.E., Brown P. & Evans P.A., 2006, GCN 5553

[-] Mukherjee, S., E. D. Feigelson, G. Jogesh Babu, F. Murtagh, C. Fraley, & A. Raftery, 1998, ApJ., 508, 314

[-] Mundell C.G. & Steele I.A., 2006, GCN, 5119

[-] Mundell C. G. et al., 2007, ApJ, 660, 489

[-] Nakar E., & Piran T., 2002, MNRAS 331, 40

[-] **Nardini M.**, et al., 2006, A&A, 451, 821

[-] **Nardini M.**, et al., 2006b, Il Nuovo Cimento, 121B, 12

[-] **Nardini M.**, Ghisellini G., & Ghirlanda G., 2008a, MNRAS, 383, 1049

[-] **Nardini M.**, Ghisellini G., & Ghirlanda G., 2008b, MNRAS, 386, L87

[-] **Nardini M.**, Ghisellini G., & Ghirlanda G., 2009a, arXiv:0907.5426v1

[-] **Nardini M.**, Ghisellini G., Ghirlanda G., & Celotti A., 2009b, arXiv:0908.0338v1

[-] **Nardini M.**, Ghisellini G., Ghirlanda G., & Celotti A., 2009c, arXiv:0908.0734v1

[-] **Nardini M.**, Ghisellini G., Ghirlanda G., & Celotti A., 2009d, MNRAS, submitted (pre-print arXiv:0907.4157v1)

[-] Nava L., et al., 2007, MNRAS, 377, 1464

[-] Nava L., Burlon D., Ghirlanda G., Ghisellini, G., & **Nardini M.**, 2009, GCN, 9235

[-] Norris J. P., R. J. Nemiroff, J. T. Bonnell, J. D. Scargle, C. Kouveliotou, W. S. Paciesas, C. A. Meegan, & G. J. Fishman, 1996, ApJ., 459, 393

[-] Norris J., Barbier L., Burrows D., et al., 2005, GCN, 4013

[-] Norris J.P. & Bonnell J.T., 2006, ApJ, 643, 266

[-] Nousek J. A. et al., 2006, ApJ, 642, 389

[-] Novak R., 2005, GCN, 4027

[-] Novak R., 2008, GCN, 4504

[-] Nysewander, M., Henden, A., Lopez-Morales, M., Reichart, D. & Schwartz, M., 2003, GCN, 1861

[-] Nysewander M., Reichart D., Ivarsen K., Foster A., LaCluyze A. & Crain J.A., 2006, GCN, 5545

[-] Nysewander M., Fruchter A.S., & Pe'er A., 2008, ApJ submitted(arXiv:0806.3607v1)

[-] O'Brien P.T., et al., 2004, ApJ, 647, 1213

[-] Oates S. R. & Grupe D., 2006, GCN, 5519

[-] Oates S. R., de Pasquale M., Page M.J., et al., 2007, MNRAS, 380, 270

[-] Odewahn, S.C., Djorgovski, S.G., Kulkarni, S. R. & Frail, D.A., 1997, IAUC, 6730

[-] Odewahn, S.C., Bloom, J.S. & Kulkarni, S.R., 1999, IAUC 7094

[-] Ofek, E. & Leibowitz, E.M., 1999, GCN 210

[-] Ohashi, H., Kato, T., Senda, T., Mii, H., Mizuno, K., Yasaka, Y. & Yamaoka, H., 2002, GCN, 1515

[-] Oksanen, A., Hyvonen, H., Price, A., et al., 2001, GCN, 1019

[-] Paczynski, B., 1991, Acta Astronomica 41, 257

[-] Page K.L., Barthelmy S.D., Beardmore A.P., et al. 2006, GCN, 5823

[-] Palazzi, E., Masetti, N., Pian, E., et al., 1999, GCN, 262

[-] Palazzi, E., Masetti, N., Pian, E., et al., 2000, GCN, 691

[-] Palazzi, E., Masetti, N., Pian, E., et al., 2000b, GCN, 699

[-] Palazzi, E., Masetti, N., Pian, E., et al., 2000c, GCN, 767

[-] Palazzi, N., Pian, E., Masetti, N., et al., 1999b, GCN, 413

[-] Palazzi, N., Pian, E., Masetti, N., et al., 1999c, GCN, 449

[-] Palazzi, E., Masetti, N., Pian, E., et al., 2000a, GCN, 691

[-] Palazzi, E., Masetti, N., Pian, E., et al., 2000b, GCN, 699

[-] Palazzi, E., Masetti, N., Pian, E., et al., 2000c, GCN, 767

[-] Pal'shin V., Golenetskii S., Aptekar R.,et al. 2008, GCN, 8256

[-] Panaitescu, A. & Kumar, P., 2000, ApJ, 543, 66

[-] Panaitescu, A. & Kumar, P., 2001a, ApJ, 554, 667

[-] Panaitescu, A. & Kumar, P., 2001b, ApJ, 560, L49

[-] Panaitescu, A. & Kumar, P., 2002, ApJ, 571, 779

[-] Panaitescu, A., Mészáros, P. et al., 2006, MNRAS. 366, 1357

[-] Panaitescu, A., 2008, MNRAS, 383, 1143

[-] Pandey, S.B., Stalin, C.S. & Mohan, V., 2001, GCN, 1040

[-] Pandey S.B., Anupama G.C., Sagar R., Bhattacharaya D., Castro-Tirado, A.J., Sahu, D.K., Padmakar Parihar & Prabhu, T.P., 2003, A&A, 408, L21

[-] Pandey, S.B., Sahu, D.K., Resmi, L., et al., 2003b, Bullettin of Astronomical Society India, 31, 000-000

[-] Pandey S.B., Sagar R., Anupama Bhattacharaya, D., Sahu D.K., Castro-Tirado A.J. & Bremer M., 2004, A&A, 417, L919

[-] Pandey S.B., Castro-Tirado A.J., McBreen S., et al., 2006, A&A, 460, 415

[-] Pavlenko, E., Rumyantsev, V., Antoniuk, O., Primak, N. & Pozanenko, A., 2003a, GCN 2067

[-] Pavlenko, E., Rumyantsev, V., Antoniuk, O., Primak, N. & Pozanenko, A., 2003b, GCN 2083

[-] Pavlenko, E., Rumyantsev, V., Antoniuk, O., Primak, N. & Pozanenko, A., 2003c, GCN 2097

[-] Pavlenko E., Efimov Y., Shlyapnikov A., Baklanov A., Pozanenko A. Ibrahimov M., 2005, GCN, 3744

[-] Pe'er, A., Mészáros, P. & Rees, 2006, ApJ 652, 482

[-] Pedersen, H., Lindgren, B., Hjorth, J., Andersen, M.I., Jaunsen, A.O., Sollerman, J., Smoker, J. & Mooney, C., 1999, GCN, 192

[-] Pedersen, H., Hjorth, J., Jensen, B. L., Rasmussen, M. B., Jaunsen, A. O. & Hurley, K., 1999b, GCN, 139

[-] Pedersen, Jensen, B.L., Hjorth, J. & Gorosabel, J., 2000, GCN, 625

[-] Pedersen, Jensen, B.L., Jórvinen, A. & Andersen, M.I., 2003, GCN, 2350

[-] Pei, Y. C. 1992, ApJ, 395, 130

[-] Peng F., Königl A., Granot J., 2005, ApJ, 626, 966

[-] Perley D. A. et al., 2008a, ApJ, 672, 449

[-] Perley D.A. & Bloom J.S., 2008, GCN, 7535

[-] Perley D.A., Li, W., Chornock R., et al., 2008b, ApJ submitted (arXiv:0805.2394v2)

[-] Perna R., & Lazzati D., 2002, ApJ, 580, 261

[-] Piran, T., 1999, Phys.Rept., 314, 575

[-] Piranomonte S., Magazzu A., Mainella G., et al., 2005, GCN, 4032

[-] Piro L. et al.,1999, A&A, 138, 431

[-] Piro L. et al., 2000, Science, 290, 955

[-] Piro L. et al., 2002, ApJ, 571, 680

[-] Piro L. et al., 2005, ApJ, 623, 314

[-] Pizzichini, G., Ferrero, P., Bartolini, C., Guarnieri, A., Piccioni, A. & Righini, A., Bruni, I., 2003, GCN 2228

[-] Porciani C., & Madau P., 2001, ApJ, 548, 522

[-] Porciani C., Viel M., & Lilly S.J., 2008, ApJ, 659, 218

[-] Preece R.D., et al., 1998, ApJ., 506, L23

[-] Press W. H., Teukolosky S. A., Vetterling W. T., Flannery B. P., 1992, Numerical Recipes in C, 2nd edn. Cambridge Univ. Press, Cambridge, p. 626

[-] Price, P., Axelrod, T. & Schmidt, B., 2000a, GCN, 640

[-] Price, P., Axelrod, T. & Schmidt, B., 2000b, GCN, 898

[-] Price, P., Axelrod, T. & Schmidt, B., 2001c, GCN, 1038

[-] Price, P., Morrison, G. & Bloom, J.S., 2001d, GCN, 919

[-] Price, P., Axelrod, T., Schmidt, B. & Reichart, D.E., 2001e, GCN, 1022

[-] Price, P., Axelrod, T. & Schmidt, B., 2001f, GCN, 1038

[-] Price P.A., Kulkarni S.R., Berger E., et al., 2002, ApJ, 571, L121

[-] Price, P., Hunt, M.P. & Fox, D.W., 2002b, GCN, 1368

[-] Price, P., Schmidt, B., Axelrod, T. & Bloom, J.S., 2002c, GCN, 1441

[-] Price P.A., Kulkarni S.R., Berger E., Fox D.W., Bloom J.S., et al., 2003, ApJ, 589, 838

[-] Price P.A., Kulkarni S.R., Berger E., et al., 2002, ApJ, 571, L121

[-] Price P.A., Schmidt B.P. & Axelrod T.S., 2002, GCN 1326

[-] Price P.A., Schmidt B.P. & Axelrod T.S., 2002, GCN 1333

[-] Price, A. & Mattei, J., 2003, GCN 2071

[-] Price, A., 2003, GCN 2058

[-] Price, P., Hauser, M., Pühlhofer, G. & Wagner, S.J., 2004, GCN, 2639

[-] Protassov R., van Dyk D.A., Connors A., Kashyap V.L., & Siemiginowska A., 2002, ApJ., 571, 545

[-] Quimby R. M., Rykoff E. S., Yost S. A. et al., 2006, ApJ, 640, 402

[-] Racusin J.L., et al., 2008, Nature, 455, 183

[-] Racusin J.L., et al., 2009b, ApJ., 698, 43

[-] Rees, M. J. & M≪esz≪aros, P., 1998, ApJ, 496, L1

[-] Reeves J.N., et al., 2002, Nature, 416, 512

[-] Rhoads, J.E., Burud, I., Fruchter, A., Kouveliotou, C. & Wood-Vasey, M., 2001, GCN, 1140

[-] Rol, E., Palazzi, E., Masetti, N., et al., 1999, GCN, 358

[-] Rol, E., Vreeswijk, P., Galama, T., et al., 1999b, GCN, 374

[-] Romano, P. et al., 2006b, A&A, 450, 59

[-] Romano P., Campana S., Chincarini G., et al. 2006a, A&A, 456, 917

[-] Ruffini R. et al., 2008, Proc. XI Marcel Grossmann Meeting, in press (arXiv:0804.2837)

[-] Rumyantsev, V., Pavlenko, E., Antoniuk, O. & Pozanenko, A., 2003a, GCN 2028

[-] Rhoads 1997, ApJ, 487, L1

[-] Ruiz-Velasco A.E., Swan H., Troja E., et al., 2007, ApJ., 669, 1

[-] Rujopakarn, C., Guver T., Pandey S.B.,& Yuan F., 2009, GCN, 9515

[-] Rumyantsev, V., Pavlenko, E., Antoniuk, O. & Pozanenko, A., 2003a, GCN 2028

[-] Rumyantsev, V., Sergeeva, E., Doroshenko, V., Pavlenko. E., Antoniuk, O., Primak, N. & Pozanenko, A., 2003b, GCN 2146

[-] Rumyantsev V. & Pozanenko A., 2006, GCN, 5181

[-] Rykoff, E.S. & Smith, D. A., 2003, GCN 1995

[-] Rykoff E. S., Yost S. A., Krimm H. A. et al., 2005, ApJ, 631, L121

[-] Rykoff E. S., Mangano V., Yost S. A., et al., 2006, ApJ, 638, L5

[-] Rykoff et al., 2009, ApJ submitted (arXiv:0904.0261v1)

[-] Sagar, R., Pandey, A.K. Yadav, R.K.S., Nilakshi & Mohan, V., 1999, GCN 227

[-] Saracco, P., Covino, S., Ghisellini, S., 2001, GCN, 1205

[-] Sari, R., & T. Piran, 1997, ApJ, 485, 270

[-] Sato, R., Yatsu, Y., Suzuki, M., Kawai, N., 2003, GCN 2080

[-] Sato G., et al., 2009, GCN, 9263

[-] Sarugaku, Y., Aoki, T., Urata, Y., Huang, K.Y. & Tamagawa, T., 2004, GCN, 2537

[-] Schady P., Mason K. O., & Page M. J., 2007, MNRAS, 377, 273

[-] Schady P., Beardmore A.P., Cummings J.R., et al. 2008, GCN, 8217

[-] Schaefer, J., Savage, S., Canterna, R., Nysewander, M., Reichart, D., Henden, A. & Lamb,D., 2002, GCN, 1776

[-] Schaefer, J., Gibbs, D., Nysewander, M., Canterna, R. & Reichart, D., 2003, GCN, 2137

[-] Schlegel, D.J., Finkbeiner, D.P. & Davis, M., 1998, ApJ, 500, 525

[-] Schmidt B., Peterson B. & Lewis K., 2006, GCN, 5258

[-] Semkov, E., 2003, GCN 2179

[-] Shao L., & Dai Z. G., 2007, ApJ, 660, 1319

[-] Shao L., Dai Z. G., & Mirabal N., 2008, ApJ, 675, 507

[-] Sharapov D., Djupvik A. & Pozanenko A., 2006, GCN, 5267

[-] Silvey, J., Allen,D., Canterna, R. & Price, P.A., 2003, GCN, 2447

[-] Skvarc J., 2006, GCN, 5511

[-] Soderberg A.M., Nakar E., Cenko S.B., et al., 2007, ApJ, 661, 982

[-] Sokolov, V.V., Kopylov, A.I., Zharikov, Feroci, M., Nicastro, L. & palazzi, E., 1998, A&A, 334, 117

[-] Sollerman J., Fynbo, J.P.U., Gorosabel J., et al., 2007, A&A, 466, 839

[-] Sota A., Castro-Tirado A.J., Guziy S., Jelínek M., de Ugarte Postigo A., Gorosabel J., Bodganov A., & Pérez-Ramírez M.D., 2005, GCN, 3705

[-] Soyano T., Mito H. & Urata Y., 2006, GCN, 5548

[-] Stamatikos M., Barthelmy S.D., Baumgartner W., et al. 2008, GCN, 8222

[-] Stanek, K.Z., Garnavich, P.M. & Berlind, P., 2000, GCN, 706

[-] Stanek K.Z., Matheson T., Garnavich P.M., Martini P., Berlind P., et al., 2003, ApJ, 591, L17

[-] Stanek, K.Z., Martini, P. & Garnavich, P.M., 2003b, GCN 2041

[-] Stanek, K.Z., Latham, D.W. & Everett, D.M., 2003c, GCN 2244

[-] Stanek, K.Z., Bersier, D., Calkins, M., Freedman, D.L. & Spahr, T., 2003d, GCN 2259

[-] Stanek K.Z., Garnavich P.M., Nutzman P.A., Hartman J.D., Garg A., et al., 2005, ApJ, 626, L5

[-] Stanek K.Z., Dai X., Prieto J.L., et al., 2007, ApJ, 654, L21

[-] Stratta G., Fiore F., Antonelli L. A., Piro L., & De Pasquale M., 2004, ApJ, 608, 846

[-] Stratta G., Perna R., Lazzati D., Fiore F., Antonelli L. A., Conciatore M. L., 2005, A&A, 441, 83

[-] Stanek K.Z., Dai X., Prieto J.L., et al., 2007, ApJ, 654, L21

[-] Still M., Roming P. W. A., Mason, K. O. et al. 2005, ApJ, 635, 1187

[-] Sudilovsky V., Savaglio S., Vreeswijk P., & Ledoux C., 2007, ApJ., 669, 741

[-] Suzuki, J., Sekiguchi, T., Miyasaka, S., Aoki, T., Urata, Y. & Tamagawa, T., 2003, GCN 2116

[-] Swan H., Yuan F & Rujopakarn W., 2008, GCN, 7470

[-] Tagliaferri, G. et al., 2005, Nature, 436, 985

[-] Tanvir N.R., Perley D.A., Levan A.J., Bloom J.S., Fruchter A.S. & Rol E., 2008, GCN, 7621

[-] Tanvir N., et al., 2009, GCN, 9219

[-] Terra F., Greco G., Bartolini C., et al., 2007, GCN, 6064

[-] Toma K., Ioka K., Yamazaki R., & Nakamura T., 2006, ApJ, 640, L139

[-] Thöene C.C., Kann D.A., Johannesson G., et al., 2008, A&A submitted (arXiv:0806.1182v1)

[-] Tinney C., Stathakis R., & Cannon R., 1998, IAUC, 6896.1

[-] Torii, 2003, GCN 1986

[-] Torii, K., Kato, T., Yamaoka, H., et al., 2003, ApJ, 597, L101

[-] Torii K., & BenDaniel M., 2005, GCN, 3470

[-] Torii K., 2006a, GCN, 5642

[-] Torii K., 2006b, GCN, 5845

[-] Troja E., Cusumano G., O'Brien P. T., et al., 2007, ApJ., 665, L97

[-] Tueller J., Barthelmy S.D., Cummings, J., et al., 2007, GCN, 6954

[-] Uemura M., Arai A. & Uehara T., 2006, GCN, 5828

[-] Uemura M., Arai A. & Uehara T., 2007, GCN, 6039

[-] Uglesich, R., Halpern, J. & Thorstensen, J., 1999, GCN, 428

[-] Uglesich, R., Mirabal, N., Halpern, J.P., Vanlandingham, K., Noel-Storr, J., Wagner, R.M. & Eskridge, P., 2000, GCN, 663

[-] Uhm L. Z., & Beloborodov A. M., 2007, ApJ, 665, L93

[-] Updike A.C., Haislip J.B., Nysewander M.C., et al., 2008, ApJ, in press (arXiv:0805.1094v1)

[-] UrataY., Miyata, T., Nishiura S., Tamagawa T., Sekiguchi T., Miyasaka S. & Yoshizumi C., 2003, GCN 2106

[-] Urata Y., Chen T.W., Huang K.Y., Huang K.Y., Im M. & Lee I., 2008a, GCN, 7415

[-] Urata Y., Im M., Lee I., Huang K.Y., Zheng W.K. & Xin L.P., 2008b, GCN, 7435

[-] Vaughan S. et al. 2006, ApJ, 638, 920

[-] Van Paradijs, J., Groot, P.J., Galama, T., et al., 1997,Nature, 386, 682

[-] Veillet, C., 1999, GCN 253

[-] Veillet, C., 1999, GCN 260

[-] Vestrand, W. T. et al. 2004, Astronomische Nachrichten, 325, 549

[-] Vietri, M., 1997, ApJ, 488, L105

[-] Vreeswijck, P.M., Rol, E., Hjorth, J., et al., 1999, GCN, 496

[-] Vreeswijk P., Wijers R., Rol E., & Hjorth J., 2003, GCN, 1953

[-] Vreeswijk P. M. et al., 2004, A&A, 419, 927

[-] Vrba, F.J., Henden, A.A., Canzian, B., et al., 1999, GCN, 305

[-] Watson, D., J. N. Reeves, J. Osborne, P. T. O'Brien, K. A. Pounds, J. A. Tedds, M. Santos- Lleó, & M. Ehle, 2002, A&A, 393, L1

[-] Watson D., Fynbo J. P. U., Ledoux C. et al., 2006, ApJ, 652, 1011

[-] Watson D. et al., 2007, ApJ, 660, 101

[-] Wegner G., Garnavich P., Prieto J.L. & Stanek K.Z., 2008, GCN, 7423

[-] Willingale R. et al., 2007, ApJ, 662, 1093

[-] Woosley S. E., & Bloom J. S., 2006, Annual Review of Astronomy & Astrophysics, 44, 507

[-] Woźniak P. R., Vestrand W. T., Wren J. A., White R. R., Evans S. M. & Casperson D., 2005, ApJ, 627, L13

[-] Woźniak P. R., Vestrand W. T., Wren J. A., White R. R., Evans S. M. & Casperson D., 2006, ApJ, 642, L99

[-] Woźniak P. R., Vestrand W. T., Wren J. A. & Davis H., 2008, GCN, 7464

[-] Xing L.P., Zhai M., Qiu Y.L., Wei J.Y., Hu J.Y., Deng J.S., Urata Y. & Zheng W.K., 2007, GCN, 6035

[-] Yadigaroglu, I.A., Halpern, J.P., Uglesich, R. & Kemp, J., 1999, GCN 242

[-] Yamazaki, R. et al., 2006, MNRAS, 369, 311

[-] Yonetoku, D., Murakami, T., Nakamura, T. et al. 2004, ApJ, 609, 935

[-] Yoshida, A., M. Namiki, C. Otani, N. Kawai, T. Murakami, Y. Ueda, R. Shibata, & S. Uno, 1999, A& A, 138, 433

[-] Yoshida M., Yanagisawa K. & Kawai N., 2007, GCN 6050

[-] Yoshida M., Yanagisawa K., Shimizu Y., Nagayama S., Toda H. & Kawai N., 2008, GCN, 7410

[-] Yost S.A., Swan H.F., Rykoff E.S., et al., 2007, ApJ, 168, 925

[-] Zerbi, R. M. et al. 2001, Astronomische Nachrichten, 322, 275

[-] Zhang, B. & Mészáros, P., 2002, ApJ, 566, 712

[-] Zhang, B. & Mészáros, P., 2004, nternational Journal of Modern Physics, 19, 2385

[-] Zhang B. et al., 2006, ApJ, 642, 354

[-] Zhang B., 2007, Adv. Space Res., 40, 1186

[-] Zhang B., Zhang W., Woosley S. E., Heger A., 2007a, ApJ, 679, 639

[-] Zhang B., et al., 2007b, ApJ, 666, 1002

[-] Zhang Z.B. & Choi C.S., 2008, A&A, 484, 293

[-] Zharikov, S., Benitez, E., Torrealba, J. & Stepanian, J., 2003a, GCN 2022

[-] Zharikov, S., Benitez, E., Torrealba, J. & Stepanian, J., 2003b, GCN 2075

[-] Zharikov, S. & Tovmassian, G., 2003c, GCN 2265

[-] Zharikov, S., Tovmassian, G. & Richer, M., 2003d, GCN 2171

[-] Zhu, J. & Zhang, H.T., 1999, GCN 204

[-] Zhu, J. & Zhang, H.T., 1999, IAUC 7095

[-] Zhu, J., 2000, GCN, 904

[-] Zhu, J., 2001, GCN, 946